



**HAL**  
open science

# Developing a wearable automated system for measuring bio-impedance

Umme Tabassum Sarah

► **To cite this version:**

Umme Tabassum Sarah. Developing a wearable automated system for measuring bio-impedance. Micro and nanotechnologies/Microelectronics. Université Gustave Eiffel, 2023. English. NNT : 2023UEFL2041 . tel-04299941

**HAL Id: tel-04299941**

**<https://theses.hal.science/tel-04299941v1>**

Submitted on 22 Nov 2023

**HAL** is a multi-disciplinary open access archive for the deposit and dissemination of scientific research documents, whether they are published or not. The documents may come from teaching and research institutions in France or abroad, or from public or private research centers.

L'archive ouverte pluridisciplinaire **HAL**, est destinée au dépôt et à la diffusion de documents scientifiques de niveau recherche, publiés ou non, émanant des établissements d'enseignement et de recherche français ou étrangers, des laboratoires publics ou privés.

Une thèse présentée pour l'obtention d'un diplôme de doctorat de

**Université Gustave Eiffel**  
**ÉCOLE DOCTORALE Mathématiques, Sciences et Technologies de**  
**l'Information et de la Communication (MSTIC)**

**Thèse de doctorat**  
**Electronique, Optronique et Systèmes**

**Umme Tabassum SARAH**

**Comparison of Electrodes with Conventional, and Non-  
Conventional Biomaterials to Novel Full Diamond  
Electrodes for Biomedical Applications**

Cette thèse a été menée à l'ESIEE Paris - Université Gustave Eiffel (UGE,  
France), et laboratoire ESYCOM et est soutenue le **11 juillet 2023** devant le  
jury de thèse composé de :

<b>Marjorie Lucas-GRZESKOWIAK</b>	<b>MCF - HDR</b>	<b>Institut National des Sciences Appliquées</b>	<b>Rapporteure</b>
<b>Christian BERGAUD</b>	<b>Directeur de Recherche</b>	<b>LAAS CNRS</b>	<b>Rapporteur</b>
<b>Marie FRÉNÉA-ROBIN</b>	<b>Professeure</b>	<b>Université Lyon 1</b>	<b>Examinatrice</b>
<b>Bruno Le PIOUFLE</b>	<b>Professeur</b>	<b>ENS Paris Saclay</b>	<b>Président du Jury Examineur</b>
<b>Lionel ROUSSEAU</b>	<b>Dr. Ingénieur Process en BIOMEMS (HDR)</b>	<b>Université Gustave Eiffel</b>	<b>Directeur de thèse</b>
<b>Patrick POULICHET</b>	<b>Enseignant-Chercheur</b>	<b>Université Gustave Eiffel</b>	<b>Co-encadrant</b>
<b>Hakim TAKHEDMIT</b>	<b>MCF</b>	<b>Université Gustave Eiffel</b>	<b>Co-encadrant</b>



## Acknowledgment

I would like to thank everyone who helped me throughout the period of this thesis, my professors, colleagues, peers, friends, and family. I am deeply grateful for their individual and timely contribution.

First of all, the heartfelt director of my thesis, Lionel Rousseau, was there for me every step of the way and guided me to finish my work until the end. My supervisors Patrick POULICHET and Hakim TAKHEDMIT, who was always there to help me steer me in the right direction even when they had extremely hectic schedules already. On multiple occasions, Lionel stayed after working hours to have meetings with me, Patrick ran back and forth in between his countless hours of classes, labs, and students, and Hakim came to ESIEE for every meeting from UPEM' for these my gratitude and thanks to them. Last but not least, Olivier Francais and Gaëlle LISSORGUES were a part of the brilliant team who guided me throughout the thesis with their infinite wisdom, knowledge, and counsel without which I could not have possibly come thus far.

My thanks and gratitude go to the entire SMM team, namely Magdalena, Alexandre, Nicolas, Fred, and Serge, from whom I learned the tips and tricks of becoming an expert in cleanroom technology.

I would like to extend my appreciation towards our professors, researchers, and collaborators of the project NEURODIAM in l'Institut de la Vision (IDV), Commission de l'Énergie Atomique (CEA), University Grenoble Alpes (UGA) who helped make this work into fruition.

My regards and thanks to Marjorie GRZESKOWIAK-LUCAS, Christian BERGAUD, Marie FRÉNÉA-ROBIN, and Bruno Le PIOUFLE for sparing the time for reading, evaluating the manuscript, and being present in my thesis defense.

Subsequently, I would like to thank my talented colleagues, many of whom I am lucky enough to call my dear friends viz. Jaafar, Claudi, Francesco, Antonella, Thuy, Jordan, and Issam, through whom I got to know Jonathan, Ophelie, Marine, Quyt, Oi, and Devi (Names in chronological order in which I met them). Working with Claudi and Thuy has taught me more about being meticulous, focused, precise, and goal-oriented than I could have ever expected.

It would not be possible for me to finish and accomplish the enormous task without Kim, who provided me with a home away from home and helped me through my toughest periods, Jeff, and Jennifer who were the beacon of joy in dark times, Jason, who has helped me with his infinite patience when I felt like giving up, and Layla who was there for me with her incomparable wisdom and level-headedness, friendship, and support.

I would like to thank Taika and Catherine for providing me with the warmth I needed to feel like a human being amidst all the pressure and aloofness of being a researcher and a Ph.D. student.

I would also like to extend my indebtedness to my family, my mammony, baba, miang, and chia, who have always been my anchor and my last resort to turn to when I had no

one else by my side. By the time of editing this thesis, beautiful and precious baby Irina had already been born with such bigidi energy! I cannot finish this section without thanking my dear friends Nosheen, Plats, Kecho, Nuves, Gen, Shaily, and Sushmita Apu. They have been by my side through thick and thin. They were the only people who never left my side, and I knew that I could always rely on them. These people are my forever!

One must separate their personal life from their career, is the popular opinion. However, as a scientist, specifically a PhD candidate, it can sometimes be very difficult to do so. As it is the scientist who interprets the truth in their vernacular based on scientific truth and logic. A Ph.D. is the first and one of the most important steps in an academic's life in terms of embracing what kind of scientist one will become. For the author, it was very difficult at times to separate herself from the external turmoil happening globally, and on a personal level as well.

In the beginning, the project provided a very broad scope to explore, which can be considered both a blessing and a disadvantage in disguise. In a sense, as a researcher when presented with an opportunity to explore multiple interesting topics, it often poses a challenge to abandon some of the tasks. The desire to explore all the aspects was overwhelming and it is a strong probability given the opportunity to do it again, it could have been beneficial if one of the fields was chosen right away. Standing in the present, it would have been microfabrication. However, in all fairness, if given an opportunity to do the thesis again, the temptation of knowing all the parts at least a little to get a global idea of the whole project, it is difficult for me to promise that the opportunity would not be easily passed on!

The first year of the project was on and off remote work due to the global pandemic, so work possible via distance like bibliography and understanding the electronics in use, etc. was done in this period.

Soon after, it was time for mid-defense, and it was suggested by the mid-defense jury to take a more focused approach to the research topic. At that time, it was put as the focus of the thesis going forward.

It was not until the middle of the second year that the focus of the thesis was steered to microfabrication. I am appreciative of the fact that the vast and interesting field of microfabrication was opened in front of her to learn and explore further. As of now, it was determined that the researcher would pursue the field of microfabrication as the future field of study.

The unforeseeable personal difficulties suffered amid the contract were something that hindered the advancement of the project on multiple occasions. As a result, the project seemed daunting and overwhelming to me at times, and took more than the anticipated amount of time to finish the writing process. I am hopeful about the prospects of the project because establishing the protocol is the most time-consuming and complicated part and since it is already done, developing the technology will hopefully be smooth proceeding onward.

Finally, I would like to remind myself of the enormous feat I accomplished despite being in one of the most disadvantageous situations in my entire life and would like the future me to acknowledge and remember what I went through and how I accomplished what I did. This is a reminder to myself to extend the same kindness I have always tried my best to extend to everyone around me.

## Glossary

AC	Alternate Current
AD2	Analog Discovery 2
AlN	Aluminum Nitride
AM	Additive Manufacturing
AMP	Age Related Molecular Degeneration
AP	Action Potential
BBB	Blood Brain Barrier
BDD	Boron Doped Diamond
BIS	Bio Impedance Spectroscopy
BPF	Band-Pass Filter
Ct	Carat
CE	Counter Electrode
CNS	Central Nervous System
CNTs	Carbon Nanotubes
CPE	Constant Phase Element
CV	Cyclic Voltammetry
CVD	Chemical Vapor Deposition
DBS	Deep Brain Stimulation
DEXA	Dual X-ray absorptiometry
DLC	Diamond-like Carbon
DUT	Device Under Test
ECoG	Electrocorticography
EDLC	Electric Double Layer Capacitance
EIS	Electrochemical Impedance Spectroscopy
ERC	European Research Council
FDA	Food and Drug Administration
GIA	Gemological Institute of America
GLC	Graphite-like Carbon
GO	Graphene-Oxide

HDL	Helmholtz Double Layer
HMI	Human Machine Interface
HPHT	High-Pressure High Temperature
IDA	Interdigitated Electrode Array
IDE	Interdigitated Electrodes
IR	Infra-Red
MCN	Melbourne Centre for Nanofabrication
MEA	Micro Electrode Arrays
MPCVD	Microwave Plasma Chemical Vapor Deposition
MUI	Material Under Investigation
NCD	Nanocrystalline Diamond
NV	Nitrogen-Vacancy
NIH	National Institutes of Health
NP	Nanoparticles
PBS	Phosphate Buffer Saline
PCD	Poly Crystalline Diamond
PDDAC	Poly Diallyl-Dimethyl-Ammonium Chloride
PEB	Post-Exposure Bake
PL	Photoluminescence
PPy	Polypyrrole
PVD	Physical Vapor Deposition
RE	Reference Electrode
RIE	Reactive Ion Etching
RMIT	Royal Melbourne Institute of Technology
RF	Radio Frequency
RP	Retinitis Pigmentosa
RPE	Retinal Pigment Epithelium
RSD	Relative Standard Deviation
SiC	Silicon Carbide
SEM	Scanning Electron Microscope
SLM-Ti	Selective Laser Melting Titanium
SNR	Signal-to-Noise Ratio
STE	Strip Type Electrodes

TiN	Titanium Nitride
TMB	Trimethylboron
TSA	Top Side Alignment
US	Ultrasound
WE	Working Electrode
VEP	Visual Evoked Potential





## PROLOGUE

The technological excellence of the 21st century has allowed blessed humanity with improvements in medical sciences and biotechnology, thus extending not only the life span but also the quality of life dramatically. Recent scientific findings and developments have enabled scientists, researchers, doctors, and engineers from various fields to share their knowledge and collaborate toward a common goal. Things that existed only in science fiction and the imagination of the hopeful are now starting to become reality. One of the “never thought of before” developments is the current advancement in the field of biotechnology. The revolutionary **Brain Computer Interface (BCI)** has paved the way for scientific researchers everywhere to help fight birth defects, traumatic loss of a limb, and/or motor function of a specific area. BCI incorporates biomedical implants with an external electrical or electronic device to read, write (stimulate), or store (record) the data from the local tissue.

With an astounding vision of fabricating full Diamond implants on a micro-scale for application in medical sciences, the project NEURODIAM [1] has been working since 2018. This manuscript presents the work and advancement of the NEURODIAM project from a research and development angle.

The researchers of this project have previously been involved in different national (ANR) and European (FP7) projects in the last few years to develop innovative fabrication processes for microelectrode arrays. Over the years, members of this project have developed expertise in the different microfabrication techniques for various implants, electrodes, and **Micro Electrode Arrays (MEAs)**. Project ERC – NEURODIAM (758700) (has also been the inspiration behind establishing multiple interdisciplinary collaborations with different groups working in this field. The current collaborators are attached with **l’Institut de la Vision (IDV)** in Paris, **Commission de l’Énergie Atomique (CEA)**, and **University Grenoble Alpes (UGA)** to name a few. The team in IDV deals with the in-vivo experimentation of the sub-retinal implants fabricated in the ESIEE cleanroom under the NEURODIAM project. CEA collaborators provide their expertise and consultancy in the growth of the Diamond layer (Both Intrinsic and Doped).

The idea of **Chapter-1** is to give some basic ideas about the vast topic that is bio-implants and how they relate to this thesis. The goal of project NEURODIAM is to fabricate flexible, full Diamond electrodes or **Micro-Electrode Arrays (MEA)**, which would have various applications in bio-medical fields.

Going forward, this thesis demonstrates the bottom-up approach to characterizing a specific metal from laboratory to in-vitro tests and with the possibility to incorporate that technology for application in-vivo, and later animal testing, which is some of the steps of fabricating bio-implants. An infographic (*see Figure A*) here shows how the broad topic of Biomedical implants has been narrowed down to the thesis topic which is an integral part of NEURODIAM.

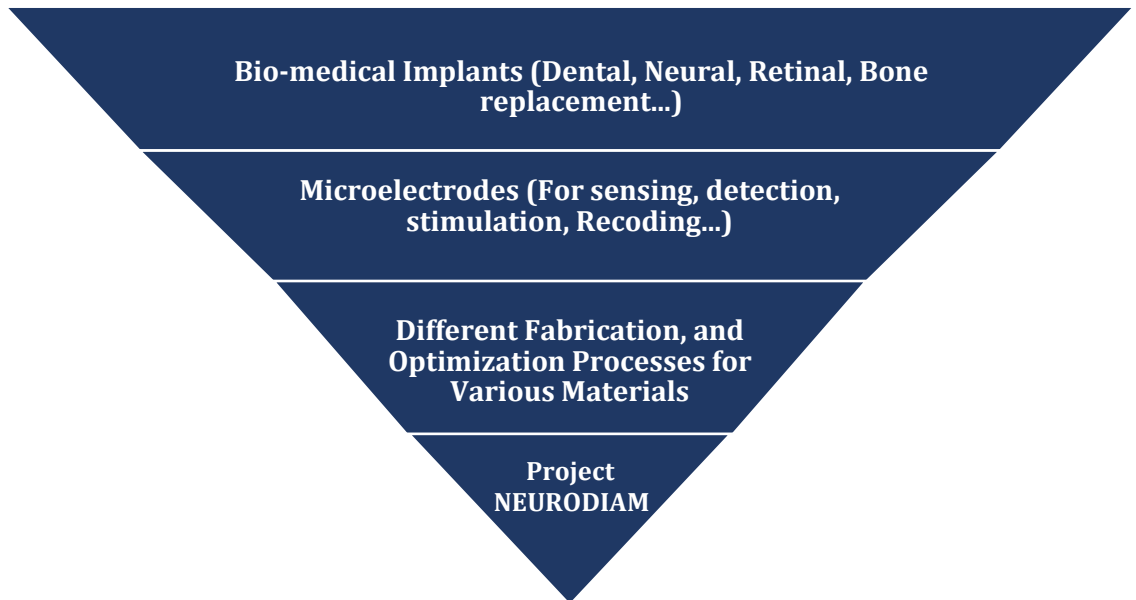


*Figure-A Graphical representations of the simplified flow of progression on the thesis*

**Chapter 2** is a more narrowed-down version of the materials used and the different types of electrodes, details of the microfabrication process used in the thesis, in short, methods used in characterization, and the rationales behind those. To begin with, the chapter breaks down the fabrication procedure of the different types of electrodes to understand the different parts of the samples (conducting and non-conducting parts) using conventional materials, e.g.: Gold and SU8. The Chapter starts showing the progression of employing different materials like TiN, black TiN, etc. This chapter explains in detail the different methods used using specific protocols and equipment in the cleanroom. This chapter also shows the treatment methods employed for different samples at various stages.

**Chapter 3** demonstrates the characterization of the electrodes and how this helps achieve the final goals. This chapter entails the characteristics of different materials using multiple electrochemical operations, graphic representation tools, and theoretical calculations. During the fabrication process in the cleanroom, due to the complex, multiple-step fabrication process, sometimes unforeseeable circumstances might appear post-fabrication. Different methods were employed and researched as this thesis went along with analyzing and comparing performance results of different

materials based on shapes, sizes, fabrication methods, different cleaning methods employed for ameliorating the samples, etc. Some of the experiments were compared with established results and showed the relevance of the study. This chapter also presents the equivalent circuit models which were made with data extrapolated from the experimental results to show an electrical representation of the experimental data. Theoretical calculations were done to observe the calculated value of different parameters and observe the consistency of the calculation and the experimental data.

**Chapter 4** presents the simulation results using the COMSOL software of different samples and setups to understand the results in the different experimental environments. Subsequently, this chapter presents the experimental setup for the long-life setup to test the longevity of the samples, which would show the samples superiority of the proposed samples over the conventional materials. This chapter presents the complexity of setting up the experiment bench for the first time and the trial-and-error methods of finding a setup that provided the presented result.

Lastly, **Chapter 5** paints a picture of the whole project to show where the manuscript has concluded presenting this thesis and the prospect along with ongoing work regarding publications. This chapter also provides the Author's vision and perspective of the thesis.

To summarize, this Ph.D. manuscript presents the work done with the target of fabricating the first-ever full Diamond implants. To that end, the thesis was done in a "bottom-up" approach. To begin with, conventional materials were used (as both conductive and non-conductive or passivation layers) to fabricate electrode samples to understand and study the behavior of traditional matter in an electrochemical environment. This study paved the way for fabricating electrodes of similar shapes and sizes, with different materials to optimize performance, and ensure longevity while managing overall production costs, etc. Later, different shapes and structures for different materials were employed to ameliorate and enhance the performance of the electrode, resulting in the implants. Another part of this thesis was to prove the superiority of Diamond over conventional materials not only in terms of performance, thinness, and hermeticity but also in its ability to withstand the hostile environment of the human body. To that end, a longevity test setup was installed and improved step by step to demonstrate the lasting performance of the full Diamond samples.

In the first chapter, all the ideas that were necessary going into starting this thesis work are presented. The second chapter gives a clear, chronological approach to the workflow of the thesis, which includes the work done toward microfabrication and optimization of the implants. The third chapter shows the results and analytic findings of the experimental work. The fourth chapter presents a protocol in detail to inspect the superiority of intrinsic Diamond over SU8, a conventional bio-compatible passivation material. The accelerated aging experiment shows the superior performance of the Diamond layer as the passivation layer over the conventional SU8 passivation layer. Last but not least, the fifth chapter presents the future perspective and possibilities around the project and the author's intended vision for it going further.



## PREAMBLE

L'excellence technologique du XXI<sup>e</sup> siècle a permis à l'humanité de bénéficier d'améliorations dans le domaine des sciences médicales et de la biotechnologie, ce qui a permis d'allonger non seulement la durée mais aussi la qualité de la vie, comme jamais auparavant. Les découvertes et les développements scientifiques récents ont permis aux scientifiques, aux chercheurs, aux médecins et aux ingénieurs de divers domaines d'unir leurs connaissances et de collaborer à l'objectif d'éradiquer les difficultés de l'existence humaine. Des choses qui n'existaient que dans la science-fiction et dans l'imagination des intrépides sont maintenant devenues réalité. L'une de ces évolutions "jamais imaginées auparavant" est l'avancée actuelle dans le domaine de la biotechnologie. **L'Interface Cerveau-Ordinateur (ICO)** révolutionnaire a ouvert la voie aux chercheurs scientifiques du monde entier pour les aider à lutter contre les malformations congénitales, la perte traumatique d'un membre et/ou la fonction motrice d'une zone spécifique. La BCI intègre des implants biomédicaux avec un dispositif électrique ou électronique externe pour lire, écrire (stimuler) ou stocker (enregistrer) les données du tissu local.

Avec une vision étonnante de la fabrication d'implants entièrement en diamant à l'échelle microscopique pour une application dans les sciences médicales, le projet NEURODIAM [1] travaille depuis 2018. Ce manuscrit présente les travaux et l'avancement du projet NEURODIAM sous l'angle de la recherche et du développement.

Les chercheurs de ce projet ont précédemment été impliqués dans différents projets nationaux (ANR) et européens (FP7) au cours des dernières années afin de développer des procédés de fabrication innovants pour les réseaux de microélectrodes. Au fil des années, les membres de ce projet ont développé une expertise dans les différentes techniques de micro-fabrication pour divers implants, électrodes et réseaux de **Microélectrodes (MEA)**. Le projet NEURODIAM a également été à l'origine de l'établissement de multiples collaborations interdisciplinaires avec différents groupes travaillant dans ce domaine. Les collaborateurs actuels sont rattachés à **l'Institut de la Vision (IDV)** à Paris, au **Commissariat à l'Énergie Atomique (CEA)**, et à **l'Université Grenoble Alpes (UGA)** pour n'en citer que quelques-uns. L'équipe de l'IDV s'occupe de l'expérimentation in-vivo des implants sous-rétiniens fabriqués dans la salle blanche de l'ESIEE dans le cadre du projet NEURODIAM. Les collaborateurs du CEA apportent leur expertise et leurs conseils pour la croissance de la couche de diamant (intrinsèque et dopée).

Ce manuscrit de thèse présente le travail effectué dans le but de fabriquer les tout premiers implants entièrement en diamant. À cette perspective, l'ensemble de la thèse a été réalisée selon une approche "Bottom-up". Pour commencer, des matériaux conventionnels ont été utilisés (à la fois comme couches conductrices et non conductrices ou de passivation) pour fabriquer des échantillons d'électrodes afin de comprendre et d'étudier le comportement de la matière traditionnelle dans un environnement électrochimique. Cette étude a ouvert la voie à la fabrication d'électrodes de formes et de tailles similaires, mais avec des matériaux différents pour optimiser les performances et assurer la longévité tout en gérant les coûts de production globaux, etc. Plus tard, des formes et des structures différentes pour des matériaux différents ont été utilisées pour améliorer et renforcer les performances de l'électrode, et par conséquent des implants. Une autre partie de cette thèse consistait à prouver la supériorité du diamant sur les matériaux conventionnels non seulement en termes de performance, de finesse et d'herméticité, mais aussi dans la capacité à

résister à l'environnement hostile du corps humain. À cette fin, une installation de test de longévité a été installée et améliorée étape par étape pour obtenir une preuve irréfutable de la performance à long terme des échantillons de diamant complets.

Le premier chapitre présente toutes les idées qui ont été nécessaires pour commencer ce travail de thèse. Le deuxième chapitre donne une approche claire et chronologique du déroulement de la thèse, qui inclut le travail effectué pour la micro-fabrication et l'optimisation des implants. Le troisième chapitre présente les résultats et les conclusions analytiques du travail expérimental. Enfin, le dernier chapitre, présente les perspectives et les possibilités futures du projet et la vision de l'auteur pour l'avenir.

## **Table of Contents**

1. Context of the Thesis.....	4
1.1 Bio-Medical Context.....	5
1.1.1 Nervous System & Neural System .....	5
1.2 Existing Technology for Bio-implants.....	9
1.2.1 Visual Prostheses and Implants.....	9
1.2.1.1 Optical Nerve Stimulator.....	10
1.2.1.2 Epiretinal Stimulator .....	11
1.2.1.3 Subretinal Stimulator .....	12
1.2.2 Neural Implants and Prostheses .....	13
1.2.2.1 Neural Implants for Stimulation and Recording .....	14
1.2.2.2 Deep Brain Stimulation (DBS) .....	14
1.2.2.3 Epidural Stimulation.....	15
1.2.2.4 Neural Prostheses .....	15
1.3 Electrodes Criteria.....	16
1.3.1 No Cytotoxicity or Biocompatibility .....	16
1.3.2 Durability.....	17
1.3.3 Young's Modulus.....	17
1.3.4 Electrical Property.....	18
1.3.5 Bio-Inertia Effects.....	19
1.4 Limitations of the Existing Technology.....	20
1.4.1 Biological failure .....	20
1.4.2 Material Failure.....	21
1.4.3 Mechanical Failure.....	22
1.5 Carbon as a Bio-implant Material.....	23
1.5.1 Why Diamond.....	25
1.5.2 Diamond for Project NEURODIAM .....	27
1.6 Take Away from this Chapter.....	28
2. Microfabrication & Cleanroom Procedures.....	28
2.1 Different Types of Electrodes Fabricated.....	31
2.1.1 Interdigitated Electrode (IDE) .....	31
2.1.1.1 Primary Version of the Mask.....	32
2.1.1.2 Second version of the Mask.....	33
2.1.2 Strip Type Electrode (STE).....	34
2.2.1.1 Mask.....	35
2.2.1.1 Circular STE.....	36
2.2.1.2 Hexagonal STE.....	36



*Comparison of Materials for Fabrication of Implants for Functional Rehabilitation*

2.2.1.3 Honeycomb Structure .....	37
2.2.1.4 Noble Material Electrodes (Gold and Platinum Microfabrication.....	38
2.2.2 Different Methods of Diamond Fabrication .....	42
2.2.2.2 3-Dimensional (3-D) Printing .....	43
2.2.2.3 Chemical Vapor Deposition.....	44
2.2.3 Diamond Microfabrication Process.....	45
2.2.4 Titanium Nitride (TiN) Fabrication.....	46
2.2.5 TiN-Pt-TiN Stack Model.....	48
2.3 CLEANROOM Characterization Process.....	48
2.3.1 Short-cut test after fabrication.....	48
2.3.2 Optical Microscope, Profilometer, and Scanning Electron Microscope (SEM)..	49
2.4 Post-Fabrication Process in Cleanroom (Electrode Cleaning or Activation.....	50
2.4.1 Oxygen Plasma Cleaning (Cleaning Method - 1) .....	51
2.4.2 UV and H <sub>2</sub> O <sub>2</sub> Cleaning (Cleaning Method - 2).....	51
2.4.3 Acetone and IPA Cleaning with Ultrasound (US) (Cleaning Method - 3).....	52
2.4.4 Acid Clean (Cleaning Method - 4).....	52
2.4.5 Black TiN .....	53
2.4.6 UV Treatment for Full Diamond Electrodes .....	54
2.5 Take Away from This Chapter.....	554
3. Experimental Comparison of Different Materials in IDE and Microelectrodes.....	53
3.1 Physical Electrochemistry and Equivalent Circuit Elements.....	58
3.1.1 Bio-Impedance Spectroscopy (BIS) .....	58
3.1.2 Cyclic Voltammetry (CV) .....	64
3.1.4 Some Popular Equivalent Circuits .....	66
3.2 Different Equipment Used for Characterization.....	67
3.2.1 The Arduino UNO with AD5933 Shield .....	67
3.2.2 Analog Discovery 2 .....	68
3.2.3 EC Lab.....	68
3.2.4 Hewlett Packard 4194A .....	69
3.2.5 Home-made multiplexer.....	69
3.3 Equivalent/Fit Circuit.....	71
3.4 Experimental Comparison of Different Materials in IDE.....	72
3.4.1 Primary Design of the Mask .....	72
3.4.1 Gold IDE Covered in SU8 .....	73
3.4.2 TiN-Pt-TiN IDEs.....	77
3.5 Second Version of the Mask.....	79
3.5.1 TiN-Pt-TiN IDEs.....	80

3.6 Microelectrodes with Different Materials.....	84
3.6.1 Gold (Au) Electrodes with SU8 as Passivation .....	86
3.6.1.1 Electrical Impedance Spectroscopy (EIS) .....	86
3.6.1.2 Fit Parameters .....	88
3.6.2 Platinum (Pt) Electrodes with SU8 as Passivation.....	91
3.6.2.1 Electro-Impedance Spectroscopy (EIS) .....	91
3.6.2.2 Fit Parameters .....	93
3.6.2.3 EIS in Different Concentrations.....	94
3.6.2.4 Comparison Between the Potentiostat and AD2 (Clean Platinum).....	95
3.6.2.5 Cyclic Voltammetry (CV) in Clean Platinum Electrodes.....	96
3.6.4 TiN-Pt-TiN Electrodes with SU8 as Passivation.....	97
3.6.5 Black TiN .....	101
3.6.5.1 EIS in Black TiN .....	102
3.6.5.2 Light Absorption Test.....	103
3.6.5.3 Cyclic Voltammetry in Black TiN .....	104
3.6.5.4 Fit Parameters .....	106
3.6.6 Diamond Electrodes .....	109
3.6.6.1 Impedance Spectroscopy .....	109
3.6.6.2 Fit Parameters .....	111
3.6.6.3 CV of Full Diamond Electrodes .....	112
3.7 Different Cleaning Methods.....	113
3.8 Take Away from this Chapter .....	114
4. Longevity Test.....	116
4.1 Introduction and General Purpose of Ageing Tests.....	117
4.1.1 Ageing Test Set-Up Description.....	120
4.2.2 Automatic Data Collection with Analog Discover 2.....	121
4.2 Preparing Samples.....	122
4.2.1 Impedance measurement.....	123
4.3.1 Replacement of PCB With Wire .....	125
4.3 Establishment of Experimental Protocol.....	125
4.3.2 Primary Experimental Protocol.....	126
4.3.1 Second Packaging for the Long-Life Experiment.....	127
4.4 Results of Long-Life Setup.....	128
4.4.6 Scope of Improvement in the Experimental Set-up .....	133
4.5 Take Away from this Chapter .....	133
5. Conclusion and Final Statement.....	130
5.1 Future Work.....	137

5.2 Summary of the Thesis.....	137
5.3 Personal Statement.....	138
A.1 Fabrication Methods.....	140
A.1.1 Thermal Oxidization of the Silicon Wafer .....	140
A.1.2 Priming/Wetting of the Wafer .....	140
A.1.1.1 Cathodic Pulverization.....	141
A.1.1.2 Photolithography Process .....	143
A.1.1.3 Etching of the Metal .....	146
A.1.1.4 Passivation layer .....	147

## **Chapter 1**

### **Context of the Thesis**

With technological improvement, the interface between medical implants [2] and the human nervous system has been growing rapidly and proving to be more and more efficient, yet complex. This rise in complexity is driving the need for increasing numbers of densely packed electrical feedthrough [3] to carry signals to and from the implanted devices [4], commonly mentioned in literature as microelectrodes, **Micro Electrode Arrays (MEA)**, implants, biomedical implants, or bio-implants. In the field of bio-implant various micro and nano-scale fabrications have been made popular. This is particularly crucial in the field of neural prosthesis [5] where high-resolution stimulating or recording arrays near peripheral nerves or in the brain could dramatically improve the performance of these devices. With the target of fabricating and optimizing a full Diamond implant on a microscale with conducting **Boron Doped Diamond (BDD)** with intrinsic polycrystalline Diamond [6] as passivation, project NEURODIAM was launched in 2018. **NEURODIAM** has a 'Starting Grant' worth 1.49 million euros from the **European Research Council (ERC)** to finance and develop the design over the coming five years [1]. The **NEURODIAM** design substantially consists of negotiating new **ECoG (Electrocorticography)** thin implants grounded on Diamond nano structure combined with microtechnology.

As a part of this project, this thesis focuses on understanding the nature and function of conducting and non-conducting parts comparing different materials and methods of their fabrication. Multiple electrical and electrochemical tests were done to collect data for the understanding of the performances of the said devices. The materials used for fabrication are all shown to be non-cytotoxic. New fabrication strategies, such as the one described here, combined with the exceptional biostability of Diamond can be employed to generate a range of biomedical implants that last for the lifetime of the user without fear of degradation [3], [7] while providing one of the best performances in different sectors compared to a lot of other existing options.

## 1.1 Bio-Medical Context

Bio-implants are, simply put, man-made medical devices [8] manufactured to replace a missing biological structure, support a damaged biological structure, enhance an existing biological structure, and receive and/or record transmit data from and to various body parts; whereas transplants [9] involve generated or fabricated biomedical components. The surface of implants that contact the body might be made of a biomedical material [10]–[12] such as Gold [13], Titanium [14], [15], Silicone [16]–[19], or Apatite [19]–[22], etc., various alloys [23], or different carbon-based allotropes [24] depending on what is the most functional and useful to the specific cause [25]. In some cases, implants contain electronics, e.g. artificial pacemakers [14], [26] cochlear implants. Some implants are dedicated to the stimulation and recording of data from neural networks [27]. Some implants are bioactive [28], such as subcutaneous [29] drug delivery devices in the form of implantable pills or drug-eluting stents [28].

### 1.1.1 Nervous System & Neural System

The neuron is the primary practical unit of the nervous system, and it is responsible for receiving, processing, and transmitting information between the numerous specific parts of the body. Hence, they play a key position in the information exchange between the sensory receptors distributed all over the body and brain, as well as in the transmission of facts from the brain to the muscle tissues [30].

An average neuron (*see Figure 1-1 (a, b, c)*) gives several morphological characteristics to the cellular body or soma with the nucleus and one-of-a-kind organelles; the small dendrites branched extensions around the soma and acquire data from different neurons, and the axon is an extended extension in the price of undertaking the electrical impulses from the soma to another cellular. Unlike the dendrites, axons may be very lengthy, attaining lengths up to 1 meter inside the human body which permits them to move distinct signals between two remote points.

To insulate this long axon and speed up the propagation of the action potential, there are multiple cells coiled around the axon (Shawn cells), that produce a substance known as myelin that insulates it from the environment. The areas of the myelinated axons that are not covered by those systems are called Ranvier nodes [27].

As per their respective characteristics, neurons can be labeled as sensory, motor, and interneurons. Sensory neurons (also known as afferents) transmit information from sensory receptors or internal organs to the cerebra-spinal nervous system (also known as the central nervous system). Motor neurons (also known as efferent), transmit signals from the significant stimulation to the effector organs, particularly muscle tissues, and glands. Subsequently, there is a third type of neuron placed among motor and sensory pathways that are concerned with signal integration, and most of these are integrated within the crucial apprehensive system. Neural conversation has a double nature: electric and chemical. Electrical signals propagate via the axon of the neuron and, the transmission among neurons is mounted with the aid of electrical or chemical synapse [27], [31].

In electric synapses, the charge passes from the axon of a neuron to the dendrite of some other. In chemical synapses, the neuron releases a chemical referred to as a

neurotransmitter into the medium via a few systems within the membrane of the neuron, which may additionally initiate an electrical reaction with the subsequent neuron [32], [33].

The part of the neuron that plays an imperative role in this mechanism is the membrane. The membrane consists of a lipid bilayer that isolates the cell cytoplasm of the cellular from the medium, and it has some embedded proteins that manage the ionic change between the intracellular and the extracellular medium (*see Figure 1-2*). These proteins called ion channels and ion pumps (also known as transporters), accommodate ions to diffuse down the awareness gradient and actively circulate ions against the gradient of concentration [33]–[35].

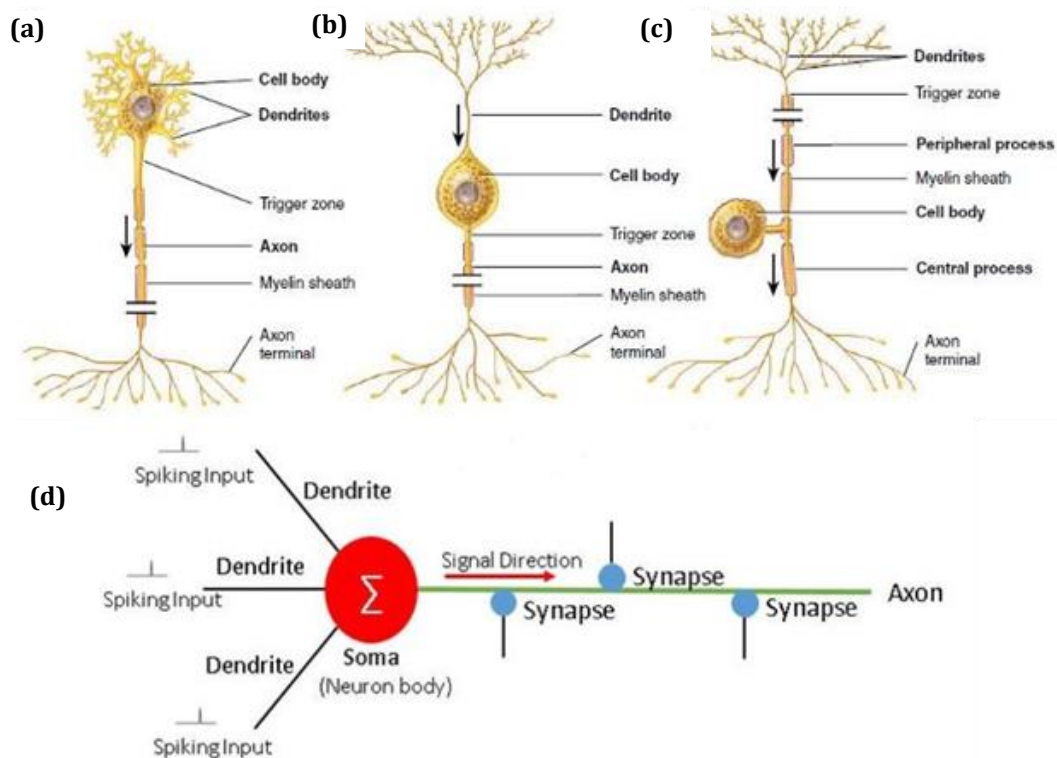


**Figure 1- 1** Different neuron configurations: (a) multipolar, (b) bipolar and (c) unipolar [35], (d) propagation of signal in neuron [33]

The action of these proteins creates intracellular versus extracellular variations in ion concentration, along with sodium (Na), potassium (K), or chloride (Cl) that creates a potential across the membrane called resting membrane capacity. The potential depends on the type of neuron and commonly varies between -40 mV and -90 mV, particularly due to numerous open k<sup>+</sup> channels within the membrane [36]–[38]. A change in this transmembrane potential results in a higher negative potential. When the negative action potential goes over a certain threshold, it triggers an electrochemical pulse that propagates along the neuron’s axon and establishes synaptic connections with the subsequent cells. These pulses are called **Action potential (AP)**, and these are electrical pulses that carry signals over a long distance [39].

An action potential generated at one factor alongside an axon spreads passively to the section next to it, in which it triggers the hole of voltage-gated Na<sup>+</sup> channels and therefore any other movement ability. The propagation of the movement capacity

occurs in a single path simplest because of the fast inactive period of the Na<sup>+</sup> channels and the quick hyperpolarization due to k<sup>+</sup> efflux [40], [41].

In neurons, action potentials are the key to communication between cells. The propagation of signals along the neuron's axon occurs in the direction of synaptic knobs situated at the ends of an axon. Afterward, these indicators can then connect with other neurons at synapses, or to motor cells or glands. In another kind of cell, their essential characteristic is to activate intracellular approaches. Action potentials in neurons also are referred to as "nerve impulses" or "spikes", and the temporal series of motion potentials generated with the aid of a neuron is known as its "spike rain". A neuron that emits an action potential, or nerve impulse, is often stated to "fire" [37], [39].

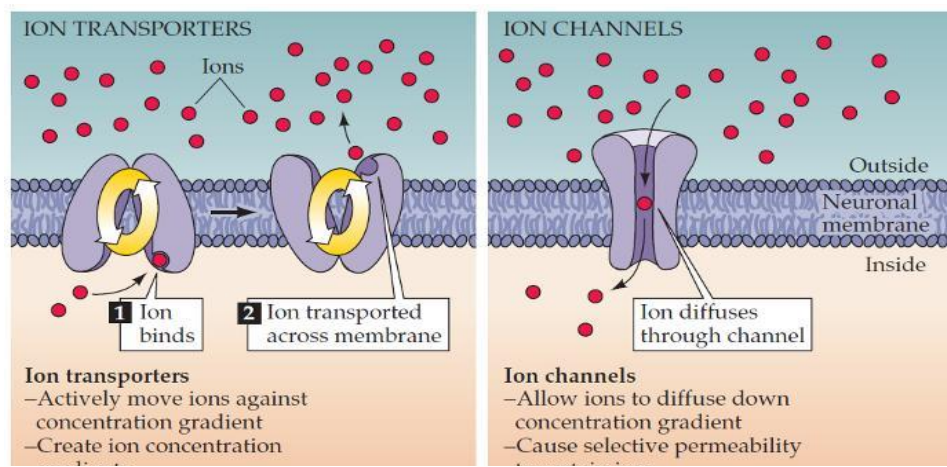


**Figure 1- 2** Neural membrane structure [35]

It occurs from the sequential closing and opening of voltage-gated ion (cation) channels. First, the outlet of Na<sup>+</sup> channels enable the Na<sup>+</sup> ions to go with the flow for approximately 1 ms (1 kHz), inflicting an unexpected and big depolarization of a part of the membrane. The channel then closes and can't be reopened for several milliseconds, stopping the flow of Na<sup>+</sup> (see **Figure 1-3**). The opening of K<sup>+</sup> channels as the movement potential reaches its top ends in the efflux of K<sup>+</sup> ions, which to begin with hyperpolarizes the membrane (see **Figure 1-3**). As those channels close, the membrane slowly returns to its resting position [45].

The membrane depolarization spreads passively in both directions along the axon (see **Figure 1-3**). Because the Na<sup>+</sup> channels at the 1-mm position are still inactivated (green), they cannot yet be reopened by the small depolarization caused by the passive spread. Each region of the membrane is refractory (inactive) for a few milliseconds after an action potential has passed. Thus, the depolarization at the 2-mm site at time 0 triggers action potentials downstream only; at 1 ms an action potential passes the 3-mm position, and at 2 ms, an action potential passes the 4-mm position (see **Figure 1-4**) [37], [37], [40], [42]-[44].

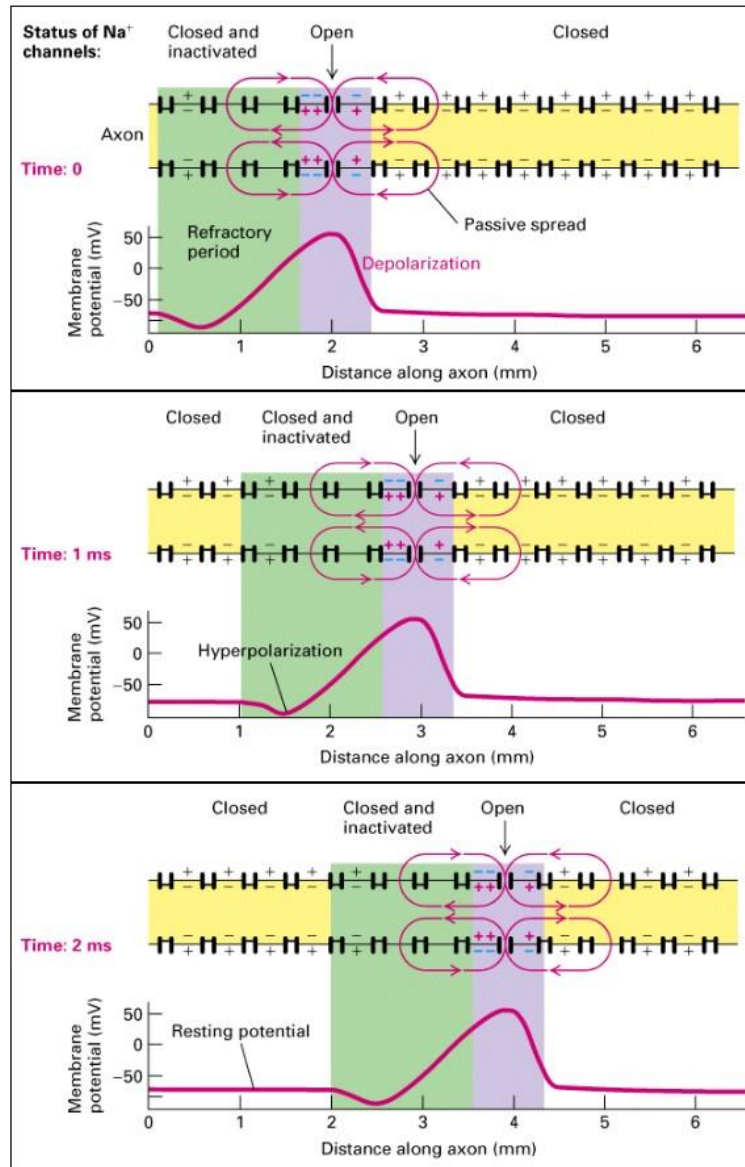


**Figure 1- 3** Unidirectional conduction of an action potential due to transient inactivation of voltage-gated Na<sup>+</sup> channels. At time 0, an action potential (purple) is at the 2-mm position on the axon. The membrane depolarization spreads passively in both directions along the axon (see Figure 1-4). Because the Na<sup>+</sup> channels at the 1-mm position are still inactivated (green), they cannot yet be reopened by the small depolarization caused by the passive spread. Each region of the membrane is refractory (inactive) for a few milliseconds after an action potential has passed. Thus, the depolarization at the 2-mm site at time 0 triggers action potentials downstream only; at 1 ms an action potential is passing the 3-mm position, and at 2 ms, an action potential is passing the 4-mm position [42]



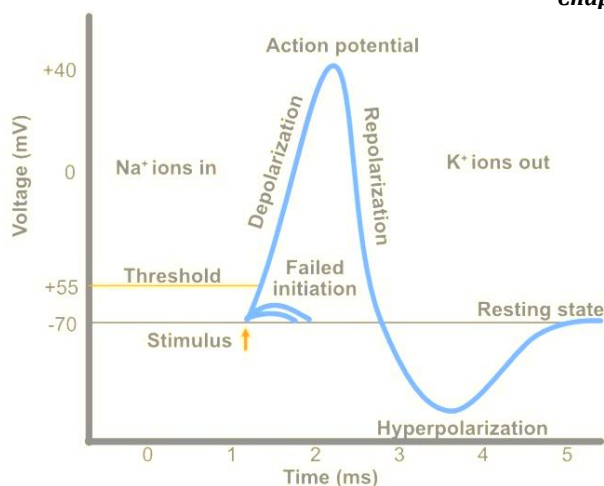


**Figure 1- 4** Action potential. When the initial resting state is perturbed by a stimulus that exceeds a certain threshold [43]

## 1.2 Existing Technology for Bio-implants

With the application in neuroscience (for neural stimulation, **Deep Brain Stimulation (DBS)** [5], [45], neural prosthesis or fake neurons, Vegas nerve stimulation, neural controlling prosthesis for stimulation and neural recording), and as retinal implants, this thesis focuses on the fabrication of electrodes (which paves the leeway for implants and MEAs) in microscale. In this section, a general discussion about the existing technology of visual and neural implants and prostheses is discussed [5], [27], [46]–[48].

### 1.2.1 Visual Prostheses and Implants

Multichannel electrophysiological sensors and stimulators, particularly those that are used to study the nervous system, are usually based on monolithic microelectrode arrays. However, the architecture of said arrays limits flexibility in electrode placement and scaling to a large number of nodes, especially across non-contiguous locations [31].

Implementation of a stable electrode-retina interface has posed several challenges over the years. Many of these challenges stem from the fact that the retina is curved, and microelectrode technology typically produces structures that are planar in shape [49]. Even if an array with the right curvature can be produced, the eye curvature varies from person to person and even a separation of 100 mm can be significant in terms of placement, performance, and efficacy of the implant [50].

Retinal prostheses are used to restore a basic sense of sight to people who suffer from severe vision loss. These prostheses require a relatively intact posterior visual pathway (optic nerve, lateral geniculate nucleus, and visual cortex). Retinal implants are used for people with severe stages of retinal degenerative disease such as retinitis pigmentosa and age-related macular degeneration [51].

A lot of retinal pathologies such as **Age-related Molecular Degeneration (AMD)** and most retinal dystrophies are still definitively incurable, meaning their progression leads to partial to complete blindness over time [50]. Moreover, while some retinal diseases have some sort of treatments, for conditions like specific types of glaucoma,

and can be prevented, as is the case with diabetic retinopathy, treatment failure, neglect of therapy or poor diet could also progress to blindness [52]. With life expectancy being increased due to the advancement of modern medicine, age-related pathologies are becoming prevalent and causing loss of sight in the older population. Sight restoration remains a critical public health issue to prevent situations like social isolation, and the risk of falling, and to improve the overall quality of life by ensuring individual autonomy. The approach adopted for restoring sight is very different depending on the prognosis and pathology [53]. It is also patient-specific and might depend on the history of overall health and genetic makeup. The loss of photoreceptors leaves the inner retina somewhat intact and therefore accessible to reintroduce neuronal activity. However, the loss of ganglion cells and atrophy of the optic nerve requires stimulation of the upper visual areas, particularly at the level of the primary visual cortex V1.

Despite various developments in alternative strategies and procedures (transplantation, optogenetic therapy, and gene therapy), **electrical stimulation** remains the most prevalent approach to vision restoration. Over 40 years of research have been dedicated to understanding the role of electrical stimulation and improving its effects in visual prostheses. Phosphenes are visual sensations that are triggered by electrical stimulation. They were first mentioned upon connection with a visual prosthesis with electrodes placed on the visual cortex of a blind subject in 1968 [54]. Over the years, several human trials have been carried out to test the effects of the electrodes on all areas of the optical pathway, intending to demonstrate the restorative properties of the vision of electrical stimulation [48]–[51], [53], [55]–[57]. Here is a small discussion about some of the prevalent existing technology used for vision restoration that uses electrical stimulation as a leeway.

### 1.2.1.1 Optical Nerve Stimulator

Optic nerve cuffs are one of the most common types of retinal stimulator. These are among the first implants employed to facilitate sight restoration. In this literature, [50] a study was done on a group of blind volunteers with **Retinitis Pigmentosa (RP)**. It was shown that the optic nerve cuffs were capable of inducing vision of phosphenes of different sizes and shapes [58], [59]. However, these phosphenes are perceived throughout the entire visual field and the proximity of nerve fibers makes it a bit complicated to select the cells stimulated to create a clear image in the central region of the visual field. Clinical trials with these devices have therefore stopped. However, new devices recently have been developed and tested in rabbits with penetrating electrodes inserted in the optic nerve [52].

**Figure 1-5** shows a volunteer's x-ray of the spiral cuff silicone rubber electrode, implanted intracranially in February 1998. The identification was done with its platinum contacts (within the dashed circle), whose leads end in the male part of the connector located outside the skull. In August 2000, the neurostimulator was implanted below the skin, within a cavity dug in the skull thickness, and connected to the previously implanted spiral cuff electrode, through the connector. It was anchored to the cranium, as the implanted antenna. The electrode diameter is about 3 mm, stimulator dimensions are 25×30 mm with a thickness of 6 mm. Before August 2000, an additional cable (not shown on the X-ray as it had already been removed at the time of the X-ray) was connected to the implanted connector and brought through the skin

at the clavicle level where it ended in an external connector. This allowed for initial optic nerve stimulation which was then achieved using external stimulators [60].

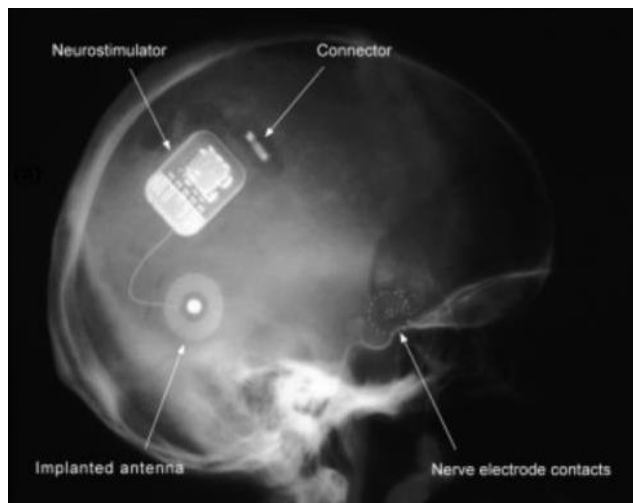


**Figure 1- 5** Implanted optical stimulator on a volunteer observed via X-Ray [60]

### 1.2.1.2 Epiretinal Stimulator

When a matrix of electrodes is placed on the surface of the retina below the vitreous humor in the eye, i.e., in the epiretinal position, electrodes are close to the ganglion cells and their axons. In cases like these, implants are usually introduced in the macular region at the fovea to target the central area of high visual acuity. Unlike optic nerve stimulation, epiretinal stimulation does not take advantage of the visual information processing performed by the retinal circuit [61]. Despite that, the primary advantage of these stimulators compared to the optical nerve ones is that the implant targets the neurons of the macular region specifically [61]–[63].

This enables a more precise projection of visual images in the central visual field. However, sometimes stimulation of more peripheral fibers might induce phosphenes in the form of an arc going toward the periphery of the fiber [80]. Epiretinal implantations require the removal of the vitreous humor and that is later replaced by artificial physiological fluid. The physiology of this implant is attached to the retina with a tack (or nail), which during placement or in the long run can damage the retina, and therefore is placed in a peripheral area. Two epiretinal systems have received European marketing approval for patients with RP, the Argus II from Second Sight, and the IRIS II implant from Pixium Vision [64], [65].

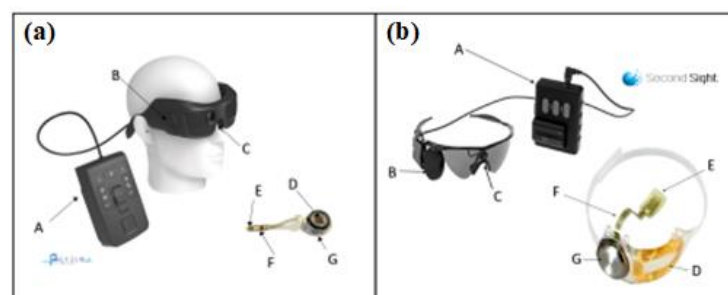


**Figure 1- 6** (a) IRIS II epiretinal implants from Pixium Vision (b) Argus II from Second Sight [61]

**Figure 1-6 (a, b)** shows the design of these two implants used for epiretinal stimulation. Both devices shown in the image consist of an implanted and an external component. In both cases, a video processing unit for visual information (A) is used to transmit information from a camera mounted on glasses (C). On the Argus II implant (right), the coded information and energy are transmitted to the wireless system through the coil (B) to a receiving antenna (D). The coded information is finally translated into electrical currents at the scleral box (G) from which the wires (F) connected to the electrode array (E) escape. A similar device on the IRIS II provides power to the implanted system via the coil (B) and the receiving antenna (D). However, the coded visual information is communicated to the implanted device by infrared transmitted from (C) and received by photodiodes (F). As with Argus, the coded information is translated into electrical currents by (G) and delivered to the electrode array (E) [61].

### 1.2.1.3 Subretinal Stimulator

Subretinal implants are placed in the location where the photoreceptors were before they degenerated. By employing this position, the direct activation of the bipolar cells is made possible which takes advantage of the biological processing of the artificial information as if it came from the photoreceptors. The residual cells of the inner retina (e.g.: bipolar, amacrine, and horizontal cells) can carry out this processing before sending it to the ganglion cells, which finally transmit the information to the brain. Retinal dystrophies initially affect the photoreceptors, leaving bipolar cells and other neurons relatively intact, despite the progression of neuronal reorganization[66]. The retinal ganglion cells in the retina are subsequently activated to transmit information to the brain via the optic nerve. The limited space at this site and the curvature of the eye constrain the dimensions of an implant in both surface area and thickness [59]. Nevertheless, the natural ability of the **Retinal Pigment Epithelium (RPE)** to prevent the formation of a cavity at this location allows the retina to be intimately placed in a visual prosthetics implant. The consequence of the tissue/implant proximity link reduces the stimulation intensities required to activate the retina compared to the epiretinal configuration, and even more so compared to the stimulation of the optic nerve or cortex [56]. **Figure 1-7 (a)** illustrates two distinct subretinal devices, Retina Implant AG's Alpha AMS, which has received CE marking, and **Figure 1-7 (b)** shows Pixium Vision's PRIMA implant currently in the clinical trial. The first implantation of the said implant was in 2022 in Italy. The PRIMAvra study is the final clinical trial needed before European market authorization can be sought for this specific product [62].

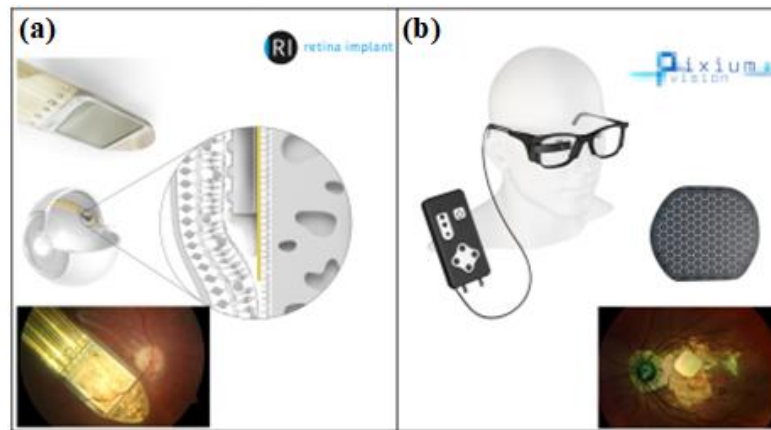


**Figure 1- 7** (a) Subretinal implants Alpha AMS (Retina Implant AG, left), (b) Prima (Pixium Vision, right) [62]

### 1.2.2 Neural Implants and Prostheses

Flexible neural implantable systems that provide intimate and intuitive interfaces with soft neural tissues serve as powerful tools for identifying complex neural circuits for diagnosing and treating neurological diseases, rehabilitation of motor function due to birth defects, traumatic loss of motor function, improve memory, controlling prosthetic limbs, etc. [67]–[70].

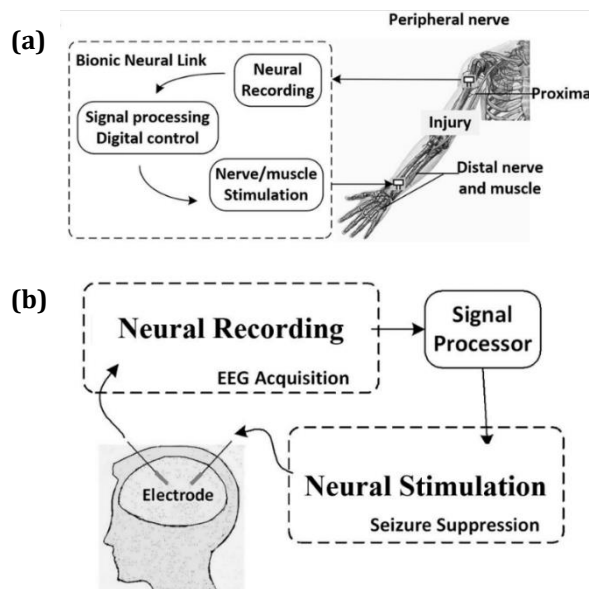


**Figure 1- 8** Concept of (a) the Bionic Neural Link and (b) the epileptic seizure detection and suppression using neural recording and stimulation circuits [70]

Furthermore, recent efforts to simultaneously integrate multiple modalities with a single system for active recordings and actuation are of potential interest [71]–[73]. A hybrid of electrophysiological and optical approaches for neural implants maximizes the synergism of the resolution of the two methods while compensating for the weaknesses of each approach [45], [69], [70], [74].

Different kinds of implants can be used as neural implants. The distinctions can sometimes be broadly made by categorizing them as their function, purpose, or just as stimulating, recording implants. In **Figure 1-8 (a)** a Bionic Neural Link is shown, and **Figure 1-8 (b)** shows a simple representation of a pair of neural implants that do stimulation and recording to facilitate a patient with a tendency to seizure.

Neural implants are placed inside the human body by surgery, with an injection, or sometimes under the skin. In this segment, the existing technological advancement in neural prostheses and implants is discussed in short.

### 1.2.2.1 Neural Implants for Stimulation and Recording

The U.S. Department of Defense and the U.S. **National Institutes of Health (NIH)** have devoted hundreds of millions of dollars in funding toward this sector. A neural implant is a device placed inside the body that interacts with neurons. Neural implants can record native neural activity, allowing scientists to observe the patterns by which healthy neural circuits communicate. Neural implants can also send pulses of electricity to neurons, overriding native firing patterns and forcing the neurons to communicate differently. Neural implants enable researchers to hack into the nervous system [47], [72].

### 1.2.2.2 Deep Brain Stimulation (DBS)

One of the most popular clinical uses of neural implants is in a treatment called **Deep Brain Stimulation (DBS)**. In this therapy, electrodes are surgically placed deep into the brain where they electrically stimulate specific structures in an effort to reduce the symptoms of various brain-based disorders [75].

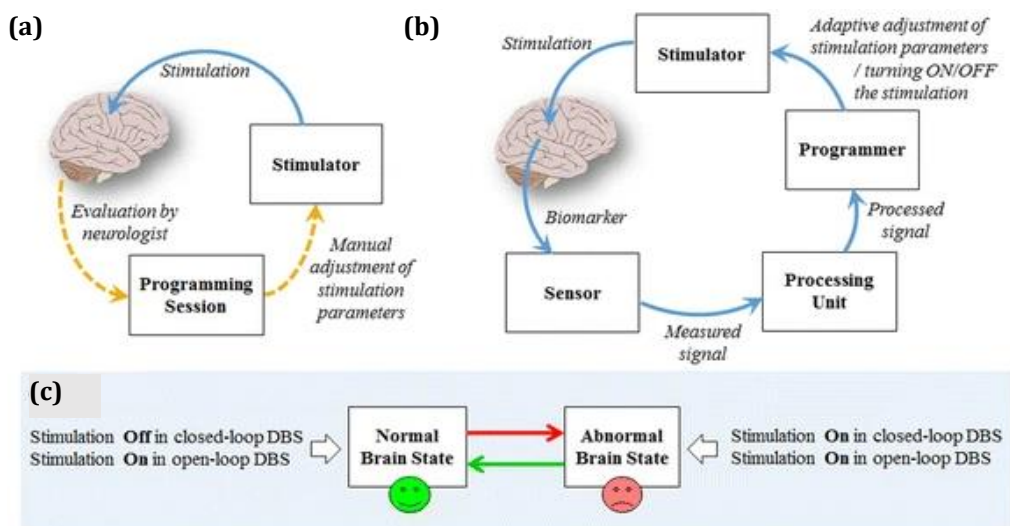


**Figure 1- 9** (a) Open-loop DBS, (b) Closed-loop DBS, (c) Simple schematic of the 2 types of DBS [108]

The U.S. **Food and Drug Administration (FDA)** first approved the use of DBS in 1997 for essential tremors [76], [77]. Since then, the FDA or other global regulators have

approved DBS for Parkinson's disease (in 2002), dystonia (in 2003), tinnitus, epilepsy, obsessive-compulsive disorder (in 2009), and neuropathic pain [74]. DBS is also being investigated as a treatment for Tourette syndrome [45] and psychiatric disorders such as depression [78].

It is estimated that more than 150,000 people globally have received a DBS implant. Broadly speaking, DBS can be divided into 2 different categories (*see Figure 1.9 (a)*) Open-loop DBS and (*see Figure 1.9 (b)*) Closed-loop DBS. In open-loop DBS, a neurologist manually adjusts the stimulation parameters every 3–12 months after DBS implantation.

On the other hand, in closed-loop DBS, programming of the stimulation parameters is performed automatically based on the measured biomarker. *Figure 1-9 (c)* Demonstration of two different brain states and the action of open-loop and closed-loop DBS. When the brain enters a specific state, it remains in that state for a short or long time. Closed-loop DBS gets deactivated when the brain enters the normal state. Open loop DBS continues the stimulation regardless of the brain state.

### 1.2.2.3 Epidural Stimulation

Some of the most impressive experiments involving neural implants (*see Figure 1-10*) have come with the stimulation of the spinal cord, also known as **epidural stimulation**. The treatment has enabled a handful of people with paralysis in their lower bodies to move, stand, and even walk a short distance for the first time since sustaining spinal cord injuries or severe post-scoliosis [79]–[81].

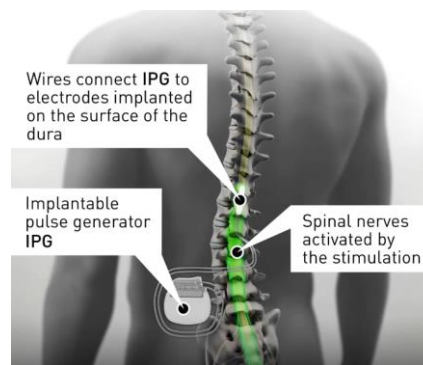


*Figure 1- 10 Spinal nerves activation provided by epidural simulation [84]*

### 1.2.2.4 Neural Prostheses

The newest and the most ambitious application of neural implants is controlling prosthetics using the neuromodulation technique, which would not only help regain motor function but would also provide the sensation in the robotic limb so that the amputee can feel the sensation of touching with their limbs [82]. These systems enable amputees to control robotic hands, arms, and legs, put lightly, using their thoughts [83]. This can be accomplished with a neural implant in the brain or the extremity above the amputation. Some of these robotic limbs can also provide sensory feedback

by stimulating nerves just above the amputation, giving the user a sense of what he or she is touching [84].

### 1.3 Electrodes Criteria

Implantable medical implants require fulfilling certain criteria to withstand the hostile working environment that is the human body. Ideally speaking, these should possess similar biochemical properties as autogenous human cell tissues without triggering any adverse effects. These implants should possess biocompatibility and hence would not trigger the generation of scar tissues, those need to be resistive to corrosion and promote bio-adhesion, and bio-functionality [11], [85]. Electrical stimulation and neurotransmitter sensing require electrodes with different properties based on various electrical and physical requirements. Fabricating an ideal electrode consists of a lot of hand-offs among some crucial properties like size, shape, conductivity, thickness, etc.

Widely speaking, these requirements can be divided into 2 classes: (i) Primary Requirements, i.e. The ones required for an electrode material to be used in contact with dwelling tissues for in-vitro and acute in-vivo research, and (ii) Advanced Requirements required for a long-term reliable prosthesis and/or special application e.g.: Neural prostheses.

The following section is dedicated to some of the required criteria for the electrodes used in biomedical applications.

#### 1.3.1 No Cytotoxicity or Biocompatibility

One of the main requirements of any kind of electrode or implant is the material with the environment i.e., the tissue in the human body. If the material proves to be not biocompatible due to its chemical makeup, and/or reaction to the biological environment, the electrodes might cause an inflammatory response triggered in the host organism [22]. The human body then sees it as a foreign object and to get rid of it, the host body's immune system attacks it [86], which results in gliosis. Gliosis is a nonspecific reactive trade of glial cells in reaction to harm to the **Central Nervous System (CNS)**. In most cases, gliosis involves the proliferation or hypertrophy of numerous specific kinds of glial cells, together with astrocytes, microglia, and oligodendrocytes. In its most extreme form, the proliferation associated with gliosis leads to the formation of a glial scar [87], [88]. The gliosis triggered by a foreign presence usually envelops the foreign object.

The glial encapsulates the electrode to isolate the foreign object and stop it from interacting with neurons. The formation of isolating structure accumulation around the electrode makes the stimulation or recording via the electrode significantly difficult and, in some cases, impossible. One solution to this problem is to apply an anti-inflammatory agent such as a dexamethasone coating, before implantation [86], [88]. Another way is to incorporate microfluidic piping allowing controlled release [89] which also reduces the reaction. The assessment of biocompatibility is dependent not only on the tested biomaterial but also on the check approach used. Therefore, clinicians want to be familiar with these techniques. Biocompatibility is measured with



3 varieties of biological assessments in vitro tests, animal experiments, and medical assessments [90]. The positive result from this step leads to animal experimentation and furthers the road to a clinical trial for implants [23].

### 1.3.2 Longevity

One of the major requirements for chronic use biomedical implants is electrode durability. The electrode material along with the non-conducting part i.e., the passivation layer (also known as packaging) ought to be able to withstand the extremely wet physiological conditions imposed by using dwelling conditions as well as any kind of corrosion that could result from repeated electrical stimulation (*see Figure 1-11 (a, b)*).

Electrode materials are usually chosen from inert metals like platinum and gold. Despite this, a few studies have proven the corrosion of gold electrodes [91], [92].

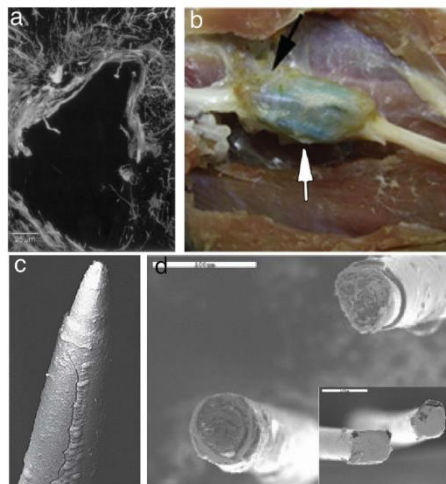


**Figure 1- 11** Types of implant failure. (a) shows GFAP staining for astrocytes of rat cortex after removing silicon intracortical probe 12 weeks post-implantation, (b) is a fibrotic encapsulation of a slant MUA placed on the cat sciatic nerve after a 6-week post-implantation, (c) presents the cracking of Parylene used to encapsulate silicon MEA at 554-days post-implantation on a non-human primate, (d) shows the corroding of Tungsten microwires packaged with polyimide and implanted in the rat cortex for 87-days. The inset is the microwires before implantation. Scale bars are 100  $\mu\text{m}$  [93]

Material failure in the implant can cause not only the breakdown of the electrode but also the breakdown of the packaging (*see Figure 1-11 (c, d)*). The term implant hermeticity describes the packaging's capacity to passivate electric components to avoid contact with biological liquids. Delamination or crack of the packaging usually exposes the metal to tissue, which can in turn lead to short-circuiting in the electrodes [93].

### 1.3.3 Young's Modulus

In addition to chemical makeup, another component that can cause gliosis is a mechanical mismatch of the tissue and the electrode fabric itself. Brain tissue has Young's Modulus of approximately 1-2 kPa (*see Figure 1-12*) whilst silicon shanks which include those on the UEA are in the Giga scale. The brain, continuously moving,

and shifting could be torn by the implant itself or the connected support, in many cases. Even if well connected to the support, gliosis tends to shape depending on the stiffness of the implant material itself as proven by existing work [90].

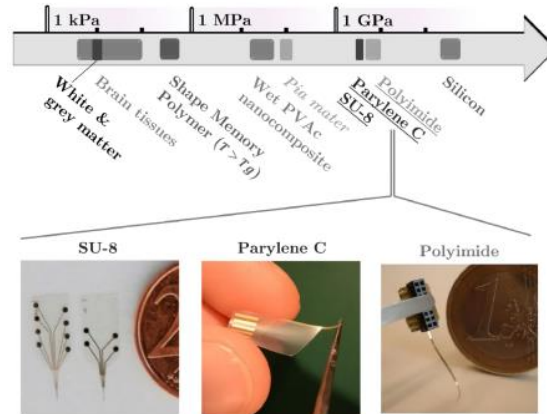


**Figure 1- 12** Young's modulus of brain tissue and passivation material for flexibility [90]

The stiffness of the device depends more on the type and the thickness of the passivation material, and much less on the electrode material, as the electrode thickness is a hundred times thinner than the passivation applied. Consequently, implant designs have caused softer passivation materials [85], and decreased the mechanical discrepancy among tissue and material, especially for retinal implants. Fabricating flexible and/or soft implants poses a new challenge for insertion. Technologies for insertable yet soft implants have been explored and successfully implemented with polymer supports, and removable 3D structures, i.e., metal shuttles like the Micro-flex system (Made popular by the Blackrock system [94]).

Strategies are being developed solely for insertion assistants such as resorbable polymer supports] and even metal shuttles such as the Micro-flex systems recently released by Blackrock Systems. The insertion-assisted mechanism requires the soft implant to be attached to a rigid fixture (with the help of a hook), that provides the required force to be inserted into the brain at the targeted location. The shuttle is subsequently separated from the implant and removed from the brain, leaving the implant inside.

### 1.3.4 Electrical Property

The implants dedicated to recording, stimulation, and/or sensing need to have low bio-impedance, which will in turn yield a high **Signal-to-Noise Ratio (SNR)**, which also allows for a low energy budget. The material should also provide a sufficient charge injection limit to trigger action potentials in the neural network.

The necessary electrode criteria will be discussed in detail and heavily focused on in the following chapter (*see Section 2.1*) while characterizing the fabricated samples and comparing the inherent electrochemical properties of the respective materials and therefore the implants. Several tests are performed to understand and observe the electrical properties of the **Device Under Test (DUT)**. Optimizing the implants starts with optimizing the fabrication and physiological properties of the electrodes to maintain good stimulation and recording capacity. To that end, a list of operations was

done during this thesis to ameliorate the samples and prepare those for biological experimentation [68]. For different applications, different electrical properties are required. For example, in case of neural implants, impedance lower than 100  $\Omega$  is unacceptable, as it often indicates a shunt or short circuit related to a salt bridge on the scalp [95]. Clinical impedance measurements for deep brain stimulation (DBS) electrodes in human patients are normally in the range 500–1500  $\Omega$  [96].

The materials used for fabricating the electrode demonstrate different electrical properties. Implantable electrodes when used for chronic stimulation and/or recording purposes suffer degradation due to the harsh environmental conditions and the transduction of electrical currents into ionic currents necessary to elicit the response of the excitable cells. Therefore, the characterization of the electrodes is necessary to compare the electrical properties of the different materials and to study the evolution of these properties under stimulation over time.

Besides the characterization of the state of the surface of the electrodes done employing **Scanning Electron Microscope (SEM)** and optical microscopy, an electrochemical characterization is required to observe the variation of their properties. The general principle of electrochemical measurements is based on the electrical perturbation of the electrode, either a current or a voltage, and the measurement of the resulting voltage or current respectively. Two main techniques are generally used to characterize the electrodes: **Electrochemical Impedance Spectroscopy (EIS)** and **Cyclic Voltammetry (CV)**. Both techniques are performed in a three-electrodes electrochemical cell. **Figure 1-13 (a)** shows the bode plot or impedance spectroscopy of BDD-coated porous **Polypyrrole (PPy)** compared to a flat Diamond and **Figure 1-13 (b)** shows the CV plot of (i) flat Boron-Doped Diamond electrode, (ii) PPy film coated with a 90 nm thick BDD layer and (iii) PPy film coated with a 170 nm thick BDD layer, recorded in 0.1 M LiClO<sub>4</sub> at 100 mV/s.

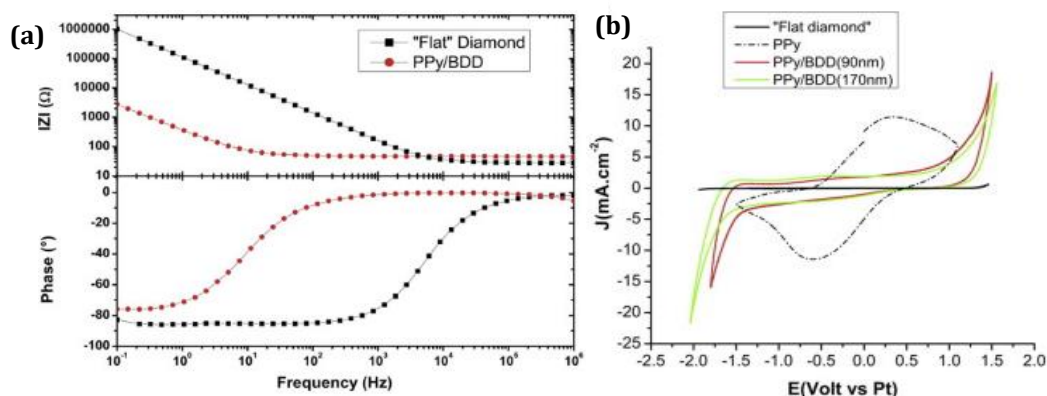


**Figure 1-13** (a) EIS Bode representations of flat Diamond & BDD coated porous polypyrrole (PPy) in LiClO<sub>4</sub> Diamond electrode measured in 0.1 M LiClO<sub>4</sub>, (b) Voltammograms of the BDD coated porous polypyrrole (PPy) in LiClO<sub>4</sub> (a) voltammograms of (i) flat boron doped Diamond electrode, (ii) PPy film coated with a 90 nm thick BDD layer and (iii) PPy film coated with a 170 nm thick BDD layer, recorded in 0.1 M LiClO<sub>4</sub> at 100 mV/s [68]

### 1.3.5 Bio-Inertia Effects

Bio-inertia outcomes are a supplementary condition: the appropriate electrode material should be invisible from the immune gadget. The detection of the material as

a foreign body by using the immune system triggers an inflammatory response. In the case of neural interfacing, this will bring about the coating of the implant with the help of a thick layer of glial cells to insulate it from the neural network. This can result in a decrease in stimulation or recording performance or a complete lack of communication between the excitable cells and the electrodes with the effect of rendering the implanted device useless. This requirement is mostly applicable in the case of neural interfacing [54].

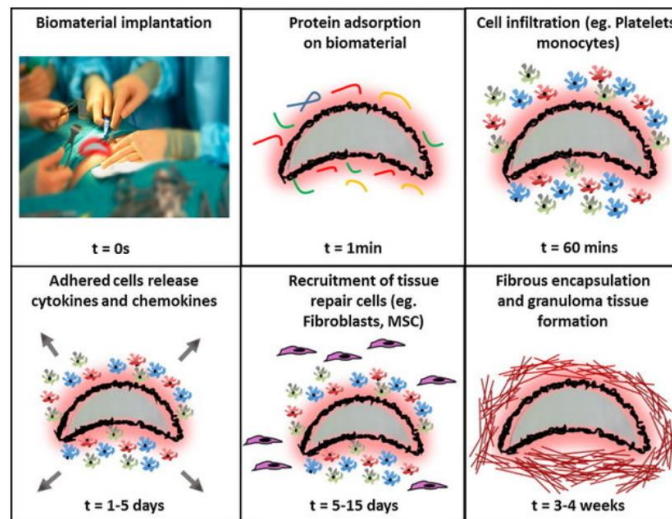


**Figure 1- 14** Natural innate immune response following biologically inert biomaterial implantation [54]

**Figure 1-14** shows the immune response of biomaterial implantation and the triggered fibrosis response of the body that happens over time.

## 1.4 Limitations of the Existing Technology

Over the past couple of decades, the usage of bio-implants has been increasingly popular. There are lots of issues with the technique of fabrication, choice of materials that fulfill the required criteria, along with performance. This part briefly sheds light on the existing issues with some of the most crucial problems with the most used materials for biomedical implants.

### 1.4.1 Biological failure

There are various reasons the implants can be subjected to biological failure, which include trauma during insertion of the device, formation of scar tissue around the implants, acute vascular damage, hemorrhage, inflammatory response, etc. Vascular damage is often observed by internal fluid displacement (*see Figure 1-15 (a)*), and eventual vessel damage due to the placement of rigid implants. The most extreme type of vascular damage is vessel rupture, which is accompanied by hemorrhage (*see Figure 1-15 (b)*) [97]. Even after the components are completely biocompatible, there's a possibility of the body rejecting the device and causing an immune response to the human body [98].

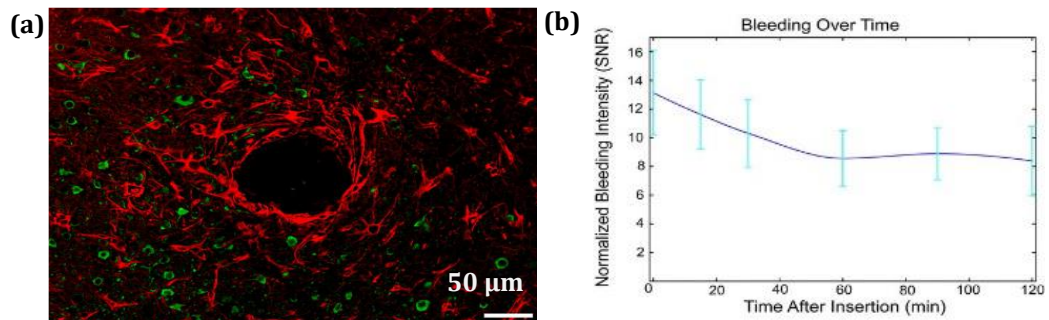


**Figure 1- 15** Immune response of tissue for penetrating electrode (a) Green Neurons, Red Glia Cells (b) **Blood Brain Barrier (BBB)** permeability following electrode insertion. Six microelectrodes were implanted into the cortex at -120, -90, -60, -30, -15, and 0 min prior to tail vein injection of 10% sodium fluorescein, 0.6 mL/kg at 0.45 mL/min. Animals were immediately perfused with saline and 4% paraformaldehyde (4–7 min). Bleeding was quantified as the mean intensity within 50 μm of the insertion site divided by the mean background intensity of a distant location. Error bars indicate standard error (N = 14). Large error bars indicate large variability [95], [96]

### 1.4.2 Material Failure

Corrosion, the sluggish degradation of materials by Electrochemical assault is of extraordinary difficulty while a metal implant is positioned in the antagonistic electrolytic surroundings of the human frame. The implants face severe corrosion surroundings which include blood and different constituents of the body fluid which embody numerous components like water, sodium, chlorine, proteins, plasma, and Amino Acids with mucin in the case of saliva [25], [99], [100]. The aqueous medium within the human body includes various Anions such as chloride, phosphate, and bicarbonate ions, and cations like Na<sup>+</sup>, K<sup>+</sup>, Ca<sup>2+</sup>, Mg<sup>2+</sup>, and so forth. Organic materials of low-molecular-weight species in addition to highly high molecular-weight polymeric additives, and dissolved oxygen [92].

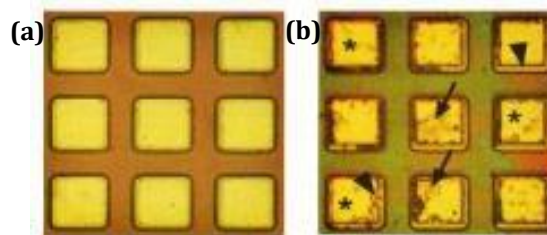


**Figure 1- 16** Surface appearance of implants. (a) Appearance of unimpacted device. Each 20 μm 20 μm square represents an individual electrically active micro photodiode subunit. The gold electrode layer is evenly distributed across the implant surface. (b) Appearance of the device explanted from cat 349 after 8 months of implantation. The gold electrode layer is dissolved, so that the chromium adhesion layer is now visible (asterisks) as is the N surface of the semiconductor which appears as a rim around each subunit (arrowheads). In addition, organic tissue is seen on the implant surface (arrows) [92]

For instance, gold is one of the best conductive materials that has been tested as a component for bio-medical implants. However, gold is susceptible to corrosion and often shows signs of delamination not long after installation. Cases were reported with the dissolution of both anodic and cathodic gold electrodes (see **Figure 1-16**) that appeared dependent on the duration of the device implantation. The delamination in

the gold layer results in not only the reduction in the amplitude of the electrical response of the implants But, also exposes the retina to potentially neurotoxic chromium ions derived from the adhesion layer.

**Table 1-1** shows a short list of effects of corrosion in the human body due to corrosion in commonly used Biomaterials [101]. Other conventional materials are susceptible to oxidization, delamination, and degradation over time. Ceramics like TiN are reported to have higher biocompatibility and increased corrosion resistance. However, they are brittle have high elastic modulus, and are prone to fracture due to having high plasticity. Magnesium (Mg) based implants show promise in case of short-term usage.

Biomaterial Metals	Effect of Corrosion
Nickel	Affects skin - such as dermatitis
Cobalt	Anemia B inhibits iron from being absorbed into the bloodstream
Chromium	Ulcers and Central Nervous System (CNS) disturbances
Aluminum	Epileptic effects and Alzheimer’s disease
Vanadium	Toxic in the elementary state

**Table 1- 1** Comparison of biomaterials [99]

The most used passivation material SU8 (an epoxy-based biocompatible photoresist- (see **Figure 1-17 (a)**)) is also susceptible to delamination due to a hostile environment in the human body over time (see **Figure 1-17 (b)**). The ideal composition of the electrode will be made of conductive and non-conductive materials both of which can withstand the hostile human environment [102].

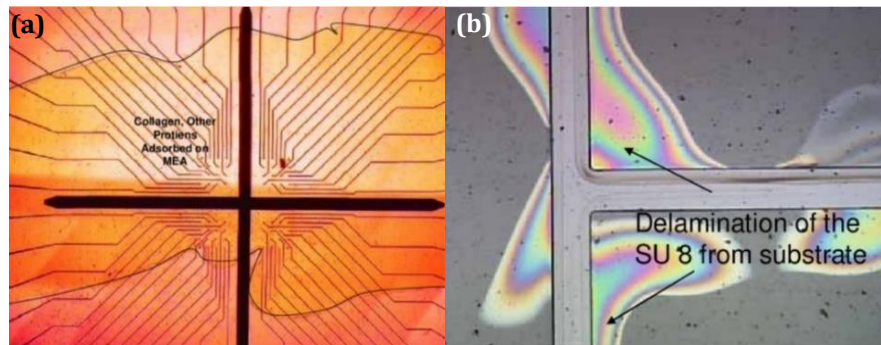


**Figure 1- 17** (a) Deposition of collagen and other proteins from the culture media and neurons on the MEA (covered with SU8) substrate due to repeated use, (b) Delamination of the SU-8 master due to repetitive use [100]

### 1.4.3 Mechanical Failure

Like any other mechanical device, biomedical implants are grossly susceptible to mechanical failure as well. This failure can often be a result of chronic use, which results in nonideal data accumulation after a certain time [103]. This is non-ideal in the case of long-time data collection. Another type of mechanical failure can happen due to mechanical error during fabrication error [104]. **Figure 1-18** shows the damage to the retina due to the mechanical failure of the implant. Due to these problems, the ideal composition for bio-medical implants would be conductive material with optimized

electrochemical properties, which are biocompatible and can withstand hostile environments over an extended period. The requirement for the passivation material would have to ensure the proper encapsulation property, a hermetic seal around the conducting part, and good contact between the conductive and passivation layer while both parts possess the size and shape in microscale and are chemically and biologically inert.

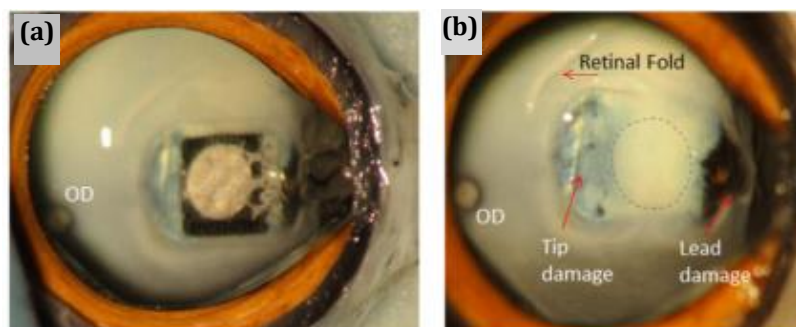


**Figure 1- 18** Dissection and histological images of the eye used for device 1 in the chronic implantation study, (a) device 1 in position and (b) the underlying retina post removal of the device [103]

## 1.5 Carbon as a Bio-implant Material

Inorganic, essential carbon is one of the oldest, and yet newest, biomaterials. Carbon application began with pre-historic human use of watercolor and continues moment with a variety of operations exploiting the physicochemical, adsorptive, structural, and biocompatible parcels of different forms of carbon. To date, the most important carbon biomaterials have been the isotropic pyrolytic imitations (PYC), produced in a fluidized bed, for use as structural blood-reaching factors for heart stopcock prostheses and small common orthopedic prostheses. There is also widespread use for toxin removal from the body either by direct ingestion, dialysis, or plasmapheresis [105], [106].

Arising trends show that carbon-grounded accouterments are fleetly taking place in medical operations. Carbon accouterments in current biomedical use are Diamond, Diamond-like carbon, graphene, and carbon nanotubes (*see Figure 1-19*). These allotropes of carbon have distinctive chemical and physical characteristics owing to their spatial arrangement of atoms. Allotropes like Diamond, carbon nanotubes, and graphene are used as a material for optics, medical electronics, towel engineering, medical implants, detectors, and other biomedical operations.

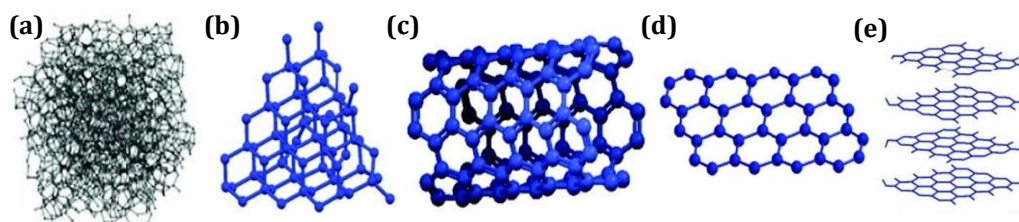


**Figure 1- 19** Different allotropes of carbon viz (a) Amorphous Carbon, (b) Diamond, (c) Carbon Nanotubes (CNTs), (d) Graphene, & (e) Graphite [71], [72], [103]

**Diamond** is used in advanced biomedical operations due to its hardness, wear resistance, and biocompatibility properties. **Diamond-like Carbon (DLC)** is used for coating hipsterism joints and other articulating shells, with an enhancement to the overall life of the implants. **Silicon Carbide (SiC)** has been employed in heart stents as well as pyrolytic carbon used within artificial hearts. Carbon nanotubes are more generally used for medicine delivery and seeing capabilities. **Graphene** is used in biomedicine with a focus on medicine delivery, cancer remedies, and natural imaging as well as in optics as an electrically separating material [107], [108].

Material	Advantages	Disadvantages
Amorphous carbon ( <b>Graphite-like Carbon (GLC), Diamond-like Carbon (DLC)</b> )	<ul style="list-style-type: none"> <li>● Moderate hardness</li> <li>● Wear resistance</li> <li>● Lower friction than Diamond</li> <li>● High load-bearing capacity</li> <li>● Good Adhesion</li> <li>● Low internal stress</li> </ul>	<ul style="list-style-type: none"> <li>● Hardness is lower for GLC than for DLC</li> </ul>
Diamond	<ul style="list-style-type: none"> <li>● Hard</li> <li>● Low friction</li> <li>● Corrosion resistant</li> <li>● Chemical inertness</li> <li>● High electrical resistance/resistivity</li> <li>● Optical transparency</li> <li>● Biocompatible</li> </ul>	<ul style="list-style-type: none"> <li>● Brittle</li> <li>● Difficult to upscale</li> </ul>
<b>Carbon Nanotubes (CNTs)</b>	<ul style="list-style-type: none"> <li>● Biocompatible</li> <li>● High surface area</li> <li>● High sensitivity</li> <li>● Soluble</li> <li>● Can be functionalized</li> </ul>	<ul style="list-style-type: none"> <li>● Safety concerns</li> <li>● Mostly impure</li> <li>● Lack of selectivity</li> <li>● High sensitivity to humidity</li> </ul>
Graphene	<ul style="list-style-type: none"> <li>● Flexible</li> <li>● Optical transparency</li> <li>● Conductive</li> <li>● Hard</li> </ul>	<ul style="list-style-type: none"> <li>● Cost</li> <li>● Difficult to upscale</li> </ul>

**Table 1- 2** Comparisons among some allotropes of Carbon

Carbon is popular due to its capacity to be formed across both the nano and micro scales. Carbon nanomaterials are revolutionizing nanomedicine due to their controllable chemistries and packaging. E.g.: **Nanocrystalline Diamond (NCD)** dust, nanodiamonds, nanostructured DLC, and fullerene. Amongst these allotropes mentioned, Diamond, graphene, and CNT have gained the utmost attention in biomedical applications. A significant number of deposit ways have been explored to produce colorful allotropes of carbon depending on the related nature (sp<sup>3</sup> or sp<sup>2</sup>) and irrespective of its physical property (Gaseous, solid, or liquid).

**Table 1-2** demonstrates that each carbon material offers different benefits for biomedical implantation [109]. Biomedical accouterments or biomaterials can be used to help, treat, form, or replace any function in all organs, or bodies. Carbon-based biomaterials are known to be biocompatible and have become increasingly common within recent decades. Polymers comprised of carbon are also of interest in biomedical operations. As nanomedicine has gained traction, these polymers are readily being used as casing for nanoparticulate and medicine delivery [107], [110].



### 1.5.1 Why Diamond

The target of **ERC - NEURODIAM** [1] is to use Diamonds to build flexible Diamond implants. The reasons behind choosing Diamond among all the allotropes of carbon are numerous. Among all the Carbon allotropes, Diamond has the lowest friction property, while being hard, resistive to corrosion, and optically transparent. Another allotrope that has gained huge popularity as a biomaterial is Graphene. The Vander Waals bond in graphene is prone to aggression under aqueous conditions and has the chance possibility of losing structure [111], which can be avoided by using **Graphene-Oxide (GO)**. However, it has a higher chance of causing bacterial adhesion which might lead to membrane damage of the cell [112]. While it is possible to fabricate both the conductive and non-conducting parts of the implants with Diamond. Both parts having been made of a Diamond ensures a hermetic sealing between the conducting and non-conducting parts which is a particularly important property in implants as it reduces the water accumulation in between layers which ensures the longevity of the implant while maintaining the performance. One of the most common queries that might arise while dealing with Diamond as a biomedical implant is the production cost. All Diamond allotropes, including Diamond, can be fabricated in both micro and nanoscale, which makes it a perfect candidate as a biomaterial. As Diamond may be tough to fabricate [90], the limitations of Diamond-primarily based devices in retinal prosthesis are obvious, however, this approach presents a suitable method to provide a massive quantity [113] of conductive Diamond feedthroughs in monolithic polycrystalline movies (256 Electrodes). Diamond is being used in biomedical applications for (a) As a growth substrate, (b) as a neurochemical sensor growth material, (c) neural recording and stimulation, and (d) optically active neural interface (Nano-Diamonds) [6], [110], [114]–[116].

Due to becoming crystalline, **Poly Crystalline Diamond (PCD)** has a larger surface area than conventional conductive biomaterials like Platinum (Pt) [90], [117]. This large-scale microscopic production helps cut the cost of bio-implant production. Because the human body is carbon-based, not only Diamond is biocompatible, However, it is also so chemically inert that the body cannot detect it as a foreign object. On top of that, numerous works of literature have proved that Diamond bio-implants promote mammal cell proliferation and enhance integration between bone tissue & implants [118], which is very important in the case of post-operating cell regeneration and the subject's well-being. Reported cases of having lower bacterial density compared to conventional biomaterials like Ti have made PCD one of the best candidates for implants [119].

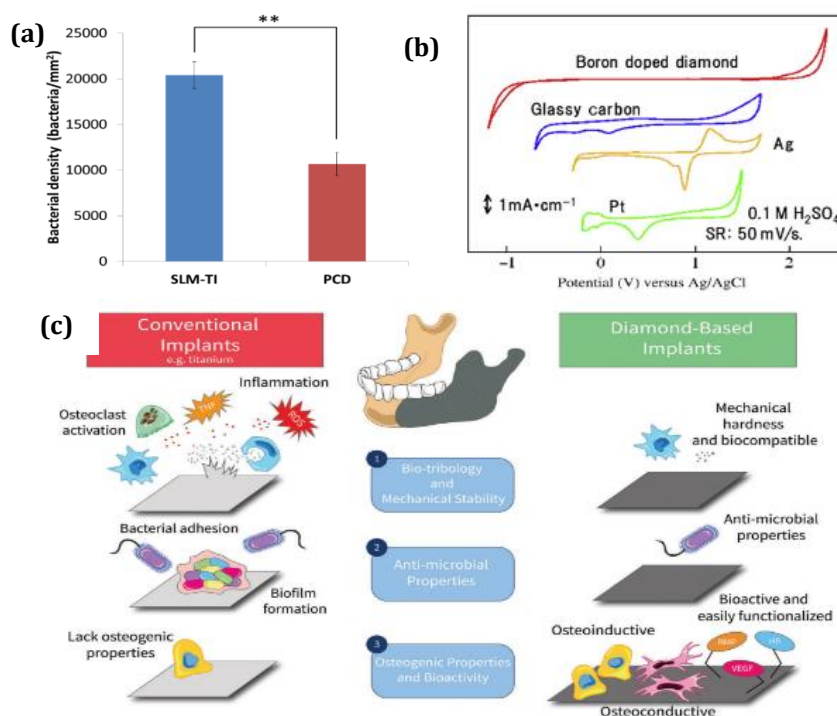


**Figure 1-20** (a) Bacterial (*S. aureus*) density on each sample averaged per unit area. Error bars are the standard error of the mean values as determined from three different areas. \*\* indicates a statistical significance of  $p \leq 0.01$  determined by the t-test [28], (b) Electrochemical properties of different electrodes based on potential windows when performed Cyclic Voltammetry (CV) [58], (c) Schematic showing comparison of some of the main characteristics of conventional implants versus Diamond coated implants [118]

When it comes to the comparison with conventional passivation material like SU8, intrinsic Diamond has also proved to be superior. SU8 is commonly used for passivation in various applications, including electronics and biomedicine. The choice of material for passivation is dependent on the specific requirements of the application, such as mechanical stability, electrical insulation, biocompatibility, and chemical stability [70], [120].

**Figure 1-20 (a)** shows the bacterial density per mm<sup>2</sup> comparison between implants after surgery made of **Selective Laser Melting Ti (SLM-Ti)** and **Poly Crystalline Diamond (PCD)**, \*\* in this figure indicates a statistical significance of  $p \leq 0.01$  determined by the t-test [121]. **Figure 1-20 (b)** shows the larger potential water window of Diamond compared to the other conventional metals used in fabricating implants which will be discussed more in **Chapters 2 and 3**. **Figure 1-20 (c)** shows a pictorial representation of a comparison between conventional materials used for implant fabrication (Ti was used here as a reference material), and Diamond-based implants in terms of mechanical stability, bacterial adhesion, osteogenic properties, and bioactivity. Diamond-based implants have been reported to promote mammal cell proliferation and bone formation [84].

The advantages of using intrinsic Diamond as passivation compared to SU8 can be found in the comparative discussion in literature. Those can be summarized as:

- (a) Chemical Stability:** Intrinsic Diamond is a highly stable material that is resistant to harsh chemicals, such as acids and bases. This makes it ideal for use in applications where chemical exposure is a concern, such as in biomedicine.

- (b) Biocompatibility:** Diamond is a biocompatible material, which means that it does not cause an adverse reaction in living tissues. This makes it ideal for use in biomedical applications, where biocompatibility is a critical concern.
- (c) Thermal stability and conductivity:** Intrinsic Diamond has a high thermal stability, which makes it suitable for use in high-temperature applications, such as in medical devices that are exposed to high temperatures during sterilization processes. Diamond also has the highest thermal conductivity compared to other biomaterials, with the value going up to 2000 W/mK [122].
- (d) High electrical insulation:** Diamond is an electric insulator with high breakdown field strength [28]. This makes it ideal for use as a passivation layer to protect electronic devices from electrical leakage and short circuits.
- (e) Durability:** Due to the octahedral material composition, Diamond is the hardest material known to science. Intrinsic Diamond is a very hard material that is resistant to mechanical stress and wear. This makes it ideal for use in applications where durability is a concern, such as in biomedicine. The low absorption coefficient of Diamond allows higher power outputs to be transmitted through the window without suffering damage or distortion.
- (f) Chemical Inertness:** Diamond is highly chemically inert. And has a wide band-gap semiconductor material. Diamond possesses the widest transmission spectrum from visible to far **Infra-Red (IR)** from 220 nm to > 50  $\mu\text{m}$ —x-ray, infrared, terahertz, and microwave.

## 1.5.2 Diamond for ERC- Project NEURODIAM

The target of the project [1] is to use Diamonds to build flexible Diamond implants. The reasons behind choosing Diamond among all the allotropes of carbons are numerous as discussed in short in **Section 1.5.1**. The target of the project is fabricating flexible implants with high performance, such as low impedance (which means low noise), low capacitance, high charge transfer capacity, and long lifetime with optimum performance [60], [123]–[125]. To that end, different methods and procedures were implemented throughout the thesis.

Intrinsic Diamond is a semiconductor with a large band gap that behaves like an excellent insulator at room temperature. It has a resistivity of about  $10^{16} \Omega\cdot\text{cm}$  [126]. P doping can be accomplished by adding boron to the carbon lattice to obtain Boron Doped Diamond (BDD). The doping ranges from  $10^{16}$  to  $10^{22} \text{at}\cdot\text{cm}^{-3}$ . It can be adjusted depending on which components need to be fabricated such as diodes, or **radio frequency (RF)** applications. By heavily doping Diamond with boron ( $[B] > 10^{20} \text{at}\cdot\text{cm}^{-3}$ ), Diamond behavior tends to be metallic-like, and can be thus used to fabricate conductive electrodes [127]–[130].

Project NEURODIAM is the first ever project to employ Diamond to fabricate both conductive and non-conductive parts of the bio-implant. As a part of the project, this thesis dealt with the fabrication, characterization, and performance improvement of the full Diamond electrode. The same technology was used by Claudia Wilfinger, who is another Ph.D. candidate working on the project and worked on the fabrication of implants using the SEIKI Diamond reactor installed in the ESIEE Paris Cleanroom in April 2019. The full Diamond implants are fabricated with the collaboration of Dr. Emmanuel Scorsone of CEA, who was responsible for fabricating the Boron Doped Diamond (Conductive Diamond). The full Diamond implants were used in vivo **Visual Evoked Potential (VEP)** recording by the collaborators in **Institut de la Vision (IDV)**

Paris, Julie Zhang, which proved the functionality of the final implants. **Figure 1-21(a)** shows the intended vision of the full Diamond implant proposed by the project NEURODIAM. Whereas **Figure 1-21 (b)** shows the Full Diamond electrode fabricated and used in this thesis. It should be mentioned that the implant has a biodegradable polymer base, which would degrade sometime after the implantation [131]. While, in the case of the electrode, the sample needs to be sturdy so that multiple operations can be carried out [132], [133].

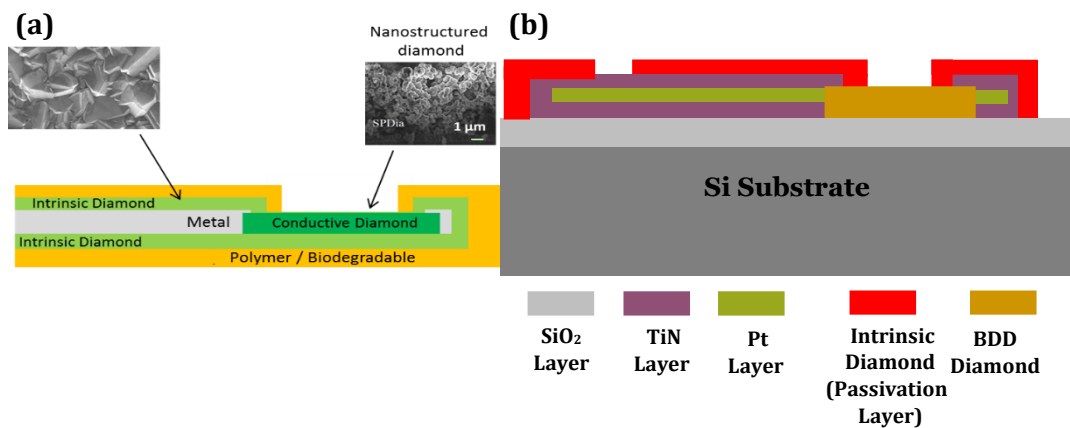


**Figure 1-21** 2-D cross-sectional view of the (a) Full Diamond implant proposed by NEURODIAM, (b) full Diamond electrode fabricated in this thesis

## 1.6 Take Away from This Chapter

The field of biotechnology has been progressing rapidly for the last decade. The implementation of bio-implants for functional rehabilitation and the brain-computer interface has gained popularity for its rate of success, efficacy, and non-invasive nature. This chapter provided the overall context of the bio-implants, their purposes, complications, and state of the art. The requirements for the implants mentioned in this chapter are pre-requisite and kept in mind while carrying out the fabrication, development process, and quality control. At the end of this chapter, the ERC funded NEURODIAM project, along with the concept of the full diamond implant is presented. The properties of diamond material are shown to demonstrate the strong interest of diamond for neural applications and for biomedical applications.



## Chapter 2

### Microfabrication and CLEANROOM Procedures

This thesis started with the goal of comparing the performances of electrodes of different materials along with fabricating and optimizing a full Diamond electrode. To that end, there were various steps of fabrications, characterizations, and optimizations were done. Throughout this thesis, various methods and techniques were used for the fabrication, characterization, and optimization of the systems. In this chapter, a categorical representation of various methods employed in the CLEANROOM for fabrication and optimization will be discussed. The methods used and employed for understanding the performances will be presented in **Chapter 3**. An implant would ideally be susceptible to surviving the hostile environment over a long period. To test that property the samples were put in longevity test and described in **Chapter 4**. Not all of the methods that were done during the thesis could lead to a conclusive result or their optimized states. Some were more successful than others, and some would be discussed from the perspective of this whole Thesis, in **Chapter 5** to give some ideas of the author as to how to propagate it further in order to lead those projects to fruition.

The majority of the fabrication of the electrodes characterized was done in ESIEE Paris Cleanroom using different protocols. The **Boron Doped Diamond (BDD)** was fabricated at CEA/LICM (Saclay) with the help of our collaborators. The fabrication of different materials and different electrodes required following different protocols. Optimizing the performance of the bio-implants starts with optimizing the fabrication in order to maintain good stimulation and recording capacity. To that end, a list of operations was done during this thesis to ameliorate the samples and prepare those for biological experimentation.

The materials used for fabricating the electrode demonstrate different electrical properties. As explained before (*see Section 1.4*), implantable electrodes when used for chronic stimulation and/or recording purposes, suffer degradation due to the harsh environmental conditions and the transduction of electrical currents into ionic currents necessary to elicit the response of the excitable cells. Therefore, characterization of the electrodes is necessary in order to compare the electrical properties of the different materials and to study the evolution of these properties under stimulation over time. This chapter will not discuss any of the percussion of different fabrication or treatment procedures in detail.

Besides the elaborate characterization explained in **Chapter 3**, to observe the general state of the electrodes some fundamental observations are done with a **Scanning Electron Microscope (SEM)** and optical microscopy right after microfabrication, in the ESIEE Paris CLEANROOM. To begin with this chapter the primary idea of fabrication technology was discussed. And going forward, the nitty gritty of the fabrication would be presented in a natural progression.

## 2.1 Different Types of Electrodes Fabricated

Micro-implants are usually made of three different parts. It consists of a conducting part that can transmit a signal from the region it was implanted at to the electrical /electronic interface for storing, analyzing, or the signal for further analyzing, or in case of stimulation, the other way around. For the protection purposes of the conductive part in the hostile environment of the human body, and minimizing the chance of compromised data due to water insertion in between the layers of the implant, protect the structure against further mechanical and/or material failure, except the part necessary for recording (often referred to as Electrodes or opening, and the part that connects to the electrical/electronic interface (also referred to as contact pad), everything else ideally remains covered in a biocompatible, but not biodegradable, non-conductive part, often referred to as passivation layer [134]–[136]. An implant is composed of a metallic layer deposited on a non-conductive substrate and covered by a passivation layer. This passivation layer opened in two areas to create the electrode and contact pad (see **Figure 2-1**).

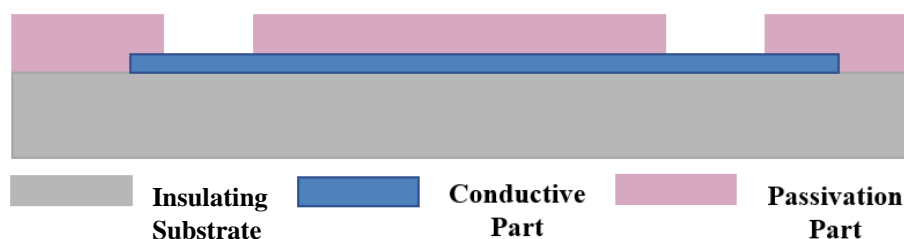


**Figure 2- 1** Simplified 2-D cross sectional view of an implant

For fabricating full Diamond flexible implants, it was imperative to forward step by step with quality control and optimization on both the conductive and passivation part of the electrodes, two different types of samples were prepared. Samples with an interdigitated electrode made with conductive parts and covered with the passivation layer are known as **Interdigitated Electrodes (IDE)** or **Interdigitated Electrode Array (IDA)**. These are used to observe the property of the passivation layer. Samples with individual openings are used to observe the properties of the conducting and passivation part of the electrode, which is mentioned in the thesis as **Strip Type Electrodes (STE)**, or simply **electrodes** on occasion.

### 2.1.1 Interdigitated Electrode (IDE)

This specific type of electrode was designed as a means to understand and improve the quality of passivation. The planar IDE shows the basic properties of two parallel plate capacitors, where the electrodes open to provide one-sided access to the **Material Under Investigation (MUI)** [137]. The electric field lines generated by the electrodes (see **Figure 2-2**) penetrate the MUI and will change the impedance of the whole structure. The sets of electrodes behave as a capacitor in which the capacitive reactance becomes a function of system properties [72], [138]. So, measuring the singular capacitive in between the two fingers/teeth of the comb leads to the overall reactance of the sensor. Since the electrodes of an interdigital sensor are coplanar, therefore the measured capacitance will give a high signal-to-noise ratio. To get a strong signal, the electrode pattern of the interdigital sensor can be repeated many times [139]–[142].

The term “Interdigitated’ refers to a digit-like or finger-like periodic pattern of parallel in-plane electrodes, which is employed to build up the capacitance associated with the electric fields that penetrate a material sample [139]. An AC voltage source is applied as an

excitation voltage between the positive terminal and the negative terminal. An electric field is formed from a positive terminal to a negative terminal [142].

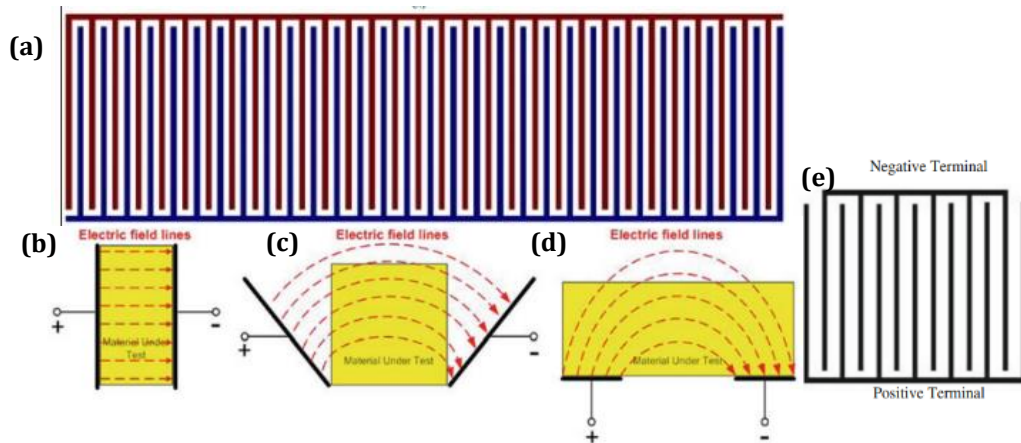


**Figure 2-2** (a) Structure of Interdigitated electrodes (IDE), (b) electric field lines of parallel plate capacitors, (c) electric field lines when the planes are moved further away from each other, (d) electric field line when the plates are at 360° apart from each other, (e) Configuration of a conventional coplaner IDE [133]

Depending on how the structure is distributed, they can be called Interdigitated (see **Figure 2-2(a)**) or IDE. The electric field distribution spreads over a larger distance depending on the angle between the two plates; the distance being minimum when the plates are in parallel (The angle being 0°) (see **Figure 2-2(b)**), when the distance between the plates is bigger than 0° but smaller than 360° (see **Figure 2-2(b)**), and the distance being maximum when the angle in between them is 360° (see **Figure 2-2(d)**). In any IDE, the opposing finger-like structures work as two plates of a capacitor (see **Figure 2-2(e)**) and the capacitance of a simple capacitor is calculated via the:

$$C = \frac{\epsilon_0 \epsilon_r A}{d} \dots \dots \dots \text{Eq 2-1}$$

Where C is the capacitance in farads (F),  $\epsilon_0$  denotes the permittivity of free space ( $\epsilon_0 = 8.8549 \times 10^{-12}$  F/m),  $\epsilon_r$  represents the relative static permittivity or dielectric constant (the value of which is 1 in vacuum), A shows the effective area in square meters, and d is the effective spacing between positive and negative electrodes in meters [143], [144].

### 2.1.1.1 Primary Version of the Mask

Designing the mask is the first step of the fabrication process. The mask is a designing plate that is used to transfer the desired shape and size of the electrode from the 2-D design to the substrate. Throughout the thesis the software **CoventorWare10.4** was used to design the mask (see **Figure 2-3 (a)**) for different layers of the samples.



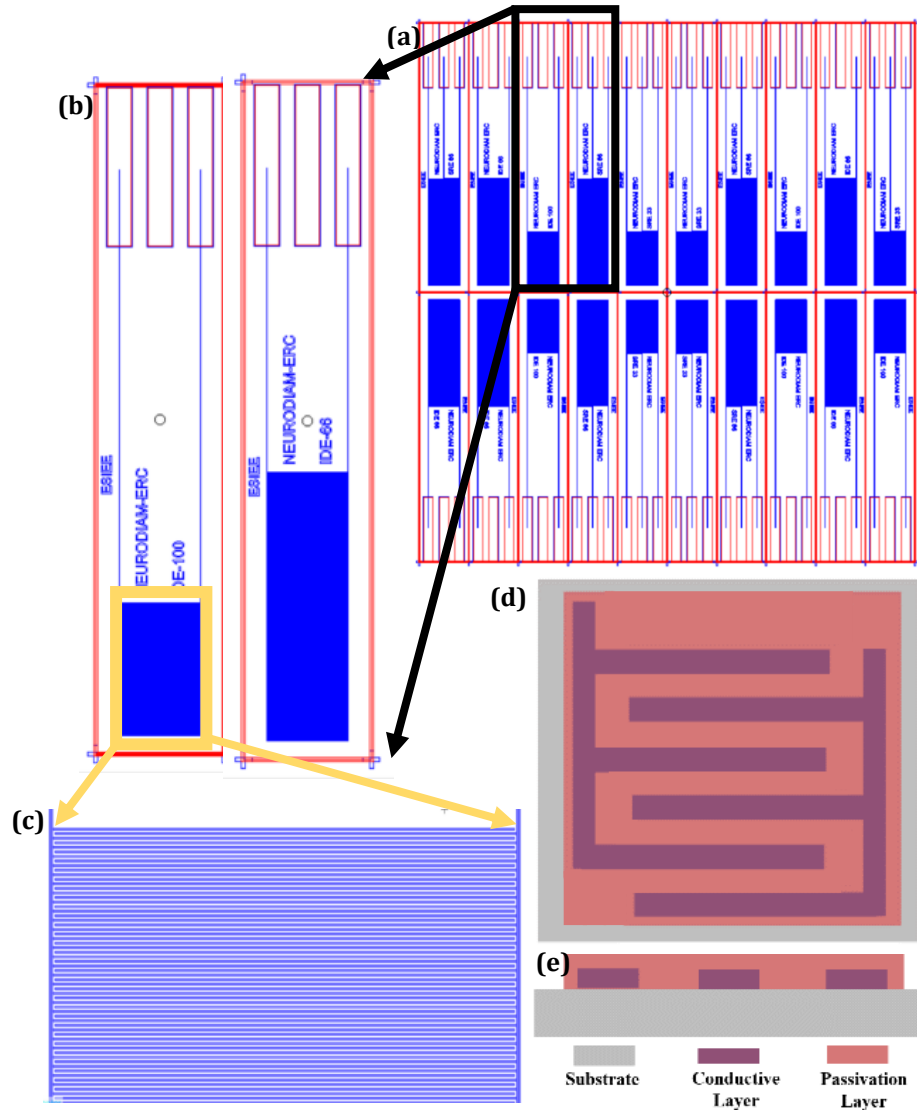


**Figure 2- 3** (a) The mask designed for fabrication of IDE with different pairs of fingers in *CoventorWare10.4*, (b) Zoomed-in vision of 2 single strip with 66 and 100 pairs of fingers, (c) zoomed-in view of the finger-like structures, (d) 2-D representation of the top view of an IDE, (e) top view of the IDE structure, (f) 2-d cross-sectional view of an IDE

### 2.1.1.2 Second version of the Mask

The method that was followed while characterizing and analyzing the IDEs was the same as the STEs, that is the structure was fabricated with the most conventional material and later the more unconventional material was introduced one by one to understand one variable at a time. To that end, the first one was Gold-covered in SU8. The primary impedance measurements were done (*see section 3.6*). While in the case of IDE, the capacitance calculation is one of the most interesting observations, Analyzing the impedance gives a primary idea of the structural integrity, i.e., if there are any open circuits anywhere (*see Figure 2-4 (b)*). The structures will be more comprehensible after the fabrication process is explained.

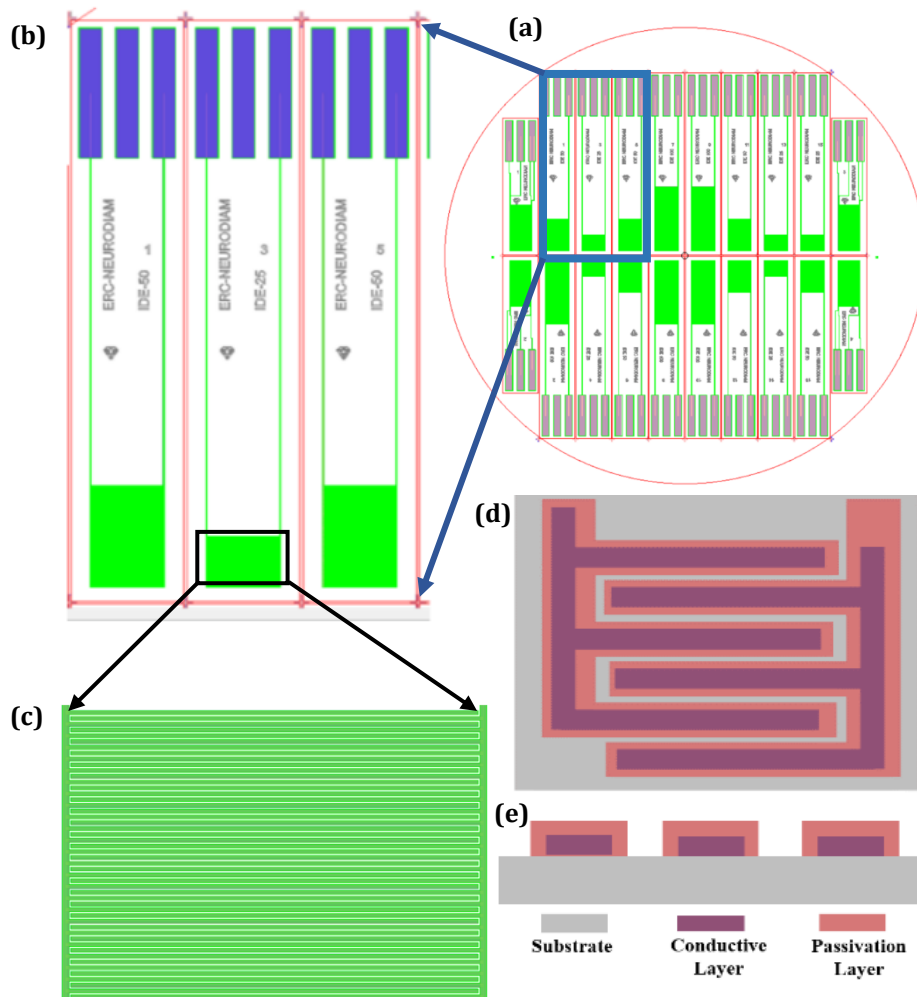


**Figure 2- 4** (a) The new mask designed for fabrication of IDE with different pairs of fingers in **CoventorWare10.4**, (b) Zoomed-in vision of 3 single strip with 25 and 50pairs of fingers, (c) zoomed-in view of the finger-like structures, (d) 2-D representation of the top view of an IDE, (e) top view of the IDE structure, (f) 2-d cross-sectional view of an IDE

The new mask for the IDE structures (see **Figure 2-4 (a), (b)**) had 25, 50, and 100 pairs of interdigitated fingers. Unlike the previous structure, the new structure was not covered by the passivation layer all over and there were gaps in between the fingers to avoid the effect of water retention in between the structure (see **Figure 2-4 (d), (e)**).

### 2.1.2 Strip Type Electrode (STE)

Strip-type electrodes are generally fabricated to understand the property of the conducting part that would be used in stimulation and/or recording. The electrochemical characterization and comparison of different parameters give insight into the quality of the electrodes at hand. The optimization in the fabrication process is later done upon varying the shape, size, and fabrication protocol.

### 2.2.1.1 Mask

Similar to the IDE Mask, the STE mask (see **Figure 2-5 (a)**) was designed using the same software as well. **Figure 2-5 (b)** shows the zoomed-in vision of a single strip in the design, **Figure 2-5 (c)** shows the 2-D representation of the top view of an electrode, and **Figure 2-5 (d)** shows the 2-d cross-sectional view of an electrode.

Conventionally, most of the STEs are usually fabricated on a Glass or Silicon wafer with silicon oxide in order to ensure the durability of the samples and to be able to perform repetitive characterization. Once the technology of fabrication and further treatment is perfected the technology can be transferred into creating flexible/supple implants. To that end, various shapes were explored during this thesis to ameliorate the performance of the samples. Here some of the shapes that were explored during fabrication are discussed.

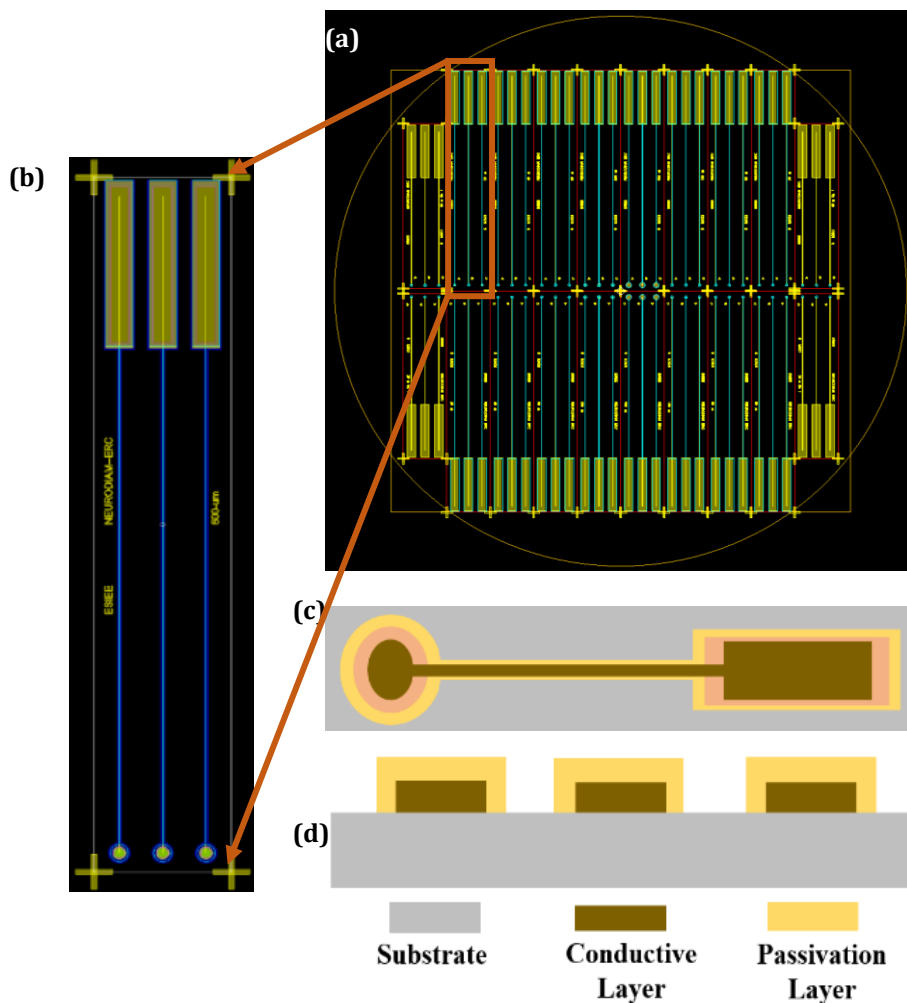


**Figure 2- 5** (a) The mask designed for fabrication of STE with circular electrode in *CoventorWare10.4*, (b) Zoomed-in vision of a single strip with 3 sperate circular electrodes, (c) 2-D representation of the top view of an electrode (the image is not to scale), (d) 2-d cross-sectional view of an electrode

### 2.2.1.1 Circular STE

Conventionally, circular electrodes extended by a track, connected to a contact pad (which connects to electronics/analyzers) are the most used electrodes in literature (due to simplicity in fabrication and calculation purposes) when still in the development phase (see **Figure 2-6 (a)**). The electrodes are fabricated on a Si or glass wafer, to make them sturdy and eligible for iterative use in an electrochemical environment. The mask designed incorporated electrodes of different diameters: 20  $\mu\text{m}$ , 30  $\mu\text{m}$ , 40  $\mu\text{m}$ , 60  $\mu\text{m}$ , 80  $\mu\text{m}$ , 100  $\mu\text{m}$ , 200  $\mu\text{m}$ , 400  $\mu\text{m}$ , and 600  $\mu\text{m}$ . The tracks were designed to be  $\mu\text{m}$  long and  $\mu\text{m}$  wide. At the end of the track, there's a contact pad with the dimension of 30/20  $\mu\text{m} \times 38000 \mu\text{m}$  (Depending on various masks that were used).

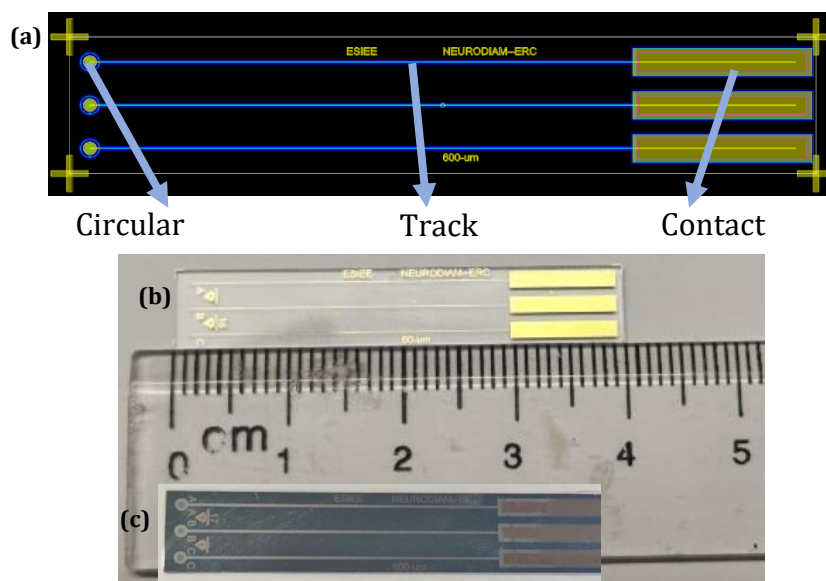


**Figure 2-6** (a) Zoomed-in view of a single sample of the mask (Circular electrodes) (b) a set of 3 separate gold electrode on a glass substrate, (c) a set of 3 separate Diamond electrode on a silicon substrate

An example of 2 samples (Au with SU8 passivation in **Figure 2-6 (b)**, BDD electrode with intrinsic Diamond passivation in **Figure 2-6 (c)**) is represented along with a ruler to comprehend the dimension of the samples.

### 2.2.1.2 Hexagonal STE

To observe the effect of change in the shapes of the electrodes, and whether there is a difference in surface charge density hexagonal shapes of electrodes were fabricated. Same as in circular electrodes, electrodes of different sizes were made with different materials. The idea of a hexagonal electrode (see **Figure 2-10**) was employed to see whether introducing edges while maintaining the same surface area would improve the charge injection due to the edge effect which was explored in various literature [145] (see **Figure 2-7**), meaning the charge density distribution during electrical stimulation around (a) a planar high-perimeter electrode and (b) a planar circular electrode is different and visibly distributed better around the edges when introduces curves in geometry. The charge densities are preferentially distributed towards the edges of the [146], [147]. In this study, the growth of the high perimeter electrode where **Polypyrrole (PPy)** was electrochemically deposited on an octagonal recording site (see **Figure 2-7 (c)**). Eight teardrop segments of PPy preferentially grew from the corners of the octagon, and an

absence of coating was observed at the very center of the structure to achieve the flower petals-like shape [148], [149].

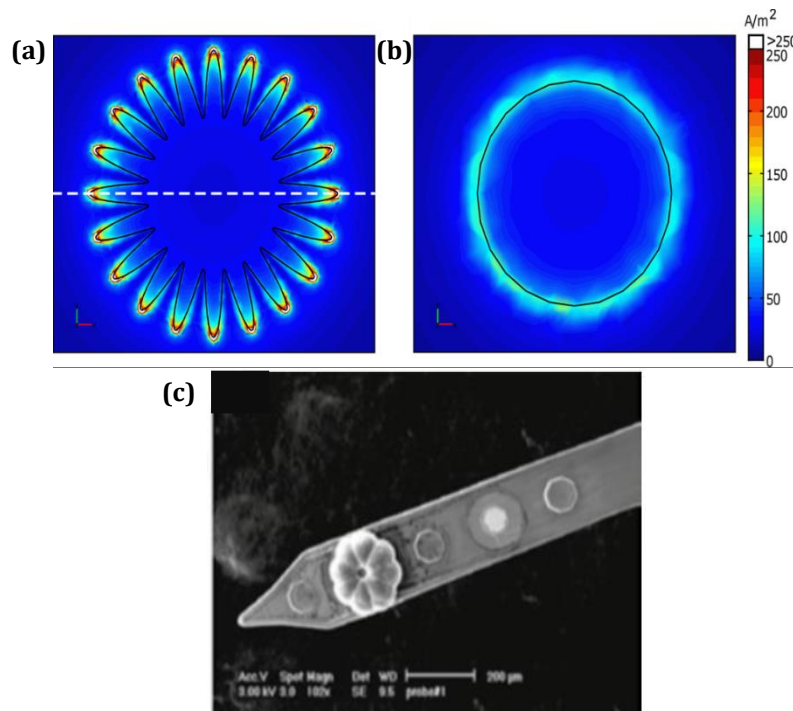


**Figure 2- 7** Charge density distribution in a (a) high perimeter electrode, (b) circular electrode, (c) octagonal shaped Polypyrrole (PPy) electrodes [139]

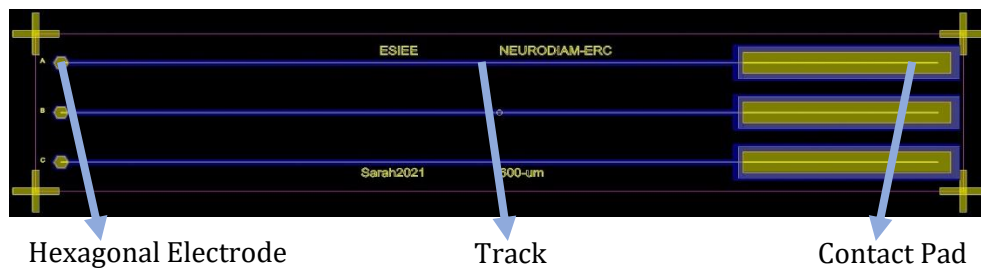


**Figure 2- 8** Zoomed-in view of a single sample of the mask (Hexagonal electrodes) of a single sample containing the design for a set of 3 separate electrodes

### 2.2.1.3 Honeycomb Structure

Electrodes with fractal structures have been used in numerous works of literature to ameliorate the quality of the stimulated and recorded signal [146], [147], [150]. Literature has reported a novel design to prolong the lifetime and function efficacy of implantable electrodes' pulse generators. The novel electrode more efficiently delivers electrical charge for stimulating the nervous system, while reducing power consumption by up to 50 percent with an increase in functionality effectiveness. **Figure 2-9 (a)** shows the Viseck fractal design parameters at different iteration levels with the minimum feature size  $l$  [151]. In **Figure 2-9(b)** the current distribution is represented in different shapes in COMSOL simulation.

Over the years different fractal and pseudo-fractal structures were explored as neural implants. The spatial distribution of the implants is related to the irregularity and/or non-uniformity of current density on the electrode surface [68]. Optimized electrode geometries

increase the efficiency of neural stimulation by maximizing the spatial variation of current density on the electrode surface (see **Figure 2-9**).

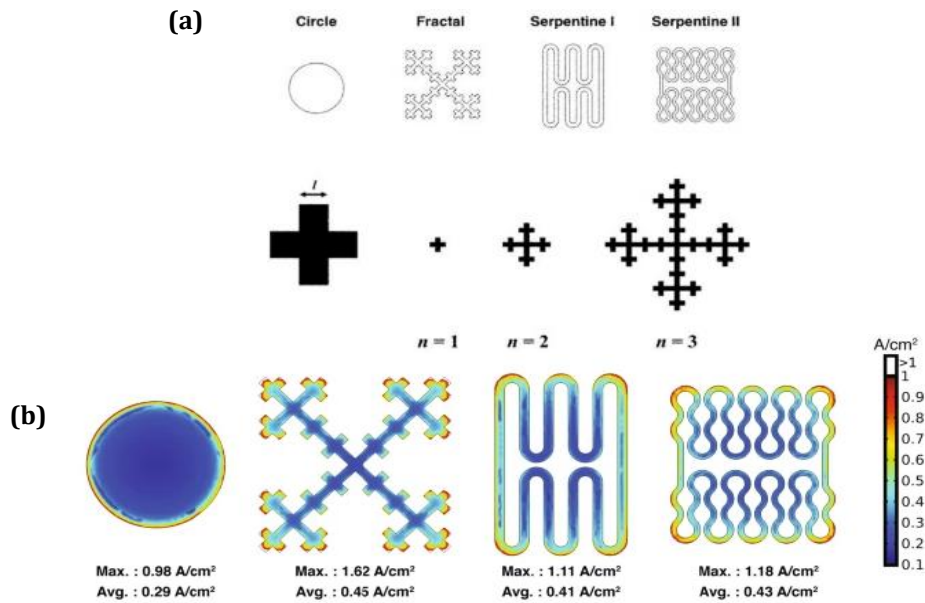


**Figure 2- 9** Literature proves the power consumption Circular > Serpentine1 > Serpentine 2> Fractal, (a) different shapes of electrodes, (b) current distribution in different shapes of electrodes [68]

The idea is to observe if the presence of the fractal shape made by SU8 creating smaller openings all around the electrodes might yield the same/similar or better results due to a simple distribution of the conductive parts (see **Figure 2-9, 2-10**). **Figure 2-10** shows the Mask for a Honeycomb structure. This was designed and fabricated in ESIEE Paris Cleanroom during the thesis to observe the edge effect due to the structure. It was later observed that the impedance was not affected by the edge effect. It is only affected by the surface area of the samples. The edge effect is specifically significant for the stimulation application.

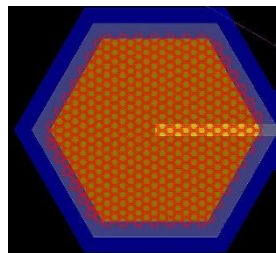


**Figure 2- 10** Zoomed-in view of the mask for a hexagonal electrode with honeycomb shapes inside

### 2.2.1.4 Noble Material Electrodes (Gold and Platinum Microfabrication

Due to being one of the most conductive materials **Gold (Au)** has been explored as an option for bio-implant materials for a long time [25], [99], [147], [152]. The reason gold is one of the most suitable candidates to be used as a biomaterial is its biocompatibility along

with providing excellent conductivity. Gold is also one of the most biocompatible materials [153], [154].

**Figure 2-11** shows the step-by-step procedure of fabricating electrodes with noble material. The procedure in detail has been explained in the *Annex*.

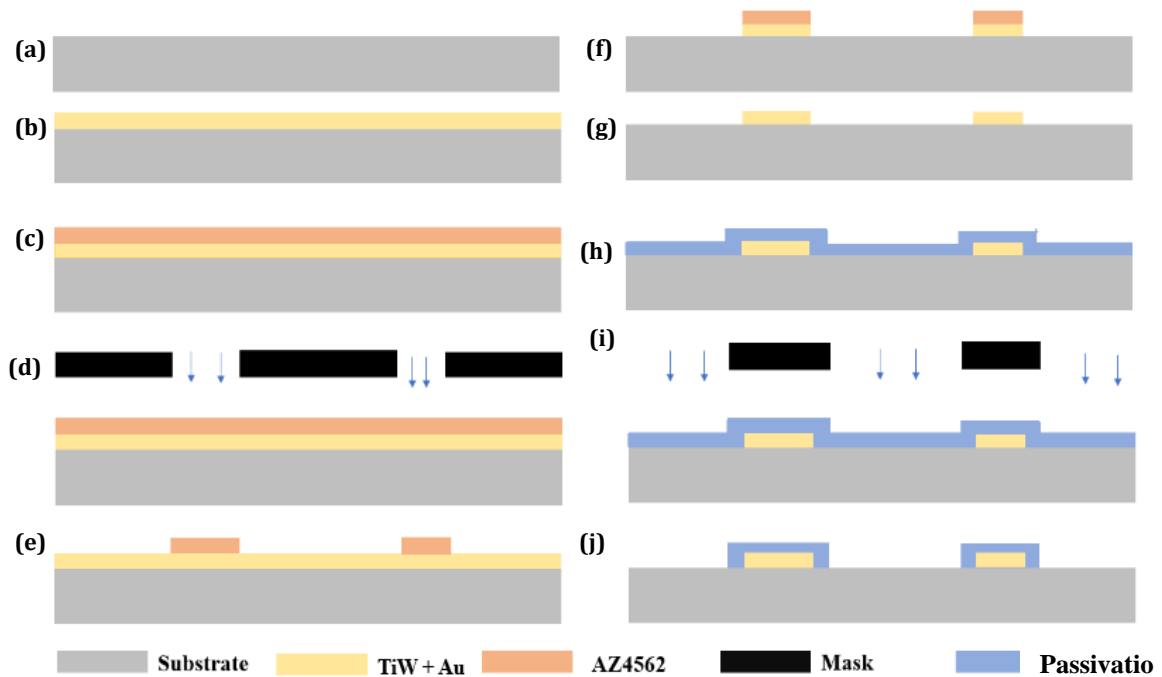


**Figure 2- 11** Flow diagram of different steps of microfabrication in cleanroom (a) Substrate, (b) metal layer, (c) photoresist layer, (d) UV exposure, (e) development of resist, (f) etching, (g) removal of resin, (h) spin-coating of passivation layer, (i) UV exposure, (j) after PEB and then development

When inserted inside the body, it does not create adverse or toxic reactions upon encountering the skin, tissue, or internal organs. This also reduces the risk of post-operative infections after the insertion of an implant. Gold implants also show malleability, which makes Au a perfect candidate for fabricating supple/flexible implants. Among all biocompatible metals, Gold shows the best corrosion resistance, and is high in density [155]. The shiny, golden color of Gold was initially one of the reasons Gold became popular among fabricators and surgeons for better visibility during insertion and later in post-operative imaging [156], [157]. Also, subacute responses to Au implantation have been reported to show no overt reactive or toxic biological reactions besides those that were triggered by the injury itself [153]. Due to its having so many preferences, Gold has been used in fabricating bio-implants since the 16<sup>th</sup> century. The abundance of literature makes it the best candidate as a reference material [157], [158].

**Platinum (Pt)** is a silverish-white noble material that has been used in bioimplant fabrication due to its having biocompatibility with very good conductivity (9.4e6 S/m at 20° Celsius) and low resistance (1.1e-7 mΩ). This material also possesses excellent charge transfer capacity (By redox in the electrolyte - very important for good neural stimulation). Pt also has good heat dissipation, which helps the implants and the enclosing environment from overheating. The implants are also radiopaque (visible to X-ray), which makes the quality control process easier [113], [157]. This is one of the most common noble materials, meaning it does not react easily with other materials, therefore doesn't oxidize, and is very resistant to corrosion. Pt has been the choice of material in case of neural stimulation and

recording for the last few decades given the fact that it is far more durable than Gold and susceptible to strain, hence maintaining the quality of the sample over the long run. In a lot of cases, Pt is used as a mix to another metal to increase the melting point of the alloys and reduce their thermal expansion [145], [159]–[161].

There is a standard protocol followed for fabricating electrodes with noble materials, like Gold (Au) and Platinum (Pt). The first step of the noble metal deposition is sputtering a thin layer of metal categorized as an adhesion layer, that helps the noble metal stick to the substrate. For Gold deposition, TiW is used as the adhesive layer, and for Platinum, Ti is used. The thickness of the adhesion layer is approximately 20 nm.

To start the deposition, the wafer is placed inside the chamber on a place holder (in ALCATEL-SCM 600, (see **Figure A-3 (a)**). The DC power of the equipment is set at 200 watts and the Argon gas flow was set at 80 SCCM. The wafer is positioned on top of the TiW target. The deposition time was set at 20 seconds, and subsequently, the cache over the TiW target is opened which results in a deposition of TiW of 20nm in height. Once the deposition of TiW is done, the cache of the gold deposition is simply opened and the wafer along with the placement holder moved to the top of the gold target. The timer is set at 5 minutes to result in a gold deposition of 500 nm (see **Figure 2-11 (b), 2-12**).

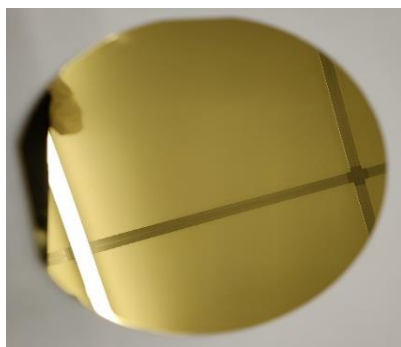


**Figure 2- 12** TiW and Gold sputtered on a glass substrate

In the photolithography room, the positive photoresist PFR7790, a yellow, liquid of low viscosity is spin-coated on top of the gold layer with a set acceleration of and velocity (3125 Turn/min) for 30 seconds which results in a 1.1  $\mu\text{m}$  high deposition of PFR7790 resist on top of the gold layer (see **Figure 2-11 (c)**). Right after the spin-coating step, the wafer is placed on a hotplate soft-baked at 110°C for 3 minutes (see **Figure A-6**).

After that, the wafer was exposed (**Top Side Alignment (TSA)**) to UV light for 3.6 seconds. After that, the resin is developed using the appropriate developer (PRD 238) for approximately 1 minute (see **Figure 2-11 (d, e)**).

Subsequently, first, the gold layer is etched (using etching agent KI: I<sub>2</sub>) by employing the wet etching method (for 3 minutes or more) and then the TiW layer is wet etched in H<sub>2</sub>O<sub>2</sub> (for 3 minutes or more). Subsequently, the resin needs to be cleaned in Acetone for 2 minutes, DI-water cleaned and N<sub>2</sub> dry (see **Figure 2-11 (f)**).

Negative PR SU8-2002 was spin-coated for 30 seconds as a passivation layer, setting the speed of rotation at 2000 rpm and acceleration at 500. This PR is transparent and has very little viscosity (see **Figure 2-11 (h)**).

After spin-coating the wafer was placed on the hotplate for subsequent heating at 65°C (For 2 minutes), then at 95°C (For 2 minutes), and at 65°C (For 1 minute) for hardening the resist (soft baking).



For the exposure, there needs to be an alignment step. However, unlike the previous one (see **Section Annex-1.1.2**) this alignment requires finesse. Because there's already a layer of metal. So, the mask for the SU8 layer should be exactly aligned over the metal layers. There are specific signs placed on the side of the mask while drawing, for simplifying the alignment.

Afterward, the wafer was exposed to UV light for 34 seconds (see **Figure 2-11 (i)**). After exposure, a **Post Exposure Bake (PEB)** was done by placing the wafer on a hotplate subsequently at 65°C (For 2 minutes), then at 95°C (For 2 minutes), and at 65°C (For 1 minute).

After that, the wafer was placed in a 100% solution of developer for SU8-2002 and stirred for 2 minutes. Right after that, there was an IPA rinse for 1 minute. This step is done since SU8 is hydrophobic and the IPA rinse makes the water bath more effective. Afterward, a 3-minute DI water bath followed by a compressed N<sub>2</sub> clean was performed (see **Figure 2-11 (j)**).

Before cutting the samples into individual pieces, a thick positive **Photoresist (PR)** AZ4562 was spin-coated on top of the wafer to protect the structures. The speed was set at 1500 rpm with an acceleration rate of 500 and it was spun for 30 seconds to get a PR layer of 15µm in thickness. After that, there is a 20-minute rest period for the resin to set on the wafer.

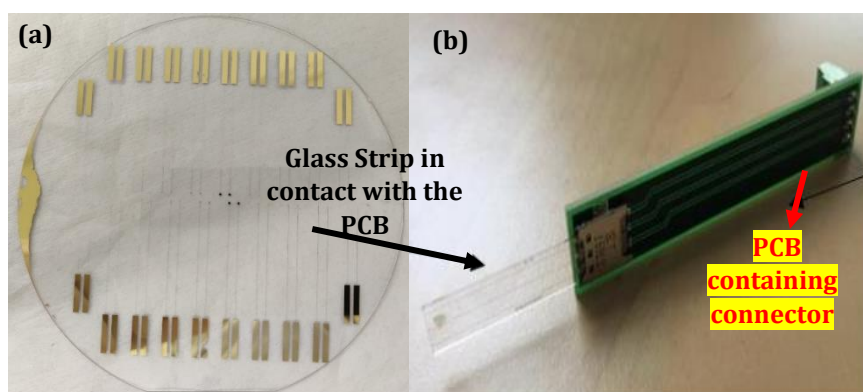


**Figure 2-13** (a) Gold electrodes on a glass wafer, (b) Electrode strip connected to the interface PCB

Afterward, it was put on a hotplate at a temperature of 65°C (For 2 minutes) and 110°C (For 5 minutes) subsequently. The baking makes the thick resist harden on top of the structure, which protects its structure when cutting with a Diamond blade into specific pieces. **Figure 2-13 (a)** shows an example of fabricated Au on a Glass wafer before cutting individual samples. **Figure 2-13 (b)** shows an individual sample that is connected to a PCB.

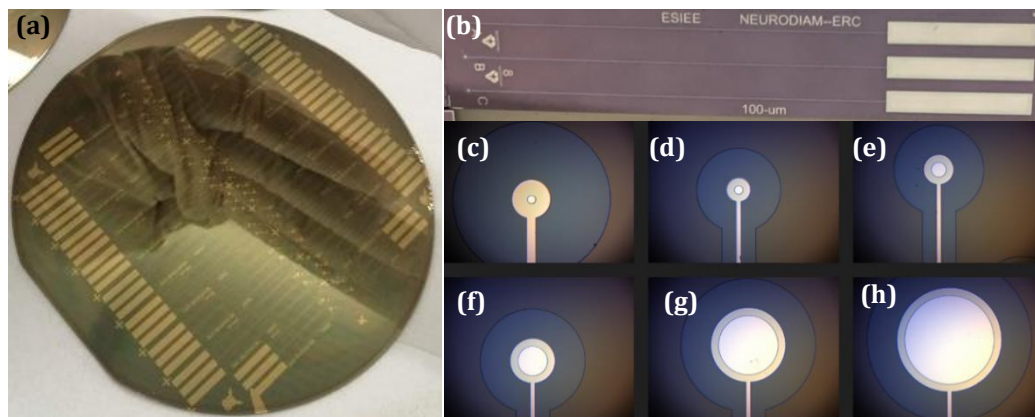


**Figure 2- 14** (a) Platinum electrodes of diameters (b) single strip of cicular Pt electodes on Si substrate with 3 indepnt smaples (c) 30mm (d) 60m (e) 100 $\mu$ m, (f) 200 $\mu$ m, (f) 400 $\mu$ m, and (g) 600 $\mu$ m

The process for platinum is almost the same (except for specific materials used). However, in the case of Platinum after priming, a negative photoresist NLOF 2020 needs to deposit before the sputtering, due to the fact that a lift-off method needs to be used for etching platinum. Upon the PR deposition, a 20 nm adhesion layer of Ti and a 150 nm high layer of platinum is deposited in 2 minutes 30 seconds by sputtering (see **Annex 1.1.1**).

For Pt lift-off, sonic vibration along with submersion in H<sub>2</sub>O<sub>2</sub> is used. Afterward, the passivation and protective layer deposition are the same as gold deposition. **Figure 2-14 (a)** shows an example of fabricated Pt on a wafer before cutting and subsequently samples of different sizes seen under a microscope.

It is notable that while gold has been the ‘gold standard’ as a biomaterial for quite some time, it is not without its challenges. One of the most crucial ones is the delamination of the metal over time which compromises the quality of the device and hence the result (see **Figure 1-16**) [25]. Gold samples when in thin and microscale become extremely susceptible to stress and tension and after a certain iteration of the experiment cracks and degradation appear in them, which has been proven in literature [100] and been observed during the work of this thesis, which compromises the results of yield from the sample [162].

While platinum is not very dangerous to human bodies, it has been reported to cause DNA alterations, cancer, allergic reactions of the skin and the mucous membrane, damage to organs, such as intestines, kidneys, and bone marrow, hearing damage [163]–[165]. It can cause potentiation of the toxicity of other dangerous chemicals in the human body, such as selenium.

### 2.2.2 Different Methods of Diamond Fabrication

Since the beginning of the invention of synthesizing Diamond, there have been multiple technologies for fabricating different types of Diamonds [114].

For this thesis, the only interesting type of Diamond is the polycrystalline Diamond. The single-crystal diamond cannot be used for microfabrication and neural implant due to the small size of the substrate (below 2 inches).

### 2.2.2.1 High-Pressure High Temperature (HPHT)

The High-Pressure High-Temperature process, often mentioned as the HPHT process is the first ever developed process and to this day used with or without some modification, as a way of fabricating Diamond since its development in the 1950s [115], [166].

**Figure 2-18 (b)** shows a 15.32 **carat (ct)**, cushion-modified Diamond, with grades equivalent to H color and I<sub>1</sub> clarity, which is the largest HPHT synthetic Diamond graded by GIA so far. **Figure 2-18 (c)** shows the fluorescent image of an HPHT Diamond, which shows a combination of apparent layered growth, along with the more common cross-pattern morphology seen in HPHT synthetics. The area of the pavilion shown here also indicates the region of **Photoluminescence (PL)** mapping. The red arrow in **Figure 2-18 (c)** indicates the regions that showed a high concentration of nickel, silicon, and **Nitrogen-Vacancy (NV)** center defects compared to the remainder of the mapped region. Above this more heavily doped layer is the metal rod inclusion. **Figure 2-18 (d)** shows the patterning in the corresponding phosphorescence image closely resembles the fluorescence image. A thin layer of material showing orange (~580 nm) phosphorescence is indicated by the white arrow [115], [167, p. 15], [168], [169].



**Figure 2- 18** (a)A reactor for fabricating HPHT Diamond, (b) the biggest HPHT Diamond reported by **Gemological Institute of America (GIA)** [146], (c) Fluorescence image of the HPHT-grown Diamond's pavilion (Taken with DiamondView), (d) The patterning in the corresponding phosphorescence image closely resembles the fluorescence image [113],[158],[159]

### 2.2.2.2 3-Dimensional (3-D) Printing

3-D printing of Diamond composites is one of the latest techniques of Diamond fabrication. With applications in defense, aerospace, and medicine, this technology is yet to be established as the go-to fabrication process in the industry. Popularizing this process can open the door to making the fabrication process extremely efficient, easy, and fast. This method, also known as **Additive Manufacturing (AM)** [170], first came to fruition on a spectacular level by biomedical engineer Dr. Kate Fox and her team at the **Royal**



**Figure 2-19** A microscopic view of 3-D printed titanium covered with the Diamond coating developed by RMIT researchers [161]

**Melbourne Institute of Technology (RMIT)** School of Engineering in 2018.

This enables a patient-specific, one-step fabrication process of **Nano Diamonds (NDs)** fabrication. The RMIT team successfully coated a 3-D printed Titanium implant with Diamond (see **Figure 2-19**), which is cheaper than Titanium powder. The coating is fabricated with a microwave plasma process at the **Melbourne Centre for Nanofabrication (MCN)** in Australia. The Titanium scaffolds and Diamond are combined to create the biomaterial [171].

### 2.2.2.3 Chemical Vapor Deposition

**Chemical Vapor Deposition (CVD)** is another method of growing Diamond in the laboratory where a ratio of hydrocarbon gas is subjected to a moderately high temperature and pressure in a vacuum [115]. For this method, Diamond seed crystals or Nanoparticles are placed in a Diamond growth chamber filled with carbon-containing gas, such as Methane ( $\text{CH}_4$ ). The chamber is heated to about  $900\text{-}1200^\circ\text{C}$  and the microwave beam causes carbon to precipitate out of a plasma cloud and deposit onto the seed layer (see **figure 2-20**).

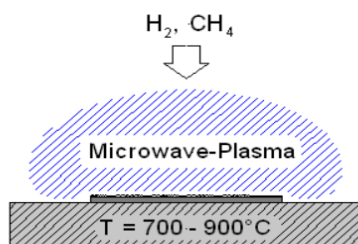


**Figure 2-20** Simplified representation of CVD Diamond growth in a vacuum [113]

To explain the procedure more (see **Figure 2-20**), in the CVD method Diamond growth takes place inside a vacuum chamber filled with hydrogen and carbon-containing gas, such as methane usually with a microwave beam as a source of energy. The microwave breaks down the  $\text{CH}_4$  molecules, and the carbon atoms diffuse toward the colder, flat Diamond nanoparticle plates. Crystallization starts and continues over weeks, while several crystal growths might take place at the same time. The exact number depends on the combination of the size of the chamber and the number of nanoparticles present. The tabular crystals often develop a rough edge of black graphite which needs to be cut away. They also display a brown color that can be removed by heat treatment before removal. Most CVD-grown colorless materials on the market were probably once brown crystals that have been decolorized by HPHT annealing [116], [172].

In the ESIEE-Paris cleanroom, the CVD method is employed using SEIKI Diamond Growth equipment to grow an intrinsic Diamond. The detailed method is discussed in **Section 2.2.3**.

CVD Diamond can be electrically doped during its growth phase. The most common dopant is Boron, used to fabricate Boron-Doped Diamond (BDD) for the project ERC-NEURODIAM. By incorporating elements from column III or V of the Mendeleev table - acceptors or free electron donors - it is possible to dope Diamond films synthesized by the CVD process. The doping gas is **Trimethylboron (TMB)**. Since ESIEE Paris' facilities do not possess this gas line, or the equipment needed, Boron-Doped samples were sourced from the French Alternative Energies and Atomic Energy Commission (CEA). There, TMB was added to the  $\text{H}_2/\text{CH}_4$  gas mixture, leading to  $2.1021 \text{ at.cm}^{-3}$  boron concentration in the crystal.

### 2.2.3 Diamond Microfabrication Process

For this thesis, the **Microwave Plasma Chemical Vapor Deposition (MPCVD)** technique is used to fabricate polycrystalline Diamond, because this method is compatible with the standard microfabrication process in ESIEE-Paris cleanroom.

Power (W)	Pressure (Torr)	H <sub>2</sub> (SCCM)	CH <sub>4</sub> (SCCM)	Temperature (°C)
3000	30	500	7.5	600-900

*Table 2-1 Parameters for Diamond fabrication*

There are 2 different types of microfabrication methods that are used, bottom-up and top-down method, as mentioned in **Figure 2-15**. The figure represents the methods as shown in literature. The bottom-up process is employed in this thesis and is explained more in detail in **Figure 2-22**.

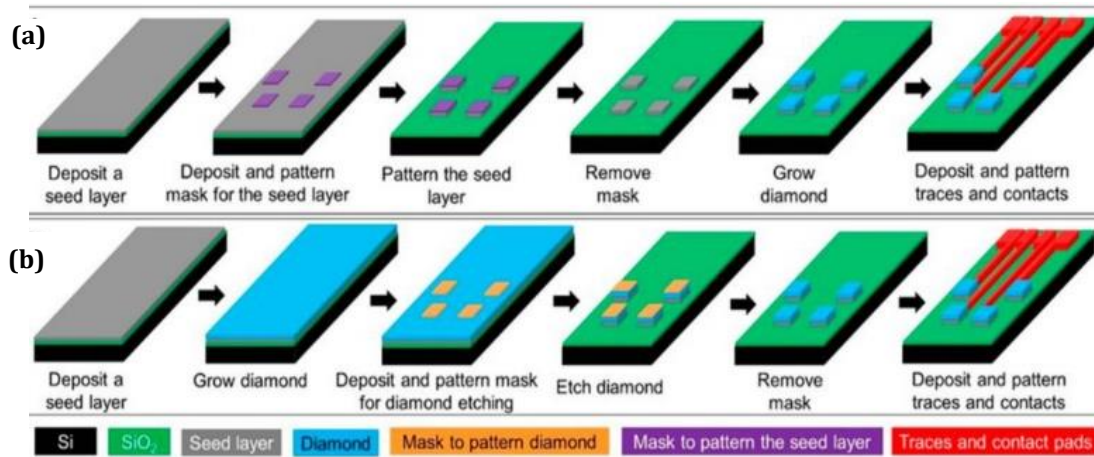


**Figure 2- 15** Schematic plots of the two typical microfabrication methods for making Diamond microelectrode arrays. (a) The bottom-up approach where Diamond electrodes are grown directly on a pre-patterned seed layer. (b) The top-down approach where a continuous Diamond film is grown on the seed layer followed by Diamond etching to form the electrode patterns [112]

This method is used to fabricate both intrinsic Diamond and conductive Diamond, e.g.: **Boron Doped Diamond (BDD)**. For the deposition, the wafers are first plasma-activated, and then the wafer is submerged in **Poly Diallyl-Dimethyl-Ammonium Chloride (PDDAC)** and then in **Diamond Nanoparticles (NP)** solution. After that, the wafer is put in the vacuum to burn the polymer a bit and place the Diamond Nanoparticles in their place [173], [174]. After that, a making layer of Aluminum is deposited on the wafer.

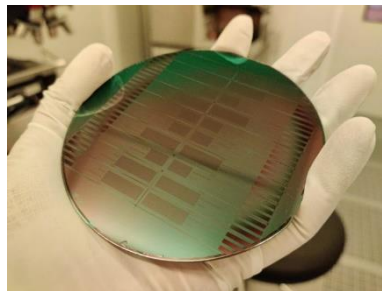


**Figure 2- 21** Just before putting in the reactor a sample with etched AlN

It is possible to grow Diamond directly. However, that would require subsequently etching the Diamond with RIE (dry etching). But etching Diamond is very time-consuming.

Therefore, another technique was used that requires fashioning a mask layer with a thin deposit of **Aluminum Nitride (AlN)**, to not expose the Diamond nanoparticles to methane and hydrogen plasma. In this case, localized Diamond growth was done. This AlN layer must be able to withstand the temperature of the plasma during Diamond growth that could reach over 650°C. In **Figure 2-38** some images of the full Diamond circular electrodes are shown under the SEM with different magnifications.

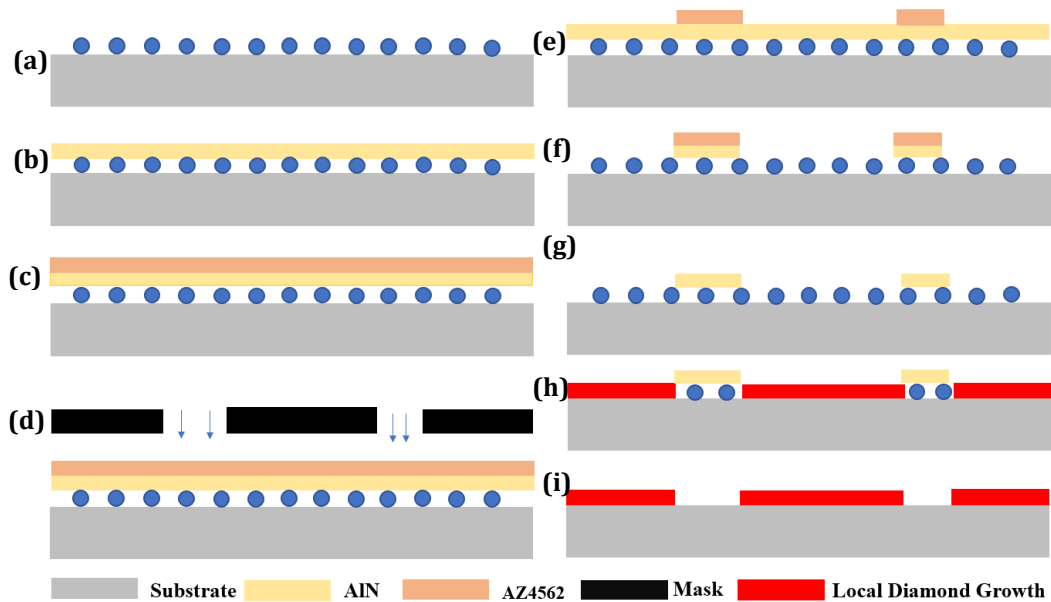


**Figure 2- 22** (a) Nanoseeding, (b) AlN layer sputtering, (c) AZ4562 layer spincoating, (d) alignment and UV exposure, (e) uncovered AlN layer etched, (f) photoresist removal, (g) wafer inside the Diamond reactor, (h) local Diamond growth, (i) AlN etching

After the seeding process (see **Figure 2-22 (a)**), AlN is deposited on the wafer using reactive cathodic pulverization (see **Section 2.2.1.1**) with the following parameters: Upon choosing the Al target, N<sub>2</sub> gas is flowed through to get a 1 μm AlN layer (see **Figure 2-22 (b)**).

A thick resist AZ4562 is used to protect AlN (see **Figure 2-22 (c)**). Then the AlN is patterned desirably using a mask (see **Figure 2-22 (d)**). Subsequently, the wafer is placed in a low-concentration base and AlN not protected by the resin is etched (see **Figure 2-21, 2-22 (e)**). The PR is then removed by using a solvent (see **Figure 2-22 (f)**). The wafer is then ready to be placed inside the Diamond reactor to grow Diamond wherever it's nano-seeded (see **Figure 2-22 (g)**). This selective Diamond growth is called local growth of Diamond (see **Figure 2-22 (h)**), and this can be used for both intrinsic and doped Diamond. Then the rest of the AlN is removed (see **Figure 2-22 (i)**). This process was used to produce all Diamond samples. The parameters mentioned in **Table 2-1** are used in the Diamond reactor in ESIEE Paris for the Diamond growth.

### 2.2.4 Titanium Nitride (TiN) Fabrication

Due to the high-temperature environment during Diamond growth (>650°C), conventional metallic material like gold cannot be used to define the metallic tracks underneath the Diamond layer. To fight this challenge, TiN is used as tracking material underneath the Diamond growth. Titanium Nitride (TiN) is a very tough ceramic material, often used as a **Physical Vapor Deposition (PVD)** coating on titanium alloys, metallic, carbide, and aluminum additives to improve the substrate's surface homes. It falls into a unique

category of refractory metals where a non-metallic element, N constitutes a transition metal element (Ti), which belongs to a unique class of refractory metals [14].

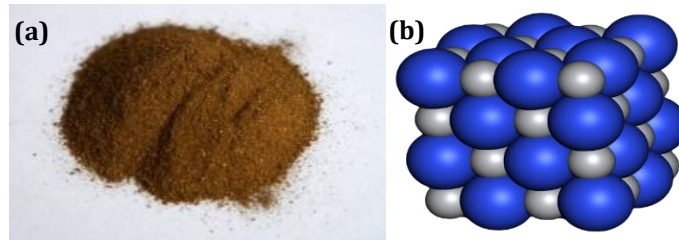


**Figure 2- 23** TiN (a) dust and (b) 3-D structure (Blue spheres represent Titanium atoms, grey spheres represent Nitrogen atom) [14], [56], [58]

TiN is often used as a thin layer of coating in order to harden and protect the surface against cuts and slides. This alloy is also used for decorative purposes, due to its gold-like appearance (see **Figure 2-23 (a)**). It is notable that the alloy has a brown color but appears to be golden when used as a coating. The typical TiN formation has a NaCl-type crystal structure (see **Figure 2-23 (b)**) and is thermodynamically stable [14].

The reason TiN has gained popularity in the bio-medical community is its rigid physical property, along with its non-toxic, biocompatible nature which is very important when it comes to the exteriors of bio-medical implants. TiN also possesses enhanced wettability, and high scratch resistance, along with a low friction coefficient [175], [176].

#### 2.2.4.1 Reactive Cathodic Pulverization

A specific process was developed to achieve the TiN layer using reactive cathodic pulverization. The TiN layer is sputtered on in a PVD by reactive sputtering technic, during Ti deposition by adding Nitrogen (N<sub>2</sub> gas), a TiN layer was achieved at a pressure of 0.68 mbar at 500 W for 30 minutes to achieve 300 nm of TiN material. To pattern the TiN layer standard lithography process (Annex) and a wet etching process were used (described below).

#### 2.2.4.2 Wet Etching of TiN

For TiN etching a chemical solution of TBR19 from Technic was used. TBR19 and Hydrogen Peroxide were mixed, and the solution was heated at 40°C. The solution was heated for 15 minutes, before submerging the wafer completely in the liquid (see **Figure 2-24 (a)**). Soon after that, it would be observable by eyes, the removal of TiN (see **Figure 2-24 (b)**).

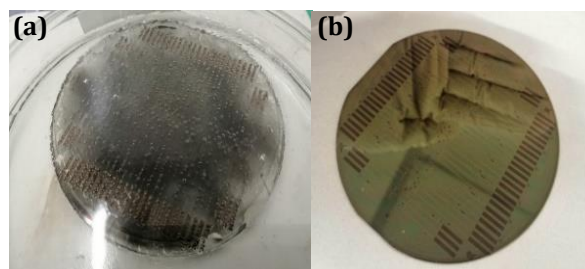


**Figure 2- 24** (a) Wafer being etched in etching liquid on heat, (b) wafer with etched TiN

### 2.2.5 TiN-Pt-TiN Stack Model

The purpose of this model is to get the best of both components. Due to TiN being an alloy, it does not possess the conductive property of Pt. So, to reduce the serial resistance of the sample, a thin layer of Platinum is stacked in between two layers of TiN. Therefore, when it comes to electrochemical interface, the high sensitivity of TiN, corrosion resistance, and increased heat resistance have made it a very popular candidate as a coating bio-material [175].

To fabricate this model first a layer of TiN is sputtered following the standard protocol (*see Annex-1*) until the deposition of the passivation (SU8) layer. Instead, platinum is sputtered following the standard protocol (*see Annex-1*), again until before the passivation layer, and finally, another TiN layer is deposited, only this time all the steps from the regular protocol are followed along with the passivation and the final protective layer for cutting. The final structure has a stack of TiN-Pt-TiN as a conductive layer, so going forward, it would often be addressed as the stack model for simplification purposes (*see Figure 2-25*). One of the reasons for this stack model being an area of interest is that this stack lowers the overall serial resistance of the electrodes and due to being temperature resistant, can support the extreme temperature inside the Diamond reactor. The resistivity of the standard deposition of TiN is  $6.16e-4 \Omega.cm$ . Whereas, for the stack, a resistivity of  $1.06e-5 \Omega.cm$  is measured. The resistivity of TiN stack model is closer to the resistivity of Au, compared to the resistivity of flat TiN.

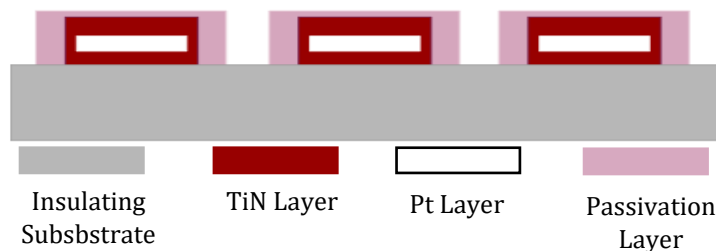


**Figure 2- 25 2-D croos sectional view of TiN-Pt-TiN stack model**

## 2.3 CLEANROOM Characterization Process

Starting right after fabrication, several tests are done to understand and maintain the performance of the samples. Here are the most frequently done, routine protocols that are used for all the samples explained in short.

### 2.3.1 Short-cut test after fabrication

To ensure that, during the fabrication process, there aren't any gaps on the tracks or residual metallic traces around the structure a simple resistance measurement test is done right after fabrication inside the cleanroom. In case of a gap on the tracks, when two probes are placed on the electrode and the respective track, an open circuit is observed. In case of some fabrication issues like metal not being etched from the surface properly, or the removal of SiO<sub>2</sub> from the top layer due to etching, resulting in exposure of the Si layer underneath might cause the appearance of a short circuit in the structure. Due to alignment issues, errors in the passivation layer, etc., an open circuit might appear, due to the lack of



connection between the electrode and contact pad (In the case of STEs). To ensure the integrity of the samples, they were tested under an optical microscope and via electrode probes.

### 2.3.2 Optical Microscope, Profilometer, and Scanning Electron Microscope (SEM)

After fabrication, to understand if the fabricated samples had the physiological properties as desired, they were checked under an optical microscope. Profilometer (see **Figure 2-26(a)**) and SEM (see **Figure 2-26 (b)**). in order to have a visual primary test of the samples.

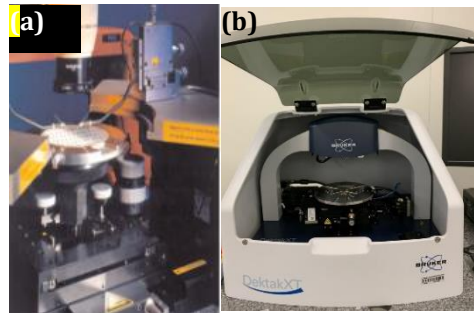


**Figure 2- 26** (a) Manual Probe System PM5, (b) the mechanical profilometer in ESIEE-Paris CLEANROOM [59]

Upon observation, they were treated accordingly based on requirements (unclean samples, over-etched structured, structured destroyed during fabrication). **Figure 2-27 (a)** shows a Pt sample that is dirty and destroyed upon fabrication observed under a simple microscope, **Figure 2-27 (b)** destroyed AlN level shown under SEM, **Figure 2-27 (c)** shows the height of Diamond passivation in an IDE sample seen in profilometer.

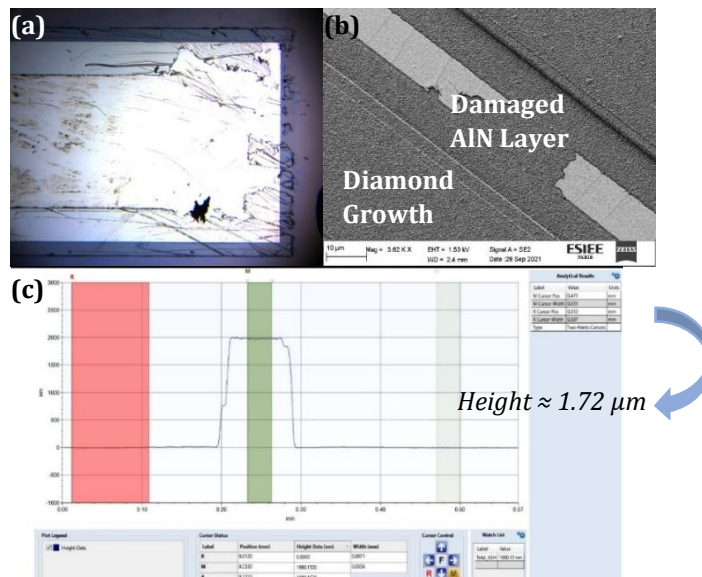


**Figure 2- 27** (a) Destroyed contact pad seen under simple microscope of a Pt sample, (b) destroyed AlN seen under SEM, (c) height of Diamond passivation in an IDE sample seen in profilometer

## 2.4 Post-Fabrication Process in Cleanroom (Electrode Cleaning or Activation)

During the characterization period, it was observed over time that repeated operation showed degradation in result (i.e., rise in impedance or lowering down the charge transfer capacity, or unstable result in general). While investigating the reason behind it, it was clear that the discrepancy in the result was due to the physiological changes in the structure. The changes were often due to salt accumulation from the salt, or due to dirt accumulation on the post-characterization wet surface because the experimentation was not done in a sterile environment. **Figure 2-28 (a,b)** shows some sample images under a simple microscope right after fabrication, and from **Figure 2-33** it can be seen how drastically they change after just one set of characterization experiments done in 0.01M of PBS at room temperature.

Sometimes the changes were due to the metal being eaten away during Faradaic charge transfer in CV, and the SiO<sub>2</sub> layer being exposed to the experimental environment.

After further investigation, it was also observed that sometimes right after fabrication the samples weren't often clean enough to yield the best result, which, in fact, is a case often reported in case of microfabrication [177]–[180], due to the area of interest being so small, even a very small amount of contamination during or post-fabrication, can cause major disturbance during characterization and other measurements [181]. To prevent these losses due to repeated characterization and get the optimum result, there were various cleaning procedures employed to see which one gave the optimum results.

**Figure 2-28 (a, b)** shows samples of different materials under a simple microscope, where the samples weren't completely clean even right after fabrication and were never taken out of the cleanroom.

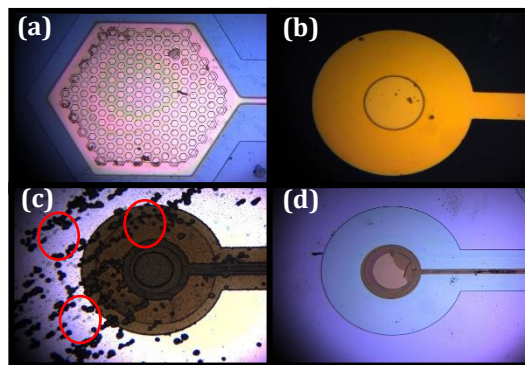


**Figure 2- 28** All samples are seen under simple microscope right after fabrication without any treatment (a) 600  $\mu\text{m}$  hexagonal TiN electrode on Si substrate with honeycomb structure on it, (b) 60  $\mu\text{m}$  circular gold electrode on Si substrate (c) 200  $\mu\text{m}$  BDD circular electrode with Diamond passivation on Si substrate (red circles show local Diamond growth), (d) 200  $\mu\text{m}$  circular TiN electrode on Si substrate

**Figure 2-28 (a)** shows the structure with some dust accumulation due to the structure having a small opening. Because of the small nature of those openings, that dust drastically changed the result of the samples, and some samples even showed a result that appeared to be almost like an open circuit. **Figure 2-28 (b)** showed a gold sample with small dust contamination right after fabrication, **Figure 2-28 (c)** shows a full Diamond electrode with unwanted intrinsic Diamond growth everywhere (marked with red boxes), and **Figure 2-28 (d)** shows TiN electrodes where there is the residual of photoresist even after cleaning the protective layer with acetone.

There were also some treatments done in order to yield better results during and/or after fabrication, the results of which are discussed in **Chapter 3**. Some of the operations which were done for cleaning and optimization purposes are discussed here:

### **2.4.1 Oxygen Plasma Cleaning (Cleaning Method - 1)**

The first cleaning method that was employed was plasma cleaning by using **Reactive Ion Etching (RIE)**. In this cleaning method, the samples were placed inside the NEXTRAL equipment (see **Figure 2-29**), with only the electrodes exposed, and the contact pads, and tracks covered with a Si wafer for both coverage purposes and for ensuring placement in position during the whole operation.



**Figure 2- 29** NEXTRAL equipment for plasma operation in ESIEE Paris Cleanroom

50 SCCM O<sub>2</sub> gas flow was flown inside the chamber for 90 seconds with the RF generator set at 90 Watts, and the pressure set at 90 mTorr. This method was used to clean some TiN samples and then the results were compared with other cleaning methods. The method did not show good results compared to other cleaning methods. For simplicity purposes, it would be addressed as cleaning method -1 moving further on.

### **2.4.2 UV and H<sub>2</sub>O<sub>2</sub> Cleaning (Cleaning Method - 2)**

In this method, the samples were exposed under UV (soft exposure setting in the equipment shown in **Figure A-7**) exposure for 5 minutes while they were submerged in H<sub>2</sub>O<sub>2</sub>. Further on, this method will be addressed as cleaning method - 2 for simplification purposes.

The advantage of this cleaning method was because of the UV exposure and the invasive nature of the H<sub>2</sub>O<sub>2</sub>, even the smallest surface was cleaned. On the other hand, sometimes this method can be intensive and damage the surface of the sample, especially if the cleaning method isn't done right after manufacturing. Because during the characterization process and the DI water cleaning in between, the samples become more susceptible to damage. Therefore, damage to the surface is often observed (when seen under a microscope), if the samples are cleaned after doing one set of characterization (see **Figure 2-30 (b)**).

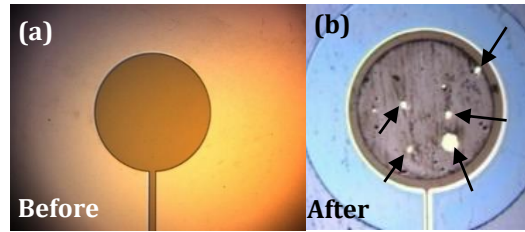


**Figure 2- 30** 600  $\mu\text{m}$  circular TiN-Pt-TiN electrode seen under microscope (a) before characterizing, (b) after characterizing and UV+H<sub>2</sub>O<sub>2</sub> cleaning (damages on the surface shown with arrow marks)

However, this is a method explored more in cleanroom technology and can be used for both conventional and non-conventional materials equally. Going further on, this proved to be one of the most practical cleaning methods, when employed right after fabrication. For simplicity purposes, it would be addressed as cleaning method - 2 moving further on. Unfortunately, this method is not well adapted for TiN structure as can be seen in the figure below. The strong reaction of H<sub>2</sub>O<sub>2</sub> with UV etches this metallic layer.

### 2.4.3 Acetone and IPA Cleaning with Ultrasound (US) (Cleaning Method - 3)

This cleaning method included submerging the samples in Acetone and putting them in a sonic bath for as long as they needed cleaning. Afterward, clean the samples in isopropanol and then in a DI water bath. This method did not clean all very thick layers of dust accumulation and it was difficult to set a strict parameter for the duration and the results were not satisfactory upon cleaning. For simplicity purposes, it would be addressed as cleaning method 3 moving further on.

To observe the effect of cleaning and the physical evolution of samples, one TiN sample was observed right after fabrication under the scope (see **Figure 2-31 (a)**), then it was characterized and cleaned with method - 2 (UV and H<sub>2</sub>O<sub>2</sub>) (see **Figure 2-31 (b)**), and afterward, it was used in measurements and cleaned subsequently with cleaning method-3 (Acetone and IPA) (see **Figure 2-31 (c)**). The black arrows show the damage on the surface of the electrode itself, and the red arrow shows the damage in the passivation level. This method reveals an adhesion issue between the TiN and Pt layers. For future reference, to avoid this issue an RIE Etching of Pt must be done to increase surface roughness and promote the adhesion between the Pt and TiN layer.

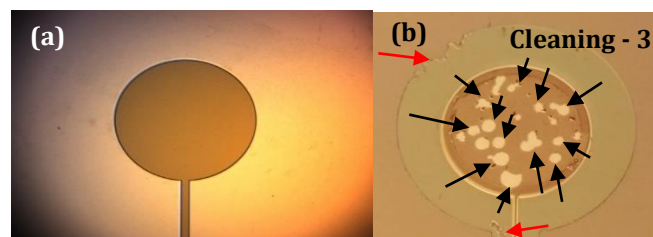


**Figure 2- 31** The same 600  $\mu\text{m}$  circular TiN-Pt-TiN electrode before and after cleaned with cleaning method -3

### 2.4.4 Acid Clean (Cleaning Method - 4)

All the samples are cleaned with acetone and IPA to remove the protective AZ4562 layer. However, in the search for a better cleaning method, the samples were cleaned with H<sub>2</sub>SO<sub>4</sub> right after fabrication. This method included taking a 98% pure H<sub>2</sub>SO<sub>4</sub> and submerging the

samples one by one carefully in the liquid and leaving it there for 3 minutes. After that, they were cleaned with DI water multiple times to make sure they had no traces of acid left. This visibly cleaned the sample the best. However, due to the invasive nature of the very pure acid and the handling issues, it was not adopted as a go-to cleaning method afterward. Moving forward, this method would be mentioned as cleaning method - 4.

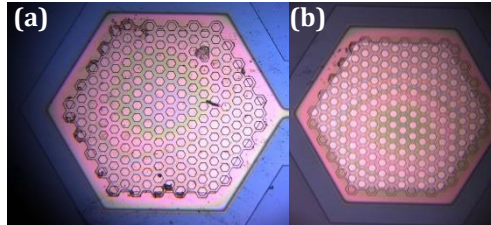


**Figure 2- 32** 2 different 400  $\mu\text{m}$  Hexagonal TiN electrodes (a) right after fabrication, (b) cleaning – 4 employed immediately after fabrication

**Figure 2-32 (a)** shows a sample right after fabrication and **Figure 2-32 (b)** shows another sample of the same size when cleaning – 4 was done before any characterization.

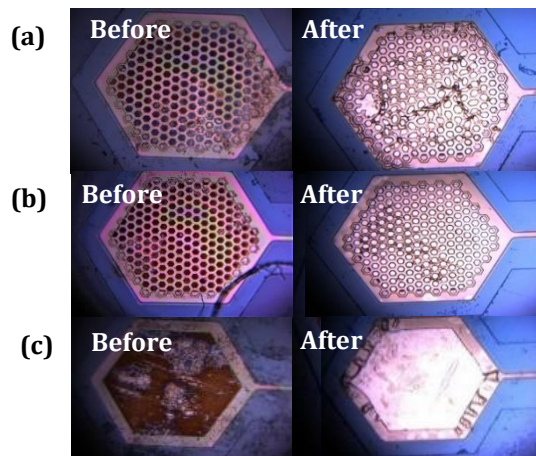


**Figure 2- 33** Three different 400  $\mu\text{m}$  hexagonal TiN electrodes before and after cleaning

**Figure 2-33** shows 3 different samples (400  $\mu\text{m}$  hexagonal TiN electrodes), where the before images show some samples after they were characterized and cleaned with cleaning method - 1 and 2, and the after images show after the same samples were cleaned with cleaning method - 4.

The observation from studying all the cleaning methods was, that considering efficiency and effectiveness in result, and the practical nature of the method, cleaning method – 2 (UV and  $\text{H}_2\text{O}_2$  Cleaning) is the best one and any kind of cleaning method should be done right after fabrication. Otherwise, the samples suffer from degradation and lose their integrity sometimes to the point that they can never be used again.

### 2.4.5 Black TiN

The TiN material fabricated during the thesis offers a way to produce a Black TiN, which basically is TiN with a nanostructured surface on the top layer to increase the effective surface area of operation. The process is the same as the wet etching of the TiN (see **Annex 1.1.3**). The single samples were taken and submerged in the etching agent, electrode-only for some time. **Figure 2-34** shows the black TiN that was obtained by putting the samples in TBR - 19 liquid and on heat and continuous stirring.

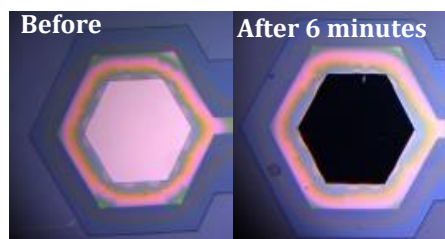


**Figure 2- 34** Hexagonal samples before and after being nanostructured

## 2.4.6 UV Treatment for Full Diamond Electrodes

Once fabricated in the chamber with the CVD procedure, all Diamond structure is Hydrogen-terminated. Often to yield a better result, and /or turn them into Oxygen terminated samples they are exposed to the UV while being submerged in H<sub>2</sub>O<sub>2</sub>. The protocol of the activation method is the same as the cleaning method - 2 (see **Section 2.4.2**). The benefits of the activation are observed in the results of impedance spectroscopy and cyclic voltammetry, which will be discussed in **Chapter 3** in detail.

## 2.5 Take Away from This Chapter

A significant part of this thesis was the microfabrication technologies carried out in the cleanroom to do several fabrication steps. This chapter gave an overall, compact idea of some of the most important techniques that were learned and employed during the period. The detailed fabrication process, with some more detailed process, is discussed in Annex, at the end of the thesis. This chapter gave an overall idea of all the processes carried out in the ESIEE Paris CLEANROOM with the target of fabricating a full Diamond implant and the relevant operations. In the following chapters, there will be results and numeric analysis of different samples based on multiple characterization processes.

To realize the fabrication of a full Diamond electrode, it was necessary to combine and understand both the conductive and non-conductive parts of an electrode. To that end, conductive (Boron Doped Diamond - BDD) and non-conductive Diamonds were analyzed separately with the help of two different types of samples. In this chapter, the fabrication of those samples was discussed. Strip-type electrodes were used to understand the conductive part (Gold, Pt, TiN, TiN-Pt-TiN, Black TiN, BDD), and the Interdigitated Electrodes were used to understand the property of the passivation layer or non-conducting part (SU8, Intrinsic Diamond). That was the primary reason for having two different types of masks and samples. There was a primary version of the IDE mask, which was revised to improve the performance as explained in detail later. In the case of strip-type electrodes, hexagonal masks were designed to fabricate and analyze the edge effect of the samples which is important for the stimulation application. The strip-type electrodes were fabricated with the material under investigation and SU8 or Intrinsic Diamond as the passivation layer. In the case of IDE, the samples were made of a conductive layer and SU8 or Intrinsic Diamond as the passivation layer. The microfabrication process is the same for a certain material, no matter the type of electrode. It is just necessary to use an appropriate mask to get the desired structure. This chapter provided an understanding of the processes involved in the fabrication process of the samples which would be characterized in the following chapter.



## Chapter 3

### Experimental Comparison of Different Materials in IDE and Microelectrodes

Starting right after fabrication, several experiments and tests are done in this chapter to understand and maintain the performance of the samples. Here are the most frequently done, routine protocols that are used for all the samples explained in short.

In this chapter, **Cyclic Voltammetry (CV)**, **Electrochemical Impedance Spectroscopy (EIS)**, and Nyquist Analysis of electrodes with different materials (Au, TiN, Pt, Diamond, and different compositions of those) will be presented. The objective is to have an electrode that is well-adapted for measuring or delivering a signal inside the body. To understand the effect of the process well, at the end of this chapter, the equivalent circuits of the electrode response were modeled. The proposed model provides a general idea of the performance of the electrodes, which gives important information regarding fabrication improvement and modification needs. These models also help predict the overall performance of the electrodes. There are well-established and used equivalent models for biomedical experiments in literature [182]–[184]. This thesis follows that path to propose the equivalent circuit for different samples.

The performance of the electrode material can be evaluated via electrochemical methods, namely, Cyclic Voltammetry, Electrochemical Impedance Spectroscopy, and Nyquist Analysis. From the electrochemical measurements, various information related to the behavior and performance of electrode materials can be obtained such as specific capacitance (also addressed as  $C_{sp}$ ), phase response, resistance, etc [185].

On the other hand, pseudo-capacitors, which appear due to the conducting parts and metal oxides as the materials for the electrodes, store the charge Faradically, which is also known as Faradic Current. Pseudo-capacitors are also mentioned as redox capacitors in the literature. The Redox capacitor possesses higher specific capacitance, i.e., can store more charges [186] when compared to **Electric Double Layer Capacitance** (also known as **EDLC** or  $C_{dl}$ ), as they can store charge via redox reaction in the bulk of the materials [187]. However, pseudo-capacitors have a lower specific power compared with EDLC as the redox reaction process takes a longer time. EDLCs rely completely on the physical storage of energy, while pseudocapacitors store parts in both physical and chemical energy [188], [189]. For electrodes to be termed as high-performance, the following properties should be owned by the sample: high specific capacitance, low impedance, considerable in size (in  $\mu$ scale), shape, and distribution method (depending on the application), and long lifecycle [190]. For stimulation application, the capacitance should be in  $\mu\text{F}/\text{cm}^2$ , and for the recording application, the impedance should be in  $\text{k}\Omega$  scale. For example, in digital EEG equipment, impedances up to **10 k $\Omega$**  are usually acceptable, but values below **5 k $\Omega$**  are still recommended, for a typical diameter of 10 mm ( $1.6 \text{ cm}^2$ ) [191], [192]. However, there is always a hand-off among, size, impedance, specific capacitance, and other parameters. For example, lower size means less insertion damage, but a larger value of impedance, and value of impedance is linked directly to noise level of electrode, yet suitable for individual data connection via small neurons. To measure the performance of the samples, the impedance spectroscopy is compared at 1 kHz, since the action potential of the neuron is recorded at 1 ms [38].

Since the beginning of this thesis, different types of samples have been characterized and treated with different methods throughout the thesis. A highlight of some of the treatment and the understanding is presented in the following chapter, as the author



saw fit. There are a bulk of experiments, data, calculations, methods, and procedures that have been done and studied, some of which will be discussed in the perspective.

### 3.1 Physical Electrochemistry and Equivalent Circuit Elements

Characterization of the samples is important for understanding the performance and subsequently ameliorating those. The characterization process is done in the ESYCOM Lab using various equipment. As one of the targeted applications of the implants would be **Electro Impedance Spectroscopy (EIS)** or **Bio Impedance Spectroscopy (BIS)**, it is also one of the most used characterization processes used to understand the samples and predict their performances in a biological environment. To that end, various solutions are used to mimic the experimental environment, e.g.: **Phosphate Buffer Saline (PBS)** is one of the most used solutions for these experiments. In this specific case, one tablet dissolved in 200 mL of deionized water yields 0.01 M phosphate buffer, 0.0027 M potassium chloride, and 0.137 M sodium chloride, pH 7.4, at 25°C. For comparison purposes, most of the BIS was carried out in the 0.01M of PBS. The electrical conductivities of the PBS buffer were  $\sigma_{\text{PBS}} = 1.4 \text{ S/m}$  and  $\sigma_{\text{PBS}} = 0.01 \text{ S/m}$ , respectively, and their relative permittivity was  $\epsilon_{\text{PBS}} = 80$ .

On the other hand, due to the CV requiring charge transfer, the experiments are usually done with salt that has a Faradic charge transfer capacity. The most used anions are  $[\text{B}(\text{C}_6\text{F}_5)_4]^-$ ,  $[\text{B}(\text{C}_6\text{H}_5)_4]^-$ ,  $[\text{PF}_6]^-$ ,  $[\text{BF}_4]^-$ , and  $[\text{ClO}_4]^-$ . The more coordinating the anion is, the more likely it is to have unwanted interactions with the cation, the solvent, or the analyte [193].

#### 3.1.1 Bio-Impedance Spectroscopy (BIS)

Bioimpedance spectroscopy is one of the most effective ways of measuring biological characteristics of tissue or environment, like the amount of body fat tissue ratio, increase and decrease in water level to diagnose a disease like renal failure, the state of a wounded cell, and the progression of its healing, etc. Compared to all the other existing methods like **Dual X-ray absorptiometry (DEXA)** [194], [195], **Bio Impedance Analysis (BIA)** [196], and **Air Displacement Plethysmography (ADP)** [197], BIS is the most accurate and non-invasive method of biological measurement. BIA is a method of measuring the Bio-Impedance at a single frequency, whereas BIS is done over a wide range of frequencies. BIS can measure until approximately  $\times\text{mL}$  of change in body water level [198], whereas all the other similar methods like BIA can measure hydration level change, but not too accurately [199]. Due to the experiments being done over a long range of frequency, the data is more accurate and by employing a **Band-Pass Filter (BPF)**, the data corruption due to interference at low frequency, and noise at higher frequency can be segregated from the result.

Impedance is typically measured by passing a small alternating current between two or more electrodes connected to the skin. Thus, the measured impedance reflects contributions from more than a single electrode [200]. The impedance of the electrode has an impact on the thermal noise of any recorded signal. A widely used technique to observe electrode impedance is electrochemical impedance spectroscopy which demonstrates the performance of the **Device Under Test (DUT)** over already recognized parameters. One of the simplest ways to display impedance data is through the bode plot (*see Figure 3-1 (a)*), which plots the frequency spectrum alongside the x-axis, the impedance,  $Z$  alongside the y-axis, and, the phase  $\theta$  or  $\varphi$  against a second y-axis (*see Figure 3- 1 (b)*) [201]. Common frequencies used for implant microelectrodes are in the variety of 0.1 Hz to 1 MHz with the electrode-tissue interface frequency taken at 1 kHz (related to the duration of an action potential, *see Section 1.1*). This range varies depending on the purpose of the implants and/or the placement of the implants inside the test subject. A higher value in impedance

results in a higher overall noise of the sign, which results in a decreased **Signal-to-Noise Ratio (SNR)**. A low SNR makes it impossible to gather the signals at higher frequencies such as neural spikes (which happen every 1 ms). BIS is also mentioned as Bio Impedance Measurement, and Electrical Impedance Spectroscopy, mostly when the experiment is done in-vitro [202], [203].

Ohm's law (see Equation 3-1) defines the resistance in terms of a ratio between voltage or tension (Denoted by V or E), and current flow (Denoted by I) (see Figure 3-1(b)).

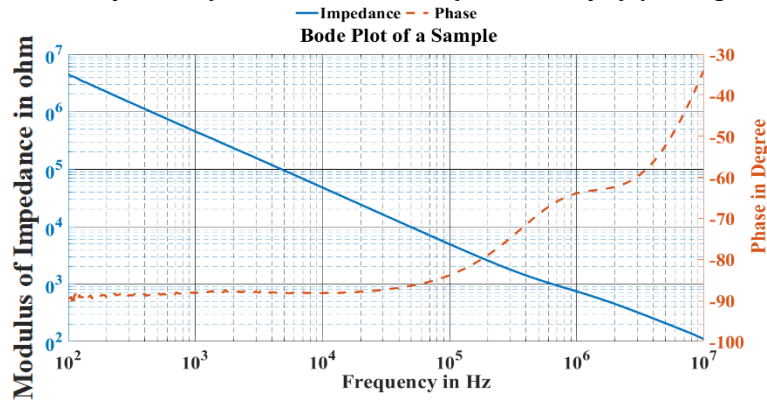


**Figure 3- 1** Bode plot of a sample presented in air medium

Electrochemical impedance spectroscopy is finding increasing use in electrochemical sensors and biosensors, both in their characterization, including during successive phases of sensor construction, and in their application as a quantitative determination technique. Much of the published work continues to make little use of all the information that can be furnished by full physical modeling and analysis of the impedance spectra and thus does not throw more than a superficial light on the processes occurring. The analysis is often restricted to estimating values of charge transfer resistances without interpretation and ignoring other electrical equivalent circuit components [201], [204]–[207]. In this thesis, the important basics of electrochemical impedance for electrochemical sensors and biosensors are presented, focusing on the necessary equivalent electrical circuit elements. This is followed by examples of its use in characterization and electroanalytical applications, at the same time demonstrating how fuller use can be made of the information obtained from complete modeling and analysis of the data in the spectra, the values of the circuit components, and their physical meaning. The outlook for electrochemical impedance in the sensing field is discussed. [208].

Usually, EIS is measured by applying a small excitation signal. The purpose is to find a linear response of the cell (If not linear, the voltage variation is considered small). The applied voltage can be expressed as:

$$V(t) = V_0 \cos(\omega t) \dots \dots \dots \text{Eq 3- 1}$$

In a linear system, the response signal, I(t), is shifted in phase and can be expressed as:

$$I(t) = I_0 \cos(\omega t - \phi) \dots \dots \dots \text{Eq 3- 2}$$

To define the impedance of the dipole, we introduce the two complex numbers:

$$\underline{V} = V_0 \exp(j\omega t) \ \& \ \underline{I} = I_0 \exp(j\omega t - \phi) \dots \dots \dots \text{Eq 3- 3}$$

Here, V(t) and I(t) are the real parts of  $\underline{V}$  and  $\underline{I}$ , respectively. The impedance can be expressed as:

$$\underline{Z} = \frac{\underline{V}}{\underline{I}} = \frac{V_0}{I_0} \exp(j\phi) = R + jX \dots \dots \dots \text{Eq 3- 4}$$

where R is ohmic resistance or the real part of the impedance. X is the imaginary part of the impedance  $\underline{Z}$ , also known as reactance.

The impedance magnitude can therefore be expressed (in ohms) as:

$$|\underline{Z}| = \frac{V_0}{I_0} \dots \dots \dots \text{Eq 3-5}$$

and its phase is given by:

$$\text{arg}(\underline{Z}) = \phi = \arctan \frac{X}{R} \dots \dots \dots \text{Eq 3-6}$$

As a rule of fundamental electronics, the impedance of a resistor is independent of frequency ( $Z = R$ ) and has no imaginary component, so the phase angle is  $0^\circ$  (see **Equation 3-4**). Due to having only a real impedance component, the current passed through a resistor stays in phase with the voltage throughout the resistor. And when there is an imaginary component, the equivalent impedance of the whole system, and phase angle can be calculated.

As a rule of fundamental electronics, the impedance of a resistor is independent of frequency ( $Z = R$ ) and has no imaginary component, so the phase angle is  $0^\circ$  (see **Equation 3-1**). Due to having only a real impedance component, the current passed through a resistor stays in phase with the voltage throughout the resistor. And when there is an imaginary component, the equivalent impedance of the whole system, and phase angle can be calculated.

**Figure 3-1 (a)** represents the bode plot at different frequencies and it is apparent from the modulus/absolute value of impedance that, in the lower and mid-range of the frequency the sample shows capacitive behavior, and the relevant phase is observed to be close to  $-90^\circ$  and in higher frequency three and the phase becomes more complex due to presence of induction introduced from the equipment and experimental environment.

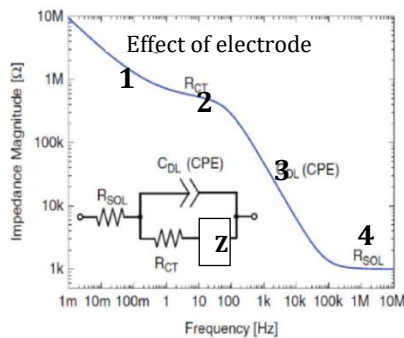


**Figure 3-2** Bode plot of the impedance magnitude of the Randles equivalent model of an electrochemical interface comprising both non-Faradaic and Faradic phenomena [196]

Most often, BIS is represented by a bode plot [209] as the simplest tool to understand the performance of the samples at different frequency ranges (see **Figure 3-2 (a)**). Also, often an equivalent circuit is designed [201], [210] to verify the experimental result and analyze the values of different components (Capacitance, serial resistance, etc.).

**Figure 3-2** [211]-[212] indicates the explanation of the Bode plot seen in EIS at different frequencies. Part 1 of these graphs is seen in very low frequencies and is indicated conventionally as a diffusion region and is indicative of the Warburg resistance component in the equivalent circuit [213], [214]. Section 2 of the bode plot usually represents the charge transfer region that comes from the ion transfers in between the liquid and the sample contact and the relevant charge transfer and in an equivalent circuit this part is represented by  $R_{ct}$ .

The Warburg diffusion element ( $Z_\omega$ ) is a **Constant Phase Element (CPE)**, with a constant phase of  $45^\circ$  (phase independent of frequency) and with a magnitude inversely proportional to the square root of the angular frequency by:

$$Z_\omega = \frac{A_\omega}{\sqrt{\omega}} + \frac{A_\omega}{j\sqrt{\omega}} \dots \dots \dots \text{Eq 3- 7}$$

$$|Z_\omega| = \sqrt{2} \frac{A_\omega}{\sqrt{\omega}} \dots \dots \dots \text{Eq 3- 8}$$

Where  $A_\omega$  is the Warburg coefficient (or Warburg constant which can be obtained by the gradient of the Warburg plot, a linear plot of the real impedance ( $R$ ) against the reciprocal of the square root of the frequency),  $j$  is the imaginary unit and  $\omega$  is the angular frequency [215]. If the thickness of the diffusion layer is known, the finite-length Warburg element [2] is defined as:

$$Z_0 = \frac{1}{Y_0} \tanh(B\sqrt{j\omega}) \dots \dots \dots \text{Eq 3- 9}$$

$$B = \frac{\delta}{\sqrt{D}} \dots \dots \dots \text{Eq 3- 10}$$

where  $\delta$  is the thickness of the diffusion layer and  $D$  is the diffusion coefficient. The thickness of the diffusion layer is related to the size of the electrodes, the ratio of surface and radius, the concentration of the liquid, excitation, temperature of the experimental environment, absence, and presence of turbulence, etc. [216], [217], [218].

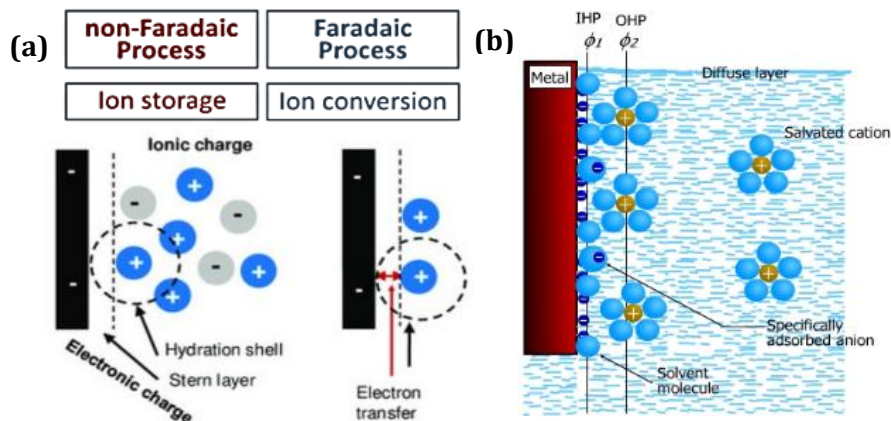


**Figure 3- 3** (a) Ion storage vs. ion conversion as the key difference between Faradaic and non-Faradaic (capacitive) electrode processes, using different examples, (b) the presence of a double layer when the sample is submerged in the liquid solution, IHP means Inner Helmholtz Plane, and OHP means Outer Helmholtz Plane [205], [210]

There are two ways in which the current is carried across the interface of a metal-to-electrolyte system, and these are known as faradaic and non-faradaic paths (see **Figure 3-3(a)**) [213]. In the **Faradaic Process**, current crosses the interface utilizing an electrochemical reaction such as the reduction or oxidation of the samples or some ions. In the **non-faradaic** operation, charged particles do not cross the interface, and the current is carried by the charging and discharging of the electrical double layer, which behaves like a capacitor in series with the **ohmic resistance** ( $R_{sol}$  or  $R_\Omega$ ) of the solution [219].

In most cases, during the Faradaic process, there is the transfer of electrons across the electrode, from a conducting (metallic) bulk phase to the electrolyte, and/or vice-versa. If electrons move to the electrolyte, the ions (or other molecules) that enter the electrode in reduced form leave as oxidized species when they return to the electrolyte phase (or to another bulk phase, such as a gas phase or solid salt). In other Faradaic processes, it is the ion that crosses the electrode, coming from an electrolyte phase and moving to the bulk metal phase that supplies the electronic charge, which is what happens in metal plating (or

the reverse, an atom dissolves as an ion). This process happens in the case of **Cyclic voltammetry (CV)** (see **Section 3.1.2**) [220], which will be discussed in more detail later on.

In a non-Faradaic electrode process, when current flows, it is noticed that charge is progressively stored. This is because ions or other species that come in contact with the electrode, cannot leave. This happens whenever there is no electrode reaction at all, and the electrodes are so to speak, 'locked onto the surface of the electrode'. **This is what causes the development of salt/species accumulation on the surface layer of the samples after an EIS experiment** (see **Figure 3-3**) [220].

When a metal dissolves continuously, it may become increasingly negatively charged because of the passage of continuous positive ions in the solution. The excess negative charge on the metal surface balances the excess positive charge and the solution side of the interface and hence, separation of charges exists [213], [221], [222].

The electrons orient themselves opposite a layer of cations of equal and opposite charges on the solution side of the interface. The electric field that is created consists of two layers of charges; hence it has been given the name double layer [223]. The separation of charges in the double layer can be compared to parallel plates in a capacitor as was done by Helmholtz. The double layer is also called the **Helmholtz Double Layer (HDL)** [224]. The capacitance coming from this layer is often called double-layer capacitance  $C_{dl}$ .

Water is a dipolar molecule. The oxygen end of the water molecule forms the negatively charged end and the hydrogen end builds up the positively charged end. Due to the dipole nature, the water molecule is attracted toward the electrode and contributes to the potential difference across the double layer [225].

The orientation of the water molecule depends on the charge on the metal surface. If the metal has a large negative charge, the  $H_2O$  molecules would be oriented with the positive ends (hydrogen) towards the metal and the negative ends (oxygen) towards the large positive charge. To break it down (see **Figure 3-3 (b)**) [223], there is an inner layer (inner Helmholtz layer-plane) in which the potential changes linearly with the distance. It comprises the absorbed Water molecules and sometimes the specifically absorbed anions. The next layer is an outer Helmholtz layer/plane comprised of hydrated (solvated) cations. The potential varies linearly with the distance. The last part is an outer diffuse layer, also called the Guoy-Chapman layer, which contains excess cations or anions distributed in a diffuse layer. The potential varies exponentially with the distance [223], [224], [226], [227].

In the case of this thesis, it will be observed that in the case of Cyclic Voltammetry, both the Faradic and Non-Faradic phenomena are present [219].

For a more precise understanding of the EIS data, Equivalent Circuit Fitting (see **Figure 3-4 (a)**) is performed [219]. **Figure 3-4 (b)** shows the influences on the impedance are then represented by an Equivalent Circuit and the value of each influence is calculated by fitting a simulation of the data to the real data. Nyquist plot of Pt electrode (blue) and carbon SPE (red) in 2.5 mM  $K_4 [Fe (CN)_6]$  + 2.5 mM  $K_3 [Fe (CN)_6]$  + 0.1 M KCl solution; the insert is a zoom-in of the blue curve [228], [229].

Specific conditions are usually created in electrochemical cells so that the observed response is due to processes occurring at the surface of the electrode or the interface between the electrode and solution. This is the case for most voltammetric and impedance experiments. Electrical equivalent circuits are used to model the working electrode interfacial region and processes. The rest of the cell can then be represented by cell

resistance, which is often referred to as the serial resistance or the ohmic resistance,  $R_{\Omega}$  [201].

The solution resistance between the reference electrode and the working electrode also referred to as the resistance of the ionic solution depends on the ionic concentration, type of ions, temperature, and the geometry of the area in which the current is carried. In a bounded area with area,  $A$ , and length,  $l$ , carrying a uniform current, the resistance is defined as,

$$R = \rho \frac{l}{A} \dots \dots \dots \text{Eq 3- 11}$$

Where  $\rho$  is the resistivity of the solution. The reciprocal of  $\rho$  ( $\kappa$ ) is more commonly used in literature.  $\kappa$  denotes the conductivity of the solution and its relationship with solution resistance is:

$$R = \frac{l}{\kappa A} \Rightarrow \kappa = \frac{l}{RA} \dots \dots \dots \text{Eq 3- 12}$$

The unit of  $\kappa$  is Siemens per meter (S/m). The Siemen is the reciprocal of the ohm, so  $1 \text{ S} = 1/\Omega$ .

Most electrochemical cells do not have uniform current distribution throughout a definite electrolyte area. The major problem in the theoretical calculation of solution resistance concerns the determination of the path through which the current flows and the geometry of the electrolyte that carries the current. That is why the solution resistance is not calculated from ionic conductance, rather it is calculated when experimental EIS data is fit to an electrical model [230].

In this section, Nyquist plots are explained (*see Figure 3-4, 3-5*) side by side as electric circuit representation, which would make the equivalent circuit segment of this dissertation more comprehensible and understandable.

The impedance plot is a vertical straight line, as shown in *Figure 3-5 (a)*, with the impedance components being given by:

$$Z' = R_{\Omega} \dots \dots \dots \text{Eq 3- 13}$$

$$Z'' = -\frac{1}{\omega C_{dl}} \dots \dots \dots \text{Eq 3- 14}$$

Where  $Z'$  is the real and  $Z''$  is the imaginary part of the complex impedance. The simple explanation of this is, that there is a certain amount of ohmic resistance which dictates the deviation from the cartesian (0,0) points. In the case of only the presence of an R, there would be only a dot point on the x-axis. However, the presence of a pure capacitance in series with the resistor yields a straight line at a point further away from the cartesian center. The value of the capacitance in this case also depends on the surface area of the electrode. The greater the area, the larger will be the value of this capacitance. This value is referred to as non-faradaic capacitance and the relevant impedance (the other part of the impedance that comes from other components that are not capacitive) as non-faradic impedance in literature [212].

*Figure 3-5 (b)* shows the electrode process that occurs at a particular applied potential, which is controlled by the rate of charge transfer across the interface between electrode and solution over a set range of frequencies. The charge transfer is represented by a charge transfer resistance, often referred to in literature and this thesis as  $R_{ct}$ .  $R_{ct}$  is placed in parallel with the double-layer capacitance,  $C_{dl}$ . The charge transfer and charge separation happen at different sites of the electrode surface. A complex plane plot of the impedance affords a spectrum with a semicircle of diameter  $R_{ct}$ , (*see Figure 3-5(b)*). The impedance of a CPE can be calculated by the following equation:

$$Z = \frac{1}{Q(j\omega)^\alpha} \dots \dots \dots \text{Eq 3-15}$$

Where the value of  $\alpha$  can range from 0 to 1 and it is 1 in pure capacitors. Generally, a CPE occurs when the material under test (e.g. the surface of a bare solid metal [231], metal with an oxide layer [232], coated metals ([233], [234]), solid electrolytes [235], dielectrics [233], semiconductors [236]) cannot be regarded as homogeneous. Ideally speaking the homogenous, solid, metallic electrodes should not show any shift, However, in real cases, a constant phase shift ( $1^\circ$  to  $2^\circ$ ) is a generally observed phenomenon for solid metals because of their respective crystal structure.

When analyzing the EIS data, CPE is one of the most complicated components to measure and predict accurately. Studies have been carried out for a very long time to understand this parameter. CPE is caused only by surface inhomogeneity at rough electrodes, the angle of depression,  $\theta$  must be independent of the kind of material. This hypothesis was backed up by measurements at electrodes of different materials but with the same roughness [237].

In this thesis, while presenting the result of EIS for the samples, 3 iterations of every specific sample were done. Only 5-10% of the **Relative Standard Deviation (RSD)** was accepted. The RSD was calculated with the formula:

$$\text{Relative Standard Deviation (RSD)} = \left( \frac{\text{Standard Deviation}}{\text{Mean}} \right) \times 100 \dots \dots \dots \text{Eq 3-16}$$

Whereas the Standard Deviation was calculated with the function STDEVPA in Microsoft Excel. While presenting the EIS curves 6 sample data were taken and a maximum of 30% RSD was accepted for the samples' performances (Up to 25% for the samples >100  $\mu\text{m}$  in diameter, and up to 30% for samples  $\leq$  100  $\mu\text{m}$  in diameter).

### 3.1.2 Cyclic Voltammetry (CV)

**Cyclic voltammetry (CV)** studies the redox reactions (Faradaic charge transfer) happening on the surface of the electrode. A controlled amount of ramping voltage is swept between the **Working Electrode (WE)** and the **Reference Electrode (RE)**, while the amount of charge transfer is measured between the WE and the **Counter Electrode (CE)**. The applied voltage of the WE is varied while keeping the potential of the RE constant.

The sweeping of the voltage passes between the forward and reverse paths between two vertices. The converting potential conducted changes the electric field at the WE, causing electrolyte ions to migrate to and from the surface of the electrode to the bulk solution (*see Figure 3-4 (A-G)*) [193]. In this figure, to explain the electrochemical reduction, an example is considered, where the reduction of ferrocenium happening at the electrode,  $[\text{Fe}(\text{Cp})_2]^+$  (Cp = cyclopentadienyl), abbreviated as  $\text{Fc}^+$ , to ferrocene  $[\text{Fe}(\text{Cp})_2]$ , abbreviated as  $\text{Fc}$ , can be presented as  $\text{Fc}^+ + \text{e}^- \rightleftharpoons \text{Fc}$  (and vice versa for oxidation). *Figure 3-8* simply shows the cycle of redox (reduction and oxidation) [193].

As the potential is scanned negatively (cathodically) from point A to point D (*see Figure 3-4*),  $[\text{Fc}^+]$  is steadily depleted near the electrode as it is reduced to  $\text{Fc}$ . At point C, where the peak cathodic current (ip, c) is observed, the current is dictated by the delivery of additional  $\text{Fc}^+$  via diffusion from the bulk solution. The volume of solution at the surface of the electrode containing the reduced  $\text{Fc}$ , called the diffusion layer, continues to grow throughout the scan. This slows down the mass transport of  $\text{Fc}^+$  to the electrode.



Thus, upon scanning to more negative potentials, the rate of diffusion of  $Fc^+$  from the bulk solution to the electrode surface becomes slower, resulting in a decrease in the current as the scan continues (C → D). When the switching potential (D) is reached, the scan direction is reversed, and the potential is scanned in the positive (anodic) direction.

While the concentration of  $Fc^+$  at the electrode surface was depleted, the concentration of  $Fc$  at the electrode surface increased, satisfying the Nernst equation. The  $Fc$  present at the electrode surface is oxidized back to  $Fc^+$  as the applied potential becomes more positive. At points B and E, the concentrations of  $Fc^+$  and  $Fc$  at the electrode surface are equal, following the Nernst equation,  $E = E_{1/2}$ . This corresponds to the halfway potential between the two observed peaks (C and F) and provides a straightforward way to estimate the  $E_0'$  for a reversible electron transfer, as noted above. The two peaks are separated due to the diffusion of the analyte to and from the electrode.

The bulk concentrations of ions are oxidized/reduced regionally inflicting an increase and decrease in the measured current level. The generated current between the Electron transfer from the WE to the electrolyte is carried to the CE. CV measurements Plot voltammograms are often used to analyze numerous factors of the electrochemical environment. For the characterization of an electrode, the electrochemical window of a material can be determined.

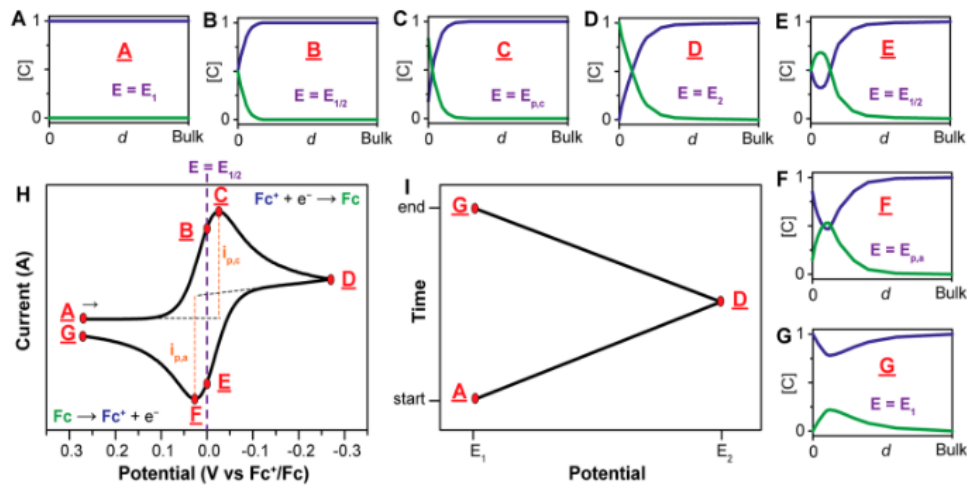


**Figure 3- 4 (A–G):** Concentration profiles (mM) for ferrocenium,  $Fc^+$  (blue) and ferrocene,  $Fc$  (green) as a function of the distance from the electrode ( $d$ , from the electrode surface to the bulk solution, e.g. 0.5 mm) at various points during the voltammogram [76]. (H): Voltammogram of the reversible reduction of a 1 mM  $Fc^+$  solution to  $Fc$ , at a scan rate of 100 mV/s. (I): Applied potential as a function of time for a generic cyclic voltammetry experiment, with the initial, switching, and end potentials represented (A, D, and G, respectively) [181]

The capacitance can be measured while applying different scan rates within a small potential window in which the value of the voltammogram is near to that of a Capacitor [186]. The charge transfer capacitance and specific capacitance can be measured from a CV. The specific charge transfer is measured by:

$$C_s = \frac{\int IdV}{2Vm\Delta V} \equiv \frac{\int IdV}{2VA\Delta V} \dots \dots \dots Eq 3- 17$$

Where  $C_s$  is the specific capacitance (F/g or F/cm<sup>2</sup> in case Area is used), where  $m$  is the mass of the active material (g),  $\int IdV$  is the integrated area under the curve,  $\Delta V$  is the difference in the potential window (V),  $V$  is the potential scan rate (mVs<sup>-1</sup>), and  $A$  is the area (cm<sup>2</sup>).

### 3.1.4 Some Popular Equivalent Circuits

In the case of BIS/EIS, at different frequencies current penetrates the cell differently. All the cells are made with a cell body, cell membrane (intra and extra), and cellular fluids [238]. At low frequencies, the electricity can penetrate the extracellular fluid but not the cell membrane and bends around it: so, it seems like there is an open circuit where there is the cell. In the case of higher frequencies (see **Figure 3-5 (a)**), the current can penetrate the extracellular fluid and the cell membrane, and in very high frequencies, it seems like there is a short circuit where the cell is. Therefore, at mid-frequency, when the electricity penetrates the cell and provides some impedance data, that's when BIS is measured.

In **Figure 3-5 (b)** there is a circuit shown, which is often used in the case of bio-impedance spectroscopy which yields the same/similar result in different frequencies and helps understand the contribution of different parts of the cells throughout the experiment. The one mentioned in **Figure 3-5 (b)** is called the simplified Randle's cell [239].

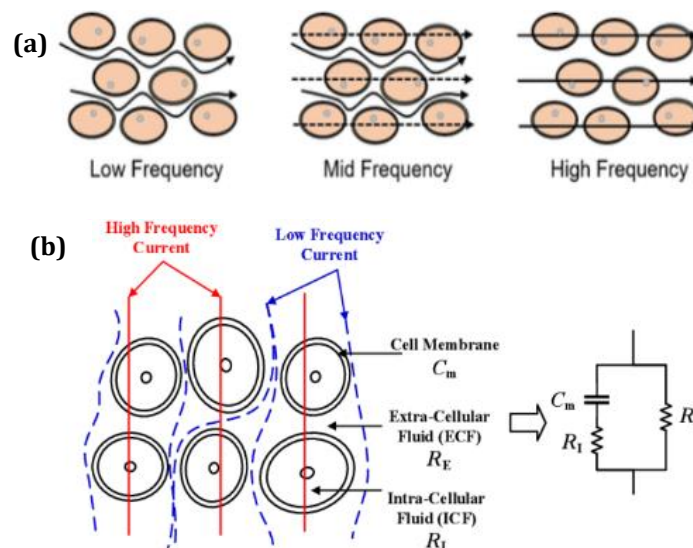


**Figure 3- 5** (a) At different frequencies the electricity behaves around the electricity differently, (b) an equivalent circuit to show the behavior of the current at different frequencies [226]

In **Figure 3-6 (a, b)** two other very popular equivalent circuit models are shown. Here,  $R_{ECF}$  is extra-cellular fluid resistance,  $R_{ICF}$  is intra-cellular fluid resistance,  $C_M$  is the capacitance of the membrane,  $R_{inf}$  is the Cole model is the value of  $R$  that is more prevalent at higher frequency ( $R \rightarrow \infty$ ), and  $R_0$  is the value of  $R$  that is more prevalent at low frequency ( $R \rightarrow 0$ ). In other words, the low-frequency signals tend to traverse in the extracellular fluid and high-frequency signals tend to penetrate the cells themselves, the Cole model utilizes  $R_{inf}$  and  $R_0$  to signify the resistive pathways at the two frequency extremes (infinite frequency and DC). In modern applications, the capacitor is replaced by a **Constant Phase Element (CPE)**, as the cell membrane is never a perfect capacitor given the membrane's polarizability and pore structure that allows ions and polar molecules to flow through the semipermeable lipid bilayer [240]. The Fricke–Morse model has applications in monitoring cell size, ionic conduction, cell polarization effects, etc. Whereas, the Cole model, published slightly after the inception of the Fricke–Morse model (1928) offers a more generalized biological model, where individual cellular components are not represented by passive circuit elements [240], [241].

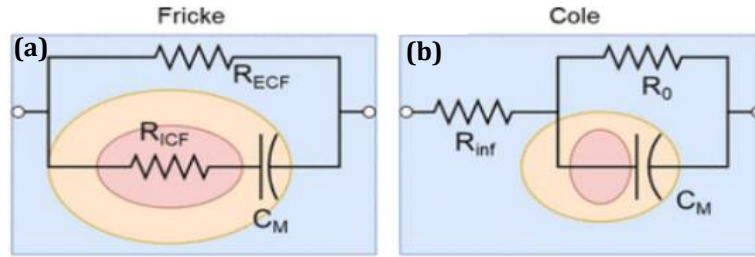


**Figure 3- 6** (a) Fricke model (b) Cole equivalent circuit models used for biological tissue [227]

At the end of the chapter, the equivalent circuits of the samples in specific environments were represented. The combination of the electrical components helps with understanding the performance at different frequencies and the values help understand the change in performance with changes in morphology, size, shape, material, etc.

### 3.2 Different Equipment Used for Characterization

The electrodes are the primary steps in understanding and analyzing the performance of flexible micro-electrodes. To predict the performance of the electrode EIS is done in a wide range of frequencies. During the thesis, different equipment was used to characterize the samples and analyze the performances of the samples. They are discussed here:

#### 3.2.1 The Arduino UNO with AD5933 Shield

With the goal to achieve a portable impedance analyzer for better facilitating in-vivo tests (small animal or test subjects) impedance spectroscopy was done in electrodes in a pseudo-biological environment, i.e., a solvent that mimics the biological property in a cell. The proposed system was powered by ARDUINO Uno and the system was connected to a homemade shield to maintain the connection with AD5933.

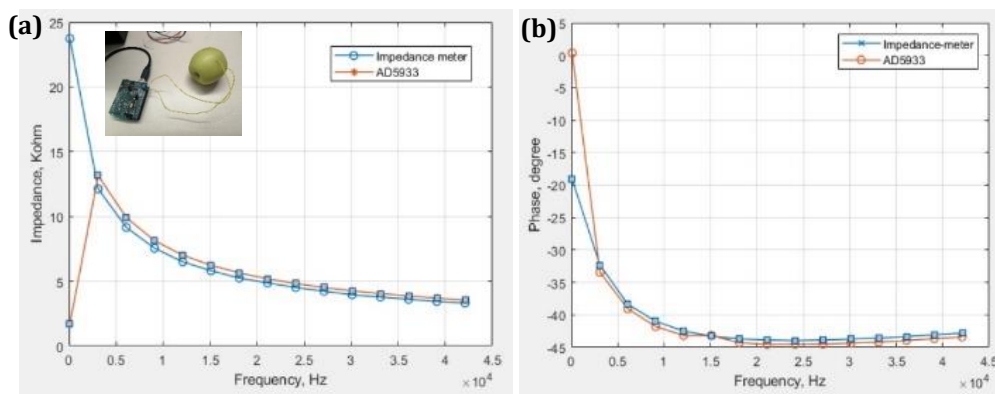


**Figure 3- 7** (a) Comparison of the impedance measured of an apple with both the HP equipment and the AD5933 shield + Arduino, (b) phase measured of an apple with both the HP equipment and the AD5933 shield + Arduino

This design was not explored intensively, because soon it was updated by the team to solve the storage issue that comes with Arduino, the lack of autocalibration in the system, and the presence of spikes present at the beginning of the experiment. In **Figure 3-7 (a), (b)** a comparison between the measurement done with the commercial equipment HP, and the

homemade device is shown. The measurement was done in an apple by inserting two wires into it. The data is represented with a linear scale for all the axes.

### 3.2.2 Analog Discovery 2

Analog Discovery 2, also known as Digilent Analog Discovery 2 (see **Figure 3-8 (a)**) is a USB oscilloscope, logic analyzer, and multi-function instrument that allows users to measure, visualize, generate, record, and control mixed-signal circuits of all kinds. This device can be used as an impedance analyzer by measuring the impedance and phase of a common capacitor over a default frequency range. The equipment can do measurements in the range of 1Hz -10 MHz.

In **Figure 3-8 (b)**, the functional diagram of AD2 is given. Here the principle of the voltage divider rule is applied in between the scope and scope 2. To do the operation, it is required to set a value of  $R_{ref}$  (This is a resistance that contributes to the gain of the current measuring part of the equipment) to do every measurement. If the  $Z_{measured}$  or  $Z_m \ll R_{ref}$ , then the value of Scope1 = Scope2. If  $Z_m \gg R_{ref}$ , then the value of Scope2=0. So, the value of  $R_{ref}$  needs to be set in a way that  $Z_m \approx R_{ref}$ .

The AD2 uses the Waveform Generator and Oscilloscope instruments in addition to an external reference resistor whose value is determined from a fixed value in the booklet mentioned and in accordance with the range of capacitance or inductance of the Device Under Test (DUT). The value for the corresponding capacitor and the inductor for a specific  $R_{ref}$  is provided by Digilent. A calibration bench is provided for compensation (open, close, with load) before running the experiment. This is a 2-port analyzing system [242].

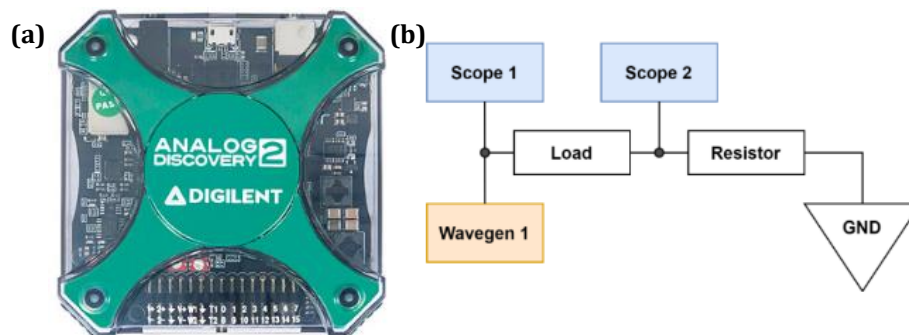


**Figure 3- 8 (a)** Top view of Analog Discovery 2, **(b)** The functional diagram of hardware setup of AD-2 [229]

### 3.2.3 EC Lab

The Bio-Logic's EC-Lab SP-200 (see **Figure 3-9 (a)**) is used to perform impedance spectroscopy, CV, and Nyquist analysis on the electrodes. In order to compare with the already published works, 0.01M of PBS and 0.5 M of  $LiClO_4$  were used as the experimental solution. Ag/AgCl was used as a RE, and a long Platinum wire (considered infinitely larger compared to the microelectrodes) was used as the CE so that all the current could pass through the wire and not through the electrodes. The example of a 3-electrode set-up is given in **Figure 3-9 (b)**.

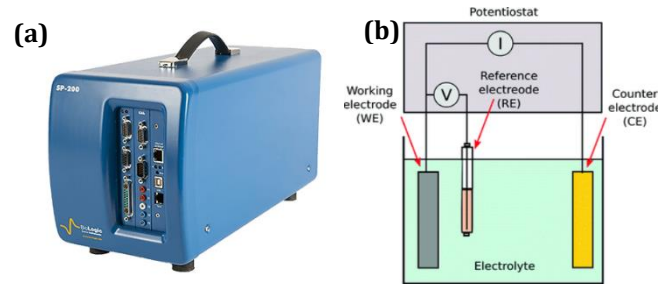


**Figure 3- 9** (a) The Bio-Logic's EC-Lab SP-200, (b) Illustration of an electrochemical cell set used for study electrochemical impedance spectroscopy (EIS) and cyclic voltammetry (CV) [230]

The standard potentiostat board in the SP-200 series provides 12 V compliance,  $\pm 10$  V reference control, and a maximum current of  $\pm 500$  mA, with a frequency range of 10  $\mu$ Hz-7 MHz [243].

### 3.2.4 Hewlett Packard 4194A

The **Hewlett Packard (HP)** 4194A Impedance/Gain-Phase Analyzer is the commercial standard equipment used as a reference to characterize and test the samples against other commercial and homemade systems.

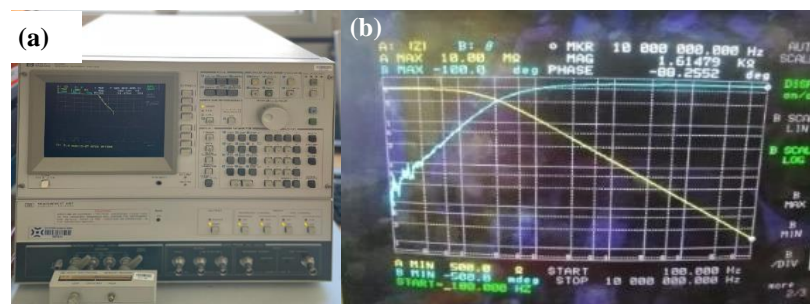


**Figure 3- 10** (a) The HP 4194A, (b) The display of HP4194A with an experimental result

The 4194A impedance/gain-phase analyzer (see **figure 3-10 (a)**) is an integrated solution for efficient measurement and analysis or go/no-go testing of components and circuits with a wide frequency range of 100 Hz to 40 MHz. This equipment features high-accuracy and error-elimination functions to ensure reliable measurements, including graphics analysis and various computations. It can successfully detect and measure resistive values ranging between 10 m $\Omega$  – 100 M $\Omega$  [244]. **Figure 3-10 (b)** shows the display with an experimental result on the screen. There are different connection benches for which there are compensation options available (open, close, with load).

### 3.2.5 Home-made multiplexer

Both the HP and EC Lab are manual experiments and data collection systems and require repetitive data acquisition.

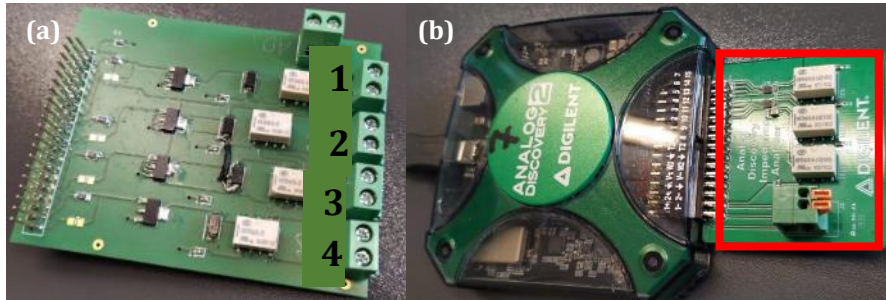


**Figure 3- 11** (a) The homemade multiplexer with 4 output ports, (b) the AD2 device with the calibration bench (red square)

So, to ensure automatic data acquisition with a commercial device at regular intervals, a homemade multiplexer was used. An **Analog Discovery-2** (see **Figure 3-11 (b)**) with a calibration table provided by the **Agilent** was connected to the multiplexer (see **Image 3-11 (a)**). A Python-based program was used for user interface, data acquisition, and storage in the Raspberry Pi.

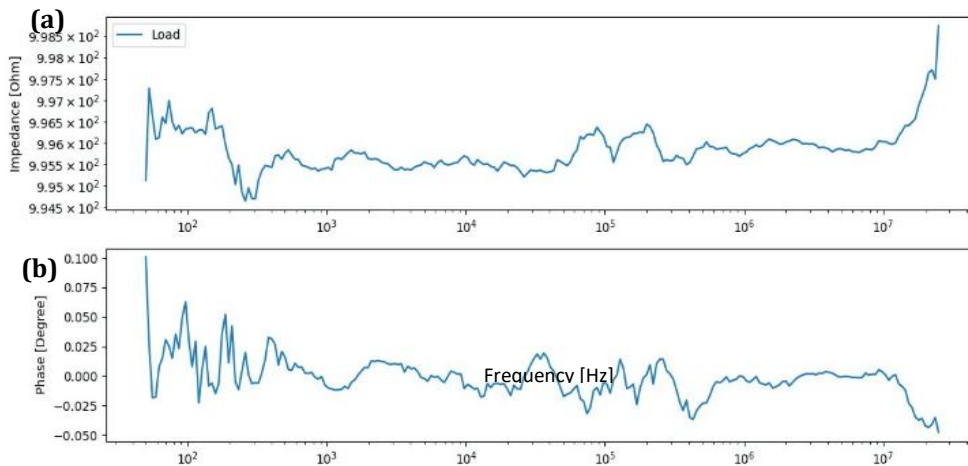


**Figure 3- 12** A 1 K ohm resistor connected to the setup to observe the accuracy of the setup observed in a frequency range of 10-10 MHz (a) absolute impedance, (b) phase

**Figure 3-12** shows the accuracy of the system when 1 kΩ sample was set as a load. The program stores data at a set interval regularly, in between a manually set period and there is a compensation method in place before starting each operation to minimize the percentage of error.

This system takes advantage of the Analog Discovery 2 technology by employing the option of 4 simultaneous outputs by adding a multiplexer. There is a local and remote **Human Machine Interface (HMI)** connected to a Raspberry Pi. There are 4 output ports (see **Image 3-11 (a)**) connected to the Raspberry Pi with a switchboard, which simultaneously measures and stores the collected data over a set period. This technology was employed by our colleagues at ESIEE Paris. The interface works using a command written in Python.

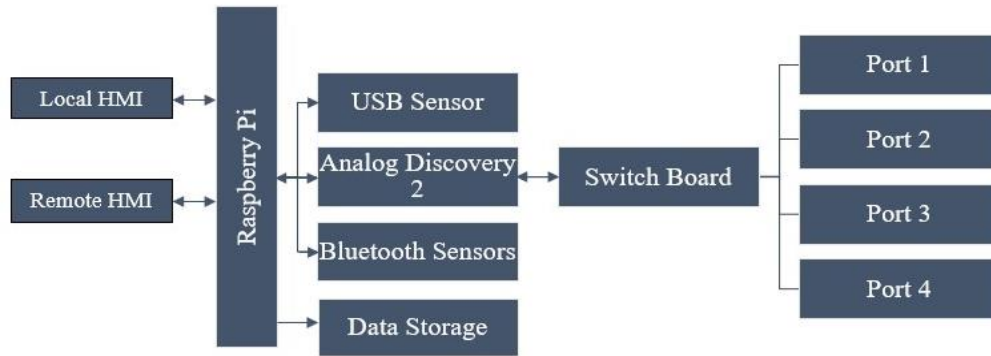


Figure 3- 13 Functional diagram of the Multiplexer

This system takes advantage of the same principle as AD2. However, it improves on the part of choosing a  $R_{ref}$ , by employing a method where the  $R_{ref}$  is set by the program after the first experiment is done, and the  $R_{ref}$  is set at a value close to the measured value (see Figure 3-12). The purpose of the Bluetooth sensor is to collect data via Bluetooth in the storage device. For our operation, we did not require this feature. Figure 3-13 shows the functional diagram of the system that was set with AD2 and the multiplexer for data acquisition.

### 3.3 Equivalent/Fit Circuit

In the case of electrochemical characterization of electrodes to be used in a biological environment, it is very common to use the Randles circuit model (see Figure 3-14 (a)) [245].

Therefore, to make an equivalent circuit in order to understand the value of specific components of the circuit, in EC lab biologic a similar circuit is used (see Figure 3-14 (b)). In the circuit, an inductive component was added to compensate for the effect of added wire in the experimental setup.  $R_s$  in Figure 3-14 (a) and  $R_1$  in Figure 3-14 (b) are indicative of ohmic resistance (see Section 3.1.2).

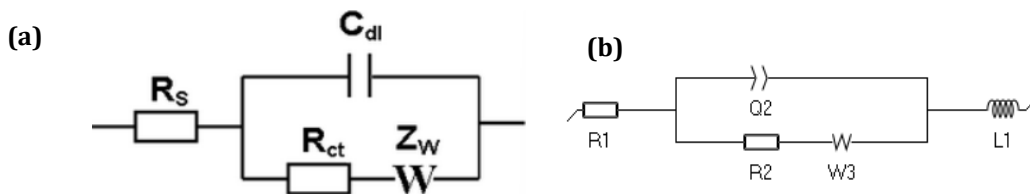


Figure 3- 14 (a) Randles circuit model [54], (b) Equivalent circuit of the model drawn in EC lab

$Q_2$  is CPE which is used to replace  $C_{dl}$ . The  $Z_w$  (see Figure 3-14 (a)) and  $W_3$  (see Figure 3-14 (b)) indicate the presence of the Warburg component and represent the value of the impedance of the component. The Warburg component is the most commonly used circuit element for modeling diffusion behavior. This component models semi-infinite linear diffusion, which is diffusion in one dimension that is only bound by a large planar electrode on one side (which is the case in the setup used in this thesis) [218]. The impedance of the Warburg component can be expressed by:

$$Z_w = \frac{2\sigma}{\sqrt{j\omega}} \dots \dots \dots Eq 3-18$$

And  $\sigma$  can be expressed by:

$$\sigma = \frac{\sqrt{F}}{2\sqrt{c}} \dots \dots \dots Eq 3-19$$

Where  $r$  and  $c$  are respectively the resistance and capacitance of the short-circuit transmission of the total model.

### **3.4 Experimental Comparison of Different Materials in IDE**

Impedance spectroscopy can be an important technique in the study of interdigitated electrodes (IDEs) in the air. Impedance spectroscopy provides information about the electrical properties of a system by measuring the complex impedance as a function of frequency. In the case of IDEs in air, impedance spectroscopy can be used to study the electrical properties of the electrodes and their interface with the air, which can provide insights into various processes such as corrosion, oxidation, and gas sensing. By measuring the impedance of the IDEs, it is possible to determine the resistance, capacitance, and inductance of the electrodes and their interface, which can be useful for a range of applications, such as the development of sensors and energy storage devices. Impedance spectroscopy can also reveal the presence of defects in a passivated layer by showing changes in the impedance magnitude and phase as a function of frequency. The specific changes in impedance depend on the type and size of the IDE, as well as the properties of the passivation material.

In this thesis, the impedance spectroscopy was done in the air, and subsequently in 0.01M of PBS. As shown in Chapter 2, the two backbones of the IDE are used as 2 different terminals. The excitation voltage is passed through the samples and the test is done in HP1494A to use as a reference. When impedance spectroscopy is performed on an IDE covered in intrinsic Diamond, such as a gold IDE or a TiN-Pt-TiN stack IDE, the impedance data provides information about the electrical properties of the IDE and the surrounding material (*see Section 2.2.4*).

When impedance spectroscopy is performed in PBS, the impedance data will show the complex impedance (resistance and reactance) of the IDE as a function of frequency. The impedance magnitude (magnitude of the complex impedance) will provide information about the resistance of the IDE, and the impedance phase angle will provide information about the capacitance of the IDE.

In the case of a gold IDE covered in intrinsic Diamond, the impedance spectroscopy data may show changes in the impedance magnitude and phase angle that are indicative of the presence of the IDE.

For example, a gold IDE covered in the intrinsic Diamond may exhibit an increase in impedance magnitude and a shift in impedance phase angle compared to the reference impedance spectra of the intrinsic Diamond alone. The specific changes in impedance depend on the size, shape, and location of the IDE, as well as the electrical properties of the Diamond and gold materials.

Analyzing the impedance spectra provides insights into the electrical properties of the IDE and the surrounding material: This information can be used to study the properties of the material, the presence of defects, and their effect on the material properties. It can also be used to optimize the materials and improve their performance for various applications.

#### **3.4.1 Primary Design of the Mask**

To begin with, analyzing the structures, the experiments were done step-by-step in terms of moving from the most conventional material to the unique ones. This mask was used to fabricate the samples with Gold and TiN-Pt-TiN stack as the conductive layer and SU8 as



the passivation layer to be used as a reference, which was compared with the stack as the conductive layer and intrinsic Diamond as the passivation layer.

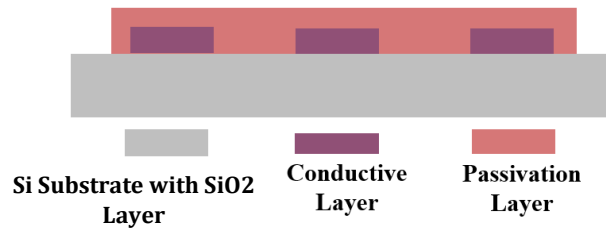


**Figure 3- 15** 2-D cross sectional view of the IDE

In this specific design shown in **Figure 3-15**, there were 66 and 100 pairs of fingers that constructed the IDE electrodes. The IDEs of this batch had interdigitated electrodes with two separate backbones and the whole capacitive area was covered with the passivation layer, as can be seen in **Figure 3-15**.

### 3.4.1 Gold IDE Covered in SU8

The first samples that were analyzed were fabricated with Gold as a conductive part and with SU8 as a classical material used for passivation (*see Figure 3-16*). The measurement of the impedance was done with HP4194A and in a different environment.

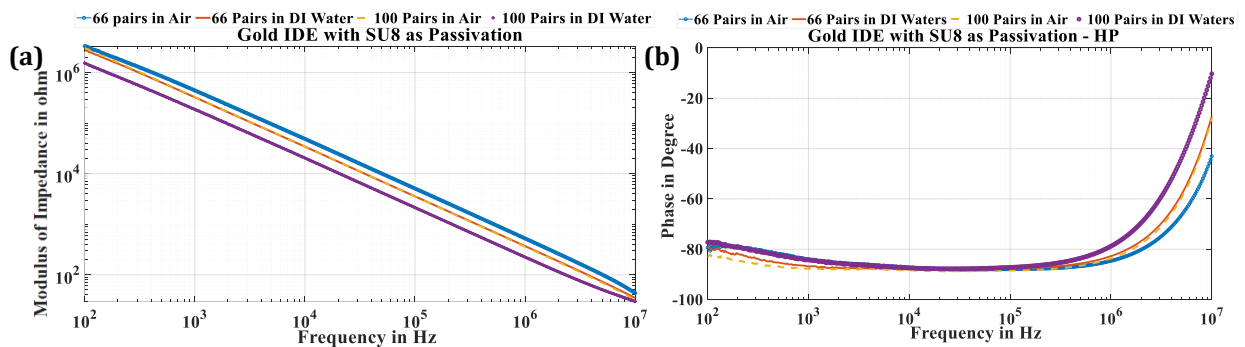


**Figure 3- 16** (a) Absolute value of impedance of IDE in different environment, (b) phase of IDE in different environment

The structure was fabricated with the mask mentioned in **Section 2.2.3**. As this structure is supposed to be purely capacitive, and the capacitive part of them is covered in passivation, it is very logical for them to show the classic capacitive behavior in terms of impedance value from 100 Hz to 10 MHz (*see Figure 3-16 (a)*). In the case of the phase, the phase is really close to -90° (*see Figure 3-16 (b)*), as it should be. It is obvious, that the impedance is due to the surface area of the metallic structure underneath and to verify it, the capacitance of the structure was measured theoretically with the simplified formula of parallel plate capacitance:

$$C = \epsilon_0 \epsilon_r \frac{A}{r} \dots \dots \dots \text{Eq 3- 20}$$

Where,  $\epsilon_0$  is the dielectric constant of free space,  $\epsilon_r$  is the dielectric constant of the material, which in this case is air, hence the value is 1. A is the area of the plates and d is the distance between the two plates. Then the value was put in **Equation 3-13**.

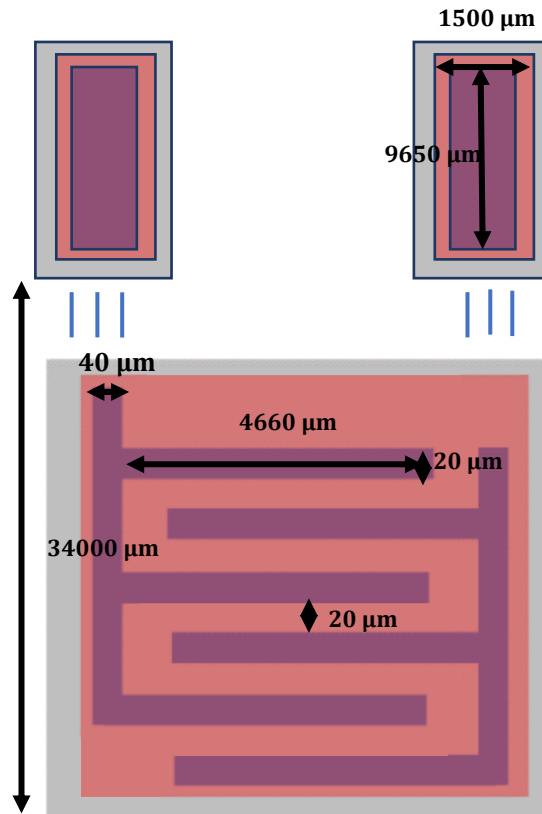


**Figure 3- 17** Dimension of IDE (primary mask)

For a 500-nanometer thick sheet of gold with a cross-sectional area of  $15 \times 10^{-6}$  square meters:  $L = 500 \times 10^{-9}$  meters,  $\rho = 2.44 \times 10^{-8} \Omega.m$  (The resistivity of gold at room temperature, a constant). The area of the IDEs can be calculated to be:  $(20 \mu m \times 4660 \mu m)$  for the individual fingers, and the area of the backbones is  $(40 \mu m \times 34000 \mu m)$ . And each contact pad is  $(9560 \mu m \times 1500 \mu m)$ . The dimensions of such a sample are shown in **Figure 3-17**.

$$\text{Area} = (20e-6 \times 4660e-6) \times \text{Numbers of finger} \times 2 + (40e-6 \times 34000e-6) \times 2 + (9560e-6 \times 1500e-6) \times 2 \approx 43.70 \times 10^{-6} \text{ m}^2 \text{ (for 66 pairs of fingers) and}$$

$$\text{Area} = (20e-6 \times 4660e-6) \times \text{Number of fingers} \times 2 + (40e-6 \times 34000e-6) \times 2 + (9560e-6 \times 1500e-6) \times 2 \approx 50.04 \times 10^{-6} \text{ m}^2 \text{ (for 100 pairs of fingers).}$$

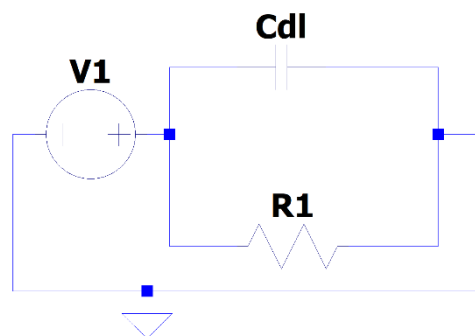


**Figure 3- 18** Equivalent circuit used to calculate the values theoretically

So, to verify the samples with further investigation, the value of the capacitance was calculated with the simplified **Equation of 3-23**, and the measured value for IDE with 100 pairs of fingers (upon calculation of the area of the IDE), considering the air as medium and plotted along with the value obtained in the experiment.

The equivalent circuit mentioned in **Figure 3-18** is the one that was used to do the theoretical calculation and it is one of the most common circuits that is used to explain, mimic, and extrapolate data in the case of BIS and a lot of other electrochemical operations in the biological environment. The value of  $R_{\Omega}$  was calculated for the Au IDEs and the value of  $C_1$  was calculated from the simplified formula of capacitance calculation mentioned in **Equation 3-21**. The value of  $R_{ct}$  is the charge transfer resistance that happens when the sample is submerged in a liquid environment. However, since the calculation was done in the air the value of  $R_{ct}$  is infinite.

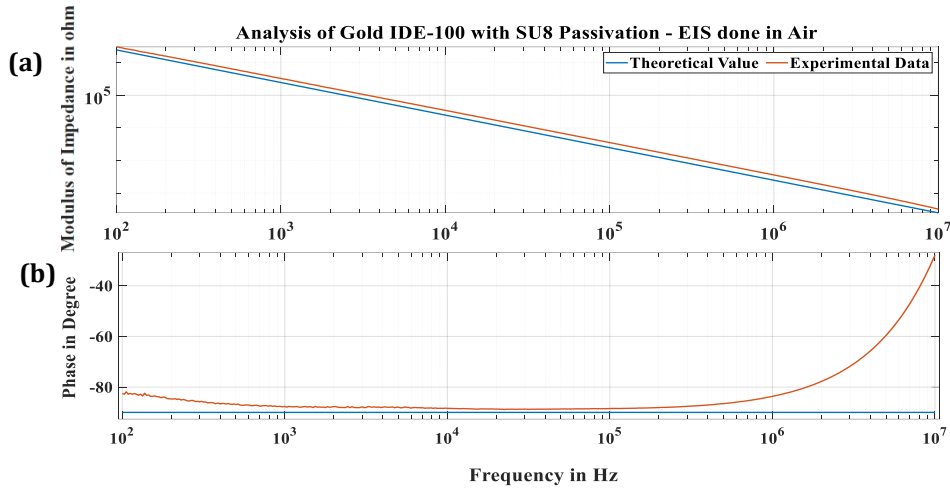


**Figure 3-19** (a) Absolute value of impedance of IDE-100 in theoretical calculation and experimental environment, (b) phase of IDE-100 in theoretical calculation and experimental

As observed from **Figure 3-19 (a)** the impedance is close to the experimental data (overall shift of approximately 2%). When the phase was measured, it was  $-90^\circ$  through the range (see **Figure 3-19 (b)**). Subsequently, electrical simulations were performed by establishing various boundary conditions. The purpose was to see how the change in different parameters would change the result of EIS.

Another way of verifying the result of the sample was by performing a COMSOL simulation. A primary simple structure was drawn (see **Figure 3-20**) with a structure where a substrate was drawn with a thickness of 0.5 mm, the top of which was insulated with a  $\text{SiO}_2$  layer of 10 nm (not visible in the image, due to scale discrepancy), a conductive layer of 1.5  $\mu\text{m}$  in height, along with a passivation layer of 1.7  $\mu\text{m}$ .

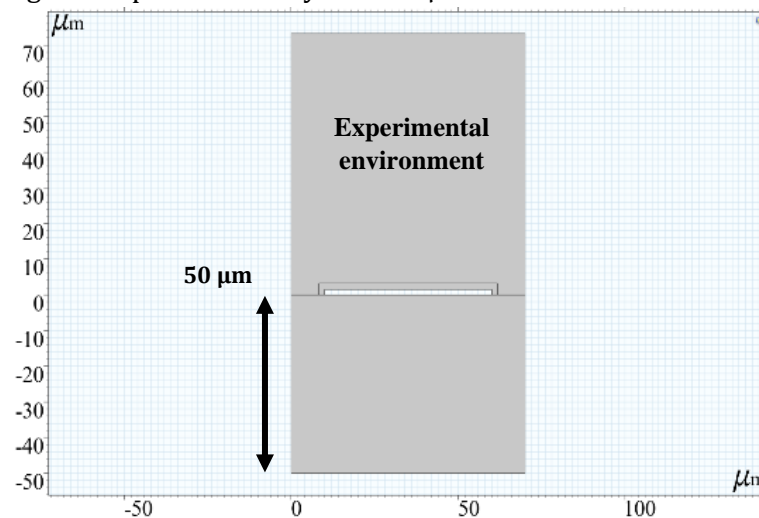


**Figure 3-20** 2-D samples drawn in COMSOL Multiphysics 6

The first simulation was done by setting the parameters for the substrate as Si (electric conductivity 16 mS/m, permittivity 11.68), and a 10 nm high insulating layer between the samples and the substrate, the terminal was set at the conductive layer and the passivation layer was set to have electric conductivity of 0 S/m and relative permittivity of 1. The result in air (see **Figure 3-21 (a), (b)**) was the same as the result yield from the equivalent circuit.

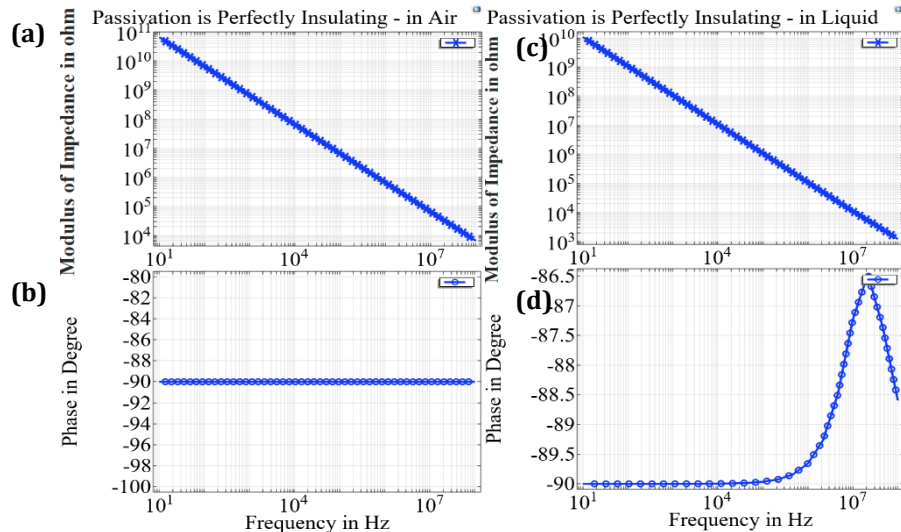


**Figure 3- 21** EIS for simulation performed in Figure 3-21 considering perfect passivation layer, (a) Impedance, (b) phase in air, (c) impedance, (b) phase in liquid

When the simulations were done in liquid it was evident that at higher frequency there was a shift in the phase which is also observed in all the experiments done with the samples going further. The substrate was changed to a perfect insulator to see if there was any visible change in the result. However, the only noticeable change was in higher frequency when the phase reached a slightly higher value (-84°). It is also noticeable that in liquid the overall impedance is decreased by a factor of 10, and the curve follows the same capacitive trend in both. In both cases, the thin layer between the substrate and IDE is considered purely insulating (electrical conductivity 0, relative permittivity 1). Further simulations were done to see the change in result by changing the thickness of the passivation, However, the result was not significantly different. However, when the simulation was performed by changing the electrical property of the passivation (i.e.: changing the value of electrical conductivity and permittivity), significant changes were noticed. The value of the conductivity of the passivation was set at 1  $\mu$ S/m and relative permittivity at 0.5.

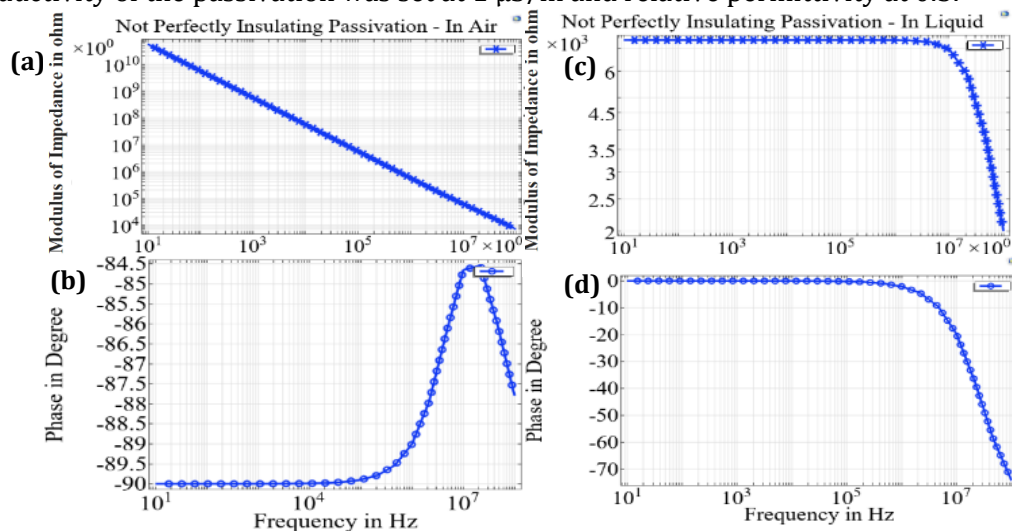


**Figure 3- 22** EIS for simulation performed in Figure 3-21 considering imperfect passivation layer, (a) Impedance, (b) phase in air, (c) impedance, (b) phase in liquid with conductivity of 0.01 S/m and relative permittivity of 80

In **Figure 3-22**, the impedance in air follows the same trend as before, though the phrase is not as before. The value of impedance in liquid (*see Figure 3-22 (c, d)*) demonstrates the characteristics of an R-C circuit and the same is true for the phase in the lower frequency the value is closer to 0° and later in higher frequency it shifts towards -90°. Because, in the simulation, the inducting effect generated from the overall equipment was not taken into account. After that, the parameter was changed a bit, instead of a perfect insulator in between the substrate and the IDE, a 10 nm high oxide layer was placed (which is similar to the experimental condition).

Here, in **Figure 3-23** it is noticeable that, as soon as there is a presence of an oxide layer in between the IDE and the substrate, the phase starts changing due to the introduction of parasitic capacitance in between fingers over the structure in liquid and under the structure through the Si substrate. It can be concluded that imperfect passivation and the presence of an oxide layer add to deviation from perfectly capacitive behavior by adding parasitic capacitance into the result [140].

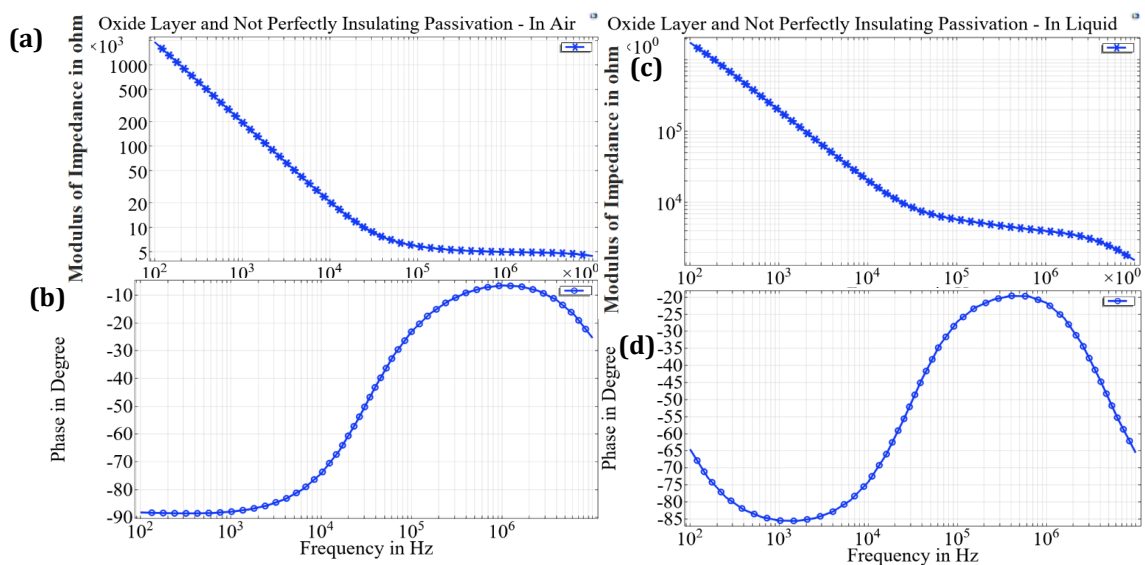


**Figure 3-23** EIS for simulation performed in Figure 3-21 considering imperfect passivation layer, (a) Impedance, (b) phase in air, (c) impedance, (d) phase in liquid

### 3.4.2 TiN-Pt-TiN IDEs

At the beginning of this segment, the IDEs were fabricated where the stack model was used as the conductive part and SU8 as passivation. While the results were supposed to be uniform and yield reasonable results similar to that of the Au IDE, it was noticed pretty quickly that it was not the case.

Upon some primary fabrication, it was apparent that only a small tear in the passivation layer was enough to compromise the integrity of the whole structure. The main target of the IDE structure was to put the durability of the passivation layer to the test and the SU8 passivation layer after a couple of characterizations did not yield uniform results anymore (*see Figure 3-24*). The result is similar to the simulation done in COMSOL Multiphysics (*see Figure 3-23 (a), (b)*), meaning there is no perfectly capacitive behavior, which can be a result of the physical damage of the passivation layer or a presence of an oxide layer.

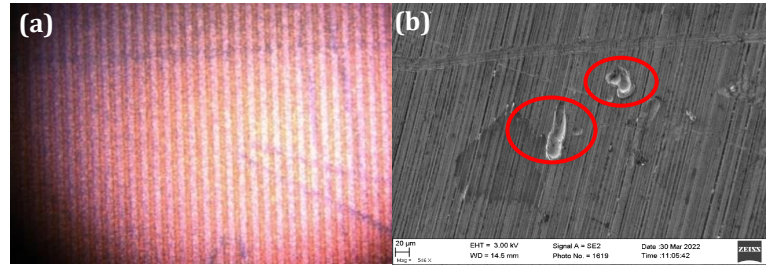


**Figure 3- 24** IDE samples with SU8 passivation seen under (a) simple microscope (b) SEM microscope (red marks show imperfection in the structure)

In **Figure 3-24** the samples with the SU8 passivation are shown under the microscope and SEM where there are visible tears/imperfections in the passivation layer. **Figure 3-25** shows an example of IDE with Diamond Passivation in air showing capacitive behavior whereas IDE with SU8 passivation did not show perfectly capacitive behavior as expected (see **Figure 3-26**).

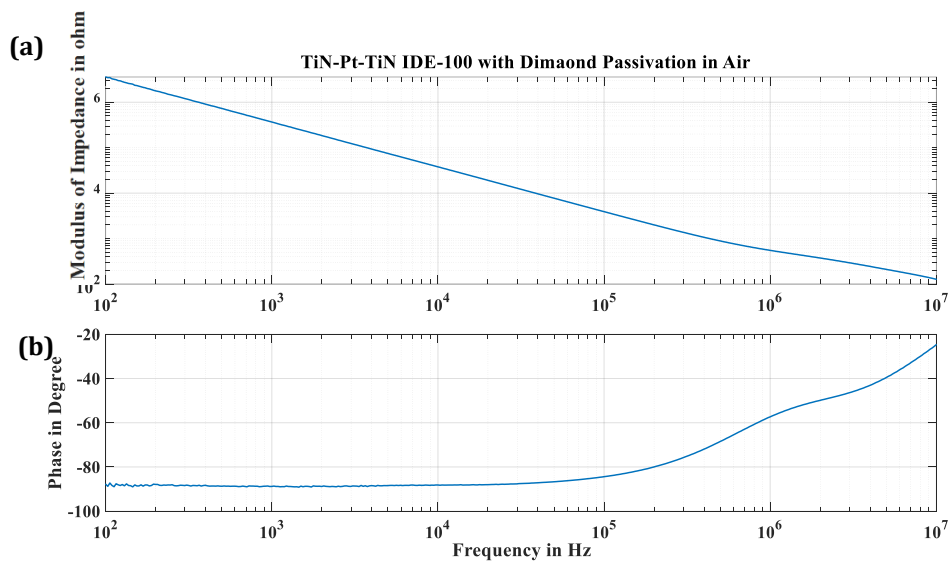


**Figure 3- 25** (a) Absolute value of impedance, (b) phase

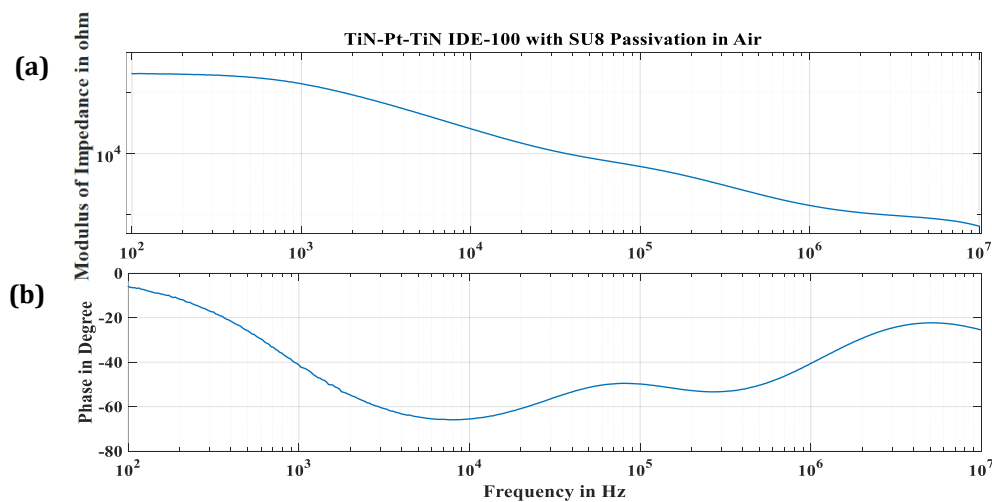


**Figure 3- 26** (a) Absolute value of impedance, (b) phase

In the impedance spectroscopy in air (see **Figure 3-25**), the samples show the result as expected and similar to that observed in the Au samples (see **Figure 3-16**). Upon further investigation, it was observed that (see **Figure 2-24(b)**), on the AlN mask part there were some small tears which led to the possibility of the AlN mask not being complete and the same problem of water retention issues appearing in several places (shown in red circles).

**Figure 3-27** shows that the IDE with Diamond passivation shows R-C-like characteristics when put in a liquid medium similar to the simulation result in **Figure 3-22 (c, d)**. This proves that the passivation layer was causing water retention in a way. So, a second version of the mask was proposed.

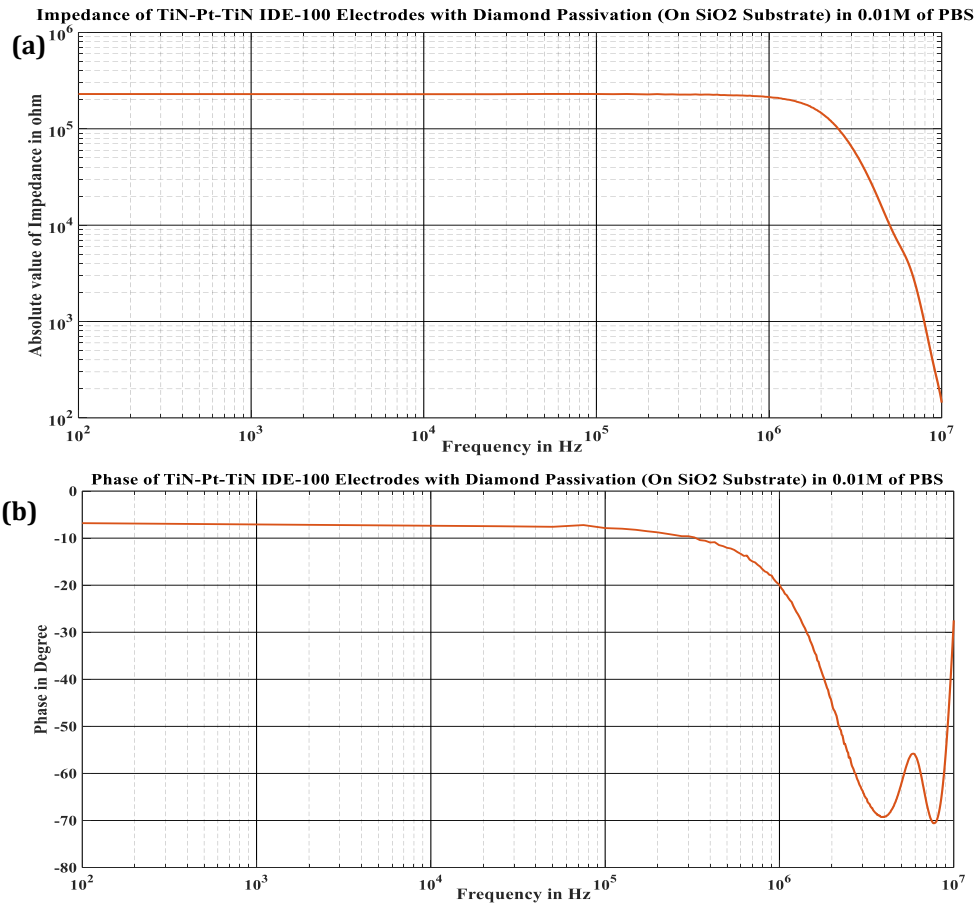


**Figure 3-27** R-C like characteristics of Diamond passivation due to water retention (a) absolute value of impedance, (b) phase

### 3.5 Second Version of the Mask

As a part of the improvement of the structure, there was Diamond growth on top of the regular height of the samples to verify if the passivation layer was simply too thin to provide good passivation. However, the results seem to be not satisfactory enough in terms of the impedance spectroscopy done in liquid. Therefore, a new mask was designed to realize another vision for the samples with the same materials. In this new mask, there were gaps in between fingers in the passivation layer (see **Figure 3-28, 3-30**) and the rest of the configuration was kept the same. This mask was used to fabricate the samples with TiN-Pt-TiN stack as the conductive layer and SU8 as the passivation layer to be used as a reference, which was compared with the stack as the conductive layer and intrinsic Diamond as the passivation layer.

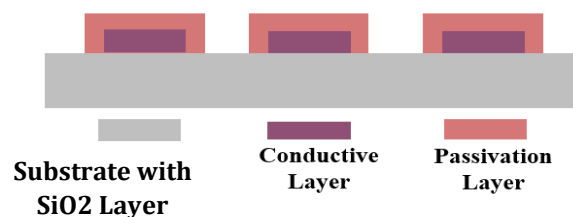


**Figure 3-28** 2-D cross sectional view of the second version of IDE

### 3.5.1 TiN-Pt-TiN IDEs

The primary step of the new mask was to fabricate the conducting part with TiN-Pt-TiN and the passivation part with SU8 to have a reference and to ensure the performance of the capacitive structure. To that end, it was observed, that the samples show purely capacitive results in the air as they should, and the phase is around 90° until 100 kHz (see **Figure 3-34 (a, b)**). From **Figure 3-34** it is apparent that the samples show classic capacitive behavior in air, as the impedance shows pure capacitive behavior, and the phase is close to -90° until 100 kHz. The area of the IDEs can be calculated to be: (30μ x 4660) for the individual fingers, and the area of the backbones is (40μ x 34000μ). And each contact pad is (9560μ x 1500μ). **Figure 3-22** was used to calculate the theoretical result here as well.

Area = (30e-6 x 4660e-6) x Numbers of finger x 2 + (40e-6 x 34000e-6) x 2 + (9560e-6 x 1500e-6) x 2 ≈ 38.50 x 10<sup>-6</sup> m<sup>2</sup> (for 25 pairs of fingers), and

Area = 45.50 x 10<sup>-6</sup> m<sup>2</sup> (for 50 pairs of fingers), and

Area = 58.5 x 10<sup>-6</sup> m<sup>2</sup> (for 100 pairs of fingers). **Figure 3-30** shows the dimensions more clearly.

The dimensions to support this calculation are presented in **Figure 3-30**. As seen in **Figure 3-31 (a, b)** both the experimental and theoretical values are capacitive in nature. The reason behind the discrepancy between the experimental and theoretical value (overall 2.3% approximate increase in the overall resistance), is possibly the result of the resistance due to the whole experimental setup (equipment and samples). The theoretical calculation does not take into consideration this value. Also, at low frequencies (100-1000 Hz), the phase shows a bit of a sign of perturbation, which might be a result of leakage of current.

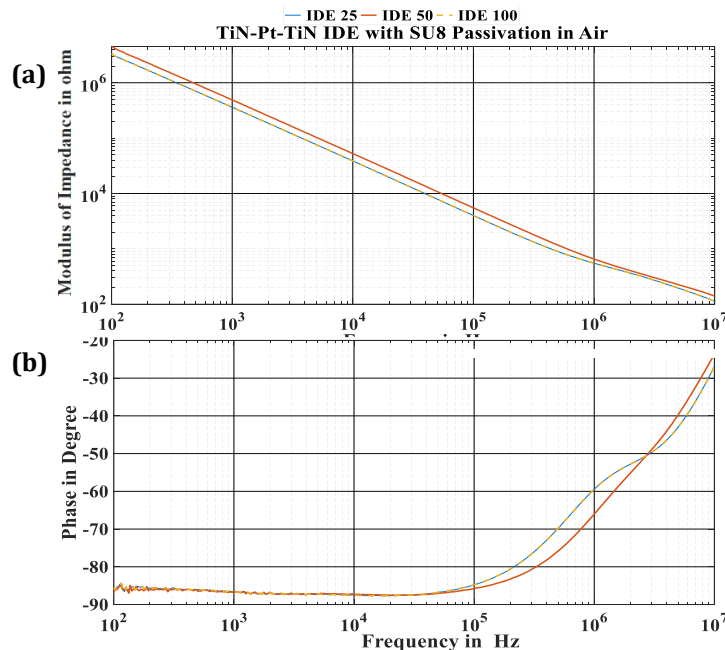


**Figure 3- 29 (a) Absolute value of impedance, (b) phase**



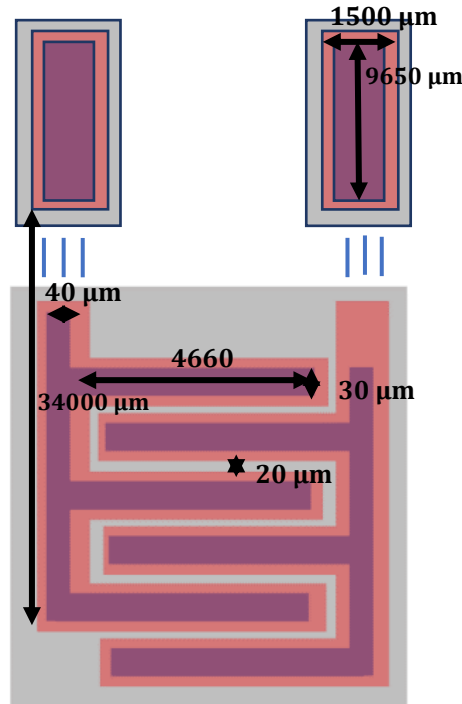


Figure 3- 30 Dimensions of the second version of IDEs (second version of mask)

As already explained, there is an increased resistance which shifts the phase value toward resistive spectra ( $-0^\circ$ ). And in higher frequencies ( $10^6$ - $10^7$  Hz) the experimental result shows a shift, which is a result of inductive elements present in the result.

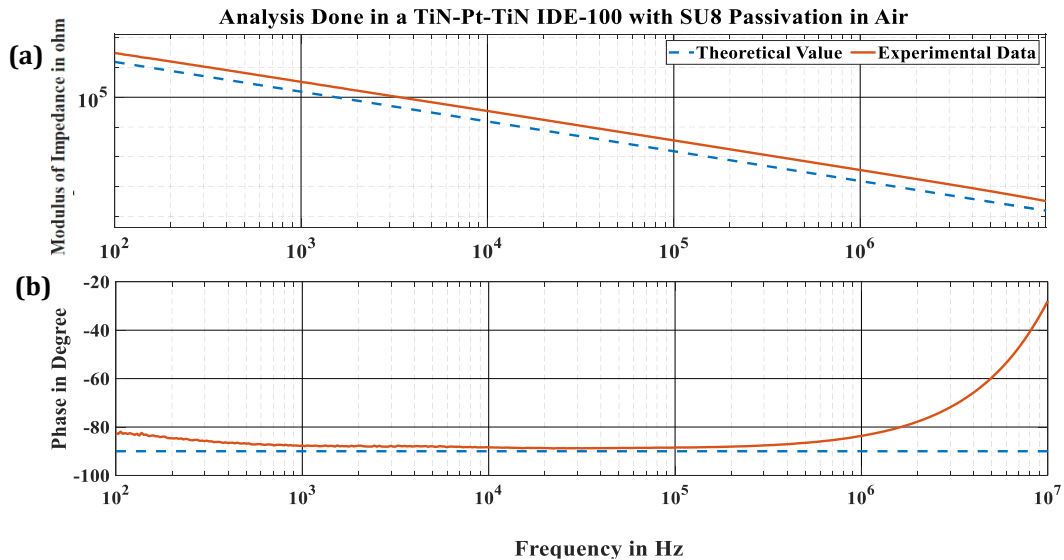
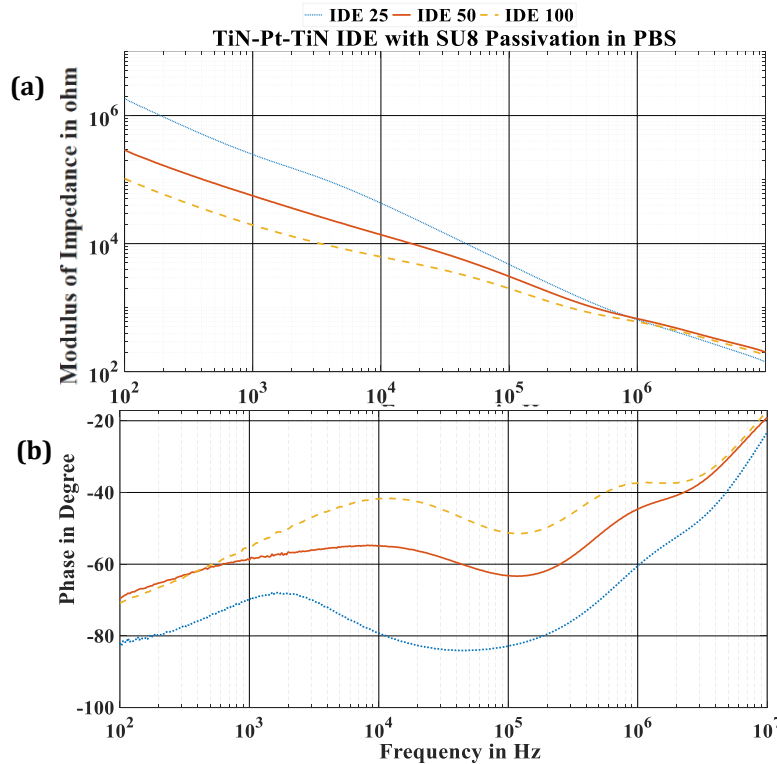


Figure 3- 31 (a) Absolute value of Impedance, (b) phase

The observations from the graphs in the new model were very apparent that, once they were put in liquid, they did not demonstrate the purely capacitive behavior as observed in the samples with Glass substrate, TiN-Pt-TiN electrodes with SU8 passivation (see Figure 3-29). The primary hypotheses were water retention, parasitic capacitance, possible tears in the passivation layer, and the Diamond layer not being completely non-conductive due to the samples being Hydrogen-terminated. Necessary steps were taken to annul those possibilities one by one by making necessary modifications. However, even after making improvements, the results were not completely capacitive in liquid (see Figure 3-32 (a),

(b)). It was observed that in air, the response was as expected in terms of both impedance and phase (see **Figure 3-24 (a), (b)**). One of the possibilities that were hypothesized was the substrate Si being semiconductive in nature, and the presence of a thin oxide layer, once in liquid, there was some resistive and capacitive component derived from the substrate part of the structure. And the COMSOL simulation mentioned in **Figure 3-23, and Figure 3-33** proved it to be right. When water is retained in polycrystalline intrinsic Diamonds, it can create free charge carriers by dissociating into hydrogen and hydroxide ions. These ions can act as charge carriers and increase the electrical conductivity of Diamonds [246].



**Figure 3-32** (a) Absolute value of impedance, (b) phase in 0.01M of PBS

The exact conductivity will depend on the amount of water retained, the size and distribution of the polycrystalline Diamond grains, and other factors such as temperature and pressure. However, in general, the electrical conductivity of polycrystalline Diamond with water retention can range from a few S/cm to hundreds of S/cm, depending on the conditions [246], [247].

In the structure (see **Figure 3-34**) for Si substrate and imperfect insulator, the value of the relative permittivity was considered to be 5.7 (the value of relative permittivity of the intrinsic Diamond) and the electric conductivity to be  $1.6 \times 10^{-7}$  S/m, which is higher than the dielectric constant of the intrinsic Diamond at room temperature ( $1 \times 10^{-14}$  S/m to  $1 \times 10^{-15}$  S/m), due to the possible water retention. Here for the simulation, the layer dividing the substrate and IDE was considered to be the perfect insulator. Even then the result was close to that of **Figure 3-33** proving that the imperfection in the passivation layer would ultimately lead to imperfect capacitance.

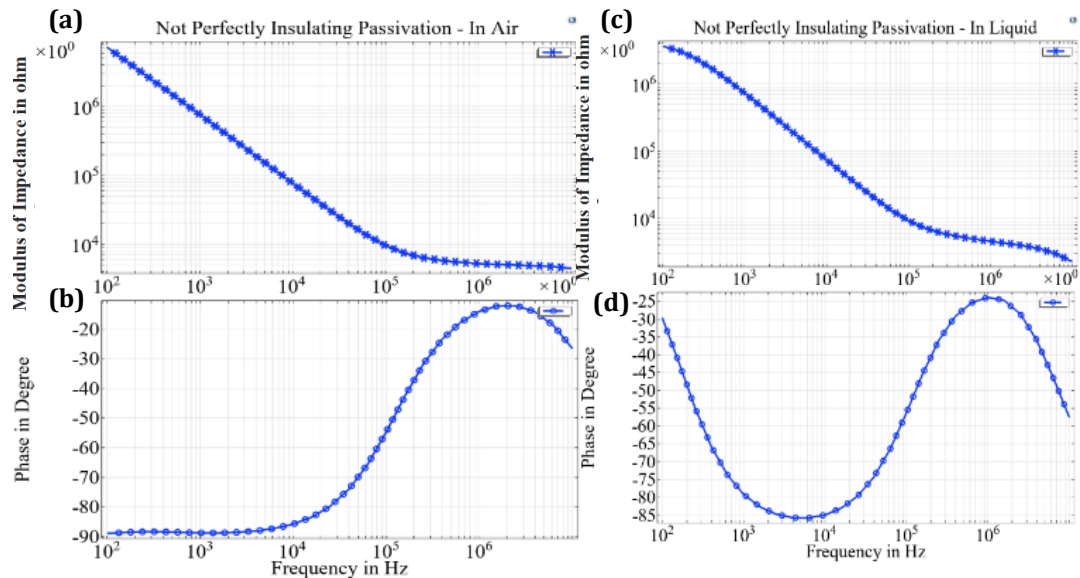


**Figure 3- 33** (a) Impedance, (b) phase in air; (c) impedance, (d) phase in liquid for structures on Si wafer with Imperfect Insulator as Passivation performed in Figure 3-21

**Figure 3-33** does not show the exact result of the experimental one. However, in both air (a, b) and liquid (c, d), the simulation and the experimental result follow the same trend. It would be impossible to predict the value of the new relative permittivity and the conductivity introduced due to the water retention without knowing the size, shape, distribution of the crystals, and doping concentration.

Similar results were obtained from the samples with Diamond passivation (see **Figure 3-26**). The samples demonstrate results close to the theoretical calculation. At lower frequencies and higher frequencies, there are inductive effects observed from the equipment. For both IDE-50 and IDE-100 the samples in the air (see **Figure 3-34**) show capacitive behavior at lower frequencies and higher frequencies, the samples show a gradual increase in phase. Whereas in liquid (see **Figure 3-36**), the appearance of the phase shift happens earlier than it does in the case of impedance, both in simulation and experimental results.

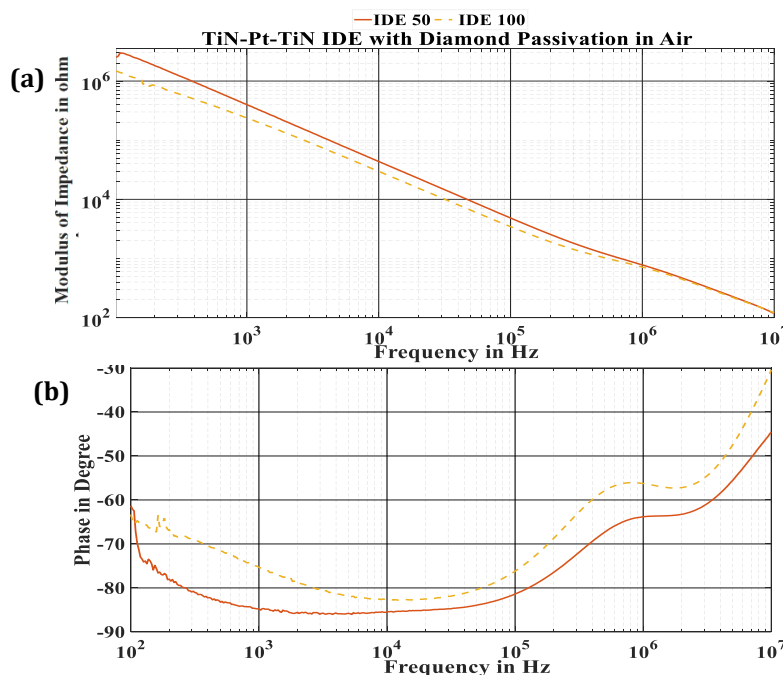


**Figure 3- 34** (a) Absolute value of impedance, (b) phase

In the second model, there were gaps in between the fingers of IDE, to design that there were AlN layers as a masking layer to stop the Diamond growth. In **Figure 3-35 (a, b)** the tears in the AlN layer during the fabrication process are shown. This issue during fabrication was further optimized by changing the height of the AlN layer.

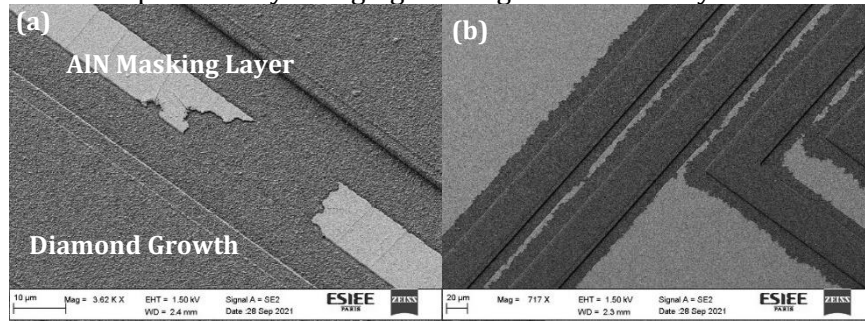


**Figure 3- 35** Tear in the AlN layer during fabrication at different magnification (a) 10  $\mu\text{m}$  scale, (b) 20 $\mu\text{m}$  scale

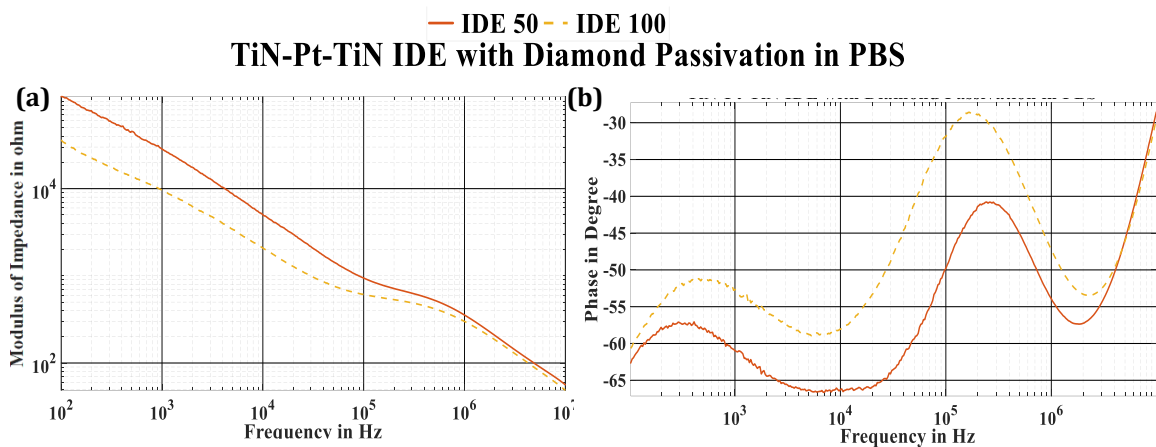


**Figure 3- 36** (a) Impedance, (b) phase

In **Figure 3-36 (a, b)** the samples in PBS show a similar result as the one shown in the simulation (see **Figure 3-33**) and how the value of impedance and phase change in case of the substrate being not completely insulating and water retention that can result in the passivation layer having imperfection, which was later treated in the cleanroom by making the samples hydrogen terminated (see **Section 2.4.6**).

### 3.6 Microelectrodes with Different Materials

Upon moving toward the microelectrodes, the BIS was more about understanding the properties of electrode materials like Au, TiN, Pt, etc. Different methods were employed to analyze the different properties of the materials. The results were compared and verified with different means.

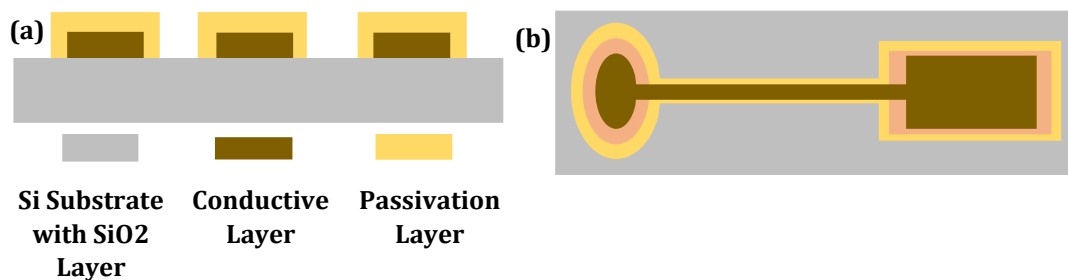


**Figure 3- 37** (a) 2-D cross section of the electrodes, (b) top view of a single electrode

A simple COMSOL simulation was done to verify the primary idea that the impedance should go down with the overall increase of the surface area of the electrodes. COMSOL Multiphysics 6 was used to do the electric simulations; the conductivity of .01M of PBS was considered 2 S/m, and relative permittivity was set at 80 [248].

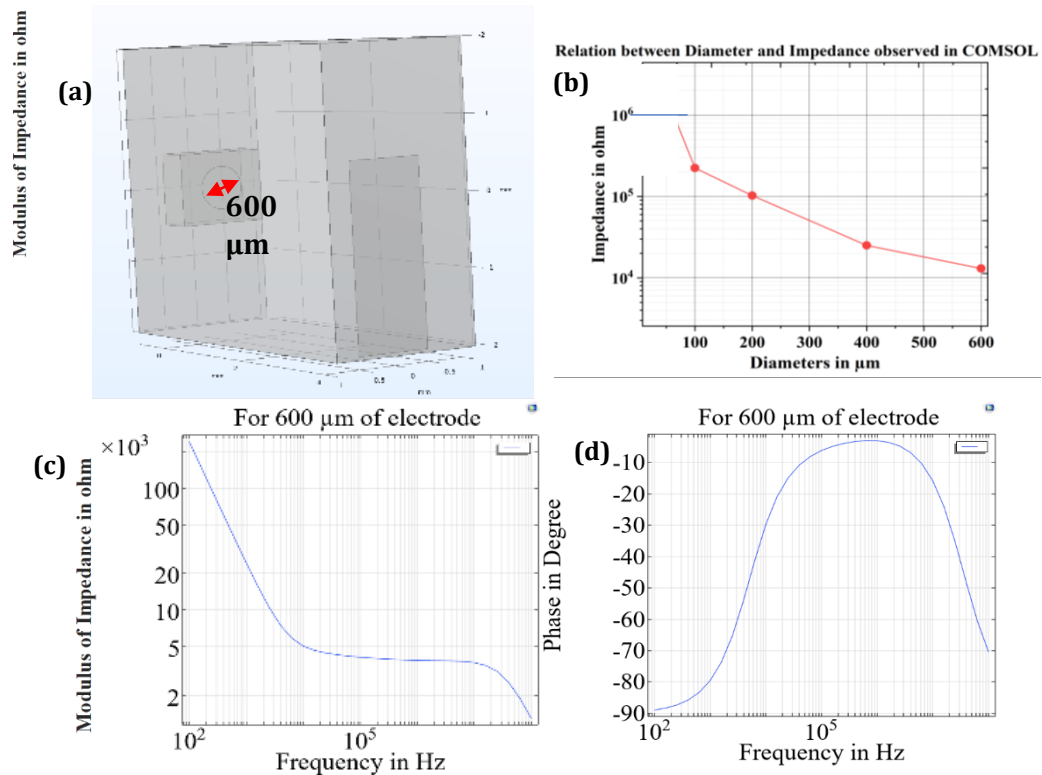


**Figure 3-38** (a) COMSOL simulation done in 600 μm of metallic gold conductive part against a reference electrode, (b) evolution of the impedance with the change in size observed at 1000 Hz, (c) the result from a sample in simulation environment

**Figure 3-38 (a)** shows a sample of 600 μm in diameter drawn in COMSOL. The simulation was carried out only with circular electrodes (without passivation, metal tracks, or contact pads). The purpose was to observe the behavior of the electrodes in a liquid environment and how they behave with the change in size. If the change of impedance follows the change of the value of the capacitor, there should be a decrease with a ratio of 4 and the result is close to that in the larger electrodes. In smaller electrodes, the effect of the double layer is more than that in the big electrodes. It will be more explained in **Section 3.6.1.2**. For simplicity purposes, only the circular part of the electrode was simulated, (see **Table 3-1**) and followed the same trend as all the experimental data in terms of impedance and size (see **Figure 3-43 (b)**), which verifies the correlation between the size and the impedance of the samples going forward. **Figure 3-43 (c, d)** shows the simulation result of the 600 μm electrode in the simulation environment.

Diameters of the Circular Electrode (μm)	Impedance at 1000 Hz in COMSOL (k ohm)
600	60
400	110
200	500
100	1900

**Table 3-1** COMSOL simulation result done with gold electrodes of different sizes

From **Table 3-1**, it is also noticeable that in the case of the larger electrodes, the impedance changes almost exponentially. However, as it moves towards a smaller size and the ratio between the overall area of the experimental environment/substrate and the size of the electrode increases, the result becomes less predictable, which is also observed in the case of all experimental values as well. After the diameter reached 100 μm, the mesh settings

needed to be changed to finer, and for 60  $\mu\text{m}$  and 30  $\mu\text{m}$  it was set as extremely fine, for the software to be able to simulate the result for a constant experimental environment.

### 3.6.1 Gold (Au) Electrodes with SU8 as Passivation

The Au electrodes were fabricated using the mask (see **Figure 3-39**) on top of an oxidized Si wafer by the sputtering method. Different diameters were fabricated and characterized for better understanding and to ensure comparative data collection.

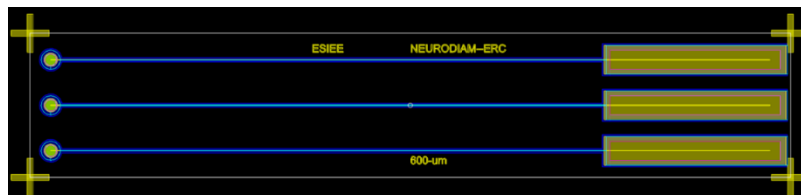


**Figure 3-39** Top view of the structure of a single electrode of the mask

#### 3.6.1.1 Electrical Impedance Spectroscopy (EIS)

As the first part of the characterization method, EIS was performed with a Potentiostat using a 3-electrodes set-up (see **section 3.2.3**). The primary observation is that the impedance of Au electrodes is inversely proportional to the size of the surface area of the structure (see **Equation 3-13**). Going forward this will be the first thing to notice to understand the basic functionality of the change in the size of microelectrodes while interpreting the bode plot.

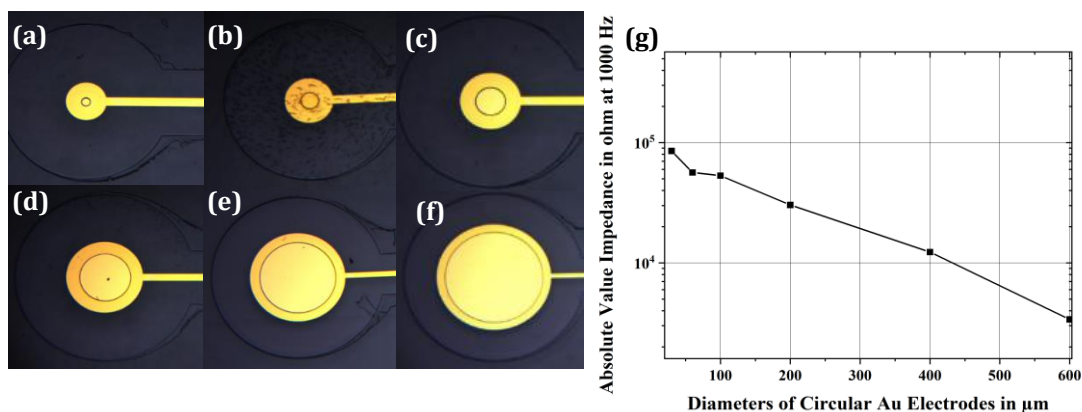


**Figure 3-40** The samples before used in characterization (a) 30  $\mu\text{m}$ , (b) 60  $\mu\text{m}$ , (c) 100  $\mu\text{m}$  (d) 200  $\mu\text{m}$  (e) 100  $\mu\text{m}$ , (f) 600  $\mu\text{m}$ , (g) relation between the size and impedances at a single frequency

To begin with, the electrodes were made with Gold, and the impedance and phase were analyzed to understand the electrochemical properties of the samples. From this point onwards, all the EIS done in the EC lab was done using a 3-electrode method with WE, RE, and CE (see **Section 3.2.3**) and when doing the EIS in AD-2 was done using WE and RE only.

The primary analysis presented about the gold electrodes was impedance spectroscopy showing the impedance (see **Figure 3-41 (a)**) and phase analysis (see **Figure 3-41 (b)**). The primary observation is the relation between size and the inverse relation with impedance. After that, from the phase analysis, it is apparent that the phase increases and reaches the ohmic resistance after 100 kHz. The relation among sizes follows the same trend observed in the COMSOL simulation (see **Figure 3-38 (b)**).

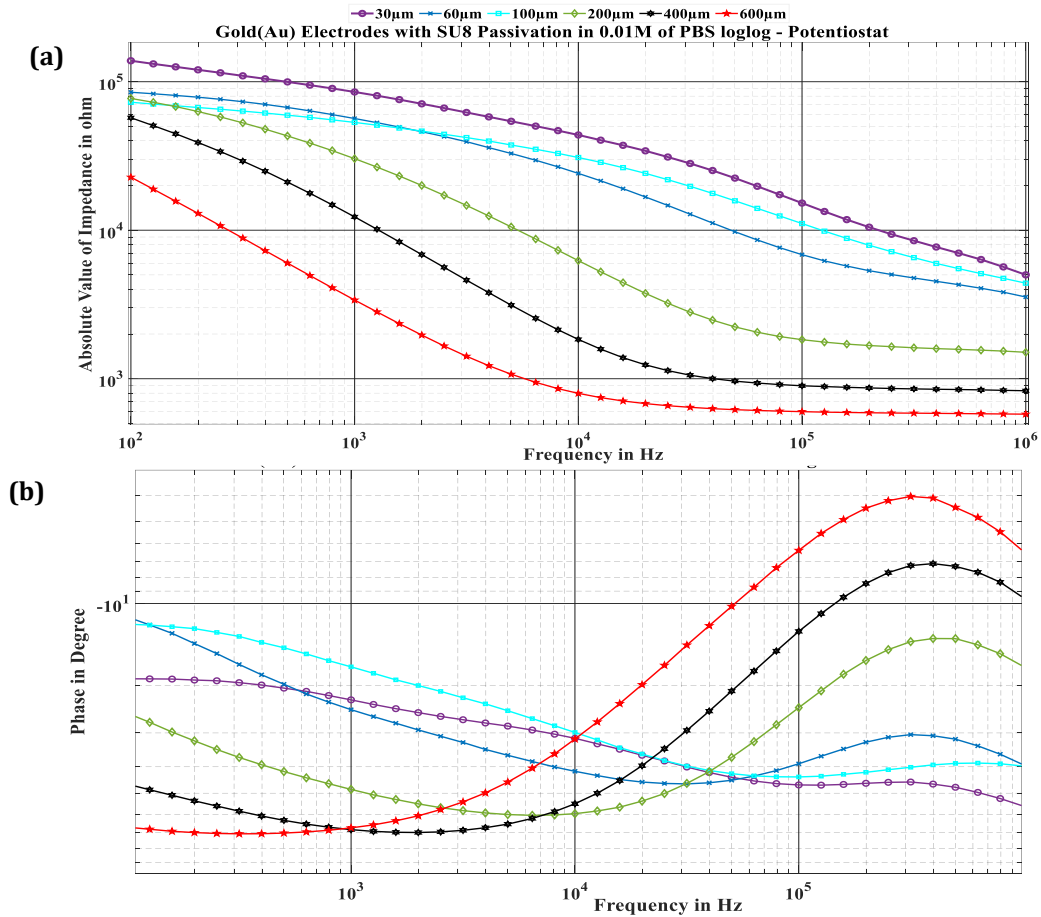


**Figure 3- 41 (a) Absolute value of Impedance, (b) phase of gold electrodes of different diameters**

As seen in **Figure 3-42** when calculating the ohmic resistance part of the EIS, not only the inherent resistance from the material is considered. However, in the case of the experimental environment, a cylinder-like shape is envisioned from the **Working Electrode (WE)** to the **Reference Electrode (RE)**. Considering the distance between the WE and RE is 2 cm, the conductivity of PBS is 1.4 S/m, and the ohmic resistance of an electrode of the diameter of 600  $\mu\text{m}$  is approximately  $1\text{k}\Omega$  (**Equation 3-1 used**). This value can justify the value of impedance at 1 kHz. Throughout the experiments, the same value was observed for all the samples of the same size and when the diameter decreases, the impedance of the electrodes increases [249].

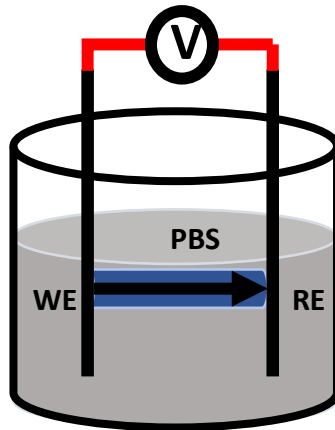


**Figure 3- 42** Schematic of an EIS in appropriate electrolyte

To understand the properties better, the fit operation in the EC lab was used to find different fit parameters in a common equivalent circuit that is used to explain the biological model in EIS (see **Section 3.3**).

### 3.6.1.2 Fit Parameters

A simplified equivalent circuit (see **Figure 3-43 (a)**) was designed with LTSpice to extrapolate and observe the different parameters of the EIS data.

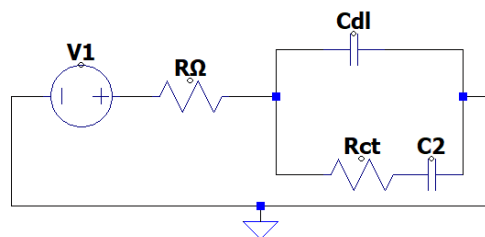


**Figure 3- 43 (a)** Proposed equivalent circuit for

Where there is an ohmic resistance that stems from the resistance of the conductive part of the sample and the experimental setup itself.  $C_{dl}$  is the double-layer capacitance that comes from the interface of the liquid and the metal.  $R_{ct}$  is charge transfer resistance, this part is derived from the negative ions of the liquids encountering the positive surface of the metal samples. There is an added capacitance to represent the added capacitive effect that stems from the liquid itself. The equivalent model used for the fit was  $R_{\Omega} + C_{dl} / (R_{ct} + C_2)$ , and the circuit is a derivative of the Rendles circuit model (see **Figure 3.14 (a)**). The extrapolated fit circuit data is mentioned in **Table 3-2**.



Diameters of the electrodes in $\mu\text{m}$	$R_{\Omega}$ in $\Omega$	$C_{dl}$ in F	$R_{ct}$ in $\Omega$	$C_2$ in F
600	1107	22.5e-12	578.27	37.87e-9
400	1358	10.01e-12	813.21	12.97e-9
200	2764	2.50e-12	1575.45	3.40e-9
100	3468	6.26e-10	1727.45	1.90e-9
60	4029	5.17e-10	50746	48.79e-9
30	4706	13.8e-10	53790	83.18e-9

**Table 3- 2** Extrapolated fit parameters for gold electrodes of different sizes

**Figure 3-43 (b)** shows that at sizes 600  $\mu\text{m}$ , 400  $\mu\text{m}$ , 200  $\mu\text{m}$ , and 100  $\mu\text{m}$ , the fit curve was close to the experimental value. That way, when the data was extrapolated, the value should have been close to the experimental value. This would also help in understanding individual values of the different components of the impedance analysis.

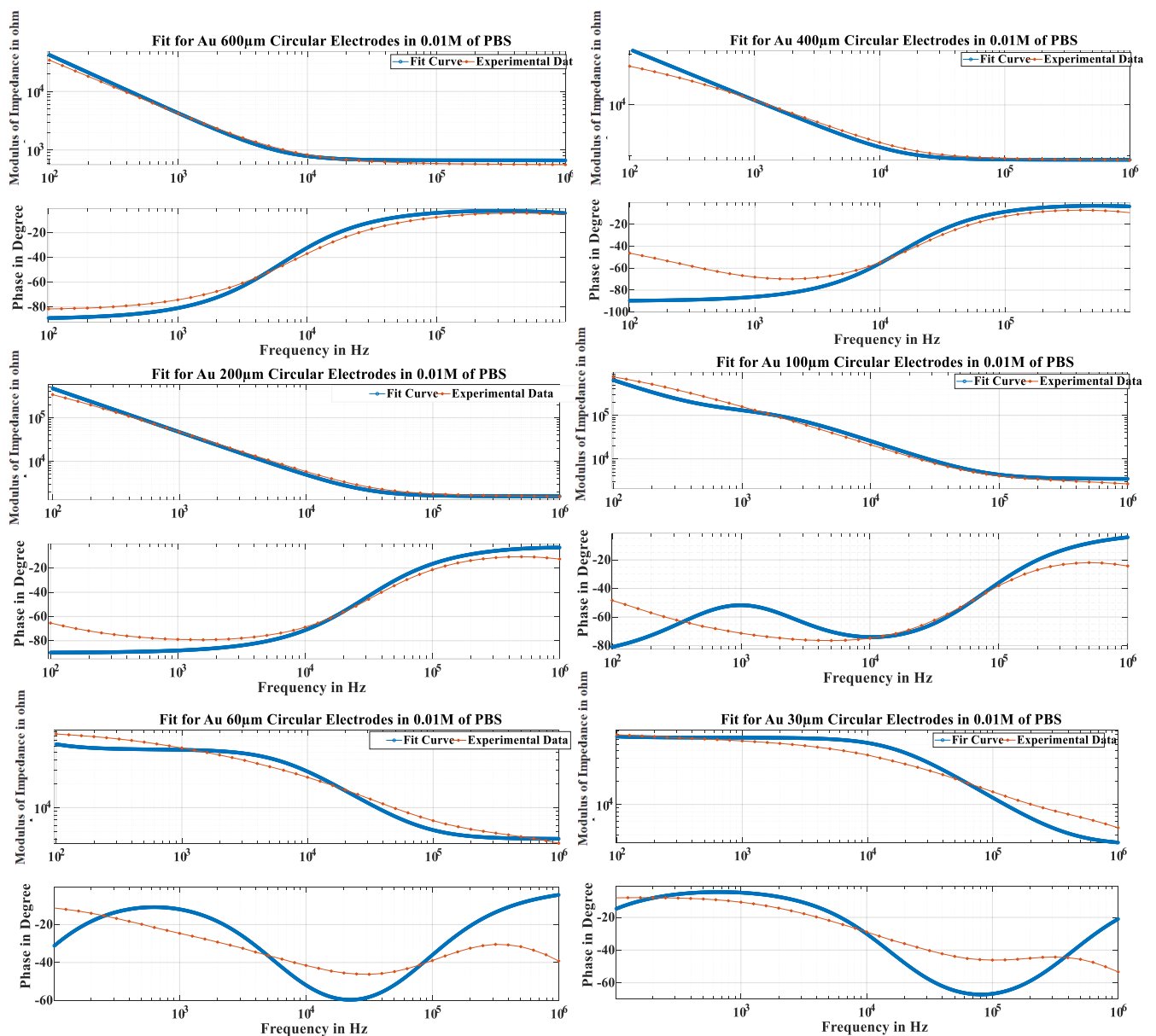


**Figure 3- 43 (b)** Experimental data plotted against fit parameters of different sizes: blue curve – fit data, red curve- experimental data

After that, the data was derived from the fit curve from the EC lab software. It is noticeable that the ohmic resistance is low in samples, which is understandable considering the material used is gold, which is highly conductive. However, as soon as the sample sizes go lower in the macro-scale, i.e., 30  $\mu\text{m}$ , 60  $\mu\text{m}$ , 100  $\mu\text{m}$ ; the sample property changes in a different way (see **Figure 3-43(b)**). This is a common phenomenon in electrochemistry that when the sizes become small, the double layer capacitance changes unpredictably, and then the values become more complex to interpret.

The reason behind this is that when moving from macro electrodes to microelectrodes, the equivalent circuit may need to be adjusted due to changes in the electrochemical behavior of the electrode-electrolyte interface. One potential difference is a shift in the double-layer capacitance due to changes in the surface area to volume ratio. Additionally, it is also possible that the electrode-electrolyte interface may become more complex, with a combination of capacitive, resistive, and inductive components.

To model the equivalent circuit for smaller microelectrodes, it may be necessary to consider additional components such as Warburg impedance, which accounts for slow ion diffusion, or Randles equivalent circuit, which includes both capacitive and resistive components. It may also be necessary to experimentally determine the appropriate equivalent circuit through electrochemical impedance spectroscopy (EIS) [201].

Diameters of the electrodes in $\mu\text{m}$	Calculated $C_1$ in F	Extrapolated $C_{dl}$ in F
600	22.5e-12	22.5e-12
400	10.01e-12	10.01e-12
200	2.50e-12	2.50e-12
100	6.26e-13	6.26e-10
60	2.23e-13	5.17e-10
30	5.63e-14	13.8e-10

**Table 3-3** Calculated capacitance compared with the extrapolated value

It is important to note that the exact equivalent circuit will depend on the specific system being studied, including the electrode material, electrolyte, and experimental conditions. Therefore, it may be necessary to carefully consider these factors and experimentally validate any equivalent circuit models used. For simplification purposes of this thesis analysis, the very apparent parameters were observed and studied.

The surface area to volume ratio (SA : V) is a crucial factor in **Electrochemical Impedance Spectroscopy (EIS)**. A higher SA : V leads to a higher reactivity and accessibility of the electrode surface, which results in larger charge transfer resistance and capacitance. In other words, the SA : V affects the impedance characteristics of the electrode-electrolyte interface, which is the main focus of EIS. Also, the impedance behavior of a microelectrode with a high SA : V will be different from that of a macro electrode with a low SA : V, due to the differing proportions of active surface area and bulk material [250], [251].

**Table 3-3** shows the comparison between the calculated capacitance value and the value the experiment presents. It is apparent that the values of the capacitance,  $C_1$  which is calculated by using a simplified formula of capacitance mentioned in **Equation 3.19** and whereas the double layer capacitance becomes smaller according to the calculation, according to the fit the value of capacitance is bigger in the smaller electrodes. The charge storage in an electrical double-layer capacitor is dependent on the accumulation of ions on the interface between the electrolyte and conducting material and the spatial distribution of ions in the electrolyte. However, it also depends on electrode potential, temperature, ionic concentrations, types of ions, oxide layers, electrode roughness, and impurity adsorption, so it is not easily calculable to this day. However, there is just an approximation [252], [253]. It is a well-known fact that the capacitance that comes from the double layer is

not pure. It is rather a CPE. However, for simplification of the equivalent circuit instead of a CPE, a simple capacitor has been used.

### 3.6.2 Platinum (Pt) Electrodes with SU8 as Passivation

The platinum electrodes were fabricated on top of Si wafers. Here the results of some samples will be discussed. **Figure 3-44** shows the samples of which the results are shown here upon different characterization methods.

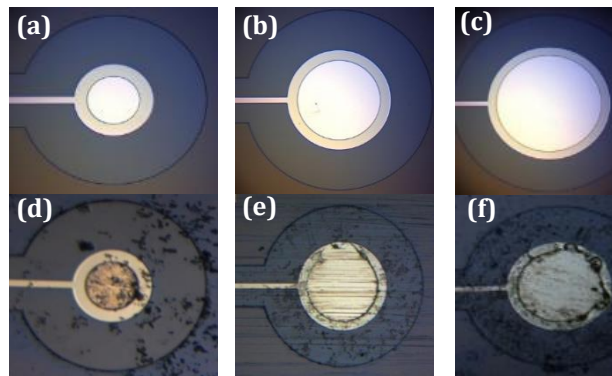


**Figure 3-44** The samples before used in characterization (a) 200 μm (b) 400 μm (c) 600 μm, and after used in characterization (d) 200 μm (e) 400 μm (f) 600 μm

#### 3.6.2.1 Electro-Impedance Spectroscopy (EIS)

Here a graph (see **Figure 3-45**) is drawn to show that the impedance of Platinum electrodes is inversely proportional to the size of the surface of the structure (see **Equation 3-13**). Going forward, this will be the first thing to notice to understand the basic functionality of the change in the sizes of microelectrodes while interpreting the bode plot.

**Platinum(Pt) Electrodes with SU8 Passivation in 0.01M of PBS loglog-Potentiostat**

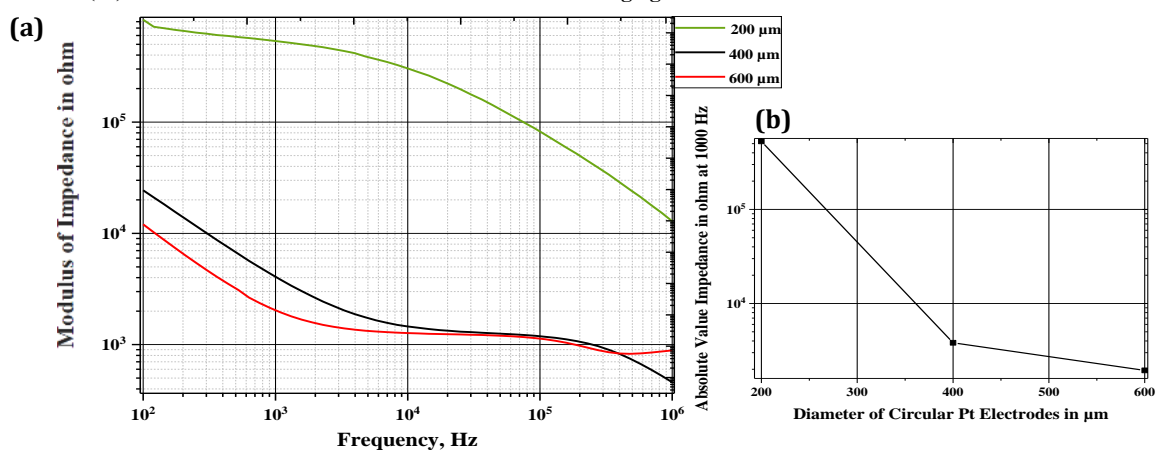


**Figure 3-45** (a) Impedance Spectroscopy data at 1000 Hz for different diameters, (b) the relation between the size and the impedance is inverse

In **Figure 3-45 (a, b)** the relation between size and impedance is shown as described in the literature [254] and verified with COMSOL simulation (see **Figure 3-43 (b)**). **Figure 3-51 (a)** demonstrates the different impedances of Pt samples in PBS.

In **Figure 3-46**, the results of using cleaning method – 1 (see **Section 2.4**). It was observed that the impedance of a 200 μm electrode is significantly lowered. In a lot of cases, it is

observed that: the smaller electrodes' surface areas get affected more by salt/dust layer accumulation on the surface because, in the case of a smaller area of interest, it is very easy for the whole area to be covered upon 1 or 2 characterizations and the ion accumulation layer is comparatively smaller in smaller electrodes and they get thinner if some surface gets coated with a non-conductive element.

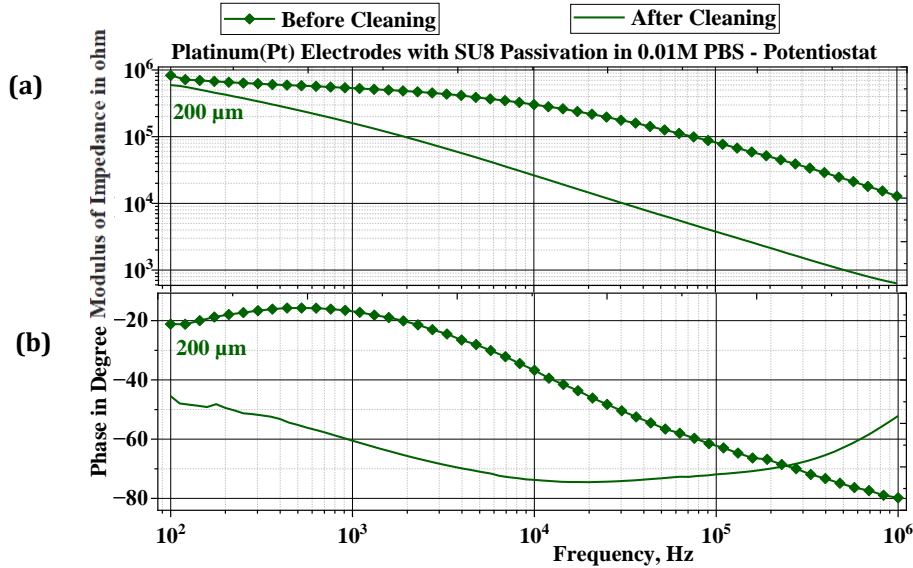


**Figure 3- 46** (a) Impedance of a 200 μm in diameter circular Pt electrode in PBS, (b) phase of a 200-in-diameter circular Pt electrode in PBS

The same experiments were done, and the results were shown for the samples of 400 μm in diameter Pt electrodes (see **Figure 3-47**). The change in the charge transfer and the  $C_{dl}$  region is non-existent in the impedance, However, there is a small phase difference, i.e., they appeared to be more capacitive before. So, it can be assumed that due to cleaning, the surface probably becomes smoother which helps attain a larger ion accumulation layer. Cleaning removes all the trace of polymer or oxidation on the surface of electrodes. However, the change is not big enough to yield a change in impedance with electrode of 400 μm. The value of the impedance at 1000 Hz for the circular Pt electrode was extrapolated at 70 kΩ.cm<sup>2</sup> surface area. The result is on the same scale as that of the literature [164], where the value is noted at around 5 kΩ at 0.05 mm<sup>2</sup> or 25 kΩ.cm<sup>2</sup>. In the later section, a comparative discussion of the different cleaning methods is given [255] in **Section 3.6**.

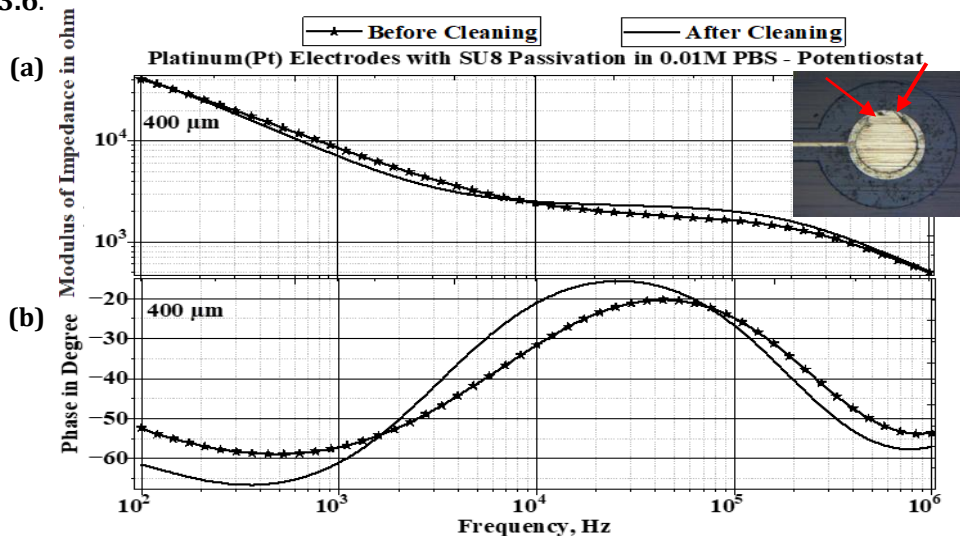


**Figure 3- 47** (a) Impedance of a 400μm in diameter circular Pt electrode in PBS, (b) phase of a 400μm in diameter circular Pt electrode in PBS

### 3.6.2.2 Fit Parameters

To explain, the data from **Table 3-4** and the theoretical data are compared and it is shown (see **Figure 3-48**) how a different equivalent circuit might have appeared. Notably, all the values of  $C_{dl}$  mentioned in the table were found to be the same as the calculated value with the simplified calculation of capacitance.

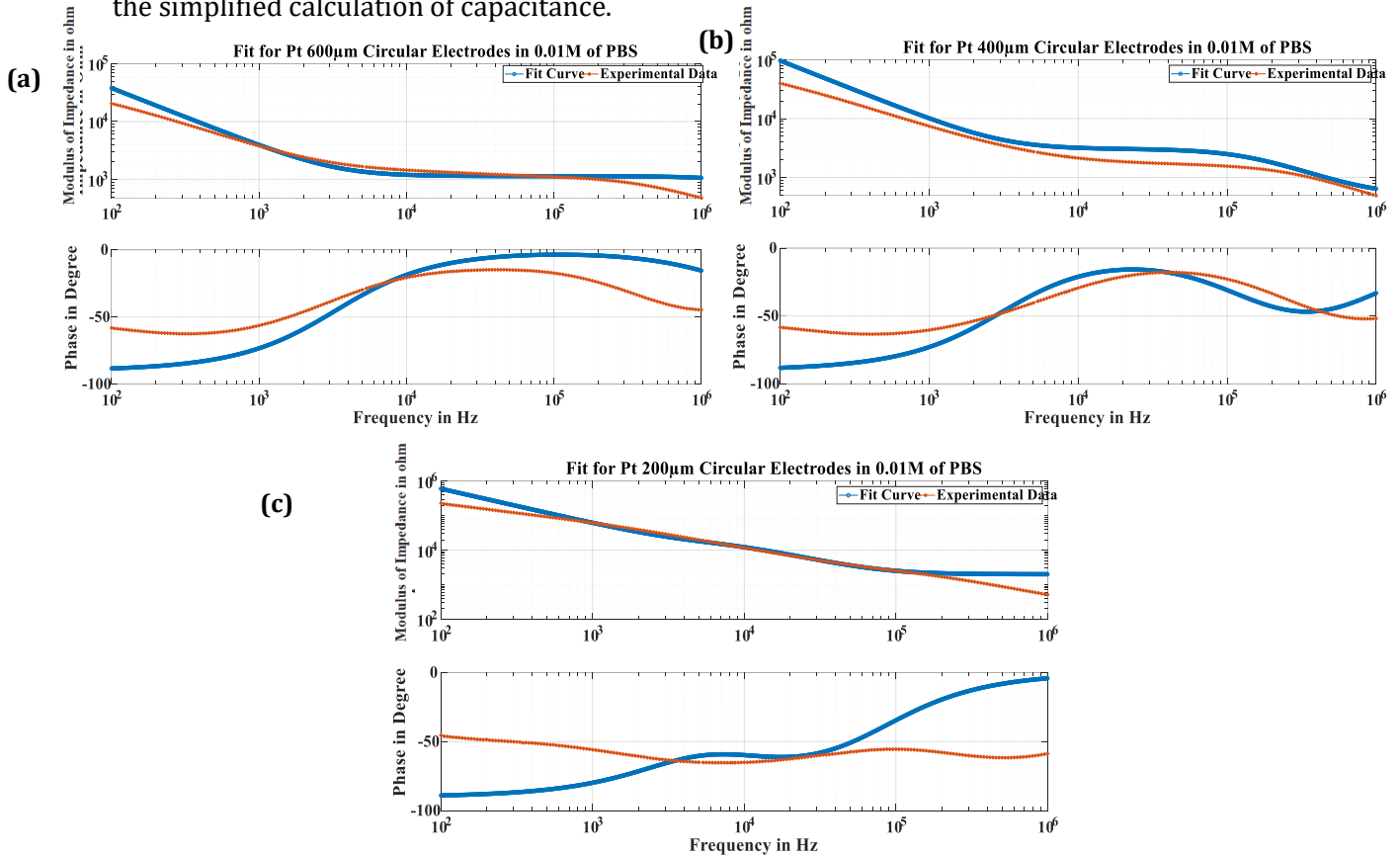


**Figure 3- 48** Experimental data plotted against fit parameter; blue curve – fit data, red curve – experimental data (a) 600  $\mu\text{m}$ , (b) 400  $\mu\text{m}$ , (c) 200  $\mu\text{m}$  of Platinum electrodes

The value derived from 200  $\mu\text{m}$  is not in accordance with the other sizes. As mentioned before, due to multiple experiments the heavy dirt accumulation and damage to the surface might lead to that increase in ohmic resistance. After that, the data were plotted in MATLAB against the experimental value to visualize the difference between the fit data and experimental value (see **Figure 3-48**). And there are still discrepancies between the experimental curve and the fit curve. Replacing both of the simple capacitors with 2 CPEs would make the fit curves closer to the experimental data [183], [256].

Diameter of the Circular Electrode in $\mu\text{m}$	$R_{\Omega}$ in $\Omega$	$C_{dl}$ in F	$R_{ct}$ in $\Omega$	$C_2$ in F
600	341.35	8.11e-11	801.77	4.19e-9
400	489.56	4.45e-10	2641	12.94e-9
200	2000	1.11e-9	27000	15.4e-10

**Table 3-4** Extrapolated data from the fit parameters of Pt electrodes of different sizes

### 3.6.2.3 EIS in Different Concentrations

Moving forward experiments were carried out using Platinum in different concentrations. Since PBS is a water-based salt solution, the increase in concentration means an increase in the number of ions in the liquid medium, hence the more current carrier. The resistivity of the PBS should change with the concentration of salt. When the concentration is reduced, the resistance increases with a ratio of approximately 2.5 (0.01M/0.004M). So, the overall impedance decreases for all the sizes (*see Figure 3-49*).

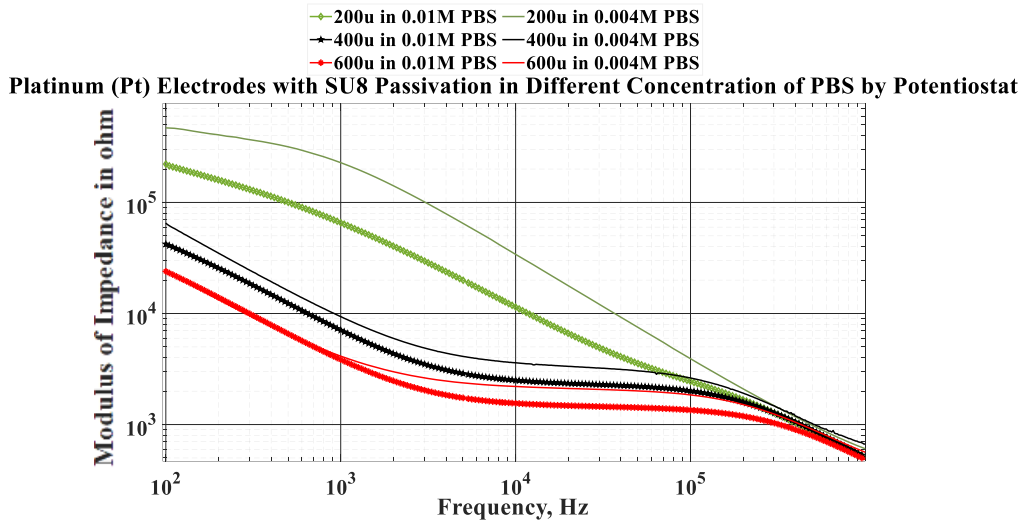


**Figure 3- 49** Impedance of 200  $\mu\text{m}$ , 400  $\mu\text{m}$ , and 600  $\mu\text{m}$  Platinum electrodes in different concentrations of PBS

**Figure 3-49** shows the performances of Platinum electrodes of the same shapes and sizes in different concentrations of liquid. The curves of the same color are representative of the same size. The green curves show the result for 200  $\mu\text{m}$ , the black ones are for 400  $\mu\text{m}$  and the red ones are for 600  $\mu\text{m}$ . When the experiments were done in 0.1M and .004M of PBS, it was observed that the liquid with higher concentration, i.e., the solution containing more salt ions would better propagation of current and, as a result, lowered impedance. This observation should be true for all the cases and the same test was done with all the samples, However, the results are not shown due to the fact all the results signify the same relations and there should not be any exceptions [152]. The difference between 400  $\mu\text{m}$  & 600  $\mu\text{m}$  is smaller compared to the difference observed between 200  $\mu\text{m}$  and 400  $\mu\text{m}$ , which is normal because the impedance changes more on the smaller scale.

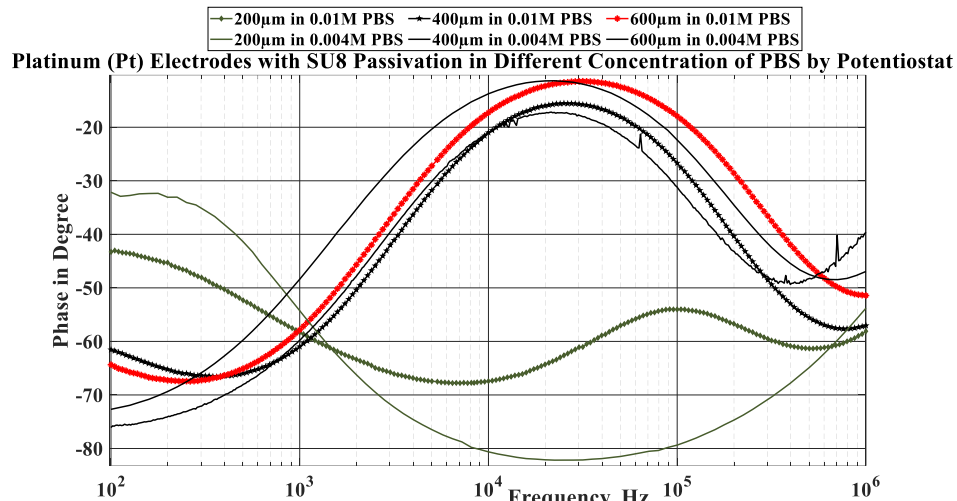


**Figure 3- 50** Impedance of 200  $\mu\text{m}$ , 400  $\mu\text{m}$ , and 600  $\mu\text{m}$  Platinum electrodes in different concentrations of PBS

As observed in **Figure 3-50**, the phase change is more prominent in the frequency range of 100 Hz-100 KHz. As was seen in **Figure 3-2**, this is the charge transfer range. Therefore, the change in the phase values due to the charge transfer contributes to the change in the phase more significantly.

### 3.6.2.4 Comparison Between the Potentiostat and AD2 (Clean Platinum)

These tests were done with (see **Figure 3- 51**) both Potentiostat and AD2 in 0.004 M of PBS. The purpose of these was to observe the test results vary with different equipment. Going forward, these test results were not done for all the samples with different materials, as these do not help provide important information about the performance of the samples themselves.

While characterizing the microelectrodes of different diameters fabricated with Pt only on top of the Si wafer, a quick comparison between the 2 results of EIS done with EC Lab and Analog Discovery2 is shown. The observations are as area increases, impedance decreases, because they become more resistive. The value after the frequency of 100 kHz is because of the cut-off frequency of the machine. And it is different on different machines.

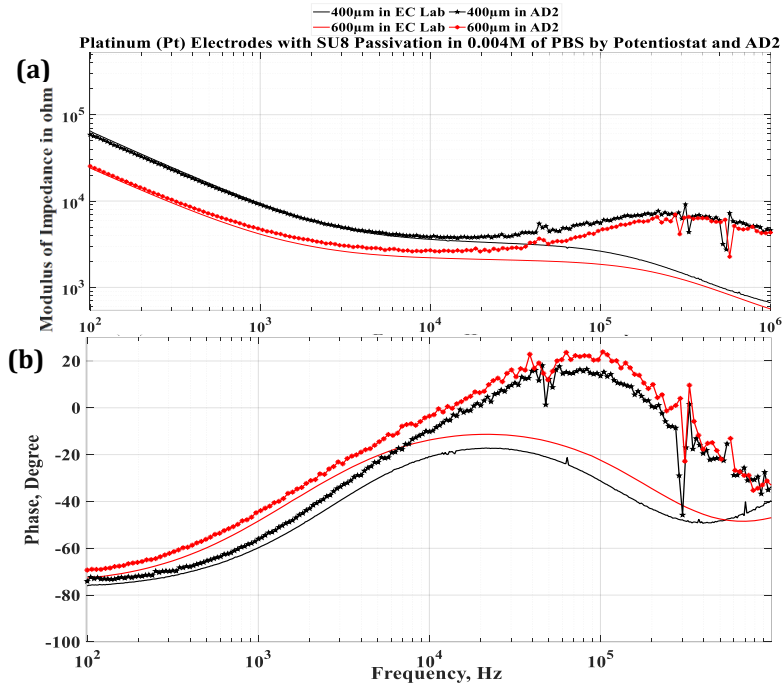


**Figure 3- 51** (a) mpedance, and (b) phase of 400  $\mu\text{m}$  and 600  $\mu\text{m}$  Pt samples done in potentiostat and AD2

The first decade in the frequency range is a direct result of the impedance of the WE (Working Electrode) and RE (Reference Electrode) in the electrolyte (Open Circuit Value). In **Figure 3-51**, the impedance values of 400  $\mu\text{m}$  and 600  $\mu\text{m}$  are similar as they should be. In higher frequencies ( $>100$  kHz), the impedance spectroscopy starts showing the effect of the inductive components derived from the experimental setup. Therefore, the values are different for EC Lab (line curve) and AD (Line + marker).

### 3.6.3.5 Cyclic Voltammetry (CV) in Clean Platinum Electrodes

The cyclic voltammetry of the samples was performed in 0.5M of  $\text{LiClO}_4$  using the 3-electrode method in EC Lab software with the potentiostat equipment. **Figure 3-52** demonstrates the result in different diameters. The charge transfer capacity was calculated from the samples in the water window of -0.8 to 0.8 volt for a scan rate of  $10 \text{ mVs}^{-1}$ , for the mass of the active material of 1 mg in case of 200  $\mu\text{m}$ , 2 mg in case of 400  $\mu\text{m}$ , and 3 mg in case of 600  $\mu\text{m}$ .



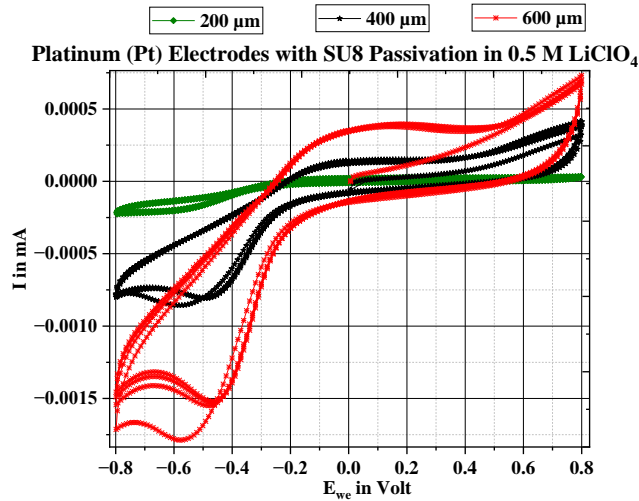


**Figure 3- 52** Cyclic voltammetry performed in Pt electrodes of different diameters

Diameter in $\mu\text{m}$	200	400	600
Specific Capacitance, $C_s$ in F/g	11.23	45.23	66.88

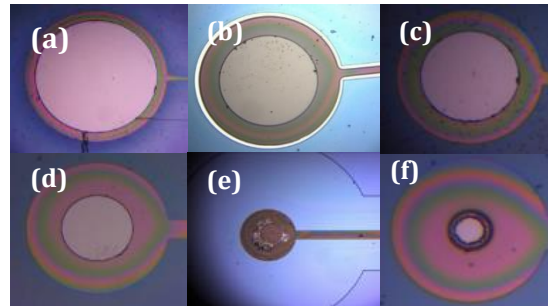
**Table 3- 5** Specific Capacitance of Pt electrode of different sizes

While comparing the values in **Table 3-5**, it was observed that the value of specific capacitance is not the same for all sizes. It can be concluded that the value of the specific capacitance is not the same for all the diameters. Considering the value of the double layer changes, However, not proportionally, and the effective surface area deteriorates at a different rate in different samples. SU8 not being the best protective material and being stripped off (see **Figure 3-44 (d, e, f)**) with multiple experiments poses some discrepancies in results.

From the impedance spectroscopy of the 200  $\mu\text{m}$ , it was noticeable that the result was not ideal and the distance between the 200  $\mu\text{m}$  - 400  $\mu\text{m}$ , and 400  $\mu\text{m}$  - 600  $\mu\text{m}$  doesn't follow the same trend. It was probably since, in 200  $\mu\text{m}$  the sample was covered in dirt (see **Figure 3-44 (d)**), and in 400  $\mu\text{m}$  and 600  $\mu\text{m}$  upon multiple usages and SU8 removal, there was a larger experimental area exposed.

### 3.6.4 TiN-Pt-TiN Electrodes with SU8 as Passivation

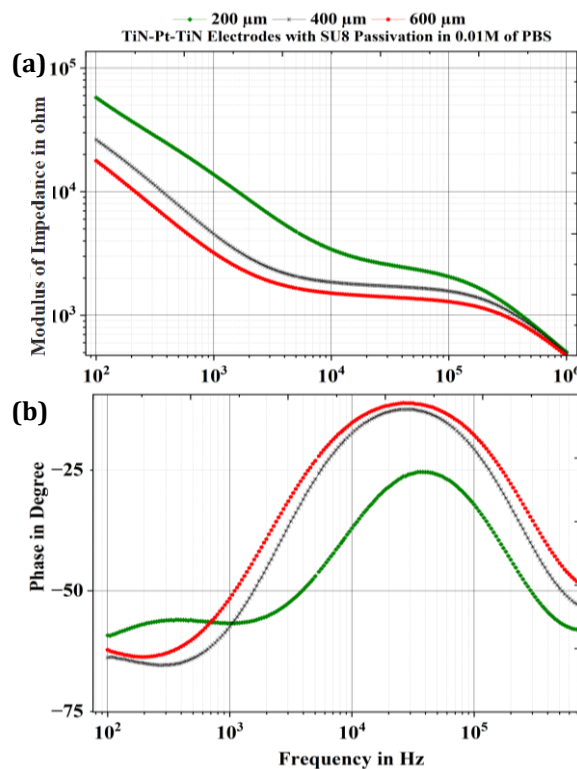
The purpose of this model is to exploit the advantages of TiN as a coating material, which was later used extensively in the case of Diamond fabrication while taking advantage of a reduced overall ohmic/serial resistance due to the presence of Pt in between the stack (see **Figure 2-25**). In the stack model, there are two layers of TiN ( $\sim 200$  nm) which encapsulate one standard layer of Pt ( $\sim 200$  nm). The resistivity of TiN is  $25\text{e-}6 \Omega\cdot\text{cm}$  [257]. For a  $\sim 600$  nm thick sheet of TiN-Platinum-TiN with a cross-sectional area of  $15 \times 10^{-12}$  square meters, the resistivity will be a combination of TiN and Pt. So, the overall resistance will be lower than that of TiN, However, higher than that of Platinum electrodes. **Figure 3-53** shows the samples of different sizes after fabrication (under a simple microscope).



**Figure 3- 53** The TiN-Pt-TiN samples before used in characterization of diameter (a)30  $\mu\text{m}$ , (b) 60  $\mu\text{m}$ , (c) 100  $\mu\text{m}$  (d) 200  $\mu\text{m}$  (e) 100  $\mu\text{m}$ , (f) 600  $\mu\text{m}$

### 3.6.4.1 EIS in Clean TiN-Pt-TiN Electrodes

The primary observation of the impedance spectroscopy (see **Figure 3-54 (a)**) is the relation between the size of the surface area and the impedance, which is in accordance with the previous results and COMSOL simulation done before (see **Figure 3-43**).

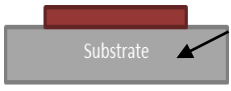
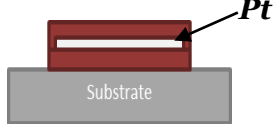


**Figure 3- 54** (a) Absolute value of impedance, (b) phase in samples of different diameters

At 1 kHz, the impedance of the stack samples shows a value of 3548.12 ohm, which is close to the value observed by the samples of platinum (3.5 k $\Omega$ ). This incredible value is achieved due to the fact that the TiN has a much rougher surface than that of platinum and reportedly has higher capacitance than that of platinum [144]. 6 samples were taken into consideration for all the sizes and the samples showed up to 25% RSD.

In these samples, due to the stack model having TiN as an outer layer, which has a much higher roughness than Pt, the effective surface area increases, and when compared to the same diameter (e.g.: 600  $\mu\text{m}$ ), the TiN-Pt-TiN has a much larger surface area compared to that of a Pt electrode [237]. When observing the phase, it is noticed that the value of the phase of Pt and TiN becomes similar. Because Phase is more affected by surface area

compared to magnitude. **Table 3-6** represents the measured value of resistance and resistivity of the bare TiN and TiN-Pt-TiN samples, done in ESIEE Paris Cleanroom.

Cross-section scheme	Bare TiN	TiN - Pt - TiN
	 <p style="text-align: center;">Bare TiN TiN: L: 2 cm / W: 20 μm / T: 400 nm</p>	 <p style="text-align: center;">TiN - Pt - TiN TiN: L: 2 cm / W: 20 μm / T: 400 nm Pt: L: 2 cm / W: 15 μm / T: 120 nm</p>
Resistance and resistivity (at 20°C)	20 kΩ and $8 \times 10^{-6} \Omega \cdot m$	1.2 kΩ and $5 \times 10^{-7} \Omega \cdot m$

**Table 3-6** The comparison of resistance and resistivity of TiN with TiN-Pt-TiN stack model

When compared to the literature, the stack model shows similar impedance ( $3.5 \text{ k}\Omega \rightarrow 10.79 \text{ }\Omega \cdot \text{cm}^2$ , measured at 1 kHz in 600 μm electrode) compared to the samples made with TiN/Pt-Ir alloy [144]. This lower impedance compared to other biomaterials makes it a better biomaterial for recording applications when compared to bare Ti or TiN. TiN also showed better performances as a coating material when compared to Ir and Platinum which is explained in the literature. The resistivity and the resistance of the stack model are lower than TiN only and close to the TiN alloys mentioned in literature [258]-[260].

### 3.6.4.2 Fit Parameters

The same fit circuit (see **Figure 3-55**) as before was used to extrapolate the value and analyze the experimental data.

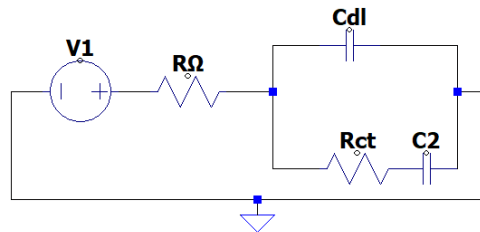


**Figure 3- 55** Simplified fit circuit used to extrapolate the value

Diameters of the electrodes in μm	R in Ω	C <sub>dI</sub> in F	R <sub>ct</sub>	C <sub>2</sub> in F
600	304.91	15e-12	1395.14	60.43e-12
400	291.97	7.06e-12	1324.30	34.97e-9
200	272.63	13.84e-9	1880.30	11.57e-9

**Table 3-7** Extrapolated data from the fit parameters

Then the data was extracted and put in **Table 3-7** to plot against the experimental data to visualize the discrepancy between the experimental and fit data. In **Table 3-7**, the data from the fit curve is extrapolated and displayed, which shows overall close to the ohmic resistance as the Pt samples of the same size. The C<sub>2</sub> was larger than that of the Pt samples, However, the overall Impedance is better in comparison to the Pt samples of the same size. From **Figure 3-56** it can be concluded that the experimental value is not the same as the fit parameters. The fit equivalent circuit needs to be revised for a better fit. One of the

modifications should be the replacement of the simple capacitors with CPE, as mentioned in **Section 3.6.2.2**.

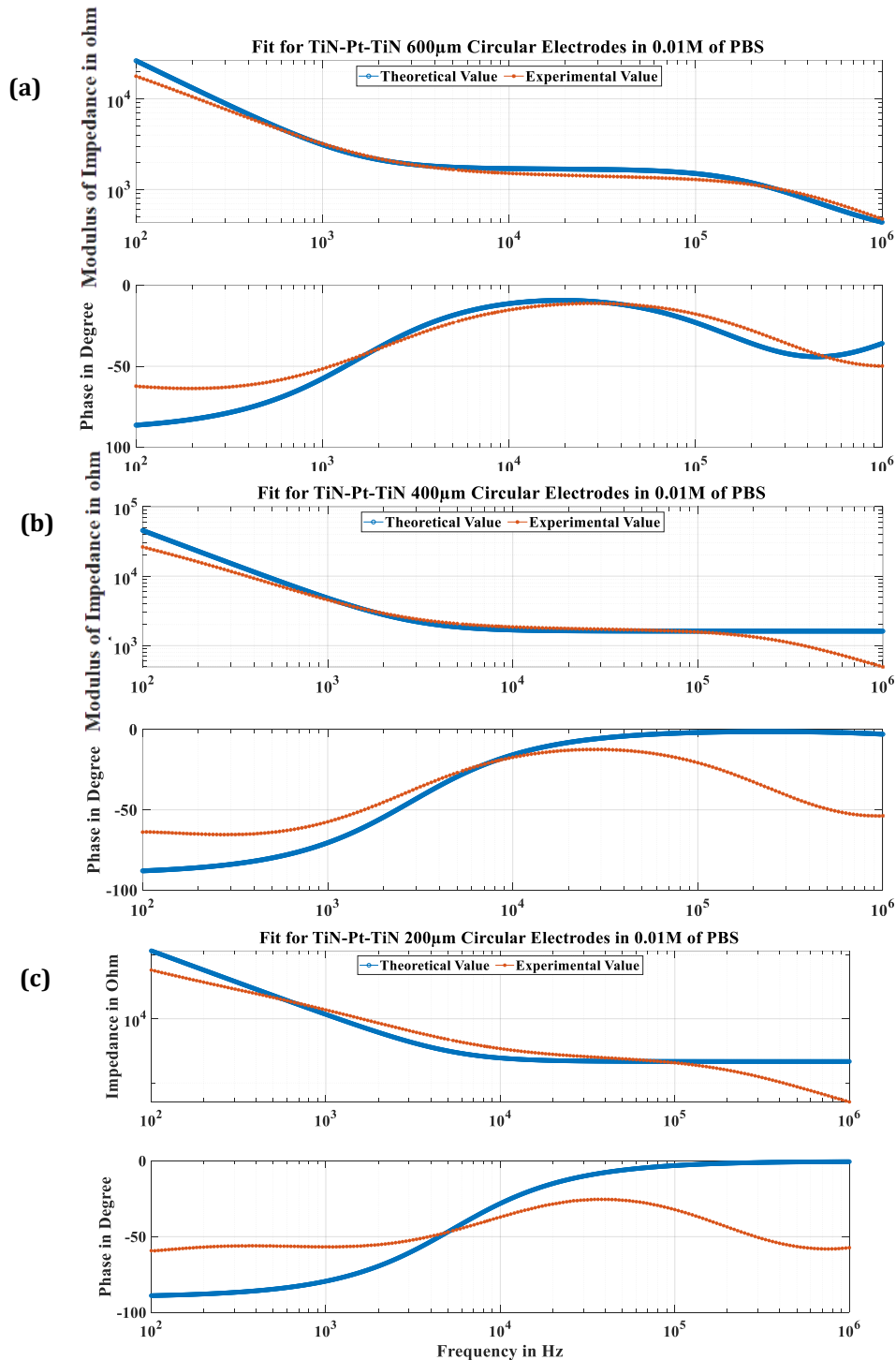


**Figure 3- 56** Experimental data plotted against fit parameter; blue curve – fit data, red curve – experimental data (a) 600 μm, (b) 400 μm, (c) 200 μm of TiN-pt-TiN electrode

### 3.6.4.3 CV in the Stack Model

The CV was performed with the same potentiostat as before using 10 mV as excitation V and at 100 mV/s scan rate using the same equipment as before. The conventional duck-shaped CV curve is shown in **Figure 3-57**.

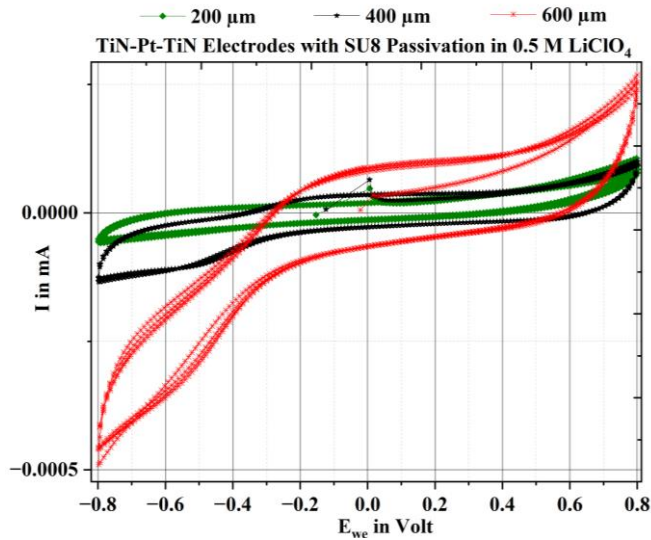


**Figure 3- 57** CV performed in TiN-Pt-TiN electrodes of different diameters

The specific capacitance was calculated from the samples in the water window of -0.8 to 0.8 volt for a scan rate of 100 mVs<sup>-1</sup>, measured at  $3.54 \times 10^{-3}$  F/cm<sup>2</sup>. This value is higher than bare Ti only, bare Pt, and bare TiN, and in the same scale as the Platinized Ti, and Ti alloys mentioned in literature[46], [144]. These results make it a better candidate for stimulation application. So, it can be undoubtedly said that using the stack model is better in terms of overall performance (both recording and stimulation application) as a candidate for biomedical applications.

### 3.6.5 Black TiN

The black TiN was first fabricated with conventional circular samples, However, then it was explored with the hexagonal shape of electrodes. In this case, only TiN was used. So, there will be a significant increase in the serial/ohmic resistance compared to both the Platinum and stack model (TiN-Pt-TiN)

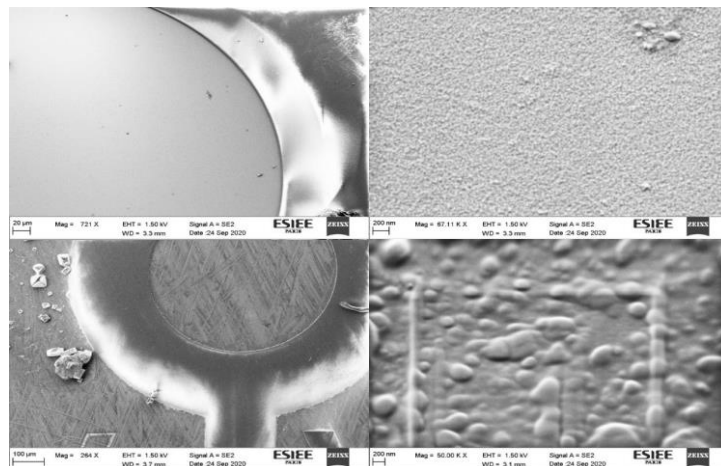


**Figure 3- 58** Black TiN sample seen under SEM (magnification written on each image)

Here the SEM image of both flat and black TiN is shown (see **Figure 3-58**). In the images, the magnification is the same for the zoomed-in view and the rough TiN has a much rougher surface area compared to that of flat TiN. The purpose of this was to improve the effective surface area of the samples and reduce the impedance for the same surface area to a higher degree.

### 3.6.5.1 EIS in Black TiN

New hexagonal-shaped electrodes were fabricated with a new mask and in this case the stack (TiN-Pt-TiN) design was not followed, since lowering the serial resistance was not the purpose. Rather understanding the structure and performance of the black TiN was.

Since the fabrication was done on a glass substrate there was less parasitic capacitance which is evident from **Figure 3-59**. Unlike the previous BIS curves, these do not follow the same shape. However, the overall trend of size and performance relation is the same.

**Figure 3-59** shows the impedance spectroscopy done in 0.01M of PBS with the potentiostat and the impedances follow R-C characteristics, the same as all materials. However, there is much less capacitance for the samples compared to those of Pt or the stack model, which ensures a better performance.

The impedance recorded at 1000 Hz is 15 k $\Omega$ . **Table 3-8** shows the changes in relative surface area between the circular and hexagonal shapes. 6 samples were taken into consideration for each of the sizes. The sample with 600  $\mu\text{m}$  of diameter showed 18.61%, 400  $\mu\text{m}$  of diameter showed 20.61%, 200  $\mu\text{m}$  of diameter showed 24.83%, 100  $\mu\text{m}$  of diameter showed 24.83%, 60  $\mu\text{m}$  of diameter showed 26.23%, 30  $\mu\text{m}$  of diameter showed 27.17% RSD.

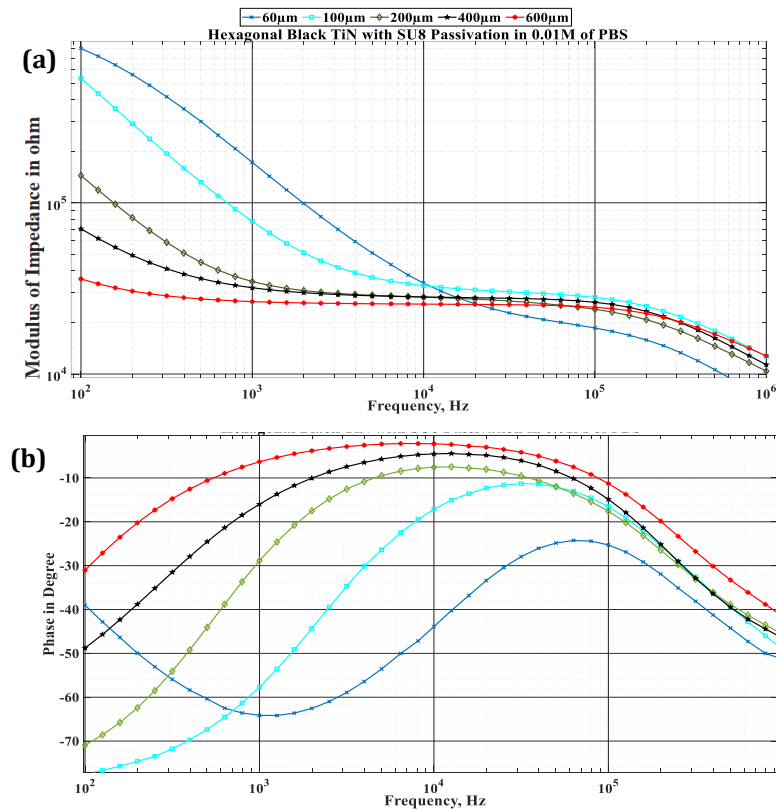


**Figure 3- 59** Impedance spectroscopy performed in hexagonal black TiN (a) Impedance analysis, (b) phase analysis

As is seen from **Table 3-8**, the hexagonal samples had a slightly smaller surface area compared to the circular ones. Because the diameter of the circular electrodes is equal to the long diameters of the hexagonal samples. The primary purpose was to observe the change in charge injection capacity. However, in the case of impedance there is not a huge difference due to the shape of the electrodes, only the sizes. As discussed in **Section 2.1.2**, the edge effect is observed and starts changing the performance of the electrodes due to the presence of edges. However, there was no visible change in the impedances when the shape was changed from circular to hexagonal. This means that there is negligible effect of shape on the overall impedance of the electrodes [148], [149].

Long Diagonal or Diagonal in $\mu\text{m}$	Area for Hexagonal in $\mu\text{m}^2$	Area for Circle in $\mu\text{m}^2$
30	584.56	706.86
60	2338.27	2827.43
100	6495.19	7853.98
200	25980.76	31415.93
400	103923	125664
600	233827	282743

**Table 3- 8** Comparison of the areas of hexagonal or circular electrodes

When compared to the samples of the stack model, in terms of impedance in  $\Omega\cdot\text{cm}^2$ , the value calculated from a hexagonal electrode with black TiN is  $46.653 \Omega\cdot\text{cm}^2$  at 1 kHz. The value is at the same scale as the stack model (see **Section 3.6.4.1**). However, when compared with electrodes made with Ti/Pt-Ir alloy [46], which makes it more suitable for recording application, with increased surface area due to roughness.

### 3.6.5.2 Light Absorption Test

There was a light absorption test carried out in 0.01M of PBS to determine whether there were light-induced changes in electrical impedance. However, the impedance spectroscopy was inconclusive, and further tests need to be carried out to quantify the change in light absorption due to the change in surface porosity [195], [261].

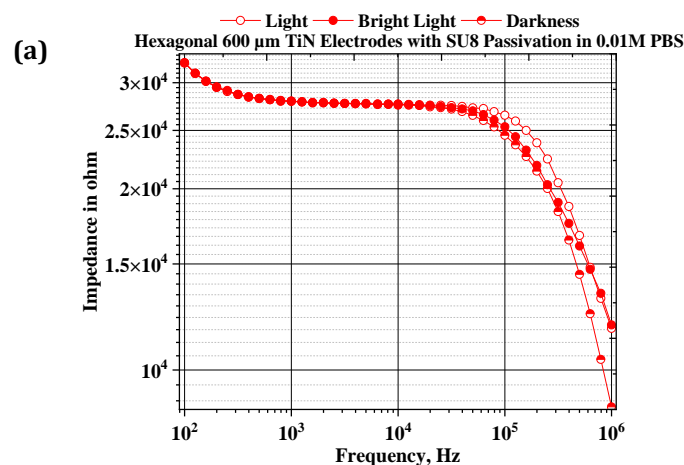


**Figure 3-60 (a)** Absolute impedance in 0.01M of PBS with hexagonal black TiN electrodes

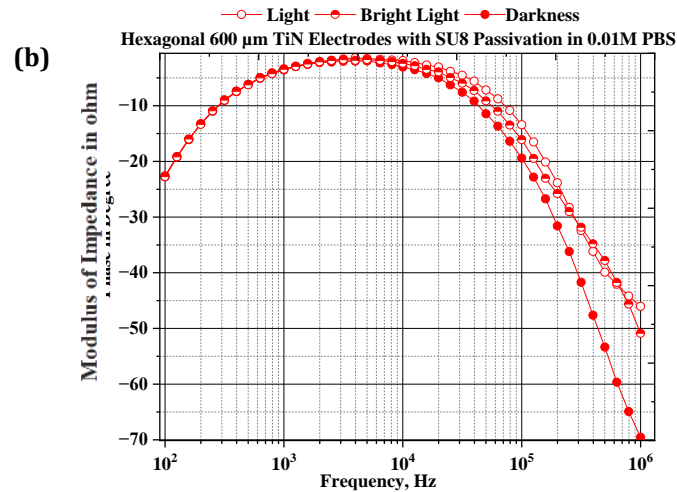


Figure 3- 60 (b) phase in 0.01M of PBS with hexagonal black TiN electrodes

It was explored to see if it was due to light absorption of the black TiN structure. It was exposed to light, darkness, and bright light to see if there was a change in the impedance due to exposure to light. However, there were no visible changes (see Figure 3-60) in impedance spectroscopy (a) and phase analysis (b).

### 3.6.5.3 Cyclic Voltammetry in Black TiN

CV was carried out using the same equipment and the solution of 0.5 M of LiClO<sub>4</sub> using a 3-electrode method (see Figure 3-67).

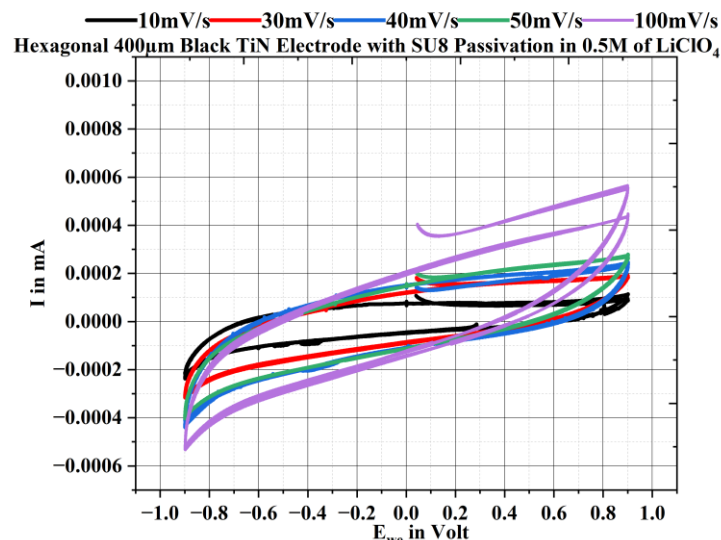


Figure 3- 61 CV performed in 400 μm of hexagonal black TiN electrode in different scan rate

Figure 3-61 shows a bigger potential window compared to that of TiN stack models and Pt samples (-0.9 V to 0.9 V). That ensures a bigger window of operation and, therefore, better performance over a larger window in case of application in stimulation and recording. Here the same samples were observed to verify that the higher the scan rate, the larger the specific capacitance.

As can be observed from the table and the curve the specific capacitance decreases with the increase in scan rate, since at a higher scan rate, a faster redox reaction happens, which



reduces the electrolyte ion diffusion into the active material and consequently lowers the capacitance [235], [262, p. 4]. In the graph, the inserted curve on the right corner shows the triangular excitation potential applied for all the scan rates and the graph represents the response at different scan rates. It is shown that the back curve (response at 10 mV) takes almost 200 seconds (*see Figure 3-62 (b)*) to compile one redox cycle and the redox cycle time observed from the response time goes down with the increase in scan rate. So, for the scan rate of 100 mV the samples have the fastest compilation time of a redox cycle (see Figure, which takes around 25 seconds) and the value of the specific capacitance is the lowest at 100 mVs<sup>-1</sup> (3.14 F/g, *see Table 3-9*). At a higher scan rate, a faster redox reaction happens, which reduces the electrolyte ion diffusion into the active material and consequently lowers the capacitance [262], [263], [264].

Similar to all the specific capacitance calculations, **Equation 3-19** was used to calculate the values of **Table 3-9**.

Scan Rate (mV/s)	10	40	50	100
Specific Capacitance, C <sub>s</sub> (Fg <sup>-1</sup> ) at 400 μm	10.12	5.49	4.3	3.14
Specific Capacitance, C <sub>s</sub> (Fg <sup>-1</sup> ) at 200 μm	3.76	1.08	0.88	0.55

**Table 3-9** Comparison of the specific capacitance at different scan rates

**Figure 3-62 (a)** shows the trendline of the specific capacitors with the scan rate, which is increasing. **Figure 3-62 (b)** shows the same thing However, with a time vs. current curve. Both of those means, that as the scan rate increases (that means the same amount of excitation voltage is passed through the samples in a smaller amount of time), the faster the current passes through the sample [265].

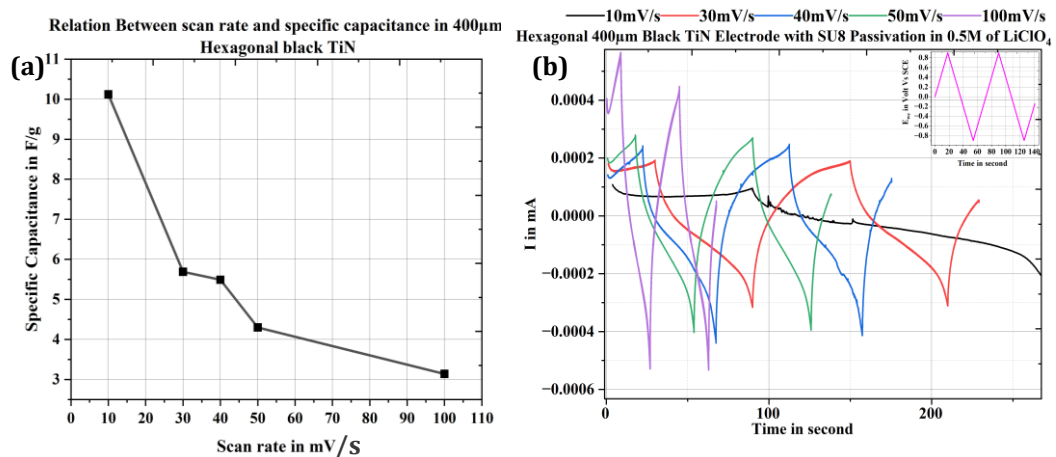


**Figure 3- 62** For 400 μm hexagonal black Tin electrode (a) The decrease in specific capacitance with the increase in scan rate, (b) redox reaction rate decreases with the increase in scan rate

The overall charge transfer in the same samples stays almost the same (a little change might happen due to the shift in the experimental setup, stirring, salt accumulation, etc., but ideally the change would be negligible). In **Figure 3-62 (a)** the specific capacitance decreases as the scan rate increases. In **Figure 3-62 (b)** the current is observed as a function of time. In the inserted graph the excitation voltage sweep is shown, which is the same for all the cases (better view of the graph in Annex), However, what changes in different scan rates is how fast the sweeping is being done in the sample of the same size. Starting from 10 mV/s (black curve) takes the longest (approximately 250 s+), and the fastest scan rate 100 mV/S (purple curve) takes the shortest amount of time for a single sweep and one whole sweep is done in approximately 60 s.

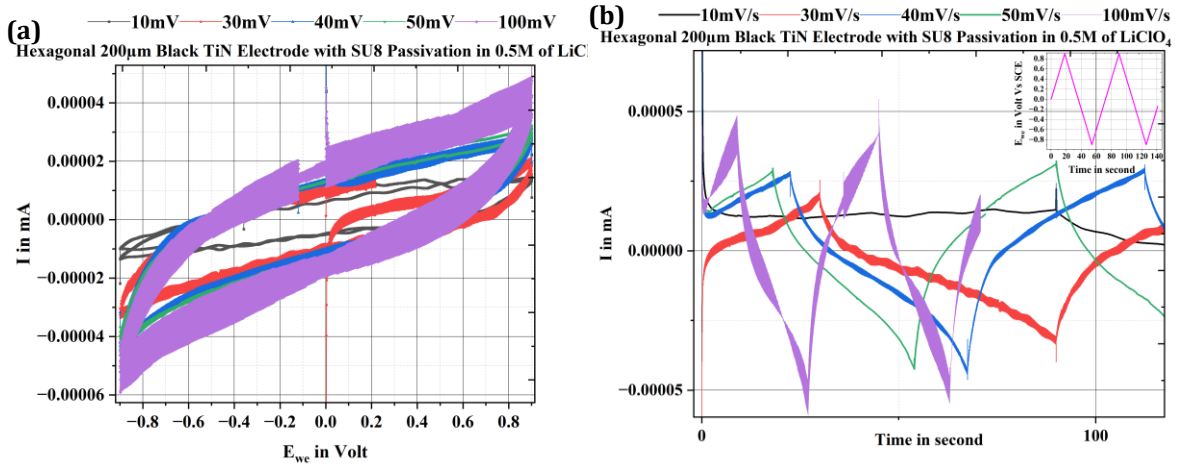


**Figure 3- 63** For 200  $\mu\text{m}$  hexagonal black Tin electrode (a) The decrease in specific capacitance with the increase in scan rate, (b) redox reaction rate decreases with the increase in scan rate

As explained for the 400  $\mu\text{m}$  sample, **Figure 3-63** shows similar trends. The biggest scan rate 100 mV/s has the fastest sweep (**Figure 3-63 (b), purple curve**), and the widest charge transfer for the same amount of excitement (**Figure 3-63 (a), purple curve**).

### 3.6.5.4 Fit Parameters

In order to find a good fit circuit, the first step is to keep in mind the application, in the case of this thesis which is bio-electrical experiments. After that, upon seeing the shape of the Nyquist curve it should be apparent what the possible equivalent circuits might be. Then comes understanding which part contributes to which part of the value, and that is the most complicated part. Due to the law of equivalent impedance, several circuits may fit this experiment. Since the value of the double layer is not exactly known for this specific case, and the amount of roughness is random, there remains a number of variables that can affect the components. So, unlike the previous samples, this fit circuit was not very apparent.

#### (a) For Circuit 1:

The first proposed equivalent (*see Figure 3-64*) circuit is similar to before. Previously, for simplification capacitors were used instead of CPE (frequency-independent capacitor). However, because one of the biggest traits of black TiN is surface porosity, CPE (Q) is derived majorly in electrochemistry due to that. So, there were 2 CPE (Q1 and Q2) included in the device to represent both the double-layer capacitance of the Helmholtz layer and the capacitance in the environment and the results were perfect fit curves [228], [266].

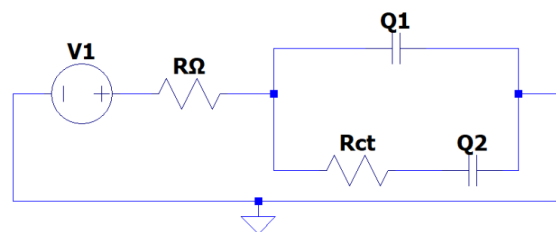


**Figure 3- 64** Proposed equivalent circuit 1

From **Figure 3-65**, it is apparent that the fit was more accurate and closer to experimental data when compared to the fit done in Pt samples. However, even in this case, a better understanding and interpretation of the data needs to be achieved with further studies.

Here 2 equivalent circuits are proposed, and, in both cases, the fit data is close to the experimental data in the presence of two CPEs, the model gives closer results to the experimental data. The presence of CPE is due to the crystalline surface of the electrode and how it affects the EDLC. It is also notable that in the case of samples of 30  $\mu\text{m}$ , 60  $\mu\text{m}$ , and 100  $\mu\text{m}$ , the working electrode: surrounding SU8 is smaller when compared to the electrode with a larger surface area (*see Section 3.6.2.1*).

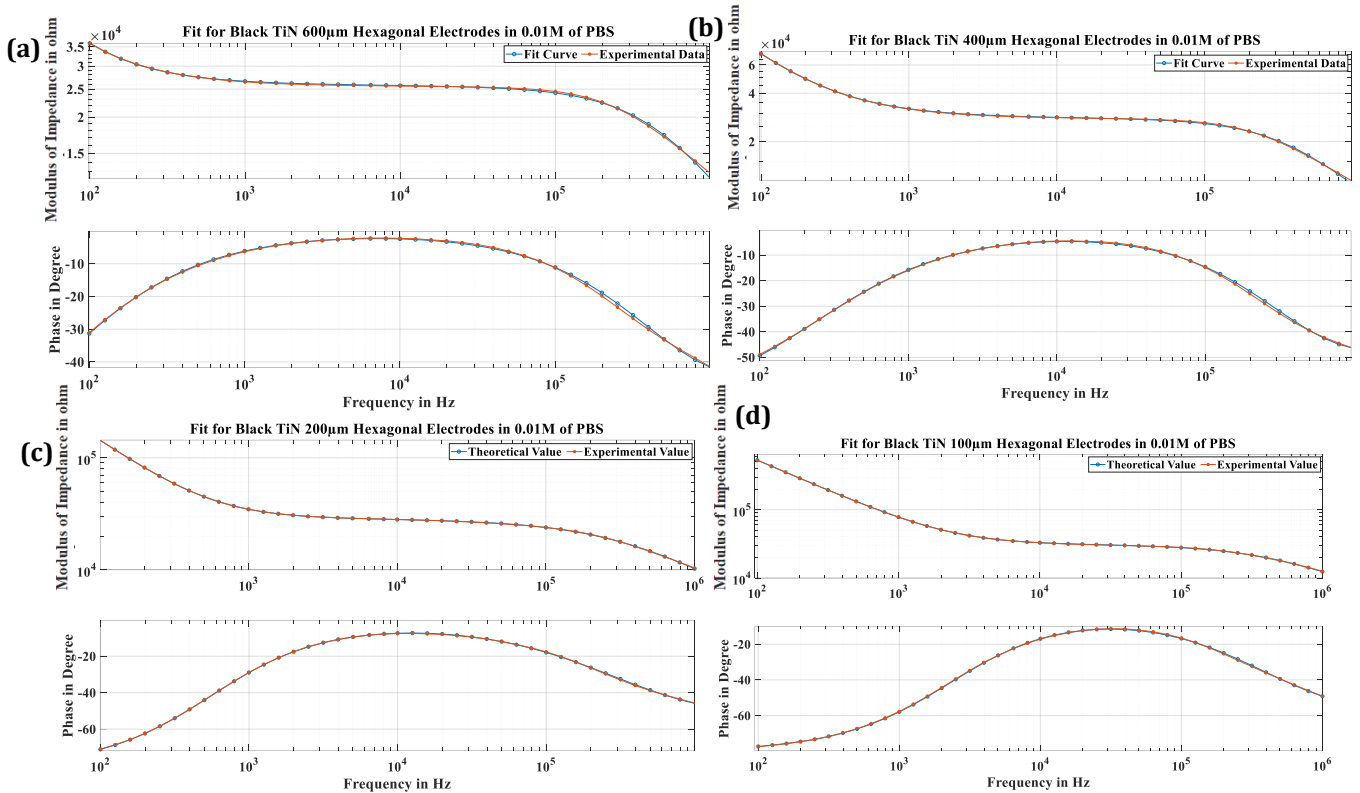


**Figure 3- 65** Experimental data plotted against fit parameter; blue curve – fit data, red curve – experimental data (a) 600  $\mu\text{m}$ , (b) 400  $\mu\text{m}$ , (c) 200  $\mu\text{m}$ , (d) 100  $\mu\text{m}$  of Black TiN electrode

**(a) For Circuit 2:**

When it comes to the samples that are smaller in size, it was apparent that the one CPE was not enough to explain and acquire a reasonable fit circuit for the samples. So, 2 new circuits were proposed (*see Figure 3-66 (a)*), due to the increased surface area and radius ratio. Also as already seen from the MATLAB simulation when moving down to the sizes under 100  $\mu\text{m}$ , the characteristics don't change linearly anymore. **Figure 3-66 (b)** shows a visible difference in the fit curve and the experimental data.

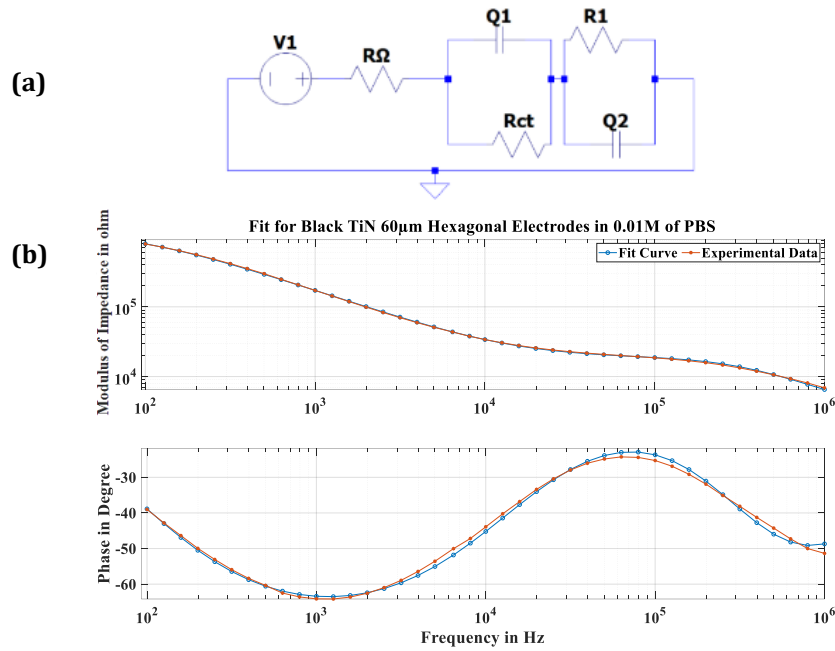


**Figure 3- 66 (a) Proposed equivalent circuit -2, (b) fit curves for this circuit**

For 60  $\mu\text{m}$  electrodes, the equivalent circuit 2 is used and the data is extrapolated and placed in **Table 3-10**.

Long Diameter in $\mu\text{m}$	$R_{\Omega}$ in $\Omega$	$Q_1$ in $\text{F} \cdot \text{s}^{\alpha_1}$ ( $\alpha_1 - 1$ )	$\alpha_1$	$R_1$ in $\Omega$	$Q_2$ in $\text{F} \cdot \text{s}^{\alpha_2}$ ( $\alpha_2 - 1$ )	$\alpha_2$	$R_{ct}$ in $\Omega$
60	0.28e-48	0.51e-9	0.79	19602	3.07e-9	0.86	1.21e6

**Table 3- 10 Extrapolated data from the fit parameters**

**(b) For Circuit 3:**

Another equivalent circuit was proposed (see **Figure 3-67 (a)**) solely for the 60  $\mu\text{m}$  electrode, to show that there are multiple possibilities for the circuit to fit the experimental data. Also, because the structure of the circuit is explainable where only the CDL is represented by CPE, all other capacitive components are considered to be perfect capacitance.

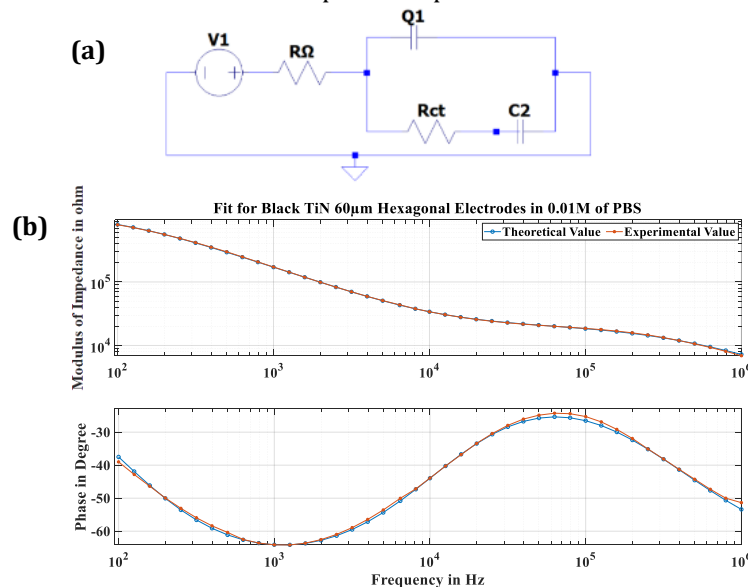


**Figure 3- 67 (a) Proposed equivalent circuit -3, (b) fit curves for this circuit in comparison with the experimental data**

Here **Table 3-11** shows the extrapolated data for the same sample. However, a different equivalent circuit and extrapolated data from the fit curve are shown in **Figure 3-73 (b)**, which shows a very close resemblance to the experimental data.

Long Diameter( $\mu\text{m}$ )	$R_{\Omega}$ in $\Omega$	$R_1$ in $\Omega$	$Q_1$ $F.s^{(a-1)}$	$\alpha_1$	$R_3$ in $\Omega$	$C_1$ in F
60	2726	1.29e-6	3.625e-9	0.8441	14811	32.56e-12

**Table 3- 11** Extrapolated data from the fit parameter for circuit - 3

**Table 3-10** and **Table 3-11** shows the extrapolated data from EC Lab where there were CPEs present, instead of simple capacitors. As was seen from **Figures 3-66, and 3-67** the fit curves are much closer to the experimental data than the fits where there were only simple capacitors. However, understanding the different values of the components is not usable here, since there are too many unknown variables for a new material that is black TiN, along with the surface roughness, which changes the double-layer capacitance. There needs to be further study for a better fit and better understanding of the equivalent circuit for this material. The same thing was observed for Diamond samples, since BDD has surface roughness [267], [268].

### 3.6.6 Diamond Electrodes

The “Full Diamond” electrodes are made on top of an oxidized Si wafer. It is not very practical to fabricate Diamond electrodes on top of a glass wafer. Because the glass wafers upon being exposed to extreme heat inside the Diamond reactor became extremely fragile and prone to breakage. Circular electrodes were fabricated with BDD with the intrinsic Diamond as passivation with diameters of 30  $\mu\text{m}$ , 60  $\mu\text{m}$ , 100  $\mu\text{m}$ , 200  $\mu\text{m}$ , 400  $\mu\text{m}$ , and 600  $\mu\text{m}$ .

#### 3.6.6.1 Impedance Spectroscopy

To begin with, **Figure 3-68** of the samples are provided under SEM (**a,b**) and the images under a simple microscope (**c-h**). The full Diamond electrodes were analyzed (see **Figure 3-69**) following the same principle as the other conventional materials.

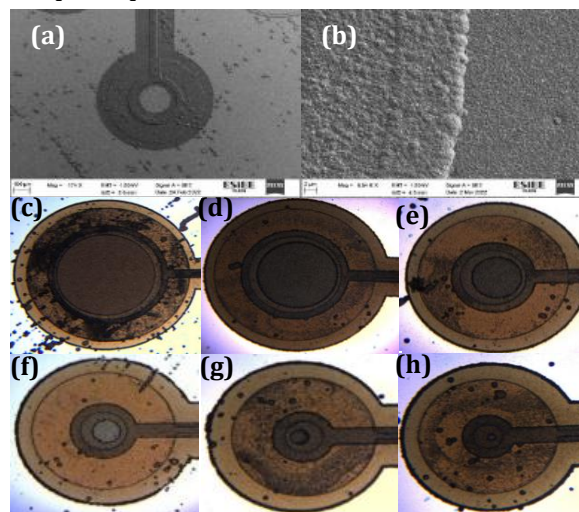


**Figure 3- 68** (a), (b) BDD electrode passivated with intrinsic Diamond seen under SEM, (c) 600  $\mu\text{m}$ , (d) 400  $\mu\text{m}$ , (e) 200  $\mu\text{m}$ , (f) 100  $\mu\text{m}$ , (g) 60  $\mu\text{m}$ , and (h) 30  $\mu\text{m}$  samples seen under simple microscope

The curves in **Figure 3-75** follow a similar progression with the change in size as the other electrodes. The value of impedance for an electrode of 600  $\mu\text{m}$  in diameter, measured at 1000 Hz is approximately 7 k $\Omega$ . While it is higher than highly conductivity noble materials like Au (1400-1700 ohm), and Pt (1778 ohm), it is significantly lower compared to the samples with bare BDD fabricated by the team previously. This value is a result of surface roughness present in the BDD electrode stemming from the Diamond growth arrangement used in the ESIEE-Paris cleanroom. The sample with 30  $\mu\text{m}$  showed 32.26% RSD, the 60  $\mu\text{m}$  sample 34.57%, the 100  $\mu\text{m}$  samples 32.5%, the 200  $\mu\text{m}$  sample 22%, the 400  $\mu\text{m}$  samples 24.37%, and the 600  $\mu\text{m}$  samples showed 19% RSD when 6 different samples were taken into consideration.

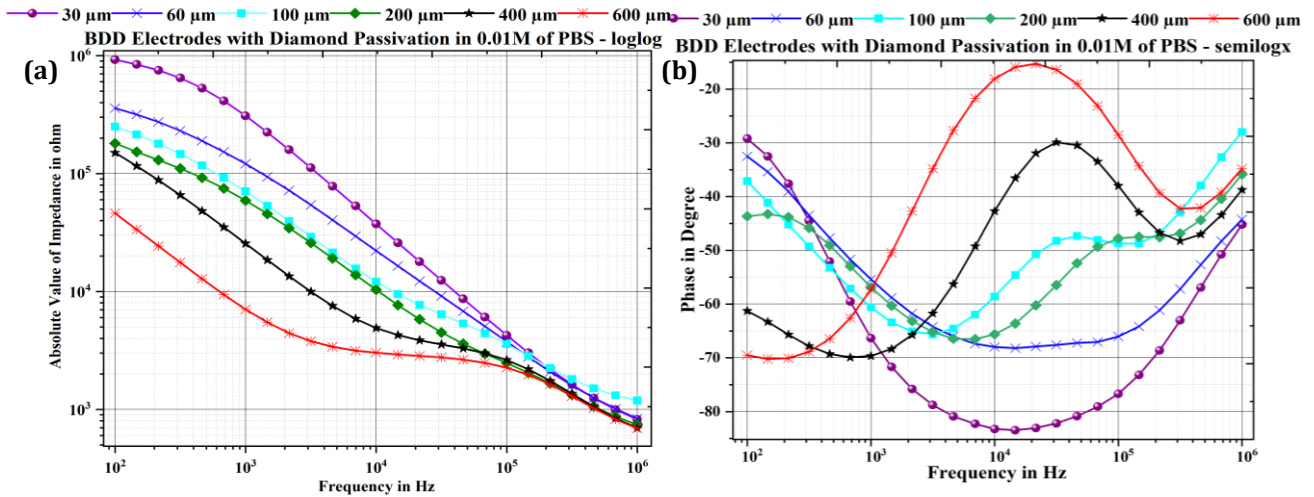


**Figure 3- 69** (a) Absolute value of impedance, (b) phase of Diamond electrodes with intrinsic Diamond passivation

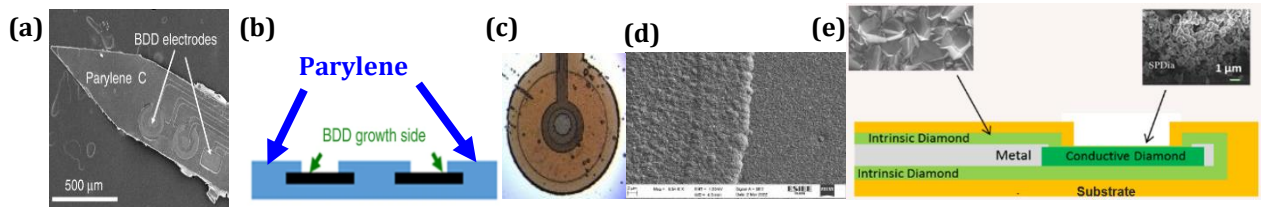


**Figure 3- 70** (a) SEM image, and (b) schematic view of the BDD electrode on Parylene in literature [108], (c) BDD electrode of the same size seen under a microscope, (d) SEM in ESIEE-Paris cleanroom, (e) schematic view of the BDD sample used in the thesis

To analyze the result, the impedance of the samples (see **Figure 3-70 (c), (d), (e)**) was compared to the results of a team with Bin Fan et al. (see **Figure 3-70 (a), (b)**) published in 2020 on Diamond based flexible electrodes [108]. The comparative result is shown in **Table 3-12**, where the value can be doubled to 10 times bigger than the impedance found in this thesis, which makes the samples a better candidate for recording applications while having the same size.

100 $\mu\text{m}$ BDD Electrode	Literature Value (k $\Omega$ )	Experimental Work (k $\Omega$ )
<b>Recorded Impedance at 1 kHz</b>	207.9 -1123.8	111.34

**Table 3-12** Comparison of the performance of the BDD sample of 100  $\mu\text{m}$  with literature

The sample mentioned in the literature does not have a passivation layer and is fabricated on Parylene. The lower impedance of the full Diamond electrode fabricated by the team proves it to be a better candidate for recording applications. The value measured at 1 kHz

mentioned in the literature (see **Table 3-12**) is higher than that of the performance of the sample tested in this thesis. To conclude, the sample characterized in this thesis is more suitable for recording applications for samples of the same size in existing technology [108].

### 3.6.6.2 Fit Parameters

Same as the black TiN, due to the presence of a rough surface, it was necessary to employ a circuit with 2 constant phase elements for the results to be explained and the fit parameters to be in accordance with the experimental data.

In this part, the table with the extrapolated data is not given in a table, because the more the number of the components increases, the harder it becomes to say which values are stemming from a specific component, as was done in sections mentioned before.

For example, **Figure 3-71 (a)** shows the same equivalent circuit that was used to model the experimental data and from the curve, it will be very prevalent that the fit curve matches the experimental result. However, as a rule of impedance transformation this equivalent circuit may also be presented as [269],[270] shown in **Figure 3-71 (b)**, where the equivalent impedance of  $R_{\Omega}$  and the second branch of **Figure 3-71 (a)** (marked in red) is equal to the impedance of  $R_{\Omega 1}$  and  $Q_p$  component, where the  $Q_p$  part is derived from the substrate when submerged and the liquid itself.

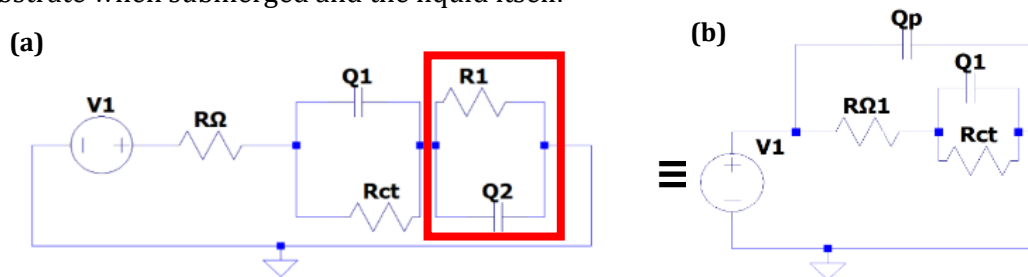


**Figure 3-71** Equivalent circuit (a) and (b) has the same equivalent impedance

Due to this impedance transfer rule, the tables are not presented further. Because due to the lack of a set equivalent circuit, the values are incomprehensible, However, it was observed that both these two circuits can yield fit curves that are very comparable to the experimental curve and have very little error (see **Figure 3-72**).

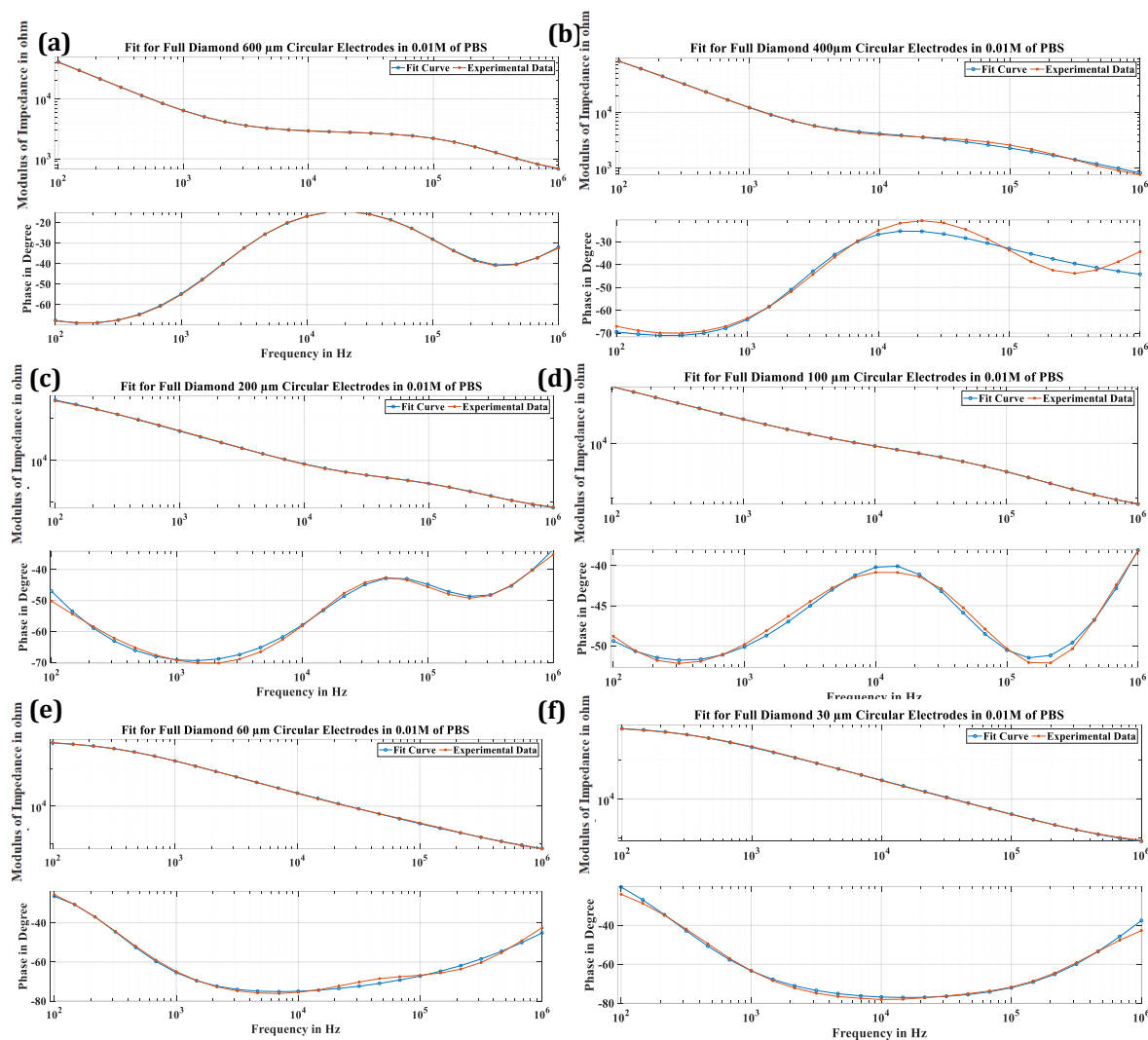


**Figure 3-222** Experimental data plotted against fit parameter; blue curve – fit data, red curve – experimental data (a) 600  $\mu\text{m}$ , (b) 400  $\mu\text{m}$ , (c) 200  $\mu\text{m}$ , (d) 100  $\mu\text{m}$ , (e) 60  $\mu\text{m}$ , (f) 30  $\mu\text{m}$  of TiN-pt-TiN electrode

### 3.6.6.3 CV of Full Diamond Electrodes

One of the advantages of Diamond is the wide water window or window of operation [271]. Compared to other materials, it has a larger window of nearly 3 V. In literature, it has been shown between -2 to +2 upon exchanging the range to achieve a 3-volt window [265]. **Figure 3-73** shows the CV for BDD samples with intrinsic Diamond passivation in different scan rates.



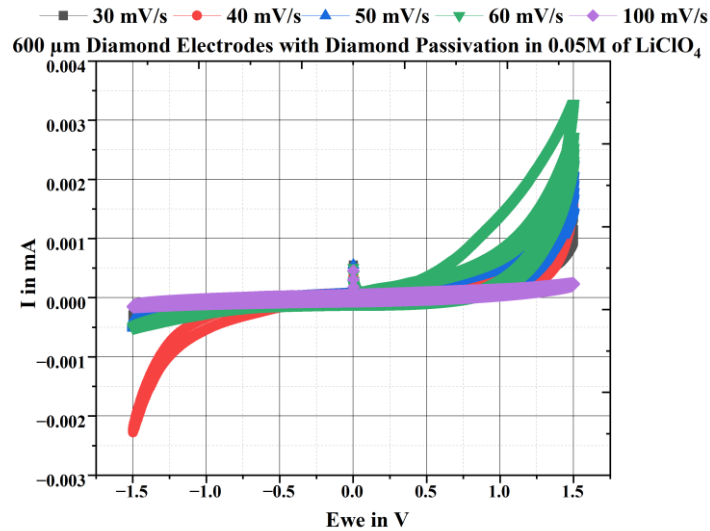


Figure 3- 73 CV performed for 600  $\mu\text{m}$  electrodes of different diameters

Diamond has gained popularity as a neurotransmitter material due to its wide potential window **Table 3-13** shows the specific capacitance of different materials and the values are lower than that of conventional materials like platinum and TiN.

Scan Rate (mV/s)	40	60	100
Specific Capacitance, $C_s$ ( $\text{Fg}^{-1}$ ) at 600 $\mu\text{m}$	10.24	9.50	1.71

Table 3-13 Comparison of the specific capacitance at different scan rates

The graphs presented here have a lot of close data points hence the congested look. The table shows the specific capacitance at different scan rates and the values go down for all the scan rates [265], [272]. The thin hysteresis loop of the CV curve proves the reversibility of the operation. The specific capacitance is measured at  $1.5 \times 10^{-5} \text{ F/cm}^2$  for a sample of 600  $\mu\text{m}$  in diameter at the diameter of 100 mV/s. The specific capacitance is lower than bare Ti, bare TiN, and TiN alloys as presented in the literature [46], [259]. The specific capacitance is also lower than the TiN-Pt-TiN stack model explored in the thesis. The specific capacitance is important for stimulation application. However, the specific capacitance is still in the range of acceptable value for the requirement of stimulation application (which is 10  $\mu\text{F}$  for an area of 1  $\text{cm}^2$ ) [273].

### 3.7 Different Cleaning Methods

Figure 3-74 shows the effects of different cleaning methods used in the cleanroom. The cleaning methods are already discussed in the previous chapter (see Section 2.4). As mentioned before, right after fabrication, due to the small structure of the microelectrodes and the characterization experiments, the structure deteriorates over time.

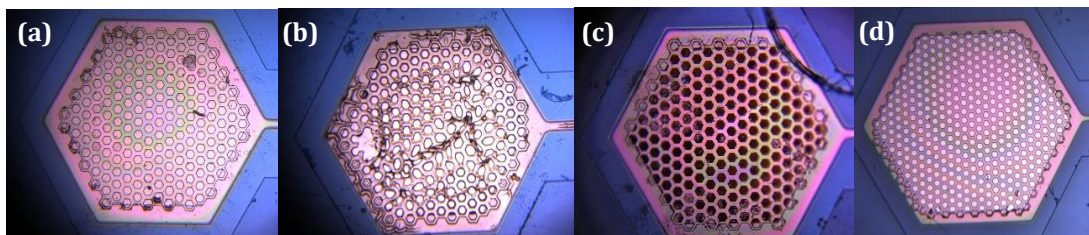
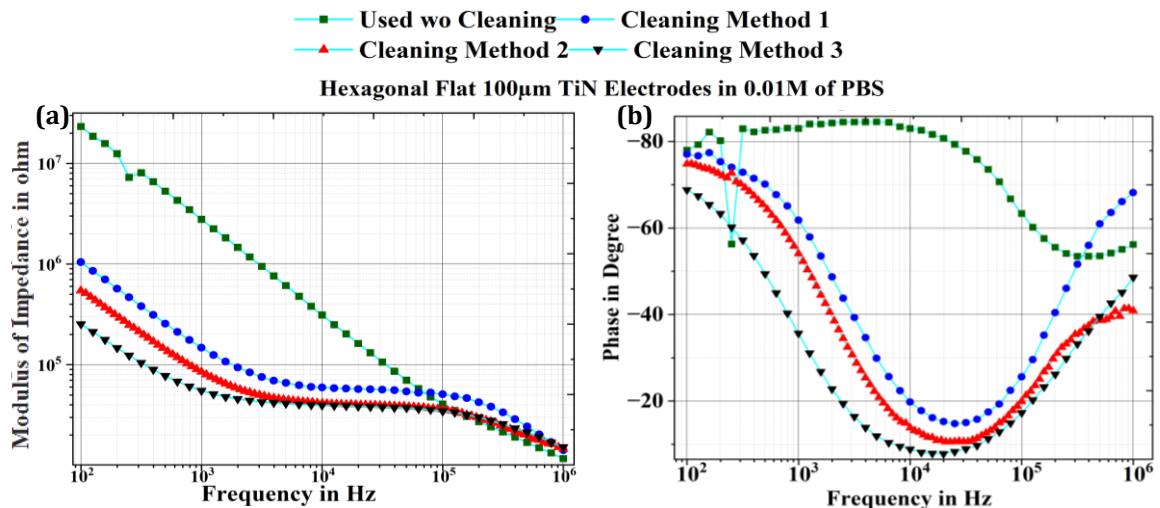


Figure 3- 74 (a) Samples right after fabrication without any cleaning, (b) samples after using once and cleaning with cleaning method- 1, (c) samples after using once and cleaning with cleaning method- 2, (d) samples after fabrication and using the cleaning method-3

After doing impedance spectroscopy, it was clear that the samples showed the best result in terms of impedance, when using cleaning method 3, without increasing the capacitance a lot. However, moving forward, during fabrication different electrode treatments had to be done for different materials. There is no “one method that fits all” when it comes to electrode treatment, and post-fabrication, in order to get better results.

In the beginning, when different cleaning methods were implemented to figure out which one was the best cleaning method - 3 (cleaning with H<sub>2</sub>SO<sub>4</sub> right after fabrication) demonstrated the best result (as it yields the least amount of impedance and smallest capacitance, as is ideal for implants (see **Figure 3-75**). However, it was proved to be not the safest for the surface integrity of all the samples (see **Section 2.4**).



**Figure 3-75** Effect of cleaning in (a) impedance, (b) phase measurement

### 3.8 Take Away from This Chapter

This chapter presented the results of most of the electrochemical experiments and characterizations done in different samples. It was observed that the samples show results that are in accordance with the established result. It is also encouraging that, when compared with the simulation result, the samples present the same trend as the one in the simulation.

Intrinsic Diamond shows great promise as a coating material by showing a capacitive response when used in IDE. This chapter shows the performance of IDE with intrinsic Diamond as a passivation layer and their capacitive nature when the sample is in air. There was an issue when the samples with Diamond passivation were put in a liquid medium. Those issues were mitigated at the fabrication level by making them hydrogen-terminated in the cleanroom. In the following chapter, the performance of the intrinsic Diamond as a passivation layer over an extended period is tested.

The samples made with gold were used mainly to determine and build a reference for all the samples going forward and later the platinum samples were characterized.

In terms of result, the impedance of the samples is compared at 1 kHz (due to the action potential being 1 ms). The approximate values of impedance of 600 µm electrodes at 1000 Hz are: Au shows 1400-1700 Ω, Pt shows 1778 Ω, TiN-Pt-TiN stack electrodes shows 1800 Ω, and the slightly smaller hexagonal electrode (long diameter 600 µm) with black TiN shows 10 kΩ. The smaller impedance of novel full Diamond samples compared to literature (111 KΩ for 100 µm sample at 1 kHz in experiment, 207.9 -1123.8 KΩ in literature), which makes it good for neural recording application [108]. The impedance of the TiN-Pt-TiN

stack model is  $10.79 \Omega/\text{cm}^2$  when it is measured at 1 kHz in an electrode of  $600 \mu\text{m}$  diameter. This value is lower than the value of the black TiN electrode. The impedance of the black TiN electrode is  $46.653 \Omega/\text{cm}^2$ . The value can be lowered by the use of a stack model and therefore lower serial resistance. When compared to the literature, the impedance of a  $100 \mu\text{m}$  diameter Boron Doped Diamond electrode is calculated at  $111.34 \text{ k}\Omega$  which is 10 times lower than that mentioned in the literature [108].

The specific capacitance of the TiN-Pt-TiN stack models ( $35.4 \times 10^{-3} \text{ F}/\text{cm}^2$ ) is bigger than bare Ti, and in the same scale compared to the literature value of the specific capacitance of TiN/Pt-Ir alloys, Platinized Ti [259]. The specific capacitance of the full Diamond electrode is a bit smaller than the stack model ( $1.5 \times 10^{-5} \text{ F}/\text{cm}^2$ ), However, still in the range of acceptable value of operation for stimulation operation.

In the case of the fit parameters, to achieve an advanced and accurate understanding of the rough surface electrodes, a more complex model should be used, which would give access to the specific values of the characteristic parameters of the samples.

The target of both the black TiN and the TiN-Pt-TiN was to reduce the serial resistance of the TiN samples. This chapter demonstrates that gold is the best conductive material, i.e., has the smallest impedance per  $\text{cm}^2$ , whereas BDD has better charge injection than a lot of other conventional materials, and black TiN has lower impedance and better charge transfer capacity compared to the reported value of TiN. A lot more comparative searches and tests were done as a part of the thesis. Only a selected few were presented to demonstrate a global idea of the study.

## **Chapter 4**

### **Longevity Test**

The advancement of technology and materials science has paved the way for the development of new and innovative materials for various applications, including in the medical field. Interdigitated Electrodes (IDEs) are one of the important concerns in the development of advanced materials, particularly in applications related to human health and safety [139], [274]. The longevity and stability of materials in various environments, such as the human brain, are crucial factors in determining their suitability for use in biomedical applications.

To understand the effects of IDE on the longevity of intrinsic Diamond as a passivation material inside the human body, a study was conducted to investigate the aging of BDD samples with the intrinsic polycrystalline Diamond passivation layer. The samples in question were placed in PBS at approximately 77°C Degrees Celsius to accelerate the aging process by 16 times as per the law of Arrhenius also mentioned as the 10°C rule in literature)[275], which would help predict the evolution of the performance of the samples over extended periods.

The Arrhenius law states that the aging process increases twice for every 10°C increase in the temperature, and thus, the high-temperature environment simulated the aging process in the human brain, and the data was collected using an electronics setup with Analog Discovery 2 by Digilent and a homemade multiplexer. The simultaneous data collection over an extended period in four different ports allows simultaneous and automatic data storage to understand the aging process and the effect of IDE on the stability of the material. The data collected through impedance spectroscopy provided us with the electrical properties of the samples, such as resistance and capacitance, and allowed the observation of changes in the material over time.

## 4.1 Introduction and General Purpose of Ageing Tests

In literature, some of the major problems with existing retinal and neural micro-scale implants are hermiticity issues, mechanical failure, inability to record/stimulate at the same scale as the retinal cells, degradation of performance, or rejection of installation [276], [277], [278], [279]. To that end, the implants must survive for a long time inside the human body [280], and testing the viability can be done by mimicking the human body or by employing Arrhenius law by accelerating aging and observing their evolution [281]. Some of the implants reportedly hold up their stable performance for around 5 years in the human body or the equivalent of accelerated aging tests.

The main criteria of an optimized implant have already been discussed in detail (*see Section 2.1.1*). This chapter deals with observing the durability of the IDE while they are put on heat to accelerate the aging process. The extreme shift in impedance is proof of the physical degradation of the capacitive plates covered with a passivation layer. Impedance spectroscopy is a powerful technique that provides information about the electrical properties of a material, including resistance and capacitance (*see Section 3.1.1*). To that end, IDEs made with TiN-Pt-TiN stack model covered with intrinsic Diamond passivation are put to test and compared to the result of the ones with SU8 passivation.

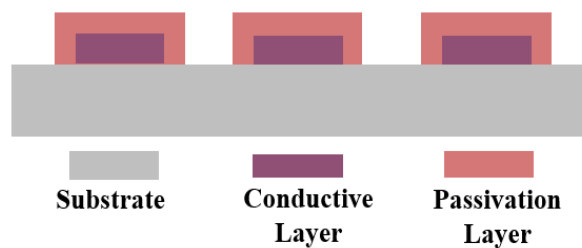


**Figure 4- 1** 2-D cross section of the IDE used for ageing test

SU8 is a photoresist material commonly used in microfabrication and microelectronics. While it has good mechanical stability, it has limited biocompatibility, physical durability, electrical insulation, and chemical stability compared to intrinsic Diamond. This can lead to potential adverse tissue reactions and degradation over time, which can impact the longevity and functionality of the implants [282].

Depending on the material used, due to the supple nature of the implant itself and the human body being in a harsh environment, there are records of performance degradation in various metals and polymers (*see Figure 4-2*) reported [283]. In this chapter, the focus will be on the passivation layer and its evolution with time to predict performance in chronic applications.

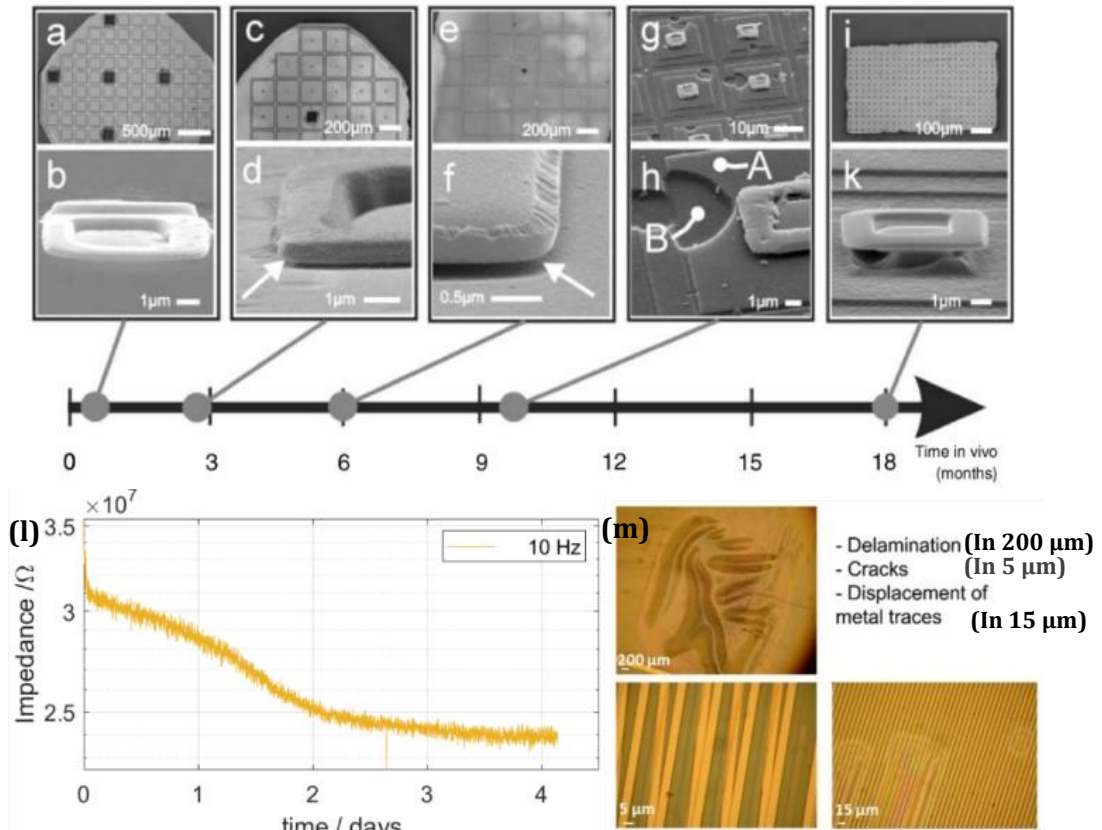


**Figure 4-2** Micro-structure analysis of MPDA explanted from animals after 3 weeks to 18 months, (l) Real-time monitored impedance (at 10 Hz) during a soak test at an elevated temperature of 70°C, (m) Microscopy images of different failure types of barrel-activated test samples in gold IDE with PI encapsulation, scale bar shown in each image [252]

The biostability of **Micro-Photodiode Arrays (MPDA)** was investigated in vitro and in vivo. No significant damage was found on chips immersed for up to 21 months in saline solution. Under in-vivo conditions, however, the *silicon oxide passivation layer* of the chip was dissolved within a period of about **6–12 months**. Subsequently, the underlying silicon was corroded. In contrast, stimulation electrodes consisting of titanium nitride were well preserved both in vitro and in vivo. **Figure 4-2 (a, b)** shows MPDA acquired from rabbits after 3 weeks. No morphological damage is observed. The integrity of the passivation layer is confirmed by the micrograph showing a homogeneous green interference color. **Figure 4-2 (c, d)** shows MPDA explanted from rabbits after 2.6 months. Light microscopy reveals laterally inhomogeneous interference color indicating the beginning corrosion of the passivation layer. SEM micrograph shows a gap between the rim of the electrode and the passivation layer. **Figure 4-2 (e, f)** shows MPDA explanted from micro-pig after 6 months. At the periphery of the chip, the passivation layer is almost completely removed. The originally green color which is indicative of a thickness of the oxide of 500 nm has turned to blue or violet and exhibits strong lateral variations in its appearance on a typical length scale of 20–100 nm. **Figure 4-2 (g, h)** MPDA explanted from rabbit after 10 months. The passivation layer is completely dissolved and pit corrosion to the underlying silicon is observed. 6h indicates the location of EDX analysis. **Figure 4-2 (k, l)** MPDA explanted from a rat after 18 months. Progressive corrosion of silicon is observed. In contrast, no sign of morphological damage is found on the electrodes indicating the biostability of titanium nitride [284].

In **Figure 4-2 (l)** the delamination of the IDE made with gold with polyamide passivation, and in **Figure 4-2 (m)** there are different kinds of failure noticed due to the delamination of gold and passivation layer.

The advantage of polymer-based neural interfaces is the possibility of reducing damage to the tissue and protecting interior signal tracks against ionic body fluid [47], [285]–[291]. The use of various polymeric materials (e.g., polyimide (PI) or Parylene C) is often reported in the literature for the fabrication of flexible neural probes [292]–[294].

Parylene C (FDA-approved material) has been established as one of the encapsulation materials for chronic implants due to the aforementioned properties and due to its approval as material for unrestricted use in implants. Its advantage is the deposition technology at room temperature that does not interfere with connection and assembling technologies [131]. However, it is not stable for a long time due to the *migration of water on it and the swelling* of the sample.

Liquid crystal polymers (LCPs) represent a separate material class among the polymers. It was supposed to be the next best thing in the domain of neural implants. However, because of not yield a better result than all the other polymers available, researchers are not too eager to explore these polymers as a means to create encapsulation in vivo or the human trial [108].

Intrinsic Diamond is currently approved by the Food and Drug Administration (FDA) to be used as biological implants [295]. In **Figure 4-3** results from Boron-Doped-Diamond (BDD) electrodes combined with a PI polymer. This result is from an experiment that was done with the research team at ESYCOM, previously to show the stability rate of Diamond as electrode.

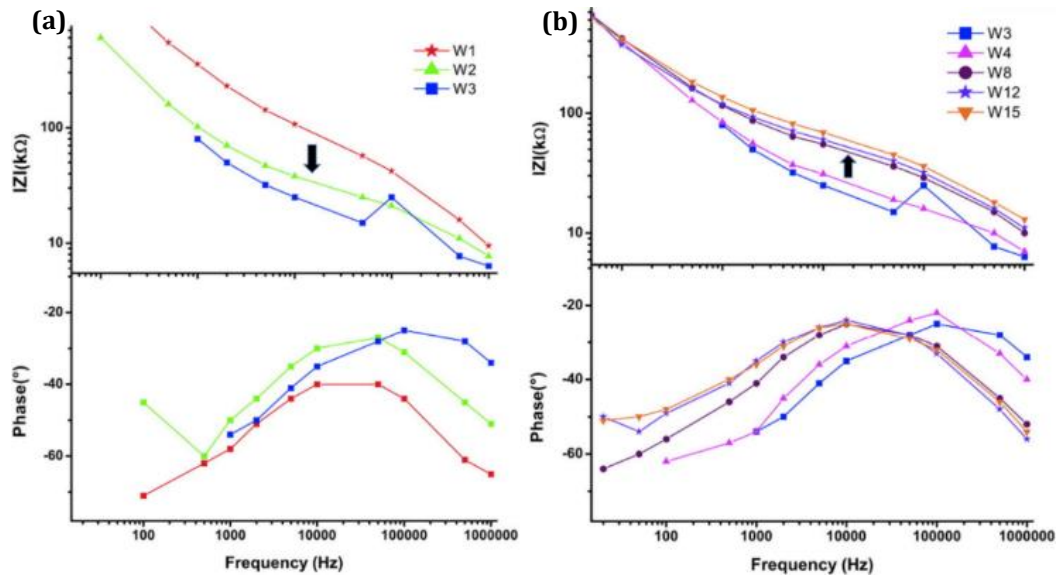


**Figure 4- 3** Bode representation of the impedance spectra recorded in vivo on 30  $\mu\text{m}$  BDD electrode at (a) 1, 2, 3, (b) 4, 8, 12 and 15 weeks [275]

The implants were thus inserted in vivo on the rat retina in the subretinal position. During the first weeks, the impedance decreases because of the resorption of the gel used to place the implants in the sub-retinal position as discussed in [296]. Indeed, **Figure 4-3(a)** demonstrates the first decrease of the impedance during the three first weeks. Once the implant is fully engulfed by the tissue, a resistive plateau appears, and its magnitude increases rather slowly over the following weeks (*see Figure 4-3(b)*). This latter is between 10 kHz and 50 kHz and ranges between 20 kΩ and

350 k $\Omega$ . This new component is due to the progressive adhesion of the retina onto the implant [297]–[299]. The recorded magnitudes are in good agreement with the results already observed or simulated in the literature on electrodes that did not undergo passivation with a gliosis layer [297]–[299]. Interestingly these figures are far smaller than the 2.8 M $\Omega$  reported on cortical implants [296]. The results show that the samples have more durability compared to the samples made with polymers as mentioned before (PI and Parylene C).

In conclusion, the choice of material for passivation is as important as the conductive material and is dependent on the specific requirements of the application. Once installed, the optimum functioning of the electrodes inside the human body over a long period, and carrying out chronic data acquisition/data transfer are some of the major requirements when it comes to neural and retinal implants (*see Section 1.3.2*) [300].

### 4.1.1 Ageing Test Set-Up Description

The neural and retinal prosthesis placements are invasive procedures and more often than not, the implants are required to function for 10 years to lifetime and collect data 24/7 for 10 hours or more every day. So, the ideal case scenario is placing an implant and ensuring the uninterrupted, smooth functioning of it until the implant is no longer required. While nowadays there are possibilities of non-invasive implant placement without craniotomy [301] on a very small scale, the possibility of post-placement complications remains an issue. Even while doing the experiments in vivo the rats are reported to become exhausted after multiple surgeries and need to be euthanized, which is not ideal. Maintaining the integrity and the performance of the implants over a long period is imperative in any case [302], [303], [32].

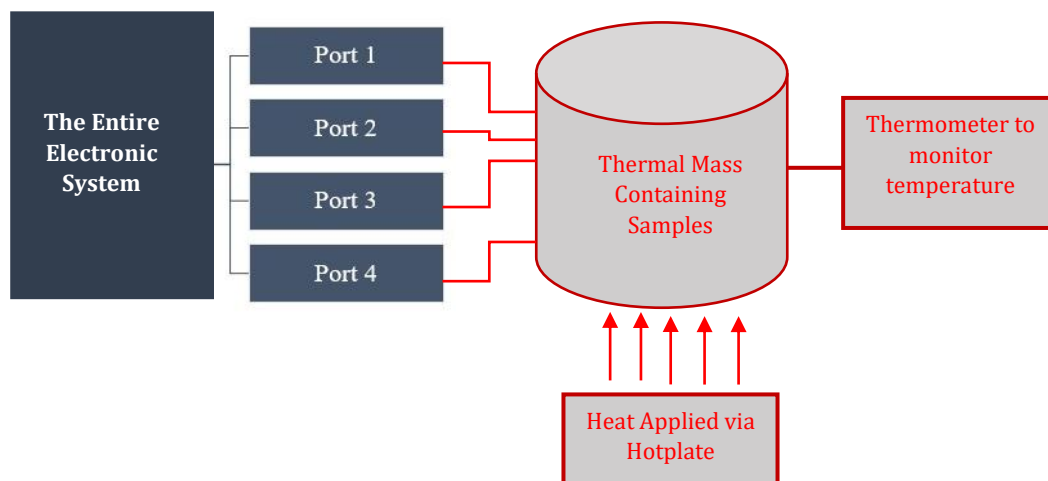
With that in mind, it was critical to establish a protocol to ensure the longevity of the samples before going to the in-vivo experiment in order to avoid or reduce animal testing. To that end, along with the fabrication and optimization process, there was also an ongoing project to find a setup that would successfully provide chronic data acquisition.

A hunt for a system began which would verify the performance of the samples with continuous experiments and tests. To simulate a sped-up process of chronic data collection putting samples on heat has gained major traction in recent years .

To test the durability and performance over time of the passivation layer, samples are submerged in 0.01M of PBS while set on heat. Increasing the heat over 37°C accelerated the speed-up aging of the samples. A well-established aging set-up not only mimics the same environment to ensure the same outcome of successive data collection in living test subjects However, also allows observing and predicting the progression of the sample over a long period, in a short time. **Figure 4-4** shows the schematic diagram of the functional setup for the longevity test.

Here the left part of the schematic (blue color) shows the electrical part and the right part of the setup (grey and red color) shows the thermodynamic part of the setup. The right part is composed electronic part to follow the evolution of samples. To check the integrity of the sample we measure impedance regularly from 100 Hz to 10 MHz. We can adjust the delay between two measurements. The left part contains a thermal management system and samples placed in PBS.





To achieve reliable measurement with the long-life setup, an important step was making a hermetic setup where the electrodes would be kept at a constant temperature to increase the effect of heating for a long period. A very well-established approach is to assume that the rate of aging is increased by a factor of  $2^{\Delta T/10}$ , where  $\Delta T$  is the temperature increase.

This result is a mathematical expression of the empirical observation that increasing the temperature by about 10°C roughly doubles the rate of aging of the substance used. So, the experimental set-up was kept at a constant heat of 78°C which would lead to an overall increase of **16 times the rate of aging**.

#### 4.2.2 Automatic Data Collection with Analog Discover 2

Automatic data acquisition is done by a homemade multiplexer with 4 connection ports along with AD2 (see **Figure 4-5 (a), (b)**) was used to do an automatic periodic data collection over any duration (in detail in **Section 3.2.5**). There are four ports for samples that were connected to them for continuous data collection. This automation part is highly required because measurements would last for a long period

**Figure 4- 4** Schematic diagram of the experimental setup. The left part - blue represents the electronic part and the right side - grey and red represents the thermal part of the experimental setup

(continuously running since August 2022), and it is impractical to do them manually.

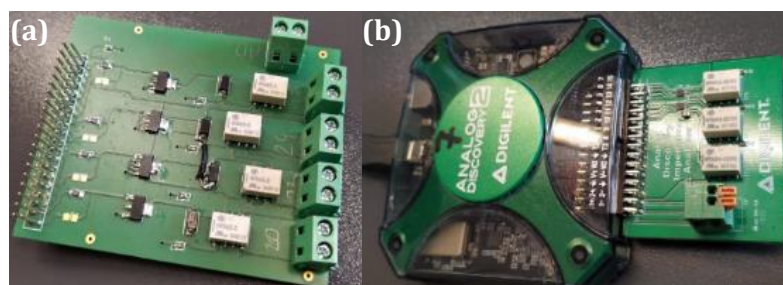


**Figure 4- 5 (a)** Homemade multiplexer and **(b)** Analog Discovery 2

The program was set to collect data (impedance and phase on frequency range: 100 Hz to 10 MHz) from all 4 ports of the multiplexer (see **Figure 4-7(a)**) at 1 hour of intervals and store them in the Raspberry Pi connected to it (see Figure 4-6). There is a

computer monitor connected to it to gather the data from the Raspberry Pi and analyze it further.

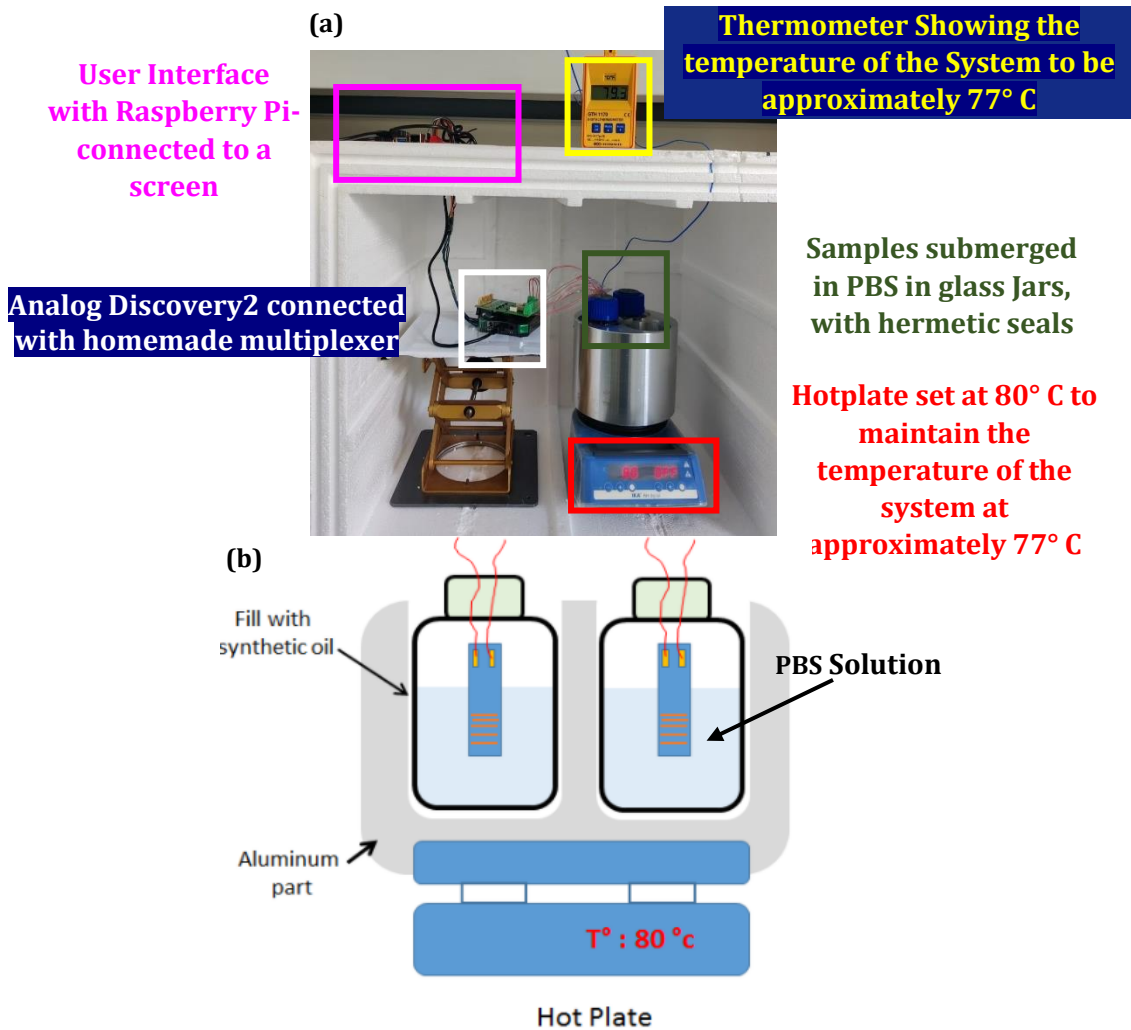


**Figure 4- 6** (a) Long-life setup for testing the electrode on heat, (b) schematic representation of the setup

**Figure 4-6 (a)** shows the whole system placed inside a Styrofoam box, which is closed from 3 sides to minimize the possibility of air interruption to the experimental setup. It is possible to close the box, to make it the least susceptible to air, wind, and possible displacement due to other movements. **Figure 4-6 (b)** shows the schematic representation of the system.

## 4.2 Preparing Samples

The first step was to test IDE structures and check their integrity before placing the samples on a long-life setup. For this, commercial equipment HP4194A Impedance Analyzer was used. This measurement is followed by specific packaging to install the implants into a long-life set-up. Mechanical characterization and SEM pictures are also taken before starting experiments.

### 4.2.1 Impedance measurement

The first step of verifying the model was always testing the samples using the HP4194A Impedance Analyzer to have a reference of the integrity of the samples' performance. To begin with, some samples were chosen. The samples were IDE with 25 and 50 pairs of fingers with Diamond Passivation, and IDE with 50 and 100 pairs of fingers with SU8 Passivation. The conductive part of the samples was made with TiN-Pt-TiN stack models. For placement in the long-life setup, the samples were mounted with wire instead of a replaceable PCB (see **Figure 4-7 (a)**). The samples were all verified both in the air and on PBS to see if they followed the performances as expected (see

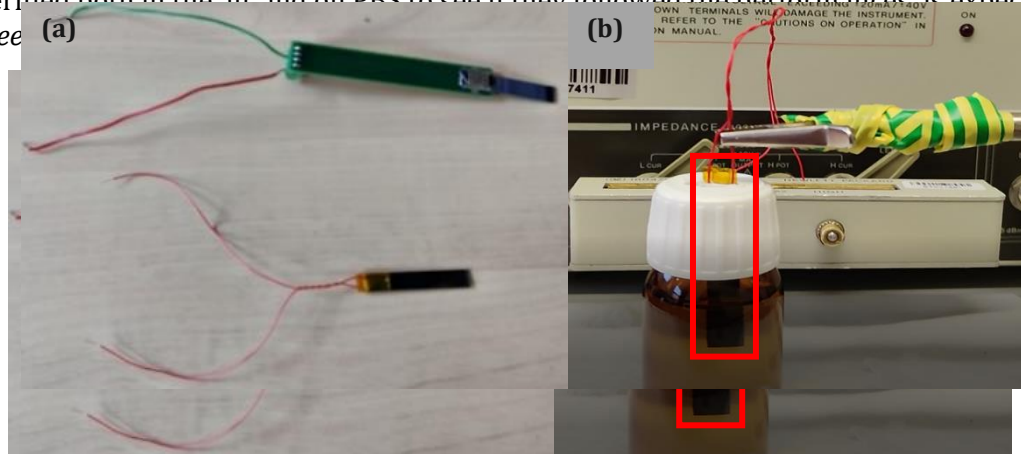


**Figure 4- 7** (a) Samples with PCB and wire, (b) manual data collection with HP4194A; the samples are made stable to avoid perturbation during data collection

To create a reference of the performance of the samples all the samples were tested using HP4194A both in air and liquid (see **Figure 4-5(b)**). And the result of IDE-50 Diamond passivation is presented in **Figure 4-6 (a, b)**.

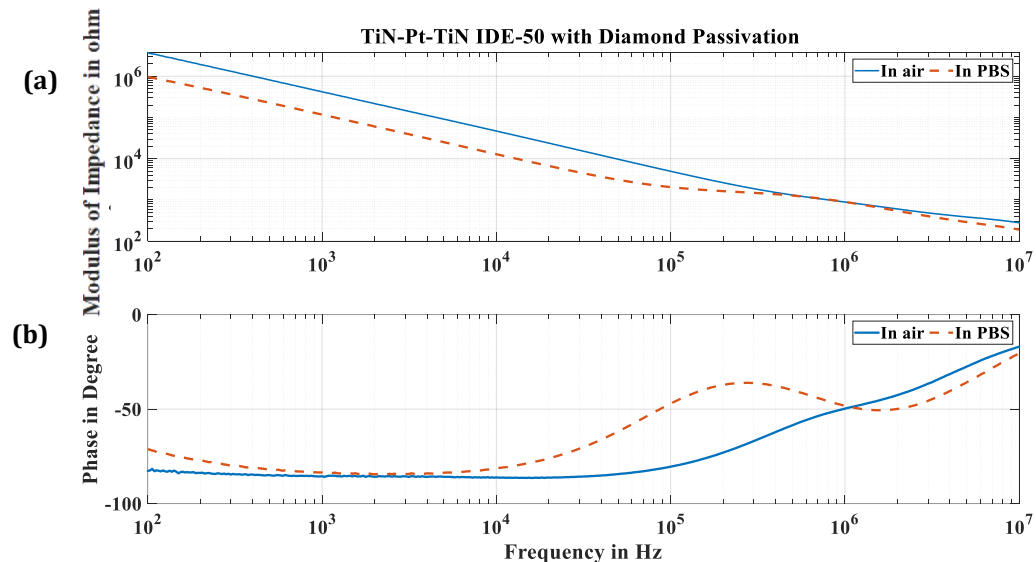
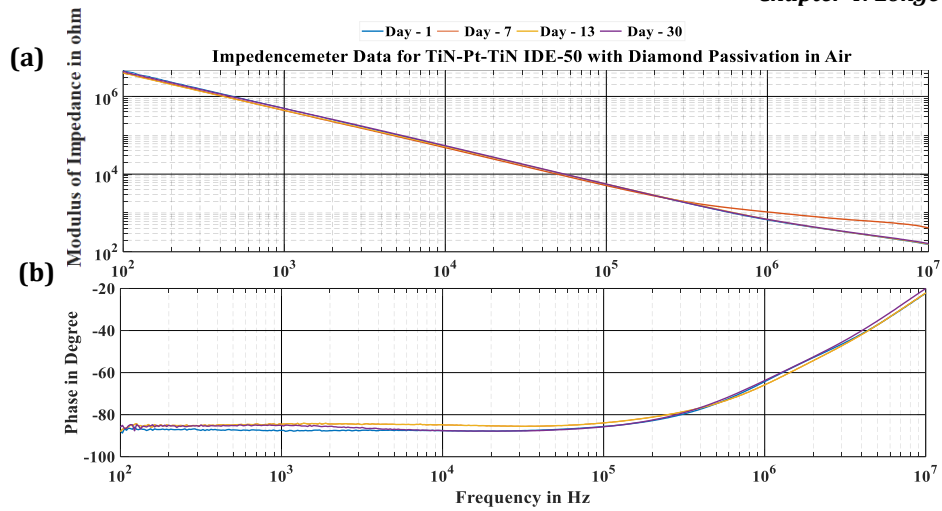
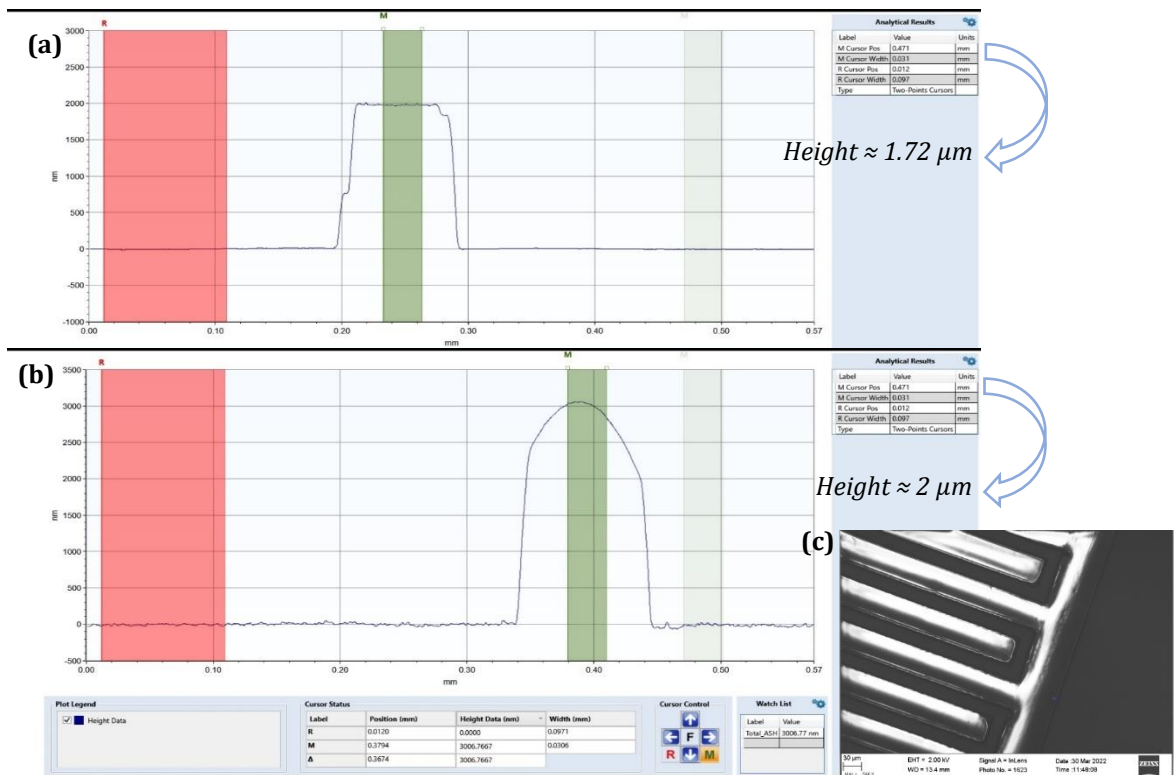


**Figure 4- 8** Diamond samples before being placed on heat, data using HP4194A (a) impedance, (b) phase

The general result of these types of samples was already discussed in detail (see **Section 3.4**). Simply having a simple idea verification via phase is the easiest way before the samples are compromised in any way and they usually show purely capacitive response (see **Figure 4-6**).



As previously mentioned, before putting them in the longevity test setup the samples were tested under a mechanical profilometer DektakXT Stylus in ESIEE Paris Cleanroom to verify the height of the passivation layer in both types. **Figure 4-10 (a,b)** shows the thickness of the passivation layer was measured on both the Diamond and SU8 layers. **Figure 4-10 (c)** shows the sample seen under SEM.



The height of deposition for the TiN-Pt-TiN layer ranges around 900 nm. Over that layer SU8/intrinsic Diamond passivation layer is desired. The height of the intrinsic Diamond is measured at 1.72  $\mu\text{m}$  (see **Figure 4-10 (a)**) and SU8 depositions are usually approximately 2  $\mu\text{m}$  high (see **Figure 4-10 (b)**).

### 4.3.1 Replacement of PCB With Wire

One of the primary steps of this setup was replacing the need to use a PCB to carry out the measurement. The samples needed to be fixed with the wire to be placed inside a hermetic environment. There needed to be a fixed connecting wire replacing the PCB. It was imperative that the wires would be connected properly, in order to maintain the performance, even after being on heat. To make the adhesion of the wire to the contact pad, first, the wires were covered in copper tape, then Kapton scotch, and then the whole contact area was encapsulated with PDMS for better hermiticity (see **Figure 4-11**) and the samples were ready to be inserted and put inside the heated, sealed off experimental environment (see **Figure 4-6**).

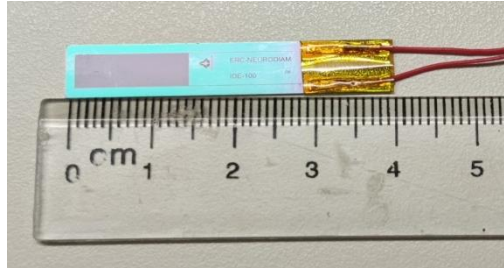


**Figure 4- 11** Sample connected to wire and contact encapsulated with copper scotch, and Kapton

Then impedance spectroscopy was performed with HP4194 (see **Figure 4-12 (a), (b)**) to verify the samples' performances before and after connecting the wires. This experiment was done to make sure there was no offset being introduced to the result due to the removal of PCB and the addition of long wires.

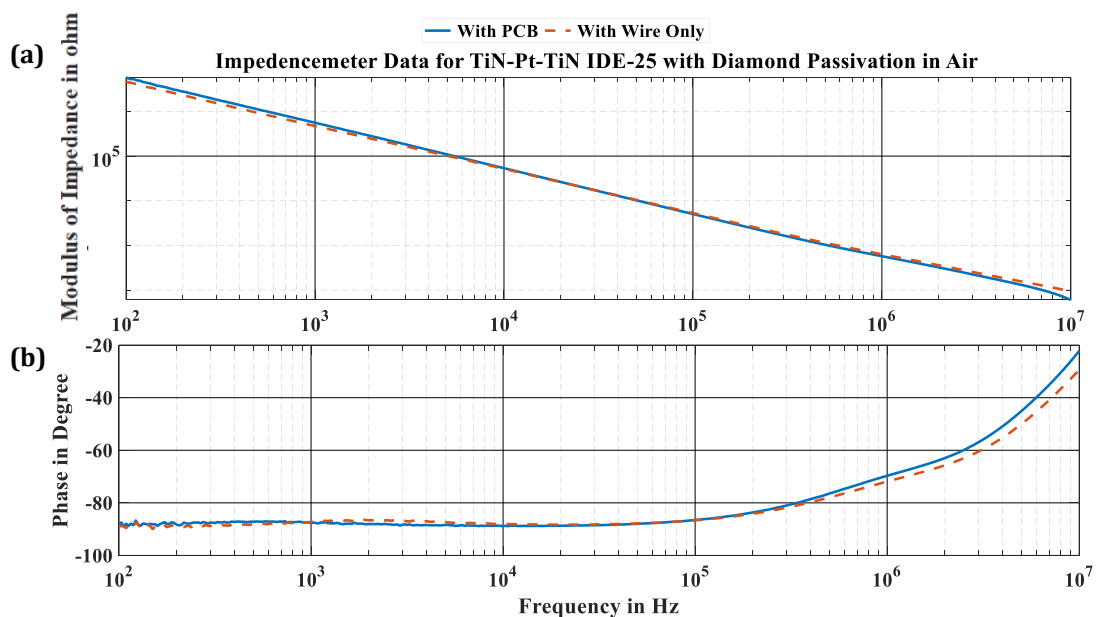


**Figure 4- 12 (a)** Impedance and **(b)** phase

### 4.3 Establishment of Experimental Protocol

The samples were put in a thick glass jar filled with PBS and the connecting wires were passed through some small openings made through the caps. Afterward, PDMS was poured into the gap to make the seal completely hermetic. In the middle, there was a

thermocouple inserted to keep track of the temperature inside the glass jars every step of the way. The glass jar was then placed inside a hollowed-out metal block and the block was filled with biological oil to ensure heat transfer all around. The metal block was then placed on top of a hotplate where the temperature was maintained at 80°C to achieve the temperature of the inside of the experimental environment at 78°C. There is a display for temperature connected to the thermocouple to keep track of the temperature every now and then to make sure that the temperature inside is constant. The whole experimental setup is shown in **Figure 4-6**, whereas **Figure 4-4** provides a short functional diagram of the system.

The system was observed continuously to check the smooth running of the electronics, proper data accumulation, and overall, no disruption. The jar shown in **Figure 4-13 (a)** contains 80 ml of 0.01 M of PBS and then the 4 samples were put in the seal that was closed off tightly and the glass bottle was put inside the thermal mess submerged in biological oil to ensure good heat transfer. Subsequently, the block was put on a hotplate heated at 80°C to maintain the heat of the inside at around 78°C. The thermocouple (see **Figure 4-13 (e)**) placed inside the glass bottle was connected to an external manual thermometer to verify the stable temperature inside the environment. With this method connected strips showed more stable results over time and the result did not drift due to connectivity issues during experiments. This is the work that will be discussed in detail in the following section.

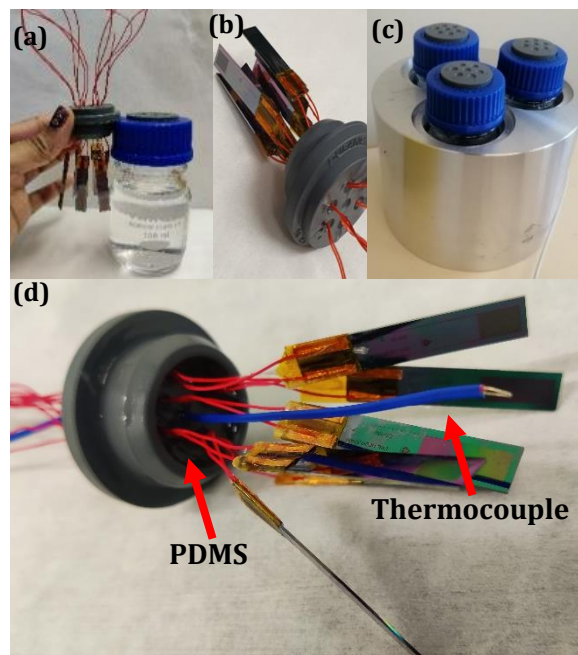


**Figure 4- 13** (a) the samples after attaching to the cap filled with PDMS, (b) the thermal mess and the glass jar placed in them and ready to be put on heat, (c) the caps with the samples and thermocouple, the red arrow shows PDMS poured inside the caps to make the system more hermetic (d) the samples in caps outside the glass jar that would be placed inside the thermal mess

### 4.3.2 Primary Experimental Protocol

The first encapsulation method required gluing the wire on a strip and then pouring liquefied PDMS around the Kapton scotch-covered part of the sample to make sure there was no water leakage inside the contact pad area. After installation, the data

observed from the setup showed a strong variation in impedance over the first 40 hours of the run time (see **Figure 4-14**).

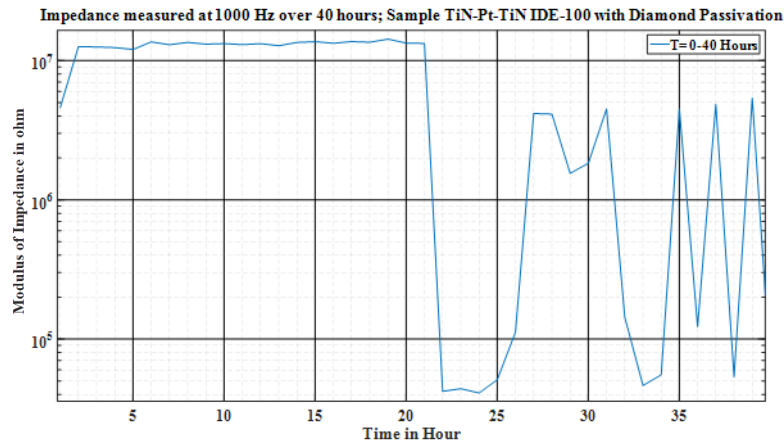


**Figure 4- 14** Drift in the result due to water leakage

The experiment was stopped, and the integrity of the samples was tested. It was clear upon observation that the error was due to the connectivity and packaging issues of the strips placed in the jar. Therefore, new and improved packaging was proposed.

### 4.3.1 Second Packaging for the Long-Life Experiment

Once the PDMS encapsulation failed, as the next step of the capsulation method, some caps of the same size as the samples were fabricated via 3-D printing, and then the samples were inserted into them. Then to make them more stable the surroundings were filled with EXPOXY Glue, and they were left overnight to turn solid. **Figure 4-15 (a, b, c)** shows the 3-D caps in the design layout, and **Figure 4-15 (d)** shows the 3-D caps installed around the contact pads and then around the caps PDMS was deposited again for better insulation.

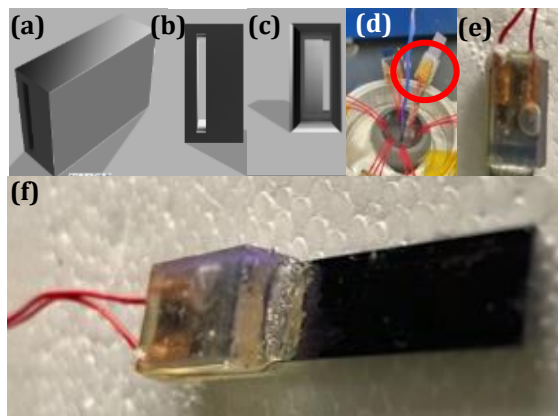


**Figure 4- 15** (a) Side, (b) front and (c) back view of the 3-D caps in the design layout, (d) the 3-D caps inserted and incapsulated in PDMS (red circle), (e)-(f) different views of the 3-D caps when the electrodes contact pads are installed inside

A new experiment was started. Upon verifying, it was quickly observed that even though the impedance did not drift, the liquid was dripping through the wire of the thermocouple and possibly through the misalignment of the cap of the jar as well (see **Figure 4-16 (a, b)**). So, the whole setup had to be dismantled and the thermocouple

was unmounted. A PDMS was poor on both sides of the wire of the thermocouple (head and on electrical connection) to avoid liquid going through the electrical sheath.

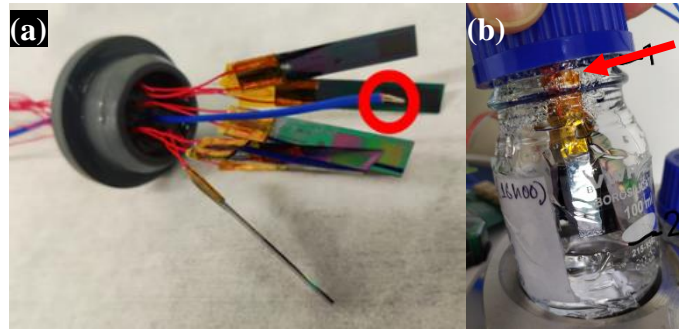


*Figure 4-16 Red mark shows the origin of non-hermeticity in a thermocouple (b) possible misposition of the cap, which also might have contributed to the reduction of the water level due to lack of proper insulation*

The whole setup was revised, and the latest experiment started with the same setup as shown in **Figure 4-6 (a)**. All the issues discussed above were solved and the whole system was placed inside a Styrofoam box, which is closed from 3 sides to minimize the possibility of air interruption to the experimental setup. When not observed the box can be closed with a Styrofoam cover creating an all-side closed box for the setup. The revised experiment was started in August 2022.

#### **4.4 Results of Long-Life Setup**

Upon the second installation on 02 August 2022, 4 samples were connected to 4 parts of the multiplexer. However, 6 samples are put on heat overall in a glass bottle. The results are shown where the samples were put on heat starting from  $T = 1$  week to  $T = 29$  weeks. It should be kept in mind that the samples are on continuous heat. So that increases the aging process of the samples is accelerated by 16 times [304] (As per Arrhenius law, explained in **Section 4**), which means the samples would suffer from the aging effect equivalent to 464 weeks (8.92 years  $\approx$  9 years). The data collected from the samples over time are shown in this section.



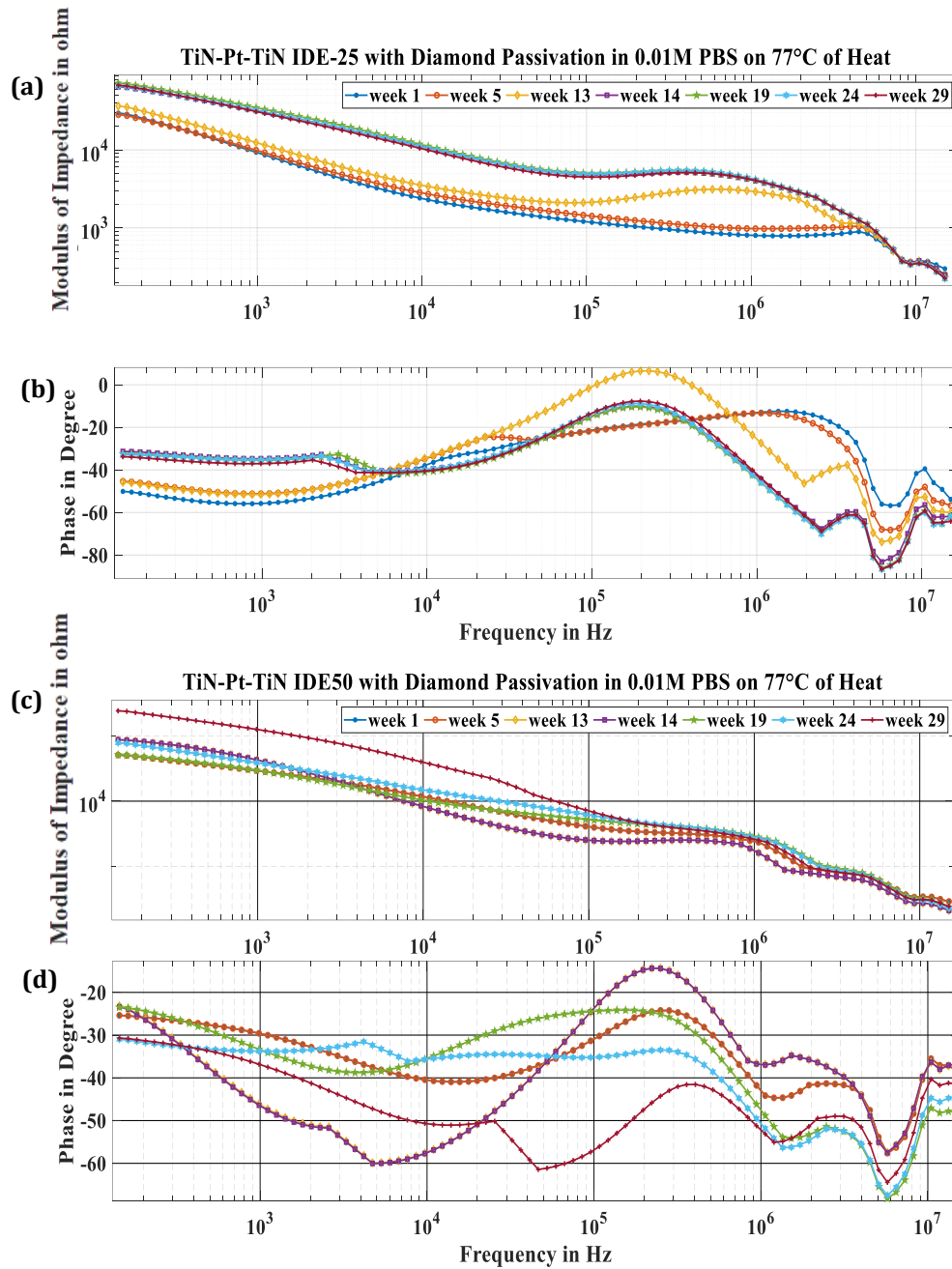


**Figure 4- 17** Data acquisition with AD2 from the samples with Diamond Passivation on heat (a) impedance, (b) phase of IDE with 25 pairs of fingers; (c) impedance, (d) phase of IDE with 50 pairs of fingers. Week 1 to 29 represent the time that the IDE is placed in PBS with temperature and week 29 is equivalent to around 9 years.

The first observation from **Figure 4-17** is that the value of the impedance and phase of the samples are not constant. It is known from the literature that the ohmic impedance slightly decreases as the temperature of the environment rises from 40°C to 80°C, However, increases rapidly when the temperature of the experimental environment rises to 90°C [305]. And during the run time of the experiment, the temperature never rose to 90°C. So, a slight change in impedance is expected and the phase also moves further away from -90° which means that the resistance changes. With the increase in temperature, the thermal conductivity of the liquid decreases, and hence the move of the phase from -90° (purely capacitive) towards 0° (purely resistive).

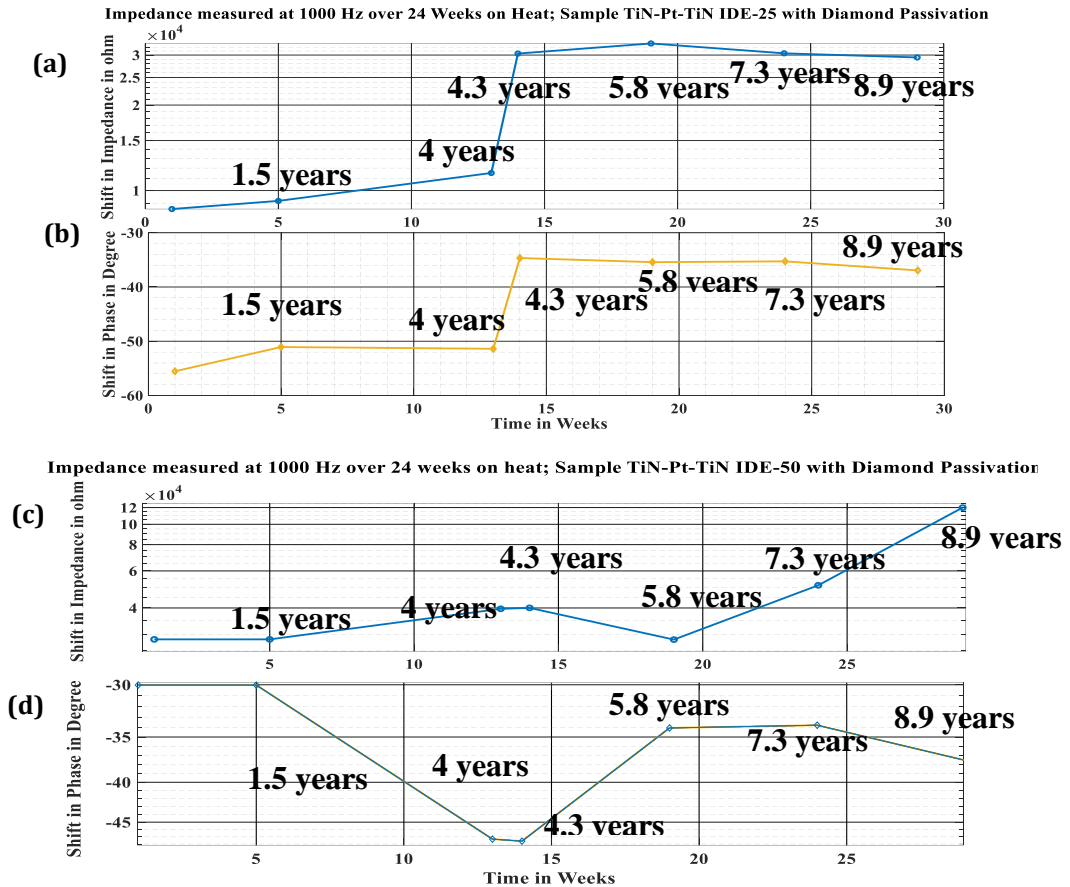


**Figure 4- 18** Trendline observed in samples' (a)impedance, (b) phase in IDE-25; (c) impedance, (d) phase in IDE-50 with Diamond passivation

As the temperature increases, some electrons of the semiconductor acquire energy and become free for conduction. Hence, resistance decreases with an increase in temperature [306].

In the case of impedance, there are also groups of responses, around the same time of the day, which might be the contribution of temperature change or perturbation around the experimental environment.

**Figure 4-18** shows the trendline of the change in terms of the accelerated aging process. The impedance was lower when the experience started. And after the equivalent time of 5 years, both samples demonstrated a sharp increase.

At the beginning of the experiment, when the samples were put on heat, it took some time for the result to become stable. So, in order to compare the percentage of increase in the result the impedance value was collected before starting the experiment using the HP equipment in 0.01M of PBS without putting those on heat.

For IDE-50 the change between the starting value measured in PBS (at 1000 Hz) and the value after 29 weeks ≈ 9 years is 2.2% and the change in the change in the value of the first week at the 29<sup>th</sup> week is 3%. The result is very encouraging and stable. In the case of IDE-25, the change before the experiment and after the equivalent of 9 years is 50%. It should be mentioned that the overall impedance of all the samples decreases right after putting them on heat due to the fast movement of atoms in the liquids that are brought up by heat. After the heat reaches a stable point, the increase in impedance is the result of the degradation of the sample. The values can be observed in **Table 4-1**.

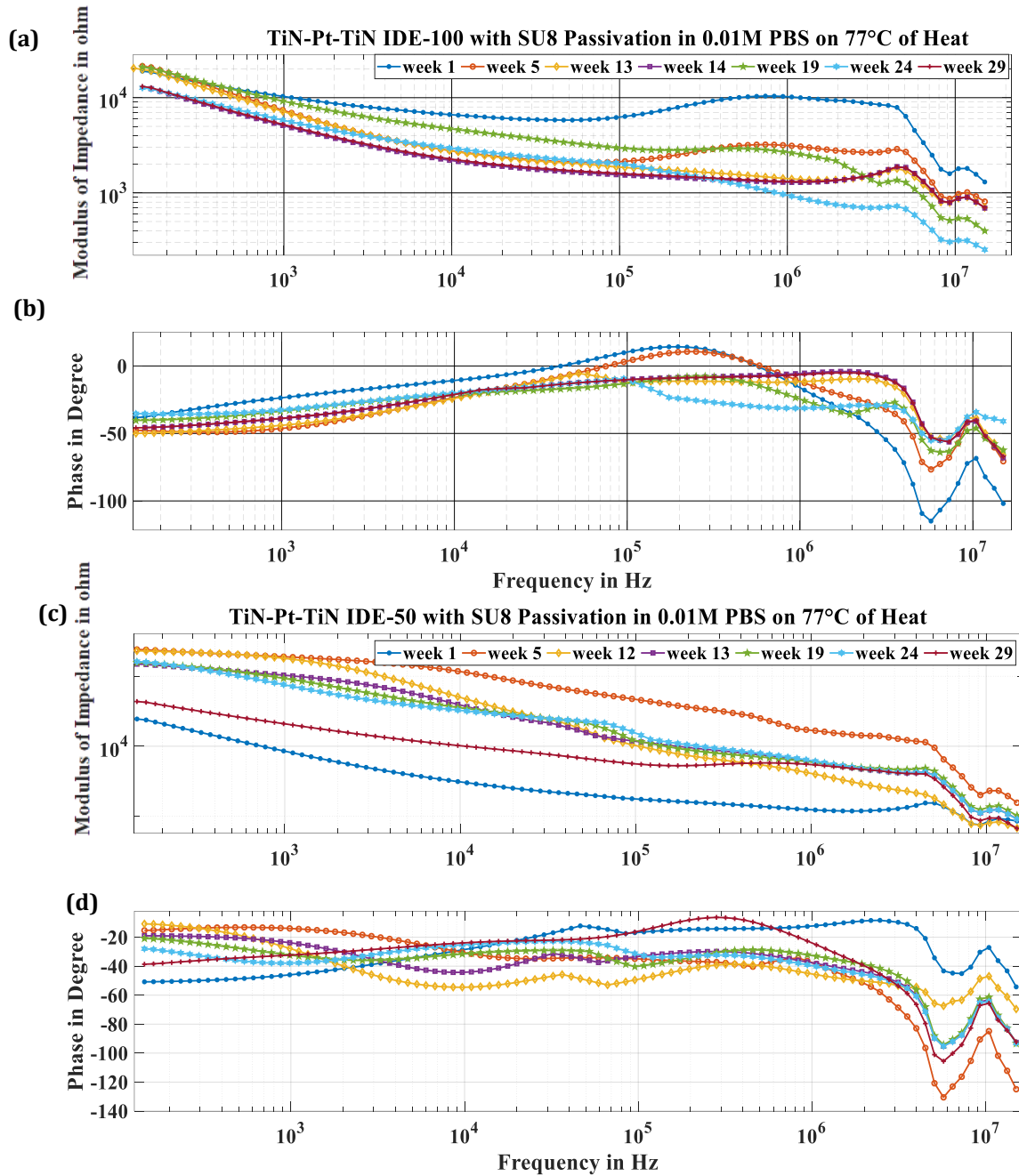


**Figure 4- 19** Data acquisition with AD2 from the samples with SU8 Passivation on heat (a) impedance, (b) phase of IDE with 25 pairs of fingers; (c) impedance, (d) phase of IDE with 50 pairs of fingers. Week 1 to 29 represent the time that the IDE is placed in PBS with temperature and week 29 is equivalent to around 9 years

While analyzing **Figures 4-19**, a similar trend is followed in terms of a decrease in impedance when the samples are put on the heat and an increase in phase values. However, it is observed from the results from the samples containing SU8 that, those do not just shift in between the range of operation ( $-90^\circ$  to  $0^\circ$ ), the results gathered from the samples containing SU8 passivation layers move beyond  $-90^\circ$  and goes up to  $-120^\circ$  in some cases. The impedance in the SU8 in general is more scattered compared to that of Diamond passivation samples. It is also noticeable that the change in the impedance does not follow a trend (eventual increase) like that of the Diamond samples. The overall shift (at 1000 Hz) in the case of the SU8-50 sample is 93% and for SU8-100 it is 97%, which can be observed in **Table 4-1**.

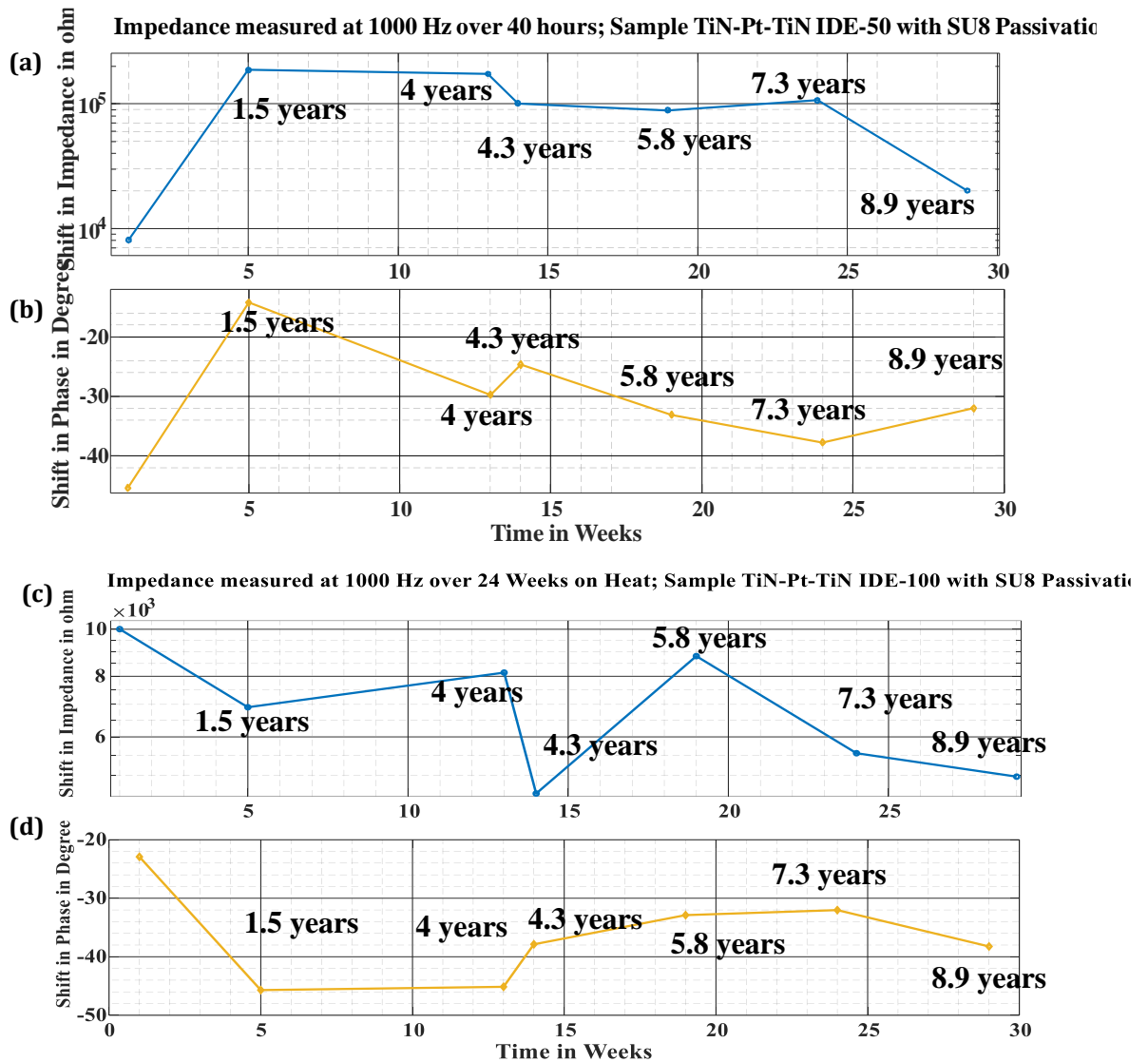


**Figure 4- 20** Trendline observed in samples' (a)impedance, (b) phase in IDE-50; (c) impedance, (d) phase in IDE-25 with SU8 passivation

**Figure 4-20** shows the trendline for the samples with SU8 passivation and the first thing that is observed is that compared to **Figure 4-18**, there is no specific trend and/or predictability of how the samples are changing in terms of impedance. This indicates that the results are less stable and not stable over a long period which makes it not an ideal candidate for a passivation material for chronic use of implants. The data were analyzed and the change in the percentage of the samples is low when considering the value of the first week and last week (60% for SU8-50 and 50% for SU8-100). However, observing the trendline makes it clear that the performance of the samples' loses coherence over time, whereas in the case of Diamond, the trend is a gradual change (increase in impedance with time).

Sample ID	Before Starting the Experiment	After 29 weeks	% Of Change at 1 kHz
Diamond 50	117372	119959	2.20
Diamond 25	69156	29422	57.01*
SU8 50	288777	20102	93
SU8 100	197504	4967	97

**Table 4- 1** Comparison of the performances of the samples at 1000 Hz in liquid at 78 degrees Celsius. \*When compared with the data of the result of week 1 and week 24, the Diamond-50 sample shows a change of only 2.41% of the result

It is very apparent from **Table 4-1** that the samples with Diamond passivation show low standard deviation at a specific frequency (1000 Hz) compared to those with the SU8 passivation layer. The difference between the lowest and highest value of the Diamond-50 sample is 3%, whereas the SU8-50 samples show a 60% difference between the lowest and highest value. Both samples show drastic shifts throughout the range of frequency in both impedance and phase. These are encouraging conclusions when it comes to using intrinsic Diamond as a passivation layer for implants in chronic use.

#### 4.4.6 Scope of Improvement in the Experimental Set-up

The experimental protocol can be proposed to yield better results by realizing the following improvements:

1. As mentioned before, the setup can collect and store data for 4 different output ports of the multiplexer. The number of outputs can be increased to collect data from more samples at a time in order to increase the reproducibility of the result.
2. Enabling a local connection to the computer, local data collection, monitoring, and restarting can be made possible.
3. A temperature sensor along with a temperature recording system can be introduced to correlate the change in temperature throughout the day, along with the change in impedance data.

#### 4.5 Take Away from This Chapter

The overall accomplishment of this part of the thesis was verifying the longevity of the samples passivated with Diamond and showing that the samples endure and show more stability than those with SU8 as a passivation layer. The experimental setup has been optimized upon correcting several steps and a protocol has been established. Establishing the protocol was the most time-consuming part. Once it was established by figuring out the best packaging choice and solving various leakage issues, the samples have been running continuously. After correction, the Diamond passivated samples demonstrated clearly more stable results compared to the SU8 samples. These results are encouraging and ongoing at the moment of reporting.

The observed result was the shift in value in the case of Diamond. For SU8-50 the shift is significantly bigger (93%) than that of intrinsic Diamond (2.20%), which provides superiority of intrinsic Diamond as a passivation layer and demands the further continuation of the research.

The trendline for the samples with Diamond passivation shows that there is a possibility of prediction as to how the sample will change and the impedance increases with time (see **Figure 4-18**). However, that is not the case for the samples with SU8 passivation. In the case of the SU8, the samples show no predictable trend in change and over the period of the test, the result fluctuated in a very unpredictable way. Therefore, even though the passivation layers are of the same height, the samples with Diamond passivation significantly show better performance. The next step would be testing more samples to observe the progression and build a predictable trend over time.

This study shows that even when being smaller in thickness of the passivation layer, Diamond gives more stable results over time. As seen before compared to the conventional material, BDD (conductive Diamond) presents encouraging results. Also, the experiment done by the previous team already demonstrated the stability of the BDD samples over time. These results show that fabricating a full Diamond implant which would give optimized results and long-term stable results is the next logical step.

Apart from the IDE samples (which only have intrinsic Diamond passivation), some BDD electrodes with intrinsic Diamond passivation were also put on the heat and will be compared with the established result.



## **Chapter 5**

### **Conclusion and Personal Statement**

This chapter would serve as the conclusion to the thesis and give an insight into the behind-the-scenes of the researcher's thought process and progressions towards the completion of the thesis work.



## 5.1 Future Work

This thesis work paves the way for continuation and the possibility of further development of various factors of the full Diamond electrodes with optimized performance. To attain that goal, the proposal for the project can be:

The development of a method to continue monitoring the performance of the electrodes amidst an in-vivo-like hostile environment in the lab and identify all the factors that contribute to the temporal changes in the electrode performance.

The development of techniques to maintain or rejuvenate the low-impedance properties of fabricated samples without deploying harmful repetitive procedures for different materials. In the case of surface modification, there needs to be a method to measure the modification of the surface not only by extrapolating the result from the data or SEM image preview, like already done in the thesis but also by developing a protocol to measure the percentage of variation and if the physical modification is justified by the calculation from the extrapolated result.

1. For full Diamond electrodes, solving the issue of water retention in between the crystallized pores of the polycrystalline structure (The issue has already been minimized). In case a very small amount is inevitable, develop a way to measure the water retention per surface area unit and/or incorporate it into the equivalent circuit model.
2. Establishing the protocol for automatic performance prediction of samples of different sizes and shapes like the equivalent circuit protocol already established.
3. Optimizing the fabrication of a full Diamond electrode will lead to the fabrication of a flexible full Diamond electrode with the desired performance.
4. As a part of the whole vision of building a prototype for a wearable impedance meter that would be used as a wireless recording and stimulating device, the electronic interface would be made more compact.
5. Inside the framework of this thesis, some primary experimental results were presented. Collecting more data in order to build a rate of reproducibility can be established.
6. Full Diamond STE electrodes are already on heat. The data from those samples would be analyzed to understand and predict the behavior of the full Diamond implants in-vivo environment.

## 5.2 Summary of the Thesis

To begin with, the first year is the most important time in terms of understanding the target and integration period of the thesis. Unfortunately, it was a very globally confusing and challenging time which made the process less than ideal and very time-consuming. However, as the saying goes, it is indeed better late than never. As the description of the project, the project NEURODIAM has a vision of expanding the project to the limit of "Electro-Impedance Spectroscopy (EIS) measurement and data acquisition with wearable technology via RFID. The interdisciplinary nature of the project offered the perspective of the potential overall vision for the project. At the beginning of the thesis, the author was presented with the opportunity to choose the part of the project that proved to be interesting. For the author that meant catching up with the bibliography along with the previous work done by the previous teams in ESIEE and the collaborations.

The team had already worked on the electronic interface part of the project with ARDUINO board AD5933 and subsequently the MSP, as was explained in **Chapter 1** and **Chapter 2**. The data was collected and compared with the commercial equipment HP4194 to prove the integrity of the homemade shield of the aforementioned setup.

Simultaneously, as a significant part of the thesis, the cleanroom fabrication of various materials involves taking part in training on different equipment to be able to operate those manually. This was one of the most exciting parts of the thesis as per the author, as it was chosen as the focus of the thesis. Thereafter the idea and various equipment for characterizing the samples in the laboratory environment (via mainly BIS technique) is explained in **Chapter 3** of this thesis. BDD samples showed better results when compared to the literature in the case of recording applications. TiN-Pt-TiN stack model and black TiN showed promising results for both recording and stimulation applications compared to popular biomaterials like bare Ti, Platinized TiN, and various Ti alloys.

As a part of the testing of the integrity and performance over time, it was required to establish an experimental protocol. Establishing the parameters was time-consuming, and it required multiple steps of trial and error as was explained in **Chapter 4**. This chapter proves that in microscale intrinsic Diamond provides a better result in terms of longevity when compared to [SU8](#) passivation layer of similar height.

For the future, the author envisions the current samples with full electrodes being prepared for in vivo procedure, since the difficulties with the fabrication of full Diamond electrodes have been minimized and there has been a protocol established to observe and analyze the result and optimize those as per application, before fabricating full Diamond implants.

### 5.3 Personal Statement

To speak a little about the overall vision of the project, as the next step, the electronic interface would be miniaturized to a scale that would be wearable. There is already ongoing technology established to acquire data simultaneously from multiple ports as a part of this thesis. The next part would be to make the data acquisition process wireless and turn off the device when data acquisition is turned off. This would save power and overheating of the electronics part being turned off.

In terms of the performance of the implants themselves can be predicted by observing the behavior of the electrodes. As was mentioned in the report before, the performances are always a handoff among the size, shape, and material. As of the time of writing this report, the performance is better when compared to other conventional materials when considering the longevity, performance (as both conductive and protection layer), structural integrity, and its reaction to the human interface.

In conclusion, the use of bio-implants made with various materials including Gold, Platinum, TiN, and Boron Doped Diamond for bio-impedance spectroscopy has proven to be an effective method in obtaining accurate and reliable results. Each material presents its unique properties and characteristics, such as biocompatibility, electrical conductivity, and durability. Gold and platinum, with their high electrical conductivity and biocompatibility, are favored for their ability to provide accurate readings. TiN, with its high resistance to wear and corrosion, is ideal for long-term implantation. On the other hand, the use of Boron Doped Diamond has shown promise as a material

with high electrical conductivity and biocompatibility, while also being durable and biodegradable.

Further research and development are necessary to optimize the use of these materials in bio-implant applications and to determine the best material for specific clinical needs. The advancement of bio-implant technology has the potential to revolutionize the field of bio-impedance spectroscopy and improve patient outcomes. In summary, the use of various materials in bio-implant technology offers exciting prospects for the future of medical technology.

## Annex

### A.1 Fabrication Methods

As mentioned before, in this chapter the general idea of the fabrication of electrodes with different materials, conventional and unconventional alike, will be explained. Here the general procedures are explained in short in chronological order:

#### A.1.1 Thermal Oxidization of the Silicon Wafer

Before starting the treatment, the wafer is hard-baked at a high temperature to get rid of the residual moisture on the wafer [10]. The growth of silicon oxide is obtained by the reaction of oxidizing species on the surface of silicon ( $O_2$  in the dry atmosphere or  $H_2O$  in the wet atmosphere) at high temperatures (800°C to 1200°C) and at atmospheric pressure according to the following chemical reactions:

- $Si + O_2 \Rightarrow SiO_2$  (dry oxidization)
- $Si + 2 H_2O \Rightarrow SiO_2 + 2 H_2$  (wet oxidization) [138]

The oxidation of silicon consumes a thickness of silicon equal to about half the thickness of the oxide layer formed. Dry oxidation produces silicon oxides with lower resistivity and therefore better resistivity along with better insulating quality than the wet oxidization process. On the other hand, the latter is faster. The ESIEE Paris CLEANROOM is equipped with 2 Semco Engineering tubular furnaces (one in the dry atmosphere and the other in the wet atmosphere) compatible with substrates of diameter 2", 3", 4" and 6" diameter substrates for silicon oxide growth, from 10 nm to 2  $\mu m$  thick. The dry oxidization furnace offers the possibility to add hydrochloric acid HCl to remove metal ions that could be present in the atmosphere, for critical applications such as MOS gate oxides [307].

This is not a necessary step in case the deposition is done on top of a glass wafer, because the glass is already an insulating material.

#### A.1.2 Priming/Wetting of the Wafer

This step is used to increase the adhesion of the photoresist layer on a  $SiO_2$  wafer. The surface of the wafer is coated with Hexamethyldisilazane, also known as HMDS, by a technique called spin coating. HMDS is a colorless organosilicon compound [308]–[310] with the molecular formula  $[(CH_3)_3Si]_2NH$  which promotes the adhesion of deposition on the wafer. **Figure A-1** shows how the hydrophobicity of the SU8 surface affects the water adhesion to it.

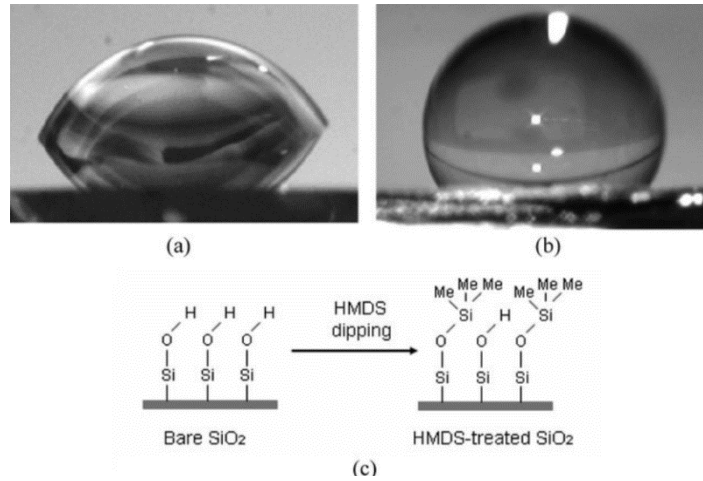


**Figure A-1** Shapes of a water droplet on an untreated (a) and a HMDS-treated (b) silicon oxide (SiO<sub>2</sub>=Si) substrate. (c) Schematic representation of the chemical reaction occurring on the surface of SiO<sub>2</sub> substrates by dipping in HMDS solution [281]

This is not a standard procedure for all depositions. Only in those cases, where a negative PR is used right before the sputtering layer, this is required to ensure good adhesion of the resist and subsequently metal.

### A.1.1.1 Cathodic Pulverization

**The Cathodic Pulverization** technique is used to sputter various materials on the substrate. The principle of sputtering is to create plasma between 2 electrodes from a neutral gas (Argon) under a vacuum. A solid source of the material in question to be deposited constitutes the cathode and the substrate on the anode [311].

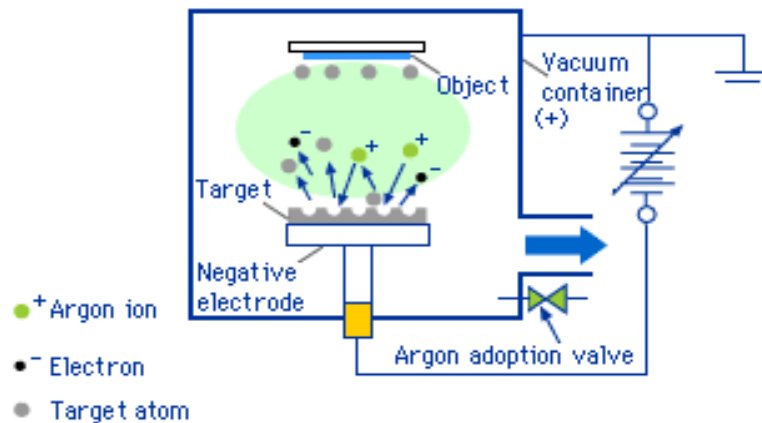


**Figure A-2** Principle of Sputtering [282]

The target on which the material is to be deposited is brought to a negative potential and is bombarded by the positive Ar<sup>+</sup> ions of the plasma. The Ar<sup>+</sup> ions tear off atoms from the surface of the target. The Ar<sup>+</sup> ions pull out atoms from the surface of the material, which will be deposited on the substrate located on the anode. The material to be deposited can be a metal, an alloy, or even an insulating material. The sputtering of insulators requires the use of RF (13.56 MHz) or DC polarization to maintain the plasma in the chamber and to allow the Ar<sup>+</sup> ions to pull the atoms from the target.



**Figure A-3** (a) Cathodic RF magnetron sputtering- ALCATEL - SCM 600 in ESIEE Paris CLEANROOM with Copper (Cu), Chromium (Cr), Titanium Tungsten (TiW), and Gould (Au) target, (b) inside of the sputtering chamber of SCM 600, the (c) Cu, (d) Cr, (e) TiW, (f) Au in the sputtering machine, (g) Magnetron sputtering equipment PLASSYS MP500S, (h) inside the sputtering chamber of MP500S

Most equipment is equipped with a device called a Magnetron (*see Figure A-3*). It is a system of permanent magnets of different magnetic polarity, placed under the target to trap the electrons and thus increase the probability that they will meet argon atoms and ionize them. This results in a higher deposition rate, However, inhomogeneous wear of the target.

In this equipment (*see Figure A-3 (g)*), the surface of the substrate can be cleaned in situ by bombardment with Ar<sup>+</sup> ions in RF mode, for example, to remove the native oxide layer on the silicon surface, or to remove part of photoresist during the lift-off process. The deposition of oxide or nitride layers is achieved by injecting oxygen O<sub>2</sub> or nitrogen N<sub>2</sub> into the chamber under vacuum in addition to Argon. In this case, sputtering is called **reactive sputtering**.

In ESIEE Paris CLEANROOM there are 2 cathodic pulverizations dedicated to the sputtering of various metals. One is dedicated to (*see Figure A-3 (a, b, c, d, e, f)*) the sputtering of Chromium (Cr), Titanium Tungsten (TiW), Copper (Cu), Gold (Au) and the other one (*see Figure A-3 (g, h)*) is dedicated to the sputtering of Titanium (Ti), Platinum (Pt), and Aluminum (Al) deposition on 4" diameter substrates. The wafers can be made of Glass or Si. In the case of a Si wafer, there needs to be a layer of SiO<sub>2</sub>, to make the surface insulating for metal deposition [312].

### A.1.1.2 Photolithography Process

The Photolithography process in CLEANROOM is composed of 3 main steps: (a) Spin Coating, (b) UV Exposure, and (c) Development.

#### (a) Spin-Coating Photoresist (PR)

Spin-coating is a method to deposit a uniform thin film of photoresist in the thickness variety of nanometers to micrometer scales [313].

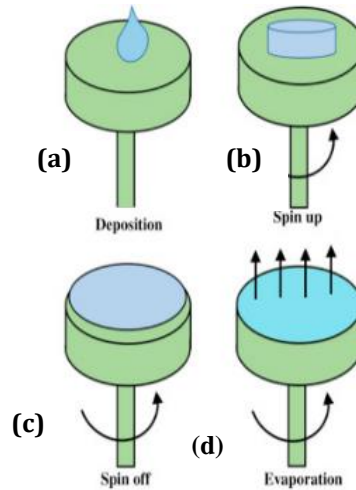


**Figure A-4** Steps of spin coating a Photoresist (a) Deposition, (b) spinning-up, (c) spinning-off, (d) evaporation [290]

The substrate is set up on a chuck that rotates the pattern, and the centrifugal force drives the liquid substantially outward. Viscous force and surface tension are the main reasons for the flat deposition on the floor. Subsequently, a thin film is fashioned with the aid of evaporation. The spin coating consists of numerous steps (see **Figure A-4,5**), consisting of (a) fluid dispense, (b) spin-up and strong fluid outflow, (c) spin-off, and (d) evaporation, respectively [135], [314]. The thickness of the spin-resist spin-coated on the wafer depends on numerous parameters:

$$h = \left[ 1 - \frac{\rho_A x}{A_0} \right] \left[ \frac{3nm}{2\rho_{A_0} \omega^2} \right]^{\frac{1}{3}} \dots \dots \dots Eq A-1$$

Where  $h$  is thickness,  $\rho_A$  is the density of a volatile liquid,  $\rho_{A_0}$  is the density of the reference liquid (commonly water),  $\eta$  is the viscosity of the solution,  $m$  is the rate of evaporation, and  $\omega$  is angular speed [14]. As the evaporation rate is calculated experimentally, a simpler equation has been suggested as given below:

$$h = A\omega^{-B} \dots \dots \dots Eq A-2$$

Where B is a constant and is an experimentally calculated parameter. In most cases, B is in the range of 0.4-0.7. From **Equation A-2**, it is clear that the thickness of the deposition is inversely proportional to the angular speed for a fixed surface area of deposition, meaning, the higher the angular speed of the substrate, the thinner will be the deposited film [162], [315]–[317].

At this step, the appropriate resin will be spin-coated on the sputtered layer following specific recipes. The purpose of this layer is to develop a softer surface to transfer the desired design of the mask to the wafer (*see Section 2.1*).

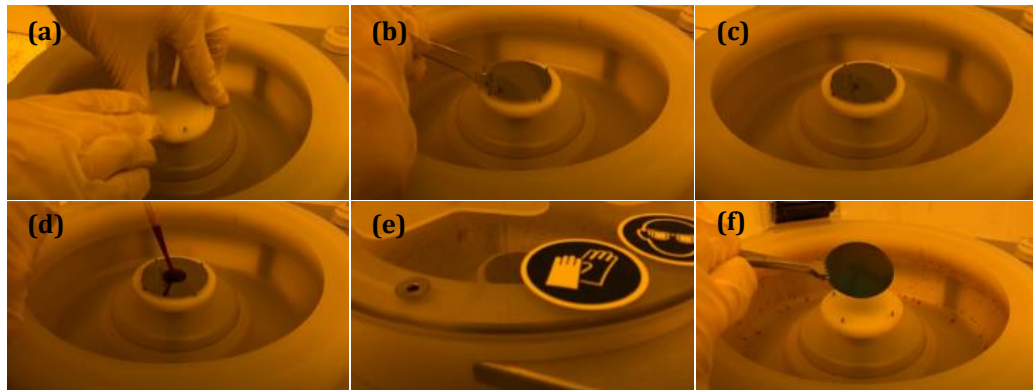


**Figure A-5** (a) Insert stable sample holder, (b) Load properly clean wafer in center, (c) Turn on vacuum (better than 0.7 bar), (d) Dispense resist of specific amount (e) Close off the lid, check for contact between the lid and the inner bowl, try the spin as per set recipe, (f) Inspect and take the wafer out carefully [287]

Right after the spin-coating step, the wafer is placed on a hotplate heated at an appropriate temperature, which is also addressed as **soft baking** in microfabrication (*see Figure A-6*). This step reduces the residual solvent from the deposited layer, hardens the liquid on the wafer to set the position on top of the wafer, and makes sure that it won't stick to the mask, also improves the adhesion of the resist to the wafer.



**Figure A-6** Hot plate in the ESIEE Paris CLEANROOM heated at 109° C, 65.2° C, 90.2° C, and 50.4° C. The wafers are put on rest period before putting on the hotplate

## (b) UV Exposure

The purpose of photolithography is to transfer the image of a mask on a substrate previously covered with a thin layer of photosensitive resin (thickness of a few hundred nanometers to a few tens of micrometers). The resins must be handled in a room isolated from UV light (*see Figure A-8 (b)*) and under extraction because they



contain dangerous solvents. The photoresist film is then exposed to UV light through a mask. The has the desired patterns, like a stencil. For a good reproduction of the patterns, the resin film must be in close contact with the mask in the plane. It is possible to align with the patterns already present on the substrate, either on the front or the back side, and with the precision of a few micrometers. The resin undergoes a chemical transformation under the effect of UV radiation, which changes - its solubility in a development solution (basic saline solution, solvent, etc.) called **Developer**. The resist itself is used as a mask for other steps such as metal deposition (lift-off), wet etching or dry plasma dry etching by plasma, etc.

There are two different kinds of photoresist/resin: Positive tone and negative tone, often referred to as just positive and negative photoresist (PR). When exposed, the chemical structure of positive resin changes and becomes soluble in specific developers. The areas of the PR not exposed to UV remain insoluble in the developer (*see Figure A-9*). Whereas, when exposed to UV, the negative photoresist starts polymerizing and becomes extremely hard and insoluble in the developer, and the unexposed parts are soluble in the developer [317].



*Figure A-7 Manual alignment equipment in ESIEE Paris CLEANROOM*

Depending on the requirement, the exposure can be set at Top Side Alignment (TSA) or Back Side Alignment (BSA). BSA or flood exposure is mostly done without a mask.

In ESIEE Paris CLEANROOM there are various alignment equipment (*see Figure A-7, A-8*). The ones that were used for fabrication are MA150 automatic alignment and exposure equipment (SÜSS MICROTEC), with specifications as follows:

Substrates up to 6" diameter, 350W Hg lamp, Broadband, i-line (365 nm) and g-line (405 nm), Single- and double-sided alignment [312], [318].



*Figure A-8 (a) Image of Alignment cross on the side of the mask in 2-D design file, (b) 58 m<sup>2</sup> area in class 100 dedicated to photolithography and substrate sealing, (c) Automatic alignment equipment in ESIEE Paris CLEANROOM [283]*

### (b) Development of Resin

After that, the resin was developed by proper developers. The process consists of using the proper solution and following the specific time for each procedure [318] (see

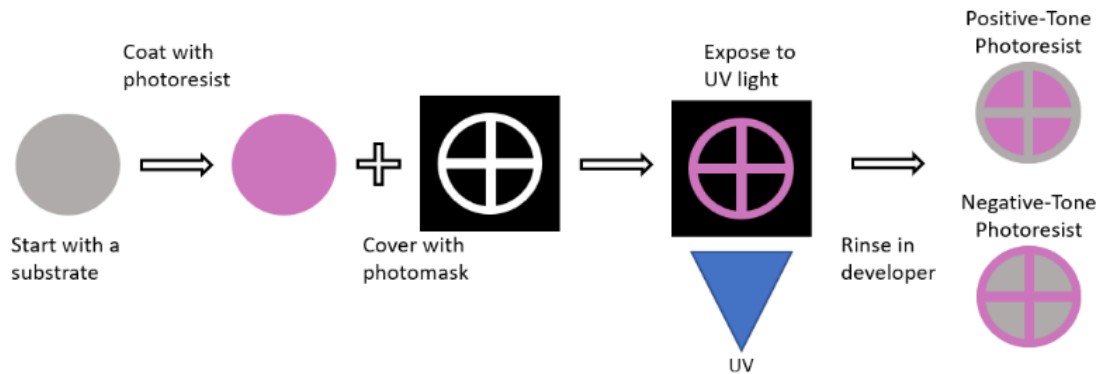


Figure A-9 Function of two different types of photoresists [289]

Figure A-9).

### A.1.1.3 Etching of the Metal

Etching is used in microfabrication to chemically dispose of layers from the surface of a wafer at a certain point of manufacturing. There are usually 2 different kinds of etching methods used in microfabrication: (a)Wet etching, and (b) Dry etching.

#### (a)Wet Etching

Wet etching is when the wafer is submerged in a liquid chemical etchant or etching agent. It can be used to strip off a whole layer of metal from the top or in some cases, it can be used to strip off a layer that is covered by a material (conductive or insulating layer) that is not attacked by the agent. In most cases, the products used to etch these layers are strong acids. Wet etching provides an isotropic etching, meaning the desired material is etched in all directions at the same speed (see Figure A-10 (b)). During the design of this aspect, the respective etching procedure must be taken into consideration. In ESIEE Paris CLEANROOM the wet etching is done in 2 separate rooms for different materials.

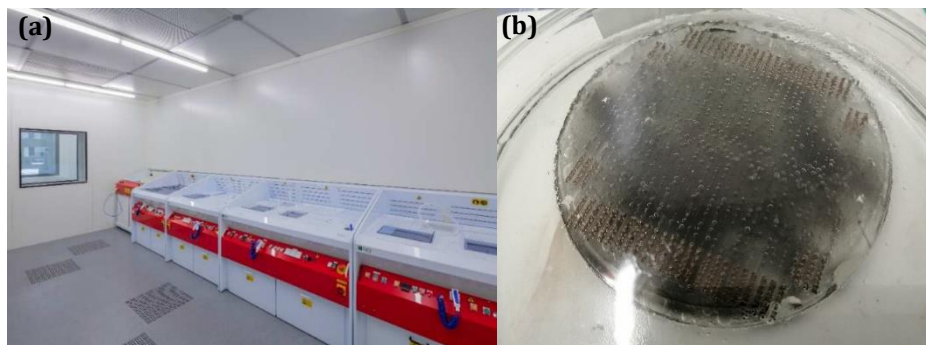
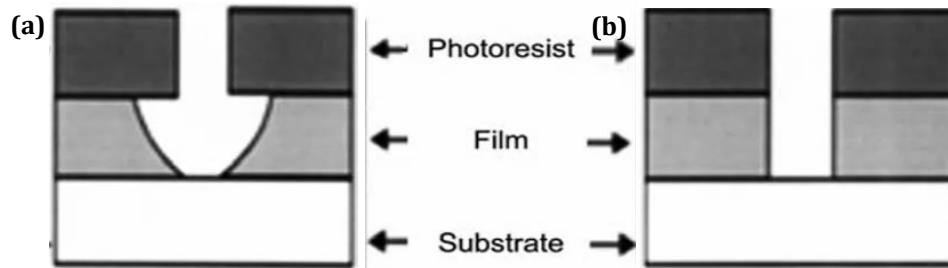


Figure A-10 (a)Chemistry-2 room in ESIEE Paris Cleanroom for Wet Etching [283], (b)Wet etching of a Glass wafer covered in TiN

### (b) Dry Etching

Dry etching, also known as plasma etching, is used to remove material from the substrate using etching gases. The principle of this etching is similar to cathodic pulverization. However, the wafer replaces the metallic target, an appropriate reactive gas is introduced to etch material layer [175], [319], [320]. With this technic, we achieve anisotropic etching. In the ESIEE-Paris cleanroom, there are two **Deep Reactive Ion Etching (DRIE)** machines available to etch different materials using a combination of different plasma and gases (*see Figure A-11 (a,b)*).



*Figure A-11 (a) Wet etching that helps acquire isotropic etching, (b) dry etching that helps acquire anisotropic etching [41]*

#### A.1.1.4 Passivation layer

A passivation layer is usually a non-conductive coating layer on top of the structure to reduce the charge recombination at surface states, increase the water oxidation reaction kinetics, and protect the semiconductor from chemical corrosion [154], [321].

One of the most used passivation layers in the cleanroom is the SU8 group. This resist is transparent, easy to deposit, and biocompatible. However, a downside of the SU8 layer is that it is biodegradable, hence with time the passivation layer loses its performance quality [322]–[324]. In this step, a desired passivation layer was spin-coated on top of the metallic structure. For this project, SU8 was used as a conventional passivation material.

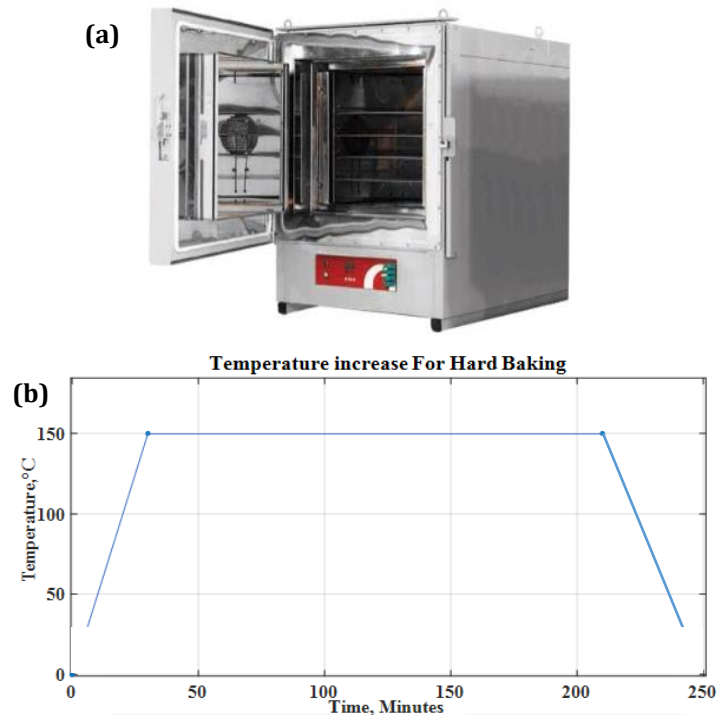


**Figure A-12** (a) The 600C CARBOLITE oven used for hard baking (Replace with Cleanroom image), (b) The temperature in the oven to set the SU8 on top of the wafer

In the case of the deposition being on glass, the wafers are hard baked in the oven (see **Figure A-12 (a)**), to polymerize the SU8 and make it stick to the structure. A ramp heating process is used to heat the wafer, where the temperature increases to 150°C in 30 minutes and stays at 150°C for 3 hours, after which the temperature goes down to room temperature again and the wafer is then taken out of the oven (see **Figure A-12 (b)**).

*Comparison of Electrodes with Conventional, and Non-Conventional Biomaterials  
to Novel Full Diamond Electrodes for Biomedical Applications*  
**Annex**

---

## Bibliography

- [1] "NEURODIAM – High density full diamond cortical implant for long life time implantation." Accessed: Sep. 14, 2022. [Online]. Available: <https://www.neurodiam.eu/>
  - [2] "Medical Implant - an overview | ScienceDirect Topics." Accessed: Sep. 14, 2022. [Online]. Available: <https://www.sciencedirect.com/topics/medicine-and-dentistry/medical-implant>
  - [3] "Feedthrough - an overview | ScienceDirect Topics." Accessed: Oct. 26, 2022. [Online]. Available: <https://www.sciencedirect.com/topics/engineering/feedthrough>
  - [4] "Implanted Device - an overview | ScienceDirect Topics." Accessed: Oct. 26, 2022. [Online]. Available: <https://www.sciencedirect.com/topics/engineering/implanted-device>
  - [5] "Neural Prosthesis - an overview | ScienceDirect Topics." Accessed: Oct. 26, 2022. [Online]. Available: <https://www.sciencedirect.com/topics/materials-science/neural-prosthesis>
  - [6] "Polycrystalline Diamond - an overview | ScienceDirect Topics." Accessed: Oct. 26, 2022. [Online]. Available: <https://www.sciencedirect.com/topics/engineering/polycrystalline-diamond>
  - [7] K. Ganesan *et al.*, "An all-diamond, hermetic electrical feedthrough array for a retinal prosthesis," *Biomaterials*, vol. 35, no. 3, pp. 908–915, Jan. 2014, doi: 10.1016/j.biomaterials.2013.10.040.
  - [8] "Medical device," *Wikipedia*. Aug. 22, 2022. Accessed: Sep. 16, 2022. [Online]. Available: [https://en.wikipedia.org/w/index.php?title=Medical\\_device&oldid=1105879546](https://en.wikipedia.org/w/index.php?title=Medical_device&oldid=1105879546)
  - [9] "Organ transplantation," *Wikipedia*. Aug. 30, 2022. Accessed: Sep. 16, 2022. [Online]. Available: [https://en.wikipedia.org/w/index.php?title=Organ\\_transplantation&oldid=1107612240](https://en.wikipedia.org/w/index.php?title=Organ_transplantation&oldid=1107612240)
  - [10] "Biomaterial," *Wikipedia*. Jul. 31, 2022. Accessed: Sep. 16, 2022. [Online]. Available: <https://en.wikipedia.org/w/index.php?title=Biomaterial&oldid=1101451842>
  - [11] R. S. Devi, "BIOMATERIAL AND ITS MEDICAL APPLICATIONS," vol. 3, no. 3, p. 10, 2017.
  - [12] B. O'Brien, "Niobium Biomaterials," in *Advances in Metallic Biomaterials: Tissues, Materials and Biological Reactions*, M. Niinomi, T. Narushima, and M. Nakai, Eds., in Springer Series in Biomaterials Science and Engineering, Berlin, Heidelberg: Springer, 2015, pp. 245–272. doi: 10.1007/978-3-662-46836-4\_11.
  - [13] "Gold," *Wikipedia*. Sep. 11, 2022. Accessed: Sep. 16, 2022. [Online]. Available: <https://en.wikipedia.org/w/index.php?title=Gold&oldid=1109660844>
  - [14] W. Li *et al.*, "Refractory Plasmonics with Titanium Nitride: Broadband Metamaterial Absorber," *Adv. Mater.*, vol. 26, no. 47, pp. 7959–7965, Dec. 2014, doi: 10.1002/adma.201401874.
  - [15] "Titanium Implants: Procedure, Side Effects, Cost, Vs. Ceramic & More," Healthline. Accessed: Sep. 17, 2022. [Online]. Available: <https://www.healthline.com/health/dental-and-oral-health/titanium-implants>
  - [16] "Silicone," *Wikipedia*. Sep. 03, 2022. Accessed: Sep. 16, 2022. [Online]. Available: <https://en.wikipedia.org/w/index.php?title=Silicone&oldid=1108288088>
  - [17] A. E. Porter, "Nanoscale characterization of the interface between bone and hydroxyapatite implants and the effect of silicon on bone apposition," *Micron*, vol. 37, no. 8, pp. 681–688, Dec. 2006, doi: 10.1016/j.micron.2006.03.006.
  - [18] S. J. Lugowski, D. C. Smith, H. Bonek, J. Lugowski, W. Peters, and J. Semple, "Analysis of silicon in human tissues with special reference to silicone breast implants," *Journal of Trace Elements in Medicine and Biology*, vol. 14, no. 1, pp. 31–42, Apr. 2000, doi: 10.1016/S0946-672X(00)80021-8.
  - [19] Q. Liu, S. Huang, J. P. Matinlinna, Z. Chen, and H. Pan, "Insight into Biological Apatite: Physicochemical Properties and Preparation Approaches," *Biomed Res Int*, vol. 2013, p. 929748, 2013, doi: 10.1155/2013/929748.
-

- [20] "Apatite," *Wikipedia*. Aug. 14, 2022. Accessed: Sep. 16, 2022. [Online]. Available: <https://en.wikipedia.org/w/index.php?title=Apatite&oldid=1104303128>
- [21] H. W. Denissen, K. de Groot, P. C. Makkes, A. van den Hooff, and P. J. Klopper, "Tissue response to dense apatite implants in rats," *J Biomed Mater Res*, vol. 14, no. 6, pp. 713–721, Nov. 1980, doi: 10.1002/jbm.820140603.
- [22] C. Y. Zhao, H. Fan, and X. Zhang, "Advances in Biomimetic Apatite Coating on Metal Implants," 2011. doi: 10.5772/14938.
- [23] M. Niinomi and C. J. Boehlert, "Titanium Alloys for Biomedical Applications," in *Advances in Metallic Biomaterials: Tissues, Materials and Biological Reactions*, M. Niinomi, T. Narushima, and M. Nakai, Eds., in Springer Series in Biomaterials Science and Engineering. , Berlin, Heidelberg: Springer, 2015, pp. 179–213. doi: 10.1007/978-3-662-46836-4\_8.
- [24] "Allotropes of carbon," *Wikipedia*. Aug. 18, 2022. Accessed: Sep. 16, 2022. [Online]. Available: [https://en.wikipedia.org/w/index.php?title=Allotropes\\_of\\_carbon&oldid=1105028571](https://en.wikipedia.org/w/index.php?title=Allotropes_of_carbon&oldid=1105028571)
- [25] R. A. Bapat *et al.*, "Recent advances of gold nanoparticles as biomaterial in dentistry," *International Journal of Pharmaceutics*, vol. 586, p. 119596, Aug. 2020, doi: 10.1016/j.ijpharm.2020.119596.
- [26] "Pacemakers." Accessed: Sep. 16, 2022. [Online]. Available: <https://www.bhf.org.uk/information-support/treatments/pacemakers>
- [27] J. Lee *et al.*, "Neural recording and stimulation using wireless networks of microimplants," *Nat Electron*, vol. 4, no. 8, Art. no. 8, Aug. 2021, doi: 10.1038/s41928-021-00631-8.
- [28] "Artificial cardiac pacemaker," *Wikipedia*. Sep. 16, 2022. Accessed: Sep. 16, 2022. [Online]. Available: [https://en.wikipedia.org/w/index.php?title=Artificial\\_cardiac\\_pacemaker&oldid=1110622750](https://en.wikipedia.org/w/index.php?title=Artificial_cardiac_pacemaker&oldid=1110622750)
- [29] "Subcutaneous tissue," *Wikipedia*. Jul. 19, 2022. Accessed: Sep. 17, 2022. [Online]. Available: [https://en.wikipedia.org/w/index.php?title=Subcutaneous\\_tissue&oldid=1099194744](https://en.wikipedia.org/w/index.php?title=Subcutaneous_tissue&oldid=1099194744)
- [30] H. An, M. A. Ehsan, Z. Zhou, and Y. Yi, "Electrical modeling and analysis of 3D synaptic array using vertical RRAM structure," in *2017 18th International Symposium on Quality Electronic Design (ISQED)*, Mar. 2017, pp. 1–6. doi: 10.1109/ISQED.2017.7918283.
- [31] "Biological activity," *Wikipedia*. Sep. 13, 2022. Accessed: Sep. 17, 2022. [Online]. Available: [https://en.wikipedia.org/w/index.php?title=Biological\\_activity&oldid=1110025227](https://en.wikipedia.org/w/index.php?title=Biological_activity&oldid=1110025227)
- [32] A. Wiegner, C. G. Wright, and M. Vollmer, "Multichannel cochlear implant for selective neuronal activation and chronic use in the free-moving Mongolian gerbil," *Journal of Neuroscience Methods*, vol. 273, pp. 40–54, Nov. 2016, doi: 10.1016/j.jneumeth.2016.08.006.
- [33] H. An, K. Bai, Y. Yi, H. An, K. Bai, and Y. Yi, *The Roadmap to Realize Memristive Three-Dimensional Neuromorphic Computing System*. IntechOpen, 2018. doi: 10.5772/intechopen.78986.
- [34] "Classification structurale des neurones Diagram," Quizlet. Accessed: Apr. 23, 2023. [Online]. Available: <https://quizlet.com/fr/265931620/classification-structurale-des-neurones-diagram/>
- [35] B. Kappen, "Introduction to biophysics," p. 97.
- [36] M. W. Barnett and P. M. Larkman, "The action potential," *Practical Neurology*, vol. 7, no. 3, pp. 192–197, Jun. 2007.
- [37] F. A. Dodge and J. W. Cooley, "Action Potential of the Motorneuron," *IBM Journal of Research and Development*, vol. 17, no. 3, pp. 219–229, May 1973, doi: 10.1147/rd.173.0219.
- [38] B. P. Bean, "The action potential in mammalian central neurons," *Nat Rev Neurosci*, vol. 8, no. 6, Art. no. 6, Jun. 2007, doi: 10.1038/nrn2148.
- [39] "What is an action potential?," Molecular Devices. Accessed: Sep. 16, 2022. [Online]. Available: <https://www.moleculardevices.com/applications/patch-clamp-electrophysiology/what-action-potential>
-

- [40] "Action potential." Accessed: Sep. 14, 2022. [Online]. Available: [https://www.zoology.ubc.ca/~gardner/action\\_potential.htm](https://www.zoology.ubc.ca/~gardner/action_potential.htm)
- [41] "Action Potential - The Resting Membrane Potential - Generation of Action Potentials," TeachMePhysiology. Accessed: Sep. 14, 2022. [Online]. Available: <https://teachmephysiology.com/nervous-system/synapses/action-potential/>
- [42] "Action potential," *Wikipedia*. Sep. 12, 2022. Accessed: Sep. 16, 2022. [Online]. Available: [https://en.wikipedia.org/w/index.php?title=Action\\_potential&oldid=1109917227](https://en.wikipedia.org/w/index.php?title=Action_potential&oldid=1109917227)
- [43] "Conduction of the Action Potential along the Nerve Fiber." Accessed: Apr. 23, 2023. [Online]. Available: <https://antranik.org/conduction-of-the-action-potential-along-the-nerve-fiber/>
- [44] S. Vroom, "The Effect on Memory of in Vitro Neural Networks Affected by  $\alpha$ -synuclein Aggregates," 2016. doi: 10.13140/RG.2.1.2605.0167.
- [45] S. C. B. Casagrande, R. G. Cury, E. J. L. Alho, and E. T. Fonoff, "Deep brain stimulation in Tourette's syndrome: evidence to date," *Neuropsychiatr Dis Treat*, vol. 15, pp. 1061–1075, Apr. 2019, doi: 10.2147/NDT.S139368.
- [46] S. F. Cogan, "Neural Stimulation and Recording Electrodes," *Annual Review of Biomedical Engineering*, vol. 10, no. 1, pp. 275–309, 2008, doi: 10.1146/annurev.bioeng.10.061807.160518.
- [47] M. Parastarfeizabadi and A. Z. Kouzani, "Advances in closed-loop deep brain stimulation devices," *J NeuroEngineering Rehabil*, vol. 14, no. 1, Art. no. 1, Dec. 2017, doi: 10.1186/s12984-017-0295-1.
- [48] C. Veraart, M.-C. Wanet-Defalque, B. Gérard, A. Vanlierde, and J. Delbeke, "Pattern Recognition with the Optic Nerve Visual Prosthesis," *Artificial Organs*, vol. 27, no. 11, pp. 996–1004, 2003, doi: 10.1046/j.1525-1594.2003.07305.x.
- [49] M. S. Humayun *et al.*, "Visual perception in a blind subject with a chronic microelectronic retinal prosthesis," *Vision Research*, vol. 43, no. 24, pp. 2573–2581, Nov. 2003, doi: 10.1016/S0042-6989(03)00457-7.
- [50] H. Sakaguchi *et al.*, "Artificial vision by direct optic nerve electrode (AV-DONE) implantation in a blind patient with retinitis pigmentosa," *J Artif Organs*, vol. 12, no. 3, pp. 206–209, Sep. 2009, doi: 10.1007/s10047-009-0467-2.
- [51] E. Zrenner *et al.*, "Subretinal electronic chips allow blind patients to read letters and combine them to words," *Proceedings of the Royal Society B: Biological Sciences*, vol. 278, no. 1711, pp. 1489–1497, May 2011, doi: 10.1098/rspb.2010.1747.
- [52] L. W. Tien, F. Wu, M. D. Tang-Schomer, E. Yoon, F. G. Omenetto, and D. L. Kaplan, "Silk as a Multifunctional Biomaterial Substrate for Reduced Glial Scarring around Brain-Penetrating Electrodes," *Advanced Functional Materials*, vol. 23, no. 25, pp. 3185–3193, 2013, doi: 10.1002/adfm.201203716.
- [53] K. Stingl *et al.*, "Subretinal Visual Implant Alpha IMS – Clinical trial interim report," *Vision Research*, vol. 111, pp. 149–160, Jun. 2015, doi: 10.1016/j.visres.2015.03.001.
- [54] G. S. Brindley and W. S. Lewin, "The sensations produced by electrical stimulation of the visual cortex," *The Journal of Physiology*, vol. 196, no. 2, pp. 479–493, 1968, doi: 10.1113/jphysiol.1968.sp008519.
- [55] <http://fyra.io>, "Johns Hopkins: Study Finds Up to 30% of Patients with Wet Macular Degeneration May Safely Stop Eye Injections," Eyewire+. Accessed: Nov. 07, 2022. [Online]. Available: <https://eyewire.news/news/johns-hopkins-study-finds-up-to-30-of-patients-with-wet-macular-degeneration-may-safely-stop-eye-injections>
- [56] D. Palanker, Y. Le Mer, S. Mohand-Said, M. Muqit, and J. A. Sahel, "Photovoltaic Restoration of Central Vision in Atrophic Age-Related Macular Degeneration," *Ophthalmology*, vol. 127, no. 8, pp. 1097–1104, Aug. 2020, doi: 10.1016/j.optha.2020.02.024.
- [57] C. Veraart *et al.*, "Visual sensations produced by optic nerve stimulation using an implanted self-sizing spiral cuff electrode," *Brain Research*, vol. 813, no. 1, pp. 181–186, Nov. 1998, doi: 10.1016/S0006-8993(98)00977-9.
-



- [58] J. Delbeke, M. Oozeer, and C. Veraart, "Position, size and luminosity of phosphenes generated by direct optic nerve stimulation," *Vision Research*, vol. 43, no. 9, pp. 1091–1102, Apr. 2003, doi: 10.1016/S0042-6989(03)00013-0.
- [59] D. Nanduri *et al.*, "Frequency and Amplitude Modulation Have Different Effects on the Percepts Elicited by Retinal Stimulation," *Investigative Ophthalmology & Visual Science*, vol. 53, no. 1, pp. 205–214, Jan. 2012, doi: 10.1167/iovs.11-8401.
- [60] "Advances in Neural Recording and Stimulation Integrated Circuits - PMC." Accessed: Apr. 21, 2023. [Online]. Available: <https://www.ncbi.nlm.nih.gov/pmc/articles/PMC8377741/>
- [61] J. zzSUEAYGhcIE, "Pixium Vision et Second Sight fusionnent pour créer un leader de la restauration de la vision," *Electroniques*. Accessed: Nov. 07, 2022. [Online]. Available: <https://www.electroniques.biz/economie/vie-des-entreprises/pixium-vision-et-second-fusionnent-pour-creer-un-leader-de-la-restauration-de-la-vision/>
- [62] "Pixium Vision - First Prima implantation in Italy," *Edison*. Accessed: Nov. 07, 2022. [Online]. Available: <https://www.edisongroup.com/publication/first-prima-implantation-in-italy/31337/>
- [63] "Pixium Vision : présente une trésorerie au 31 décembre de 14,5 millions d'euros," *Bourse Direct*. Accessed: Nov. 07, 2022. [Online]. Available: <https://www.boursedirect.fr/fr/actualites/categorie/resultats/pixium-vision-presente-une-tresorerie-au-31-decembre-de-14-5-millions-d-euros-boursier-485bc6d2116154208cd95e148af432ca623323ea>
- [64] B. W. Jones, R. L. Pfeiffer, W. D. Ferrell, C. B. Watt, J. Tucker, and R. E. Marc, "Retinal Remodeling and Metabolic Alterations in Human AMD," *Frontiers in Cellular Neuroscience*, vol. 10, 2016, Accessed: Nov. 07, 2022. [Online]. Available: <https://www.frontiersin.org/articles/10.3389/fncel.2016.00103>
- [65] R. E. Marc and B. W. Jones, "Retinal remodeling in inherited photoreceptor degenerations," *Mol Neurobiol*, vol. 28, no. 2, pp. 139–147, Oct. 2003, doi: 10.1385/MN:28:2:139.
- [66] F. Ceysens, K. van Kuyck, B. Nuttin, and R. Puers, "Long term LFP measurements with ultra-fine neural electrodes embedded in porous resorbable carrier," in *2013 Transducers & Eurosensors XXVII: The 17th International Conference on Solid-State Sensors, Actuators and Microsystems (TRANSDUCERS & EUROSENSORS XXVII)*, Jun. 2013, pp. 868–871. doi: 10.1109/Transducers.2013.6626905.
- [67] S. Huang, Y. Liu, Y. Zhao, Z. Ren, and C. F. Guo, "Flexible Electronics: Stretchable Electrodes and Their Future," *Advanced Functional Materials*, vol. 29, no. 6, p. 1805924, 2019, doi: 10.1002/adfm.201805924.
- [68] Y. U. Cho, S. L. Lim, J.-H. Hong, and K. J. Yu, "Transparent neural implantable devices: a comprehensive review of challenges and progress," *npj Flex Electron*, vol. 6, no. 1, Art. no. 1, Jun. 2022, doi: 10.1038/s41528-022-00178-4.
- [69] S. N. Obaid *et al.*, "Multifunctional Flexible Biointerfaces for Simultaneous Colocalized Optophysiology and Electrophysiology," *Advanced Functional Materials*, vol. 30, no. 24, p. 1910027, 2020, doi: 10.1002/adfm.201910027.
- [70] Y. Lu *et al.*, "Ultralow Impedance Graphene Microelectrodes with High Optical Transparency for Simultaneous Deep Two-Photon Imaging in Transgenic Mice," *Advanced Functional Materials*, vol. 28, no. 31, p. 1800002, 2018, doi: 10.1002/adfm.201800002.
- [71] M. A. Hejazi *et al.*, "Hybrid diamond/ carbon fiber microelectrodes enable multimodal electrical/chemical neural interfacing," *Biomaterials*, vol. 230, p. 119648, Feb. 2020, doi: 10.1016/j.biomaterials.2019.119648.
- [72] "How Do Neural Implants Work?," *Computer Engineering*. Accessed: Sep. 20, 2022. [Online]. Available: <https://comp-eng.binus.ac.id/2021/03/19/how-do-neural-implants-work/>
- [73] "Deep Brain Stimulation (DBS): What It Is, Purpose & Procedure," *Cleveland Clinic*. Accessed: Nov. 07, 2022. [Online]. Available: <https://my.clevelandclinic.org/health/treatments/21088-deep-brain-stimulation>
-

- [74] G. Marín *et al.*, “Deep brain stimulation in neurological diseases and other pathologies,” *Neurology Perspectives*, vol. 2, no. 3, pp. 151–159, Jul. 2022, doi: 10.1016/j.neurop.2022.03.001.
- [75] N. I. · C. News ·, “‘This is not a magic wand’: Spinal stimulation used on Humboldt Bronco promising but in early research stages | CBC News,” CBC. Accessed: Nov. 07, 2022. [Online]. Available: <https://www.cbc.ca/news/health/epidural-stimulation-spinal-injury-humboldt-broncos-1.5353221>
- [76] J.-P. Houtteville, K. Toumi, J. Theron, J.-M. Derlon, A. Benazza, and P. Hubert, “Interhemispheric Subdural Haematomas: seven cases and review of the literature,” *British Journal of Neurosurgery*, vol. 2, no. 3, pp. 357–367, Jan. 1988, doi: 10.3109/02688698809001007.
- [77] A. Rapanà, E. Lamaida, V. Pizza, P. Lepore, F. Caputi, and G. Graziussi, “Inter-hemispheric scissure, a rare location for a traumatic subdural hematoma, case report and review of the literature,” *Clinical Neurology and Neurosurgery*, vol. 99, no. 2, pp. 124–129, May 1997, doi: 10.1016/S0303-8467(97)80009-1.
- [78] C. R. P. Sullivan, S. Olsen, and A. S. Widge, “Deep brain stimulation for psychiatric disorders: From focal brain targets to cognitive networks,” *NeuroImage*, vol. 225, p. 117515, Jan. 2021, doi: 10.1016/j.neuroimage.2020.117515.
- [79] “Treatment,” Epidural Stimulation Now. Accessed: Nov. 07, 2022. [Online]. Available: <https://epiduralstimulationnow.com/treatment/>
- [80] “Spinal Cord Injury Epidural Stimulation,” Mayo Clinic. Accessed: Nov. 07, 2022. [Online]. Available: <https://www.mayo.edu/research/clinical-trials/cls-20167853>
- [81] “Next-generation spinal implants help people with severe paralysis walk, cycle, and swim.” Accessed: Nov. 07, 2022. [Online]. Available: <https://www.science.org/content/article/next-generation-spinal-implants-help-people-severe-paralysis-walk-cycle-and-swim>
- [82] C. Pandarinath and S. J. Bensmaia, “The science and engineering behind sensitized brain-controlled bionic hands,” *Physiological Reviews*, vol. 102, no. 2, pp. 551–604, Apr. 2022, doi: 10.1152/physrev.00034.2020.
- [83] C. Qian, B. McLean, D. Hedman, and F. Ding, “A comprehensive assessment of empirical potentials for carbon materials,” *APL Materials*, vol. 9, no. 6, p. 061102, Jun. 2021, doi: 10.1063/5.0052870.
- [84] P. A. Starr, “Totally Implantable Bidirectional Neural Prostheses: A Flexible Platform for Innovation in Neuromodulation,” *Frontiers in Neuroscience*, vol. 12, 2018, Accessed: Nov. 07, 2022. [Online]. Available: <https://www.frontiersin.org/articles/10.3389/fnins.2018.00619>
- [85] S. P. Lacour, G. Courtine, and J. Guck, “Materials and technologies for soft implantable neuroprostheses,” *Nat Rev Mater*, vol. 1, no. 10, Art. no. 10, Sep. 2016, doi: 10.1038/natrevmats.2016.63.
- [86] A. Ahnood *et al.*, “Diamond Devices for High Acuity Prosthetic Vision,” *Advanced Biosystems*, vol. 1, no. 1–2, p. 1600003, 2017, doi: 10.1002/adbi.201600003.
- [87] “Glial scar,” *Wikipedia*. Jun. 30, 2022. Accessed: Sep. 19, 2022. [Online]. Available: [https://en.wikipedia.org/w/index.php?title=Glial\\_scar&oldid=1095798227](https://en.wikipedia.org/w/index.php?title=Glial_scar&oldid=1095798227)
- [88] K. Stingl *et al.*, “Interim Results of a Multicenter Trial with the New Electronic Subretinal Implant Alpha AMS in 15 Patients Blind from Inherited Retinal Degenerations,” *Frontiers in Neuroscience*, vol. 11, 2017, Accessed: Sep. 14, 2022. [Online]. Available: <https://www.frontiersin.org/articles/10.3389/fnins.2017.00445>
- [89] S. Joucla and B. Yvert, “Improved Focalization of Electrical Microstimulation Using Microelectrode Arrays: A Modeling Study,” *PLOS ONE*, vol. 4, no. 3, p. e4828, Mar. 2009, doi: 10.1371/journal.pone.0004828.
- [90] W. Elshahawy, *Biocompatibility*. IntechOpen, 2011. doi: 10.5772/18475.
-

- [91] J. J. Bernstein, P. F. Johnson, L. L. Hench, G. Hunter, and W. W. Dawson, "Cortical Histopathology following Stimulation with Metallic and Carbon Electrodes; pp. 142–157," *BBE*, vol. 14, no. 1–2, pp. 142–157, 1977, doi: 10.1159/000125580.
- [92] A. Y. Chow *et al.*, "Implantation of silicon chip microphotodiode arrays into the cat subretinal space," *IEEE Trans. Neural Syst. Rehabil. Eng.*, vol. 9, no. 1, pp. 86–95, Mar. 2001, doi: 10.1109/7333.918281.
- [93] B. Kappen, "Introduction to biophysics," p. 97.
- [94] "MICROFLEX ARRAY from BLACKROCK." Accessed: Sep. 14, 2022. [Online]. Available: <https://www.brainlatam.com/knowledge-base/microflex-array-from-blackrock-72>
- [95] J. Górecka and P. Makiewicz, "The Dependence of Electrode Impedance on the Number of Performed EEG Examinations," *Sensors (Basel)*, vol. 19, no. 11, p. 2608, Jun. 2019, doi: 10.3390/s19112608.
- [96] C. R. Butson, C. B. Maks, and C. C. McIntyre, "Sources and effects of electrode impedance during deep brain stimulation," *Clin Neurophysiol*, vol. 117, no. 2, pp. 447–454, Feb. 2006, doi: 10.1016/j.clinph.2005.10.007.
- [97] C. S. Bjornsson *et al.*, "Effects of insertion conditions on tissue strain and vascular damage during neuroprosthetic device insertion," *J Neural Eng*, vol. 3, no. 3, pp. 196–207, Sep. 2006, doi: 10.1088/1741-2560/3/3/002.
- [98] D. Prodanov and J. Delbeke, "Mechanical and Biological Interactions of Implants with the Brain and Their Impact on Implant Design," *Frontiers in Neuroscience*, vol. 10, 2016, Accessed: Sep. 16, 2022. [Online]. Available: <https://www.frontiersin.org/articles/10.3389/fnins.2016.00011>
- [99] E. Demann, P. Stein, and J. Haubenreich, "Gold as an Implant in Medicine and Dentistry," *Journal of long-term effects of medical implants*, vol. 15, pp. 687–98, Feb. 2005, doi: 10.1615/JLongTermEffMedImplants.v15.i6.100.
- [100] H. Kosslick, H. Sauer, T. Just, U. Vick, G. Fulda, and L. Jonas, "Biodegradation of gold and platinum implants in rats studied by electron microscopy," *International Journal of Physics Research and Applications*, vol. 2, no. 1, pp. 041–048, Nov. 2019, doi: 10.29328/journal.ijpra.1001014.
- [101] G. Manivasagam, D. Dhinasekaran, and A. Rajamanickam, "Biomedical Implants: Corrosion and its Prevention - A Review," *Recent Pat. Corros. Sci.*, vol. 2, no. 1, pp. 40–54, May 2010, doi: 10.2174/1877610801002010040.
- [102] S. Ravula, M. McClain, M. Wang, J. Glass, and A. Frazier, "A multielectrode microcompartment culture platform for studying signal transduction in the nervous system," *Lab on a chip*, vol. 6, pp. 1530–6, Jan. 2007, doi: 10.1039/b612684g.
- [103] K. Fox *et al.*, "Development of a Magnetic Attachment Method for Bionic Eye Applications: Development of a Magnetic Attachment Method," *Artificial Organs*, vol. 40, no. 3, pp. E12–E24, Mar. 2016, doi: 10.1111/aor.12582.
- [104] A. Kashi and S. Saha, "Mechanisms of failure of medical implants during long-term use," in *Biointegration of Medical Implant Materials*, Elsevier, 2010, pp. 326–348. doi: 10.1533/9781845699802.3.326.
- [105] R. More and J. Bokros, "Biomaterials: Carbon," 2006. doi: 10.1002/0471732877.emd023.
- [106] "Advancing biomaterials of human origin for tissue engineering - PMC." Accessed: Apr. 21, 2023. [Online]. Available: <https://www.ncbi.nlm.nih.gov/pmc/articles/PMC4808059/>
- [107] A. Rifai, E. Pirogova, and K. Fox, "Diamond, Carbon Nanotubes and Graphene for Biomedical Applications," in *Encyclopedia of Biomedical Engineering*, R. Narayan, Ed., Oxford: Elsevier, 2019, pp. 97–107. doi: 10.1016/B978-0-12-801238-3.99874-X.
- [108] B. Fan *et al.*, "Flexible, diamond-based microelectrodes fabricated using the diamond growth side for neural sensing," *Microsyst Nanoeng*, vol. 6, p. 42, Jul. 2020, doi: 10.1038/s41378-020-0155-1.
- [109] H. P. Neves, "1 - Materials for implantable systems," in *Implantable Sensor Systems for Medical Applications*, A. Inmann and D. Hodgins, Eds., in Woodhead Publishing Series in Biomaterials. , Woodhead Publishing, 2013, pp. 3–38. doi: 10.1533/9780857096289.1.3.
-

- [110] A. Rifai, E. Pirogova, and K. Fox, "Diamond, Carbon Nanotubes and Graphene for Biomedical Applications," 2018. doi: 10.1016/B978-0-12-801238-3.99874-X.
- [111] D. G. Papageorgiou, I. A. Kinloch, and R. J. Young, "Mechanical properties of graphene and graphene-based nanocomposites," *Progress in Materials Science*, vol. 90, pp. 75–127, Oct. 2017, doi: 10.1016/j.pmatsci.2017.07.004.
- [112] A. N. Ghulam, O. A. L. dos Santos, L. Hazeem, B. Pizzorno Backx, M. Bououdina, and S. Bellucci, "Graphene Oxide (GO) Materials—Applications and Toxicity on Living Organisms and Environment," *Journal of Functional Biomaterials*, vol. 13, no. 2, Art. no. 2, Jun. 2022, doi: 10.3390/jfb13020077.
- [113] Q. Jian, Z. Jiang, Y. Han, Y. Zhu, and Z. Li, "Fabrication and evaluation of mechanical properties of polycrystalline diamond reinforced with carbon-nanotubes by HPHT sintering," *Ceramics International*, vol. 46, no. 13, pp. 21527–21532, Sep. 2020, doi: 10.1016/j.ceramint.2020.05.254.
- [114] E. K. Purcell *et al.*, "Next-Generation Diamond Electrodes for Neurochemical Sensing: Challenges and Opportunities," *Micromachines (Basel)*, vol. 12, no. 2, p. 128, Jan. 2021, doi: 10.3390/mi12020128.
- [115] "HPHT and CVD Diamond Growth Processes | How Lab-Grown Diamonds are Made | GIA." Accessed: Nov. 03, 2022. [Online]. Available: <http://www.gia.eduhttps://www.gia.edu/hpht-and-cvd-diamond-growth-processes>
- [116] "CVD Diamond - General Information." Accessed: Nov. 03, 2022. [Online]. Available: [http://www.cvd-diamond.com/geninfo\\_en.htm](http://www.cvd-diamond.com/geninfo_en.htm)
- [117] M. Marelli *et al.*, "Flexible and biocompatible microelectrode arrays fabricated by supersonic cluster beam deposition on SU-8," *J. Micromech. Microeng.*, vol. 21, no. 4, p. 045013, Mar. 2011, doi: 10.1088/0960-1317/21/4/045013.
- [118] J. S. L. Fong, M. A. Booth, A. Rifai, K. Fox, and A. Gelmi, "Diamond in the Rough: Toward Improved Materials for the Bone–Implant Interface," *Adv. Healthcare Mater.*, vol. 10, no. 14, p. 2100007, Jul. 2021, doi: 10.1002/adhm.202100007.
- [119] A. Rifai *et al.*, "Polycrystalline Diamond Coating of Additively Manufactured Titanium for Biomedical Applications," *ACS Appl. Mater. Interfaces*, vol. 10, no. 10, pp. 8474–8484, Mar. 2018, doi: 10.1021/acsami.7b18596.
- [120] L. Zou *et al.*, "Self-assembled multifunctional neural probes for precise integration of optogenetics and electrophysiology," *Nat Commun*, vol. 12, no. 1, Art. no. 1, Oct. 2021, doi: 10.1038/s41467-021-26168-0.
- [121] "Researchers bring the bling to improve implants." Accessed: Nov. 04, 2022. [Online]. Available: <https://www.rmit.edu.au/news/all-news/2018/mar/researchers-bring-the-bling-to-improve-implants>
- [122] "On the thermal and chemical stability of diamond during processing of Al/diamond composites by liquid metal infiltration (squeeze casting) - ScienceDirect." Accessed: Mar. 18, 2023. [Online]. Available: <https://www.sciencedirect.com/science/article/abs/pii/S0925963504001797>
- [123] C. D. Lee, E. M. Hudak, J. J. Whalen, A. Petrossians, and J. D. Weiland, "Low-Impedance, High Surface Area Pt-Ir Electrodeposited on Cochlear Implant Electrodes," *J. Electrochem. Soc.*, vol. 165, no. 12, p. G3015, May 2018, doi: 10.1149/2.0031812jes.
- [124] E. Castagnola *et al.*, "Smaller, softer, lower-impedance electrodes for human neuroprosthesis: a pragmatic approach," *Front Neuroeng*, vol. 7, p. 8, Apr. 2014, doi: 10.3389/fneng.2014.00008.
- [125] M. P. Soares dos Santos *et al.*, "Towards an effective sensing technology to monitor micro-scale interface loosening of bioelectronic implants," *Sci Rep*, vol. 11, p. 3449, Feb. 2021, doi: 10.1038/s41598-021-82589-3.
- [126] M. Vojs *et al.*, "Comparative study of electrical properties of nano to polycrystalline diamond films," *Journal of Physics Conference Series*, vol. 100, p. 2097, Mar. 2008, doi: 10.1088/1742-6596/100/5/052097.
-

- [127] P. Knittel *et al.*, "Nanostructured Boron Doped Diamond Electrodes with Increased Reactivity for Solar-Driven CO<sub>2</sub> Reduction in Room Temperature Ionic Liquids," *ChemCatChem*, vol. 12, no. 21, pp. 5548–5557, Nov. 2020, doi: 10.1002/cctc.202000938.
- [128] "Diamond for Electronics: Materials, Processing and Devices - PMC." Accessed: Aug. 28, 2023. [Online]. Available: <https://www.ncbi.nlm.nih.gov/pmc/articles/PMC8623275/>
- [129] "Review on the Properties of Boron-Doped Diamond and One-Dimensional-Metal-Oxide Based P-N Heterojunction - PMC." Accessed: Aug. 28, 2023. [Online]. Available: <https://www.ncbi.nlm.nih.gov/pmc/articles/PMC7794918/>
- [130] S. N. Demlow, R. Rechenberg, and T. Grotjohn, "The effect of substrate temperature and growth rate on the doping efficiency of single crystal boron doped diamond," *Diamond and Related Materials*, vol. 49, pp. 19–24, Oct. 2014, doi: 10.1016/j.diamond.2014.06.006.
- [131] C. Hassler, T. Boretius, and T. Stieglitz, "Polymers for neural implants," *Journal of Polymer Science Part B: Polymer Physics*, vol. 49, no. 1, pp. 18–33, 2011, doi: 10.1002/polb.22169.
- [132] E. Team, "Introduction to lab-on-a-chip 2023: review, history and future," *Elveflow*, Aug. 2023, Accessed: Aug. 16, 2023. [Online]. Available: <https://www.elveflow.com/microfluidic-reviews/general-microfluidics/introduction-to-lab-on-a-chip-review-history-and-future/>
- [133] "Electrode Materials in Microfluidic Systems for the Processing and Separation of DNA: A Mini Review - PMC." Accessed: Aug. 16, 2023. [Online]. Available: <https://www.ncbi.nlm.nih.gov/pmc/articles/PMC6190325/>
- [134] B. Rasolofoniaina, "Metallic and dielectric layers deposition," IMEP-LAHC. Accessed: Sep. 21, 2022. [Online]. Available: <https://imep-lahc.grenoble-inp.fr/en/platform/thin-layers-deposition>
- [135] U. G. Lee, W.-B. Kim, D. H. Han, and H. S. Chung, "A Modified Equation for Thickness of the Film Fabricated by Spin Coating," *Symmetry*, vol. 11, no. 9, Art. no. 9, Sep. 2019, doi: 10.3390/sym11091183.
- [136] L. Golestanirad and S. J. Graham, "Electrode designs for efficient neural stimulation," US9526890B2, Dec. 27, 2016 Accessed: Sep. 16, 2022. [Online]. Available: <https://patents.google.com/patent/US9526890B2/en>
- [137] "Thermal Oxidation - an overview | ScienceDirect Topics." Accessed: Sep. 16, 2022. [Online]. Available: <https://www.sciencedirect.com/topics/engineering/thermal-oxidation>
- [138] ~ Virginiasemi, "Thermal Oxidation For Silicon Wafers," Virginia Semiconductor - News & Blog. Accessed: Sep. 16, 2022. [Online]. Available: <https://virginiasemi.wordpress.com/2017/06/01/thermal-oxidation-for-silicon-wafers/>
- [139] M. S. Abdul Rahman, S. C. Mukhopadhyay, and P.-L. Yu, "Novel Planar Interdigital Sensors," in *Smart Sensors, Measurement and Instrumentation*, 2014, pp. 11–35. doi: 10.1007/978-3-319-04274-9\_2.
- [140] P. Gerwen *et al.*, *Nanoscaled interdigitated electrode arrays for biochemical sensors*, vol. 49. 1997, p. 910 vol.2. doi: 10.1109/SENSOR.1997.635249.
- [141] S. MacKay, P. Hermansen, D. Wishart, and J. Chen, "Simulations of Interdigitated Electrode Interactions with Gold Nanoparticles for Impedance-Based Biosensing Applications," *Sensors*, vol. 15, no. 9, Art. no. 9, Sep. 2015, doi: 10.3390/s150922192.
- [142] M. S. Abdul Rahman, K. Jayasundera, and S. C. Mukhopadhyay, "Initial Investigation of Using Planar Interdigital Sensors for Assessment of Quality in Seafood," *Journal of Sensors*, vol. 2008, Jan. 2008, doi: 10.1155/2008/150874.
- [143] "Chemical formula," *Wikipedia*. Sep. 05, 2022. Accessed: Sep. 16, 2022. [Online]. Available: [https://en.wikipedia.org/w/index.php?title=Chemical\\_formula&oldid=1108579022#Molecular\\_formula](https://en.wikipedia.org/w/index.php?title=Chemical_formula&oldid=1108579022#Molecular_formula)
- [144] A. Norlin, J. Pan, and C. Leygraf, "Investigation of interfacial capacitance of Pt, Ti and TiN coated electrodes by electrochemical impedance spectroscopy," *Biomolecular Engineering*, vol. 19, no. 2, pp. 67–71, Aug. 2002, doi: 10.1016/S1389-0344(02)00013-8.
-

- [145] "A review on biomedical implant materials and the effect of friction stir based techniques on their mechanical and tribological properties - ScienceDirect." Accessed: Apr. 21, 2023. [Online]. Available: <https://www.sciencedirect.com/science/article/pii/S2238785422000503>
- [146] H. Park, A. R. Maple, and H. Lee, "Effects of Fractal Electrode Geometry in Charge Injection Capacity of TiN Microelectrodes," in *2020 42nd Annual International Conference of the IEEE Engineering in Medicine & Biology Society (EMBC)*, Montreal, QC, Canada: IEEE, Jul. 2020, pp. 3371–3374. doi: 10.1109/EMBC44109.2020.9176725.
- [147] H. Park, P. Takmakov, and H. Lee, "Electrochemical Evaluations of Fractal Microelectrodes for Energy Efficient Neurostimulation," *Sci Rep*, vol. 8, no. 1, Art. no. 1, Mar. 2018, doi: 10.1038/s41598-018-22545-w.
- [148] T. Kozai, N. Alba, H. Zhang, N. Kotov, R. Gaunt, and X. Cui, "Nanostructured Coatings for Improved Charge Delivery to Neurons," in *Nanotechnology and neuroscience: nano-electronic, photonic and mechanical neuronal interfacing*, 2014, pp. 71–134. doi: 10.1007/978-1-4899-8038-0\_4.
- [149] X. Wei and W. Grill, "Analysis of high-perimeter planar electrodes for efficient neural stimulation," *Frontiers in Neuroengineering*, vol. 2, 2009, Accessed: Nov. 15, 2022. [Online]. Available: <https://www.frontiersin.org/articles/10.3389/neuro.16.015.2009>
- [150] G. Brankovic, Z. Brankovic, V. Jovic, and J. Varela, "Fractal Approach to ac Impedance Spectroscopy Studies of Ceramic Materials," *Journal of Electroceramics*, vol. 7, pp. 89–94, Jan. 2001, doi: 10.1023/B:JECR.0000027948.16316.bd.
- [151] J. Lim *et al.*, "Fractal microelectrodes for more energy-efficient cervical vagus nerve stimulation," *Advanced Healthcare Materials*, vol. n/a, no. n/a, p. 2202619, doi: 10.1002/adhm.202202619.
- [152] B. Fan, B. Wolfrum, and J. T. Robinson, "Impedance scaling for gold and platinum microelectrodes," *J. Neural Eng.*, vol. 18, no. 5, p. 056025, Sep. 2021, doi: 10.1088/1741-2552/ac20e5.
- [153] A. Domínguez-Bajo *et al.*, "Nanostructured gold electrodes promote neural maturation and network connectivity," *Biomaterials*, vol. 279, p. 121186, Dec. 2021, doi: 10.1016/j.biomaterials.2021.121186.
- [154] A. M. Ostdiek, J. R. Ivey, D. A. Grant, J. Gopaldas, and S. A. Grant, "An in vivo study of a gold nanocomposite biomaterial for vascular repair," *Biomaterials*, vol. 65, pp. 175–183, Oct. 2015, doi: 10.1016/j.biomaterials.2015.06.045.
- [155] E. S. Vikulova *et al.*, "Application of Biocompatible Noble Metal Film Materials to Medical Implants: TiNi Surface Modification," *Coatings*, vol. 13, no. 2, Art. no. 2, Feb. 2023, doi: 10.3390/coatings13020222.
- [156] "Gold Properties | AMNH," American Museum of Natural History. Accessed: Sep. 21, 2022. [Online]. Available: <https://www.amnh.org/exhibitions/gold/incomparable-gold/gold-properties>
- [157] "The Fascinating History of Dental Implants | Cosmetic Dentistry & General Dentistry located in Chesterfield, MO | Chesterfield Dentistry." Accessed: Sep. 20, 2022. [Online]. Available: <https://www.chesterfielddentistry.com/post/the-fascinating-history-of-dental-implants>
- [158] M. Possas *et al.*, "Comparing Silicon and Diamond Micro-cantilevers Based Sensors for Detection of Added Mass and Stiffness Changes," *Procedia Engineering*, vol. 120, pp. 1115–1119, Jan. 2015, doi: 10.1016/j.proeng.2015.08.807.
- [159] S. Nimbalkar *et al.*, "Ultra-Capacitive Carbon Neural Probe Allows Simultaneous Long-Term Electrical Stimulations and High-Resolution Neurotransmitter Detection," *Sci Rep*, vol. 8, p. 6958, May 2018, doi: 10.1038/s41598-018-25198-x.
- [160] "Guidelines to Study and Develop Soft Electrode Systems for Neural Stimulation - ScienceDirect." Accessed: Apr. 21, 2023. [Online]. Available: <https://www.sciencedirect.com/science/article/pii/S0896627320308060>
-

- [161] N. V. Apollo *et al.*, “Gels, jets, mosquitoes, and magnets: a review of implantation strategies for soft neural probes,” *J Neural Eng*, vol. 17, no. 4, p. 041002, Sep. 2020, doi: 10.1088/1741-2552/abacd7.
- [162] Y. Lu and S. C. Chen, “Micro and nano-fabrication of biodegradable polymers for drug delivery,” *Advanced Drug Delivery Reviews*, vol. 56, no. 11, pp. 1621–1633, Sep. 2004, doi: 10.1016/j.addr.2004.05.002.
- [163] “platinum | Color, Symbol, Uses, & Facts | Britannica.” Accessed: Sep. 22, 2022. [Online]. Available: <https://www.britannica.com/science/platinum>
- [164] R. De Boer and A. Oosterom, “Electrical properties of platinum electrodes: Impedance measurements and time-domain analysis,” *Medical & biological engineering & computing*, vol. 16, pp. 1–10, Feb. 1978, doi: 10.1007/BF02442925.
- [165] J. Wang and G. Swain, “Fabrication and Evaluation of Platinum/Diamond Composite Electrodes for Electrocatalysis,” *Journal of The Electrochemical Society - J ELECTROCHEM SOC*, vol. 150, Jan. 2003, doi: 10.1149/1.1524612.
- [166] “Photoluminescence Mapping of Optical Defects in HPHT Synthetic Diamond | Gems & Gemology.” Accessed: Nov. 03, 2022. [Online]. Available: <http://www.gia.edu/sites/Satellite?c=Page&cid=1495253526043&childpagename=GIA/Page/GGArticleDetail&pagename=GIA/Wrapper&WRAPPERPAGE=GIA/Wrapper>
- [167] “Green Diamond Buying Guide: Diamonds for the Elite Collector,” International Gem Society. Accessed: Oct. 09, 2022. [Online]. Available: <https://www.gemsociety.org/article/green-diamond-buying-guide/>
- [168] “15 Carat HPHT Synthetic Diamond | Gems & Gemology.” Accessed: Nov. 03, 2022. [Online]. Available: <http://www.gia.edu/sites/Satellite?c=Page&cid=1495265422761&childpagename=GIA/Page/GGArticleDetail&pagename=GIA/Wrapper&WRAPPERPAGE=GIA/Wrapper>
- [169] “Forging Cubic Synthetic Diamond Making Machine-Lab grown diamond for sale|Diamond micron powder|Metal powder|CBN powder-Henan Huanghe Whirlwind Co.,Ltd.” Accessed: Apr. 23, 2023. [Online]. Available: <https://www.huanghewhirlwind.com/products/Forging-Cubic-Synthetic-Diamond-Making-Machine.html>
- [170] W. van den Brink and N. Lamerigts, “Complete Osseointegration of a Retrieved 3-D Printed Porous Titanium Cervical Cage,” *Frontiers in Surgery*, vol. 7, p. 526020, Nov. 2020, doi: 10.3389/fsurg.2020.526020.
- [171] A. Rifai, S. Houshyar, and K. Fox, “Progress towards 3D-printing diamond for medical implants: A review,” *Annals of 3D Printed Medicine*, vol. 1, p. 100002, Mar. 2021, doi: 10.1016/j.stlm.2020.100002.
- [172] “CVD diamond—Research, applications, and challenges | MRS Bulletin | Cambridge Core.” Accessed: Apr. 21, 2023. [Online]. Available: <https://www.cambridge.org/core/journals/mrs-bulletin/article/cvd-diamondresearch-applications-and-challenges/259CD6D3BA75F89755E5AC12EB0EB05F>
- [173] C. Lee, H. W. Choi, E. Gu, M. Dawson, and H. Murphy, “Fabrication and characterization of diamond micro-optics,” *Diamond and Related Materials*, vol. 15, pp. 725–728, Apr. 2006, doi: 10.1016/j.diamond.2005.09.033.
- [174] A. H. H. Mevold *et al.*, “Fabrication of Gold Nanoparticles/Graphene-PDDA Nanohybrids for Bio-detection by SERS Nanotechnology,” *Nanoscale Research Letters*, vol. 10, no. 1, p. 397, Oct. 2015, doi: 10.1186/s11671-015-1101-2.
- [175] N. S. Lawand, P. J. French, J. J. Briaire, and J. H. M. Frijns, “Thin Titanium Nitride Films Deposited using DC Magnetron Sputtering used for Neural Stimulation and Sensing Purposes,” *Procedia Engineering*, vol. 47, pp. 726–729, Jan. 2012, doi: 10.1016/j.proeng.2012.09.250.
- [176] S. Datta, M. Das, V. K. Balla, S. Bodhak, and V. K. Murugesan, “Mechanical, wear, corrosion and biological properties of arc deposited titanium nitride coatings,” *Surface and Coatings Technology*, vol. 344, pp. 214–222, Jun. 2018, doi: 10.1016/j.surfcoat.2018.03.019.
-

- [177] "Five hidden sources of contamination in the cleanroom." Accessed: Nov. 18, 2022. [Online]. Available: [https://www.cleanroomtechnology.com/news/article\\_page/Five\\_hidden\\_sources\\_of\\_contamination\\_in\\_the\\_cleanroom/201272](https://www.cleanroomtechnology.com/news/article_page/Five_hidden_sources_of_contamination_in_the_cleanroom/201272)
- [178] S. Reynolds, "The Six Most Common Contaminants a Clean Room Removes," Swift Glass. Accessed: Nov. 18, 2022. [Online]. Available: <https://www.swiftglass.com/blog/six-most-common-contaminants-clean-room-removes/>
- [179] "Common Cleanroom Contamination Sources," <https://cleanroom.lakeland.com/>. Accessed: Nov. 18, 2022. [Online]. Available: <https://cleanroom.lakeland.com/common-cleanroom-contamination-sources/>
- [180] "How to Prevent Cleanroom Contamination," ACH Engineering. Accessed: Nov. 18, 2022. [Online]. Available: <https://www.achengineering.com/how-to-prevent-cleanroom-contamination/>
- [181] M. Ramstorp, *Introduction to Contamination Control and Cleanroom Technology*. John Wiley & Sons, 2008.
- [182] "Equivalent Circuit - an overview | ScienceDirect Topics." Accessed: Mar. 09, 2023. [Online]. Available: <https://www.sciencedirect.com/topics/engineering/equivalent-circuit>
- [183] B.-Y. Chang, "Conversion of a Constant Phase Element to an Equivalent Capacitor," *J. Electrochem. Sci. Technol*, vol. 11, no. 3, pp. 318–321, Aug. 2020, doi: 10.33961/jecst.2020.00815.
- [184] A. Karmakar and B. Biswas, "Electrical Equivalent Circuit Modeling of Various Electrically Small Antennas for Biomedical Applications," Jan. 2022.
- [185] N. H. N. Azman, S. Mamat, H. Lim, and Y. Sulaiman, "Graphene-based ternary composites for supercapacitors," *International Journal of Energy Research*, vol. 42, Feb. 2018, doi: 10.1002/er.4001.
- [186] H.-J. Choi, "Graphene for energy conversion and storage in fuel cells and supercapacitors," p. 18.
- [187] G. A. Snook, P. Kao, and A. S. Best, "Conducting-polymer-based supercapacitor devices and electrodes," *Journal of Power Sources*, vol. 196, pp. 1–12, Jan. 2011, doi: 10.1016/j.jpowsour.2010.06.084.
- [188] Z. Zhao, G. F. Richardson, Q. Meng, S. Zhu, H.-C. Kuan, and J. Ma, "PEDOT-based composites as electrode materials for supercapacitors," *Nanotechnology*, vol. 27, no. 4, p. 042001, Jan. 2016, doi: 10.1088/0957-4484/27/4/042001.
- [189] "What Is a Pseudocapacitor? - Capacitors Explained." Accessed: Mar. 09, 2023. [Online]. Available: <http://www.skeletontech.com/skeleton-blog/what-is-a-pseudocapacitor-capacitors-explained>
- [190] Q. Zheng, Z. Cai, Z. Ma, and S. Gong, "Cellulose Nanofibril/Reduced Graphene Oxide/Carbon Nanotube Hybrid Aerogels for Highly Flexible and All-Solid-State Supercapacitors," *ACS Appl. Mater. Interfaces*, vol. 7, no. 5, pp. 3263–3271, Feb. 2015, doi: 10.1021/am507999s.
- [191] S. R. Sinha *et al.*, "American Clinical Neurophysiology Society Guideline 1: Minimum Technical Requirements for Performing Clinical Electroencephalography," *J Clin Neurophysiol*, vol. 33, no. 4, pp. 303–307, Aug. 2016, doi: 10.1097/WNP.0000000000000308.
- [192] M. Nuwer, "Assessment of digital EEG, quantitative EEG, and EEG brain mapping: Report of the American Academy of Neurology and the American Clinical Neurophysiology Society".
- [193] N. Elgrishi, K. J. Rountree, B. D. McCarthy, E. S. Rountree, T. T. Eisenhart, and J. L. Dempsey, "A Practical Beginner's Guide to Cyclic Voltammetry," *J. Chem. Educ.*, p. 10, 2018.
- [194] A. Fürstenberg and A. Davenport, "Comparison of multifrequency bioelectrical impedance analysis and dual-energy X-ray absorptiometry assessments in outpatient hemodialysis patients," *Am J Kidney Dis*, vol. 57, no. 1, pp. 123–129, Jan. 2011, doi: 10.1053/j.ajkd.2010.05.022.
-



- [195] M. Adachi *et al.*, "Comparison of Electrochemical Impedance Spectroscopy between Illumination and Dark Conditions," *Chemistry Letters*, vol. 40, pp. 890–892, Aug. 2011, doi: 10.1246/cl.2011.890.
- [196] P. Von Hurst, D. Walsh, C. Conlon, M. Ingram, and R. Kruger, "Validity and reliability of bioelectrical impedance analysis to estimate body fat percentage against air displacement plethysmography and dual-energy X-ray absorptiometry: Validity/reliability of body composition methods," *Nutrition & Dietetics*, vol. 73, Apr. 2015, doi: 10.1111/1747-0080.12172.
- [197] J. J. Merrigan, S. Gallo, and J. B. Fields, "Foot-to-Foot Bioelectrical Impedance, Air Displacement Plethysmography, and Dual Energy X-ray Absorptiometry in Resistance-Trained Men and Women," 2018.
- [198] D. R. Wagner, "Bioelectrical impedance changes of the trunk are opposite the limbs following acute hydration change," *Journal of Electrical Bioimpedance*, vol. 13, no. 1, pp. 25–30, Jan. 2022, doi: 10.2478/joeb-2022-0005.
- [199] C. O'Brien, A. Young, and M. Sawka, "Bioelectrical Impedance to Estimate Changes in Hydration Status," *International journal of sports medicine*, vol. 23, pp. 361–6, Aug. 2002, doi: 10.1055/s-2002-33145.
- [200] E. S. Kappenman and S. J. Luck, "The Effects of Electrode Impedance on Data Quality and Statistical Significance in ERP Recordings," *Psychophysiology*, vol. 47, no. 5, pp. 888–904, Sep. 2010, doi: 10.1111/j.1469-8986.2010.01009.x.
- [201] C. M. A. Brett, "Electrochemical Impedance Spectroscopy in the Characterisation and Application of Modified Electrodes for Electrochemical Sensors and Biosensors," *Molecules*, vol. 27, no. 5, Art. no. 5, Jan. 2022, doi: 10.3390/molecules27051497.
- [202] "(13) (PDF) Does Impedance Matter When Recording Spikes With Polytrodes?" Accessed: Mar. 10, 2023. [Online]. Available: [https://www.researchgate.net/publication/328151307\\_Does\\_Impedance\\_Matter\\_When\\_Recording\\_Spikes\\_With\\_Polytrodes/figures?lo=1&utm\\_source=google&utm\\_medium=organic](https://www.researchgate.net/publication/328151307_Does_Impedance_Matter_When_Recording_Spikes_With_Polytrodes/figures?lo=1&utm_source=google&utm_medium=organic)
- [203] A. Suarez-Perez *et al.*, "Quantification of Signal-to-Noise Ratio in Cerebral Cortex Recordings Using Flexible MEAs With Co-localized Platinum Black, Carbon Nanotubes, and Gold Electrodes," *Front Neurosci*, vol. 12, p. 862, Nov. 2018, doi: 10.3389/fnins.2018.00862.
- [204] Z. Lukács and T. Kristóf, "A generalized model of the equivalent circuits in the electrochemical impedance spectroscopy," *Electrochimica Acta*, vol. 363, p. 137199, Dec. 2020, doi: 10.1016/j.electacta.2020.137199.
- [205] L. Khalafi, M. Rafiee, and A. Summers, "Electrochemistry Under Microscope: Measuring the Thickness of Diffusion Layer in Thin Layer Electrochemical Cells with Optical Microscope," *Meet. Abstr.*, vol. MA2021-02, no. 47, p. 1397, Oct. 2021, doi: 10.1149/MA2021-02471397mtgabs.
- [206] H. Magar, Y. Rabeay, R. Hassan, and A. Mulchandani, "Electrochemical Impedance Spectroscopy (EIS): Principles, Construction, and Biosensing Applications," *Sensors*, vol. 21, p. 6578, Oct. 2021, doi: 10.3390/s21196578.
- [207] L. Zhao, H. Dai, F. Pei, P. Ming, X. Wei, and J. Zhou, "A Comparative Study of Equivalent Circuit Models for Electro-Chemical Impedance Spectroscopy Analysis of Proton Exchange Membrane Fuel Cells," *Energies*, vol. 15, no. 1, Art. no. 1, Jan. 2022, doi: 10.3390/en15010386.
- [208] "Ohm's law," *Wikipedia*. Sep. 12, 2022. Accessed: Oct. 04, 2022. [Online]. Available: [https://en.wikipedia.org/w/index.php?title=Ohm%27s\\_law&oldid=1109893707](https://en.wikipedia.org/w/index.php?title=Ohm%27s_law&oldid=1109893707)
- [209] J. Sihvo, D.-I. Stroe, T. Messo, and T. Roinila, "A Fast Approach for Battery Impedance Identification Using Pseudo Random Sequence (PRS) Signals," *IEEE Transactions on Power Electronics*, vol. PP, pp. 1–1, Jul. 2019, doi: 10.1109/TPEL.2019.2924286.
- [210] M. Carminati, G. Ferrari, D. Bianchi, and M. Sampietro, "Impedance Spectroscopy for Biosensing: Circuits and Applications," in *Handbook of Biochips: Integrated Circuits and*
-

- Systems for Biology and Medicine*, M. Sawan, Ed., New York, NY: Springer, 2022, pp. 87–110.  
doi: 10.1007/978-1-4614-3447-4\_30.
- [211] H. S. Magar, R. Y. A. Hassan, and A. Mulchandani, “Electrochemical Impedance Spectroscopy (EIS): Principles, Construction, and Biosensing Applications,” *Sensors*, vol. 21, no. 19, Art. no. 19, Jan. 2021, doi: 10.3390/s21196578.
- [212] “Electrochemical Impedance Spectroscopy of Tap Water | Zurich Instruments.” Accessed: Mar. 10, 2023. [Online]. Available: <https://www.zhinst.com/jp/blogs/electrochemical-impedance-spectroscopy-tap-water>
- [213] J. Dykstra, “Desalination with porous electrodes,” 2018.
- [214] “(12) Graphical analysis of electrochemical impedance spectroscopy data in Bode and Nyquist representations | Request PDF.” Accessed: Mar. 09, 2023. [Online]. Available: [https://www.researchgate.net/publication/293196097\\_Graphical\\_analysis\\_of\\_electrochemical\\_impedance\\_spectroscopy\\_data\\_in\\_Bode\\_and\\_Nyquist\\_representations](https://www.researchgate.net/publication/293196097_Graphical_analysis_of_electrochemical_impedance_spectroscopy_data_in_Bode_and_Nyquist_representations)
- [215] “Warburg element,” *Wikipedia*. Jul. 18, 2022. Accessed: Dec. 11, 2022. [Online]. Available: [https://en.wikipedia.org/w/index.php?title=Warburg\\_element&oldid=1099053746](https://en.wikipedia.org/w/index.php?title=Warburg_element&oldid=1099053746)
- [216] “Diffusion layer,” *Wikipedia*. Feb. 22, 2021. Accessed: Feb. 09, 2023. [Online]. Available: [https://en.wikipedia.org/w/index.php?title=Diffusion\\_layer&oldid=1008249240](https://en.wikipedia.org/w/index.php?title=Diffusion_layer&oldid=1008249240)
- [217] A. Molina, J. González, E. Laborda, and R. G. Compton, “On the meaning of the diffusion layer thickness for slow electrode reactions,” *Phys. Chem. Chem. Phys.*, vol. 15, no. 7, pp. 2381–2388, Jan. 2013, doi: 10.1039/C2CP43650G.
- [218] M. Lacey, “Diffusion impedance,” Matt Lacey. Accessed: Jan. 17, 2023. [Online]. Available: <http://lacey.se/science/eis/diffusion-impedance/>
- [219] B.-A. Mei, O. Munteshari, J. Lau, B. Dunn, and L. Pilon, “Physical Interpretations of Nyquist Plots for EDLC Electrodes and Devices,” *J. Phys. Chem. C*, vol. 122, no. 1, pp. 194–206, Jan. 2018, doi: 10.1021/acs.jpcc.7b10582.
- [220] M. Biesheuvel, S. Porada, and J. Dykstra, *The difference between Faradaic and non-Faradaic electrode processes*. 2018.
- [221] “Practical implications of some recent studies in electrospray ionization fundamentals - PubMed.” Accessed: Mar. 09, 2023. [Online]. Available: <https://pubmed.ncbi.nlm.nih.gov/11997944/>
- [222] J. Wu, “Understanding the Electric Double-Layer Structure, Capacitance, and Charging Dynamics,” *Chem. Rev.*, vol. 122, no. 12, pp. 10821–10859, Jun. 2022, doi: 10.1021/acs.chemrev.2c00097.
- [223] “Electric Double Layer.” Accessed: Dec. 07, 2022. [Online]. Available: <https://faculty.kfupm.edu.sa/ME/hussaini/Corrosion%20Engineering/02.05.04.htm>
- [224] “Helmholtz Layer - an overview | ScienceDirect Topics.” Accessed: Mar. 09, 2023. [Online]. Available: <https://www.sciencedirect.com/topics/engineering/helmholtz-layer>
- [225] B. Rehl *et al.*, “Water Structure in the Electrical Double Layer and the Contributions to the Total Interfacial Potential at Different Surface Charge Densities,” *J. Am. Chem. Soc.*, vol. 144, no. 36, pp. 16338–16349, Sep. 2022, doi: 10.1021/jacs.2c01830.
- [226] “Water is a Polar Molecule | Chapter 5: The Water Molecule and Dissolving | Middle School Chemistry.” Accessed: Mar. 09, 2023. [Online]. Available: <https://www.middleschoolchemistry.com/lessonplans/chapter5/lesson1>
- [227] “Energies | Free Full-Text | The Characterization of the Electric Double-Layer Capacitor (EDLC) Using Python/MATLAB/Simulink (PMS)-Hybrid Model.” Accessed: Mar. 09, 2023. [Online]. Available: <https://www.mdpi.com/1996-1073/15/14/5193>
- [228] B.-Y. Chang, “The Effective Capacitance of a Constant Phase Element with Resistors in Series,” *J. Electrochem. Sci. Technol.*, vol. 13, no. 4, pp. 479–485, Sep. 2022, doi: 10.33961/jecst.2022.00451.
- [229] “Nyquist plot,” PalmSens. Accessed: Sep. 16, 2022. [Online]. Available: <https://www.palmsens.com/knowledgebase-topic/nyquist-plot/>
-

- [230] "Basics of EIS: Electrochemical Research-Impedance Gamry Instruments." Accessed: Sep. 24, 2022. [Online]. Available: <https://www.gamry.com/application-notes/EIS/basics-of-electrochemical-impedance-spectroscopy/>
- [231] I. Epelboin, P. Morel, and H. Takenouti, "Corrosion Inhibition and Hydrogen Adsorption in the Case of Iron in a Sulfuric Aqueous Medium," *J. Electrochem. Soc.*, vol. 118, no. 8, p. 1282, Aug. 1971, doi: 10.1149/1.2408306.
- [232] L. Young, "Anodic oxide films: Part 4. - The interpretation of impedance measurements on oxide coated electrodes on niobium," *Transactions of the Faraday Society*, vol. 51, pp. 1250–1260, 1955, doi: 10.1039/TF9555101250.
- [233] U. Rammelt, G. Reinhard, and K. Rammelt, "Impedance dispersion on coated metal electrodes," *Journal of Electroanalytical Chemistry and Interfacial Electrochemistry*, vol. 180, no. 1, pp. 327–336, Dec. 1984, doi: 10.1016/0368-1874(84)83590-X.
- [234] M. Kendig, F. Mansfeld, and S. Tsai, "Determination of the long term corrosion behavior of coated steel with A.C. impedance measurements," *Corrosion Science*, vol. 23, no. 4, pp. 317–329, Jan. 1983, doi: 10.1016/0010-938X(83)90064-1.
- [235] U. Rammelt and G. Reinhard, "Application of electrochemical impedance spectroscopy (EIS) for characterizing the corrosion-protective performance of organic coatings on metals," *Progress in Organic Coatings*, vol. 21, no. 2, pp. 205–226, Dec. 1992, doi: 10.1016/0033-0655(92)87005-U.
- [236] G. Reinhard, U. Rammelt, and K. Rammelt, "Analysis of impedance spectra on corroding metals," *Corrosion Science*, vol. 26, no. 2, pp. 109–120, Jan. 1986, doi: 10.1016/0010-938X(86)90040-5.
- [237] Z. Kerner and T. Pajkossy, "On the origin of capacitance dispersion of rough electrodes," *Electrochimica Acta*, vol. 46, no. 2, pp. 207–211, Nov. 2000, doi: 10.1016/S0013-4686(00)00574-0.
- [238] B. Ibrahim, D. A. Hall, and R. Jafari, "Bio-impedance spectroscopy (BIS) measurement system for wearable devices," *2017 IEEE Biomedical Circuits and Systems Conference (BioCAS)*, pp. 1–4, Oct. 2017, doi: 10.1109/BIOCAS.2017.8325138.
- [239] U. Kasiviswanathan, S. Poddar, C. Kumar, S. Jit, S. K. Mahto, and N. Sharma, "A portable standalone wireless electric cell-substrate impedance sensing (ECIS) system for assessing dynamic behavior of mammalian cells," *Journal of Analytical Science and Technology*, vol. 11, no. 1, p. 25, Jun. 2020, doi: 10.1186/s40543-020-00223-9.
- [240] S. Abasi, J. R. Aggas, G. G. Garayar-Leyva, B. K. Walther, and A. Guiseppi-Elie, "Bioelectrical Impedance Spectroscopy for Monitoring Mammalian Cells and Tissues under Different Frequency Domains: A Review," *ACS Meas. Au*, Aug. 2022, doi: 10.1021/acsmesuresciau.2c00033.
- [241] K. S. Cole, "ELECTRIC IMPEDANCE OF SUSPENSIONS OF SPHERES," *Journal of General Physiology*, vol. 12, no. 1, pp. 29–36, Sep. 1928, doi: 10.1085/jgp.12.1.29.
- [242] "Analog Discovery 2 Reference Manual - Digilent Reference." Accessed: Sep. 16, 2022. [Online]. Available: <https://digilent.com/reference/test-and-measurement/analog-discovery-2/reference-manual>
- [243] "Documentation Downloads: Quick Start Guides|Manuals|Installation Notes Gamry Instruments." Accessed: Dec. 07, 2022. [Online]. Available: <https://www.gamry.com/support-2/documentation-downloads/>
- [244] "HP Agilent Keysight, 4194A." Accessed: Sep. 16, 2022. [Online]. Available: <https://www.sglabs.it/en/product.php?s=hp-agilent-4194a&id=1521>
- [245] S. Nomura *et al.*, "Randles circuit model for characterizing a porous stimulating electrode of the retinal prosthesis," *Electronics and Communications in Japan*, vol. 104, no. 3, p. e12324, 2021, doi: 10.1002/ecj.12324.
- [246] "Water electrolysis: from textbook knowledge to the latest scientific strategies and industrial developments - Chemical Society Reviews (RSC Publishing) DOI:10.1039/D0CS01079K." Accessed: Mar. 12, 2023. [Online]. Available: <https://pubs.rsc.org/en/content/articlehtml/2022/cs/d0cs01079k>
-

- [247] "(16) Hydrogen-terminated diamond electrodes. I. Charges, potentials, and energies | Request PDF." Accessed: Mar. 12, 2023. [Online]. Available: [https://www.researchgate.net/publication/23463945\\_Hydrogen-terminated\\_diamond\\_electrodes\\_I\\_Charges\\_potentials\\_and\\_energies](https://www.researchgate.net/publication/23463945_Hydrogen-terminated_diamond_electrodes_I_Charges_potentials_and_energies)
- [248] C. Chaparro, L. Herrera, A. Melendez, and D. Miranda, "Considerations on electrical impedance measurements of electrolyte solutions in a four-electrode cell," *Journal of Physics: Conference Series*, vol. 687, p. 012101, Feb. 2016, doi: 10.1088/1742-6596/687/1/012101.
- [249] M. Grossi and B. Riccò, "Electrical impedance spectroscopy (EIS) for biological analysis and food characterization: a review," *Journal of Sensors and Sensor Systems*, vol. 6, no. 2, pp. 303–325, Aug. 2017, doi: 10.5194/jsss-6-303-2017.
- [250] D. K. Pattadar, J. N. Sharma, B. P. Mainali, and F. P. Zamborini, "Impact of the Assembly Method on the Surface Area-to-Volume Ratio and Electrochemical Oxidation Potential of Metal Nanospheres," *J. Phys. Chem. C*, vol. 123, no. 39, pp. 24304–24312, Oct. 2019, doi: 10.1021/acs.jpcc.9b06555.
- [251] M. E. Orazem, P. Shukla, and M. A. Membrino, "Extension of the measurement model approach for deconvolution of underlying distributions for impedance measurements," *Electrochimica Acta*, vol. 47, no. 13, pp. 2027–2034, May 2002, doi: 10.1016/S0013-4686(02)00065-8.
- [252] F. Yang, "Size effect on electric-double-layer capacitances of conducting structures," *Physics Letters A*, vol. 383, no. 20, pp. 2353–2360, Jul. 2019, doi: 10.1016/j.physleta.2019.04.051.
- [253] "Electric Double Layer - an overview | ScienceDirect Topics." Accessed: Feb. 10, 2023. [Online]. Available: <https://www.sciencedirect.com/topics/engineering/electric-double-layer>
- [254] "(16) (PDF) Surface-modified microelectrode array with flake nanostructure for neural recording and stimulation." Accessed: Mar. 13, 2023. [Online]. Available: [https://www.researchgate.net/publication/41139389\\_Surface-modified\\_microelectrode\\_array\\_with\\_flake\\_nanostructure\\_for\\_neural\\_recording\\_and\\_stimulation/figures?lo=1&utm\\_source=google&utm\\_medium=organic](https://www.researchgate.net/publication/41139389_Surface-modified_microelectrode_array_with_flake_nanostructure_for_neural_recording_and_stimulation/figures?lo=1&utm_source=google&utm_medium=organic)
- [255] D. Stan *et al.*, "What Is the Optimal Method for Cleaning Screen-Printed Electrodes?," *Processes*, vol. 10, no. 4, Art. no. 4, Apr. 2022, doi: 10.3390/pr10040723.
- [256] S. M. Gateman, O. Gharbi, H. Gomes de Melo, K. Ngo, M. Turmine, and V. Vivier, "On the use of a constant phase element (CPE) in electrochemistry," *Current Opinion in Electrochemistry*, vol. 36, p. 101133, Dec. 2022, doi: 10.1016/j.coelec.2022.101133.
- [257] "Titanium Nitride (TiN) Coating." Accessed: Feb. 07, 2023. [Online]. Available: [https://www.matweb.com/search/datasheet\\_print.aspx?matguid=ffbf753c500949db95e502e043f9a404](https://www.matweb.com/search/datasheet_print.aspx?matguid=ffbf753c500949db95e502e043f9a404)
- [258] J. Weiland, D. Anderson, and M. Ph.D, "In Vitro Electrical Properties for Iridium Oxide Versus Titanium Nitride Stimulating Electrodes," *IEEE transactions on bio-medical engineering*, vol. 49, pp. 1574–9, Jan. 2003, doi: 10.1109/TBME.2002.805487.
- [259] X. Li *et al.*, "Investigation of flexible electrodes modified by TiN, Pt black and IrOx," *Science China Technological Sciences*, vol. 54, pp. 2305–2309, Sep. 2011, doi: 10.1007/s11431-011-4436-7.
- [260] G. Ganske, E. Slavcheva, A. van Ooyen, W. Mokwa, and U. Schnakenberg, "Sputtered platinum-iridium layers as electrode material for functional electrostimulation," *Thin Solid Films*, vol. 519, no. 11, pp. 3965–3970, Mar. 2011, doi: 10.1016/j.tsf.2011.01.344.
- [261] J. A. Coles, "Light-induced changes in the electrical impedance of the isolated frog retina," *J Physiol*, vol. 227, no. 3, pp. 815–838, Dec. 1972, doi: 10.1113/jphysiol.1972.sp010060.
- [262] S. Arshadi Rastabi, R. Sarraf-Mamoory, G. Razaz, N. Blomquist, M. Hummelgård, and H. Olin, "Treatment of NiMoO<sub>4</sub>/nanographite nanocomposite electrodes using flexible graphite substrate for aqueous hybrid supercapacitors," *PLoS One*, vol. 16, no. 7, p. e0254023, Jul. 2021, doi: 10.1371/journal.pone.0254023.
-

- [263] A. Shameem, P. Devendran, V. Siva, R. Packiaraj, N. Nallamuthu, and S. Asath Bahadur, "Electrochemical performance and optimization of  $\alpha$ -NiMoO<sub>4</sub> by different facile synthetic approach for supercapacitor application," *J Mater Sci: Mater Electron*, vol. 30, no. 4, pp. 3305–3315, Feb. 2019, doi: 10.1007/s10854-018-00603-3.
- [264] J. Yang *et al.*, "Ultrahigh energy density battery-type asymmetric supercapacitors: NiMoO<sub>4</sub> nanorod-decorated graphene and graphene/Fe<sub>2</sub>O<sub>3</sub> quantum dots," *Nano Res.*, vol. 11, no. 9, pp. 4744–4758, Sep. 2018, doi: 10.1007/s12274-018-2059-z.
- [265] N. Mishra, S. Shinde, R. Vishwakarma, S. Kadam, and M. Sharon, *MWCNTs Synthesized From Waste Polypropylene Plastics and its Application in Super-capacitors*, vol. 1538. 2013. doi: 10.1063/1.4810063.
- [266] B.-Y. Chang, "The Effective Capacitance of a Constant Phase Element with Resistors in Series and Parallel." Rochester, NY, Apr. 09, 2022. doi: 10.2139/ssrn.4079679.
- [267] G. Palasantzas and G. M. E. A. Backx, "Roughness effects on the double-layer charge capacitance: the case of Helmholtz layer induced roughness attenuation," *Surface Science*, vol. 540, no. 2, pp. 401–406, Aug. 2003, doi: 10.1016/S0039-6028(03)00877-X.
- [268] L. I. Daikhin, A. A. Kornyshev, and M. Urbakh, "Double layer capacitance on a rough metal surface: Surface roughness measured by 'Debye ruler,'" *Electrochimica Acta*, vol. 42, no. 19, pp. 2853–2860, Jan. 1997, doi: 10.1016/S0013-4686(97)00106-0.
- [269] S. Sarkar, A. Sarrafnazhad, and A. Ghoncheh, "Understanding Resonance, Quality Factor and Series to Parallel Conversion," Rahsoft. Accessed: Mar. 12, 2023. [Online]. Available: <https://rahsoft.com/2021/08/09/understanding-quality-factor-and-series-to-parallel-conversion-with-example/>
- [270] "Series to Parallel Impedance Transformation." Accessed: Mar. 12, 2023. [Online]. Available: [https://aaronsher.com/Circuit\\_a\\_Day/Impedance\\_matching/series\\_parallel/series\\_parallel.html](https://aaronsher.com/Circuit_a_Day/Impedance_matching/series_parallel/series_parallel.html)
- [271] M. Yoshimura *et al.*, "Factors controlling the electrochemical potential window for diamond electrodes in non-aqueous electrolytes," *Diamond and Related Materials*, vol. 11, pp. 67–74, Jan. 2002, doi: 10.1016/S0925-9635(01)00522-2.
- [272] "ii) Important parameters in CV," Chemistry LibreTexts. Accessed: Feb. 13, 2023. [Online]. Available: [https://chem.libretexts.org/Bookshelves/Analytical\\_Chemistry/Supplemental\\_Modules\\_\(Analytical\\_Chemistry\)/Analytical\\_Sciences\\_Digital\\_Library/Courseware/Analytical\\_Electrochemistry%3A\\_The\\_Basic\\_Concepts/04\\_Voltammetric\\_Methods/A\\_Basics\\_of\\_Voltammetry/02\\_Potential\\_Sweep\\_Methods/b\)\\_Cyclic\\_Voltammetry/ii\)\\_Important\\_parameters\\_in\\_CV](https://chem.libretexts.org/Bookshelves/Analytical_Chemistry/Supplemental_Modules_(Analytical_Chemistry)/Analytical_Sciences_Digital_Library/Courseware/Analytical_Electrochemistry%3A_The_Basic_Concepts/04_Voltammetric_Methods/A_Basics_of_Voltammetry/02_Potential_Sweep_Methods/b)_Cyclic_Voltammetry/ii)_Important_parameters_in_CV)
- [273] S. F. Cogan, K. A. Ludwig, C. G. Welle, and P. Takmakov, "Tissue damage thresholds during therapeutic electrical stimulation," *J Neural Eng*, vol. 13, no. 2, p. 021001, Apr. 2016, doi: 10.1088/1741-2560/13/2/021001.
- [274] R. Sidhu, N. Cavallaro, C. Pola, M. Danyluk, E. Mclamore, and C. Gomes, "Planar Interdigitated Aptasensor for Flow-Through Detection of *Listeria* spp. in Hydroponic Lettuce Growth Media," *Sensors*, vol. 20, p. 5773, Oct. 2020, doi: 10.3390/s20205773.
- [275] T. Hughbanks, "Reaction Rates and Temperature; Arrhenius Theory".
- [276] G. Dagnelie, "Why aren't retinal prostheses as good as cochlear implants, and what can we do to change that?," *Journal of Vision*, vol. 19, no. 8, p. 50, Jul. 2019, doi: 10.1167/19.8.50.
- [277] M. Im, "Editorial for the Special Issue on Micro/Nanofabrication for Retinal Implants," *Micromachines*, vol. 11, no. 11, Art. no. 11, Nov. 2020, doi: 10.3390/mi11111005.
- [278] E. Borda and D. Ghezzi, "Advances in visual prostheses: engineering and biological challenges," *Prog. Biomed. Eng.*, vol. 4, no. 3, p. 032003, Aug. 2022, doi: 10.1088/2516-1091/ac812c.
- [279] E. Redolfi Riva and S. Micera, "Progress and challenges of implantable neural interfaces based on nature-derived materials," *Bioelectronic Medicine*, vol. 7, no. 1, p. 6, Apr. 2021, doi: 10.1186/s42234-021-00067-7.
-

- [280] D. Lemoine, E. Simon, G. Buc, and M. Deterre, "In vitro reliability testing and in vivo lifespan estimation of wireless Pixium Vision PRIMA photovoltaic subretinal prostheses suggest prolonged durability and functionality in clinical practice," *J. Neural Eng.*, vol. 17, no. 3, p. 035005, Jun. 2020, doi: 10.1088/1741-2552/ab8f70.
- [281] Q. Zeng, S. Zhao, H. Yang, Y. Zhang, and T. Wu, "Micro/Nano Technologies for High-Density Retinal Implant," *Micromachines*, vol. 10, no. 6, Art. no. 6, Jun. 2019, doi: 10.3390/mi10060419.
- [282] C. Hébert *et al.*, "Monitoring the evolution of boron doped porous diamond electrode on flexible retinal implant by OCT and in vivo impedance spectroscopy," *Materials Science and Engineering: C*, vol. 69, pp. 77–84, Dec. 2016, doi: 10.1016/j.msec.2016.06.032.
- [283] M. Tintelott, A. Schander, and W. Lang, "Understanding Electrical Failure of Polyimide-Based Flexible Neural Implants: The Role of Thin Film Adhesion," *Polymers*, vol. 14, no. 18, Art. no. 18, Jan. 2022, doi: 10.3390/polym14183702.
- [284] H. Hämmerle, K. Kobuch, K. Kohler, W. Nisch, H. Sachs, and M. Stelzle, "Biostability of micro-photodiode arrays for subretinal implantation," *Biomaterials*, vol. 23, no. 3, pp. 797–804, Feb. 2002, doi: 10.1016/S0142-9612(01)00185-5.
- [285] H. An, M. A. Ehsan, Z. Zhou, and Y. Yi, "Electrical modeling and analysis of 3D synaptic array using vertical RRAM structure," p. 6.
- [286] J. C. Barrese *et al.*, "Failure mode analysis of silicon-based intracortical microelectrode arrays in non-human primates," *J. Neural Eng.*, vol. 10, no. 6, p. 066014, Nov. 2013, doi: 10.1088/1741-2560/10/6/066014.
- [287] A. Lecomte, E. Descamps, and C. Bergaud, "A review on mechanical considerations for chronically-implanted neural probes," *J. Neural Eng.*, vol. 15, no. 3, p. 031001, Mar. 2018, doi: 10.1088/1741-2552/aa8b4f.
- [288] S.-H. Huang, S.-P. Lin, and J.-J. Chen, "In vitro and in vivo characterization of SU-8 flexible neuroprobe: From mechanical properties to electrophysiological recording," *Sensors and Actuators A: Physical*, vol. 216, pp. 257–265, Sep. 2014, doi: 10.1016/j.sna.2014.06.005.
- [289] A. Schander *et al.*, "Design and fabrication of novel multi-channel floating neural probes for intracortical chronic recording," *Sensors and Actuators A: Physical*, vol. 247, pp. 125–135, Aug. 2016, doi: 10.1016/j.sna.2016.05.034.
- [290] V. Castagnola *et al.*, "Parylene-based flexible neural probes with PEDOT coated surface for brain stimulation and recording," *Biosensors and Bioelectronics*, vol. 67, pp. 450–457, May 2015, doi: 10.1016/j.bios.2014.09.004.
- [291] E. Musk and Neuralink, "An Integrated Brain-Machine Interface Platform With Thousands of Channels," *Journal of Medical Internet Research*, vol. 21, no. 10, p. e16194, Oct. 2019, doi: 10.2196/16194.
- [292] C. J. Bettinger, M. Ecker, T. D. Y. Kozai, G. G. Malliaras, E. Meng, and W. Voit, "Recent advances in neural interfaces—Materials chemistry to clinical translation," *MRS Bulletin*, vol. 45, no. 8, pp. 655–668, Aug. 2020, doi: 10.1557/mrs.2020.195.
- [293] S. Han, A. G. Polyravas, S. Wustoni, S. Inal, and G. G. Malliaras, "Integration of Organic Electrochemical Transistors with Implantable Probes," *Advanced Materials Technologies*, vol. 6, no. 12, p. 2100763, 2021, doi: 10.1002/admt.202100763.
- [294] J.-M. Hsu, L. Rieth, R. A. Normann, P. Tathireddy, and F. Solzbacher, "Encapsulation of an Integrated Neural Interface Device With Parylene C," *IEEE Transactions on Biomedical Engineering*, vol. 56, no. 1, pp. 23–29, Jan. 2009, doi: 10.1109/TBME.2008.2002155.
- [295] K. Bennet *et al.*, "Raman Microscopic Analysis of Internal Stress in Boron-Doped Diamond," *Materials*, vol. 8, no. 5, pp. 2782–2793, May 2015, doi: 10.3390/ma8052782.
- [296] P. G. Losada *et al.*, "Protuberant Electrode Structures for Subretinal Electrical Stimulation: Modeling, Fabrication and in vivo Evaluation," *Front. Neurosci.*, vol. 13, p. 885, Aug. 2019, doi: 10.3389/fnins.2019.00885.
- [297] P. Pham, S. Roux, F. Matonti, F. Dupont, V. Agache, and F. Chavane, "Post-implantation impedance spectroscopy of subretinal micro-electrode arrays, OCT imaging and numerical
-

- simulation: towards a more precise neuroprosthesis monitoring tool,” *J. Neural Eng.*, vol. 10, no. 4, p. 046002, May 2013, doi: 10.1088/1741-2560/10/4/046002.
- [298] S. Shah, A. Hines, D. Zhou, R. J. Greenberg, M. S. Humayun, and J. D. Weiland, “Electrical properties of retinal–electrode interface,” *J. Neural Eng.*, vol. 4, no. 1, p. S24, Feb. 2007, doi: 10.1088/1741-2560/4/1/S04.
- [299] A. Ray, L. L. Chan, A. Gonzalez, M. S. Humayun, and J. D. Weiland, “Impedance as a Method to Sense Proximity at the Electrode-Retina Interface,” *IEEE Transactions on Neural Systems and Rehabilitation Engineering*, vol. 19, no. 6, pp. 696–699, Dec. 2011, doi: 10.1109/TNSRE.2011.2169428.
- [300] J. D. Weiland and M. S. Humayun, “Retinal Prosthesis,” *IEEE Trans Biomed Eng*, vol. 61, no. 5, pp. 1412–1424, May 2014, doi: 10.1109/TBME.2014.2314733.
- [301] C. Xie, J. Liu, T.-M. Fu, X. Dai, W. Zhou, and C. M. Lieber, “Three-dimensional macroporous nanoelectronic networks as minimally invasive brain probes,” *Nature Mater*, vol. 14, no. 12, Art. no. 12, Dec. 2015, doi: 10.1038/nmat4427.
- [302] M. A. M. Freire *et al.*, “Comprehensive Analysis of Tissue Preservation and Recording Quality from Chronic Multielectrode Implants,” *PLOS ONE*, vol. 6, no. 11, p. e27554, Nov. 2011, doi: 10.1371/journal.pone.0027554.
- [303] “EBSCOhost | 93920160 | Integrity of Implant Surface Modifications After Insertion.” Accessed: Jan. 16, 2023. [Online]. Available: <https://web.s.ebscohost.com/abstract?direct=true&profile=ehost&scope=site&authtype=crawler&jrnl=08822786&AN=93920160&h=bFr0y2Fw00v1vn%2fXSJFwgje9DYUmF%2bDWFAT0h%2bw9%2b5hGahH%2fGh9dj0mbn%2b64zgUbOTL8scBYysGqMHpNGj2Ow%3d%3d&crl=c&resultNs=AdminWebAuth&resultLocal=ErrCrlNotAuth&crlhashurl=login.aspx%3fdirect%3dtrue%26profile%3dehost%26scope%3dsite%26authtype%3dcrawler%26jrnl%3d08822786%26AN%3d93920160>
- [304] D. W. L. Hukins, A. Mahomed, and S. N. Kukureka, “Accelerated aging for testing polymeric biomaterials and medical devices,” *Medical Engineering & Physics*, vol. 30, no. 10, pp. 1270–1274, Dec. 2008, doi: 10.1016/j.medengphy.2008.06.001.
- [305] E. Métral, F. Caspers, N. Mounet, T. Pieloni, and B. Salvant, “Impedance and Component Heating,” in *Advanced Series on Directions in High Energy Physics*, vol. 24, WORLD SCIENTIFIC, 2015, pp. 269–280. doi: 10.1142/9789814675475\_0015.
- [306] “How does the heat affect resistance?” Accessed: Mar. 12, 2023. [Online]. Available: <https://www.vedantu.com/question-answer/does-the-heat-affect-resistance-class-12-physics-cbse-605d61d6dbad6a149ba8e7e8>
- [307] “7.11: Oxidation of Silicon,” Chemistry LibreTexts. Accessed: Apr. 23, 2023. [Online]. Available: [https://chem.libretexts.org/Bookshelves/Inorganic\\_Chemistry/Chemistry\\_of\\_the\\_Main\\_Group\\_Elements\\_\(Barron\)/07%3A\\_Group\\_14/7.11%3A\\_Oxidation\\_of\\_Silicon](https://chem.libretexts.org/Bookshelves/Inorganic_Chemistry/Chemistry_of_the_Main_Group_Elements_(Barron)/07%3A_Group_14/7.11%3A_Oxidation_of_Silicon)
- [308] AllAdmin, “Process procedure photoresist,” Allresist EN. Accessed: Apr. 23, 2023. [Online]. Available: <https://www.allresist.com/resist-wiki-process-procedure-photoresists/>
- [309] “HMDS,” EPFL. Accessed: Apr. 23, 2023. [Online]. Available: <https://www.epfl.ch/research/facilities/cmi/process/photolithography/hmds-application/>
- [310] Y. Didane, C. Videlot-Ackermann, H. Brisset, J. Ackermann, P. Raynal, and G. H. Mehl, “Liquid Crystal  $\alpha,\omega$ -Hexyl-Distyryl-Bithiophene: Morphology and Charge Transport Properties in Organic Thin Film Transistors,” *Molecular Crystals and Liquid Crystals - MOL CRYST LIQUID CRYST*, vol. 507, pp. 178–187, Sep. 2009, doi: 10.1080/15421400903050715.
- [311] “2. Mechanism of the vacuum thin film coating system,” ShinMaywa Industries, Ltd. Accessed: Apr. 23, 2023. [Online]. Available: [https://www.shinmaywa.co.jp/vac/english/vacuum/vacuum\\_2.html](https://www.shinmaywa.co.jp/vac/english/vacuum/vacuum_2.html)
- [312] “Annexe 3 PLATEFORMES, PROCEDES ET EQUIPEMENTS - PDF Free Download.” Accessed: Sep. 16, 2022. [Online]. Available: <https://docplayer.fr/52479242-Annexe-3-plateformes-procedes-et-equipements.html>
-

- [313] H. S. Zakria, M. H. D. Othman, R. Kamaludin, S. H. Sheikh Abdul Kadir, T. A. Kurniawan, and A. Jilani, "Immobilization techniques of a photocatalyst into and onto a polymer membrane for photocatalytic activity," *RSC Adv.*, vol. 11, no. 12, pp. 6985–7014, 2021, doi: 10.1039/D0RA10964A.
- [314] "Metal Analysis / Mineral Analysis / Gold Assay Office / PGM Catalyst Analysis / Alex Stewart International /." Accessed: Sep. 22, 2022. [Online]. Available: <https://alexstewartinternational.com/business/analysis-testing/metals-minerals-tests/>
- [315] A. Mishra, N. Bhatt, and A. K. Bajpai, "Nanostructured superhydrophobic coatings for solar panel applications," in *Nanomaterials-Based Coatings*, Elsevier, 2019, pp. 397–424. doi: 10.1016/B978-0-12-815884-5.00012-0.
- [316] N. Sahu, B. Parija, and S. Panigrahi, "Fundamental understanding and modeling of spin coating process: A review," *Indian J Phys*, vol. 83, no. 4, pp. 493–502, Apr. 2009, doi: 10.1007/s12648-009-0009-z.
- [317] *How To Spin Coat Resist*, (Mar. 02, 2018). Accessed: Apr. 23, 2023. [Online Video]. Available: <https://www.youtube.com/watch?v=WAFE6pZBT9c>
- [318] B. Faure *et al.*, "Dispersion and surface functionalization of oxide nanoparticles for transparent photocatalytic and UV-protecting coatings and sunscreens," *Science and Technology of Advanced Materials*, vol. 14, no. 2, p. 023001, Mar. 2013, doi: 10.1088/1468-6996/14/2/023001.
- [319] "Dry Etching vs Wet Etching: Everything You Need To Know," Wevolver. Accessed: Sep. 22, 2022. [Online]. Available: <https://www.wevolver.com/article/dry-etching-vs-wet-etching-everything-you-need-to-know>
- [320] B. T. Chiad, T. Al-zubaydi, M. Khalaf, and A. Khudiar, "Characterization of low pressure plasma-dc glow discharges (Ar, SF<sub>6</sub> and SF<sub>6</sub>/He) for Si etching," *Indian Journal of Pure and Applied Physics*, vol. 48, pp. 723–730, Oct. 2010.
- [321] "Passivation (chemistry) - Wikipedia." Accessed: Nov. 25, 2022. [Online]. Available: [https://en.wikipedia.org/wiki/Passivation\\_\(chemistry\)](https://en.wikipedia.org/wiki/Passivation_(chemistry))
- [322] A. Olziersky *et al.*, "Insight on the SU-8 resist as passivation layer for transparent Ga<sub>2</sub>O<sub>3</sub>-In<sub>2</sub>O<sub>3</sub>-ZnO thin-film transistors," *Journal of Applied Physics*, vol. 108, Sep. 2010, doi: 10.1063/1.3477192.
- [323] S. Ye, N. X. Williams, and A. D. Franklin, "Aerosol Jet Printing of SU-8 as a Passivation Layer Against Ionic Solutions," *J. Electron. Mater.*, vol. 51, no. 4, pp. 1583–1590, Apr. 2022, doi: 10.1007/s11664-021-09396-4.
- [324] "Passivation Layer - an overview | ScienceDirect Topics." Accessed: Nov. 25, 2022. [Online]. Available: <https://www.sciencedirect.com/topics/engineering/passivation-layer>
-